# Non-Invasive Measurement of Load Capacity of Trabecular Bones with Defects

Gregory D. Cabe
B.S. Aerospace Engineering
University of Texas at Austin, 1993

Submitted to the Department of Mechanical Engineering in
Partial Fulfillment of the Requirements for the Degree of

Master of Science in Mechanical Engineering
at the
Massachusetts Institute of Technology

January 1997
[ February ]

Signature of Author _____
Department of Mechanical Engineering

Certified by _____
Brian D. Snyder
Thesis Supervisor

Certified by _____
John A. Hipp
Thesis Supervisor

Certified by _____
Wilson C. Hayes
Thesis Supervisor

Accepted by _____
Ain A. Sonin
Chairman, Mechanical Engineering Graduate Committee

# Non-Invasive Measurement of Load Capacity of Trabecular Bones with Defects

Gregory D. Cabe

## ABSTRACT

Tumors, from benign osseous lesions common in children to metastatic tumors found in cancer patients, can weaken bones to the point that they fracture under loads common in everyday living. Unfortunately, current guidelines for assessing bones with tumors are based on old technologies and have proven imprecise, inaccurate, and inconsistent in predicting the risk of fracture. Better techniques are necessary for determining the load capacity of weakened bones in order to prevent fracture and monitor the effectiveness of various treatments.

Therefore, researches at Beth Israel's Orthopedic Biomechanics Laboratory and Children's Hospital of Boston, Massachusetts are attempting to develop a new technique that is both simple and inexpensive yet provides an accurate and reliable measurement of bone strength to aid in assessing the risk of fracture. They propose predicting bone load capacity by applying elementary composite beam theory to noninvasive measurements of a weakened bone cross-section at the site of a tumor. Non-invasive measurements could be provided through such techniques as Quantitative Computed Tomography (QCT), Magnetic Resonance Imaging (MRI), ultrasound, or Dual Energy X-ray Absorptiometry (DXA).

This thesis discusses a series of parametric experiments which investigated the ability of composite beam theory models using QCT to predict the reduction in load capacity associated with different shapes and sizes of holes in trabecular bone. One hundred fifteen cores of trabecular bone with simulated lytic defects were imaged with QCT and then tested to failure in four-point bending, tension, and torsion. The results of these experiments showed, first, that in bending, tension, and torsion, trabecular bone yields at a specific local strain. Supporting that conclusion, rigidity of a specimen's weakest cross-section was found to be the elastic property that best predicts the load capacity (both yield load and ultimate load) of trabecular bones with defects ($r^2 = 0.98$ for bending, $r^2 = 0.97$ for tension, $r^2 = 0.97$ for torsion). Furthermore, comparisons of experimental data to results from finite element models showed that stress-concentration factors were sufficiently insignificant in trabecular bone with rounded holes that they do not confound composite beam theory models in the prediction of load capacity.

Therefore, if the type of loads are known (bending, tension, and/or torsion), elementary solid mechanics calculations of the rigidity of the weakest cross-section should predict the load capacity of an entire bone weakened by a tumor. Also, the reduction in load capacity of a bone weakened by a tumor could be measured by comparing the rigidity of it's weakest cross-section to the rigidity of the corresponding cross-section in the healthy contralateral limb.

Finally, the experiments showed that QCT can accurately and noninvasively measure the rigidity of a trabecular bone cross-section ($r^2 = 0.92$ for bending, $r^2 = 0.87$ for tension, $r^2 = 0.94$ for torsion) and that QCT measurements of rigidity correlate very highly with yield and ultimate load ($r^2 = 0.92$ for bending, $r^2 = 0.95$ for tension, $r^2 = 0.89$ for torsion).

This study provides a fundamental assessment of the behavior of trabecular bone with holes from a controlled, parametric investigation. However, further tests are necessary to determine if the technique describe above is valid for cortical bone, composite cortical-trabecular bone, and composite bone *in-vivo*.

Thesis Supervisors:     John A. Hipp, Ph.D.

Brian D. Snyder, M.D., Ph.D.

Wilson C. Hayes, Ph.D.

# Acknowledgements

# Table of Contents

# Chapter 1
# Introduction

## 3.1 OVERVIEW

This research is part of a five-year project to develop a quantitative technique that predicts fracture risk in long bones with benign and metastatic defects, such as those shown in Figure 1.1. The technique predicts fracture risk by applying linear-elastic composite beam theory (Bernoulli-Euler solid mechanics) to calculate the load capacity of a bone. Non-invasive imaging techniques are used to measure the bone's mechanical properties for these calculations.
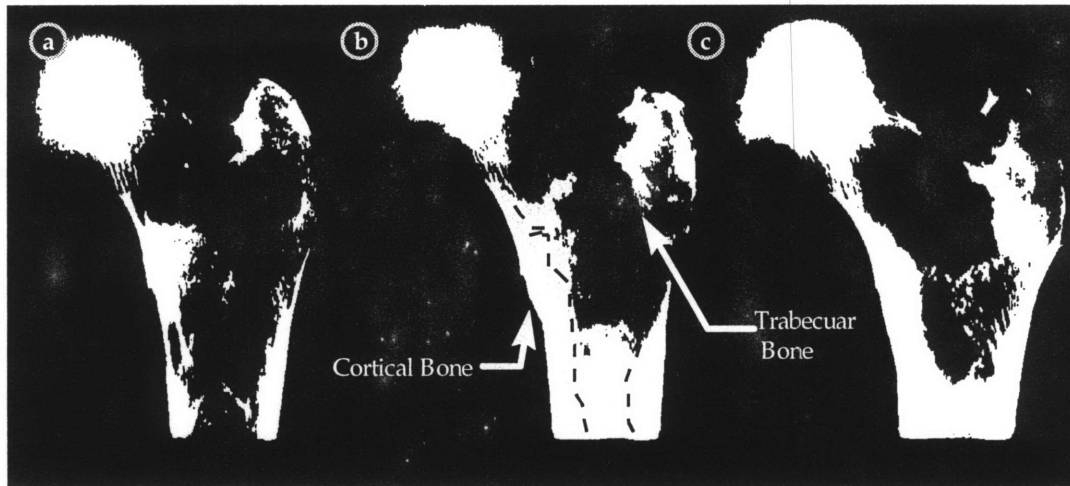


Figure 3.1 - Defects in human femurs can extend through both cortical and trabecular bone. a) defect through trabecular bone in the intertrochantric region, b) defect through the anterior cortex, c) defect through the posterior cortex, including trabecular bone.

Although the non-invasive technique is intended to predict fracture risk for entire bones (such as the femur and humerus), this thesis focuses only on its application to trabecular bone, using quantitative computed tomography as a non-invasive method of measuring mechanical properties of bone. Future studies will evaluate the technique for use with cortical and whole bones and other imaging data.

For this thesis, the prediction technique was investigated by using mechanical tests and finite element models to describe the behavior of trabecular bone specimens with holes. The results from these tests were used to determine if mechanical properties from

composite beam theory accurately predict load bearing capacity. The mechanical test results were also compared with non-invasive measurements using quantitative computed tomography in order to determine if this imaging technique, coupled with composite beam theory, can predict the mechanical behavior of trabecular bones with holes.

## 3.2 MOTIVATION - THE CLINICAL PROBLEM

Pathologic fractures resulting from benign and metastatic osseous defects in the appendicular and axial skeleton occur in people of all ages. The intractable bone pain, fear of sustaining a fracture, and morbidity of a pathologic fracture associated with these defects severely reduce the quality of patients' lives; and determining the appropriate treatment protocol is one of the most difficult problems facing orthopedists and caregivers.

Although malignant bone tumors in children are rare, benign skeletal defects are relatively common. Benign bone defects occur in 33% to 50% of asymptomatic children evaluated by random radiographs of long bones[1]. In the past ten years the Orthopaedic Oncology Service of the Massachusetts General Hospital has evaluated and treated 1,716 children and young adults with benign bone defects including: non-ossifying fibroma (131), fibrous dysplasia (231), unicameral bone cyst (157), aneurysmal bone cyst (112), giant-cell tumor (426), eosinophilic granuloma (38), enchondroma (357), hemangioma (235), and chondromyxoid fibroma (29)[2].

In adults, malignant tumors are more common, and the skeleton is the third most common site for metastatic spread of carcinoma[3]. There are over one million new cancer cases each year in the U.S.[4], and autopsies revealed that 60% to 80% of cancer victims have evidence of bone metastases[5]. Approximately 30% of bone metastases subsequently fracture or produce hypercalcemia, requiring treatment with radiation, bisphosphonates, glucocorticoid, or calcitonin[6]. When pathologic fractures occur in the femur, humerus, or periacetabular pelvis approximately 90% of patients require surgical intervention to relieve pain and restore function and mobility[7].

An accurate assessment of fracture risk is essential information for an orthopedist to determine the appropriate treatment for a bone defect, particularly when the orthopedist must decide whether or not to intervene surgically. The two guidelines (both based on plane radiographs) currently cited for making this decision are: 1) a defect greater than 2.5 cm in diameter should be considered at risk for fracture[8] and 2) greater than 50% destruction in the cortical wall indicates the need for prophylactic stabilization[9]. The guidelines are based on several retrospective clinical studies, but they are not based on engineering principles and have exhibited clinical error rates as high as 42%[8]. Several retrospective clinical reviews have shown that experienced orthopedic surgeons are unable to arrive at either subjective or simple geometric guidelines that can

effectively predict fracture risk using plane radiographs [10,11,12]. Several *in-vitro* studies of the behavior of bones with simulated defects have also indicated that load capacity depends on many factors not represented in current clinically accepted guidelines[13,14,15,16]. Taken together, these studies show that the critical parameters that determine the load-bearing capacity of a long-bone with a defect include the amount of bone lost, the geometry and elastic modulus of the remaining bone, the location of the defect with respect to the applied loads, and the type of applied loads.

To improve prevention of pathologic fracture, more accurate and precise guidelines are needed for assessing bone status when a defect initially presents as well as better techniques for assessing the success of the treatment protocol.

The assessment of bone status may be improved by calculating a factor of risk [17] which incorporates both the strength of a bone and the loads to which it may be subjected. The factor of risk is defined as the load applied to the bone (the load bearing requirement) divided by the load at which the bone would fail (the load bearing capacity):

$$\Phi = \frac{\text{Load bearing requirement}}{\text{Load bearing capacity}} \qquad [3.1]$$

When this ratio exceeds unity, the bone can be expected to fail. Unfortunately, previous investigations have only considered guidelines that include defect geometry, pain, age, anatomic site, lesion type, and activity levels[18,19,20,21,22,23]. None of these factors is a direct measure of either the numerator or denominator of the factor of risk, and they typically rely only on information from plane radiographs.

## 3.3 SUBJECT - THE POSSIBLE SOLUTION

The objective of the Whitcker Foundation grant funding this study is to develop improved, practical methods for measuring fracture risk of long-bones in children and adults with osteolytic defects and pathological skeletal deformities. It also seeks to develop a method which minimizes cost and radiation doses in order to increase the availability of the technique and to make it a practical tool for repeated measurements that can be used to assess response to treatment. It is believed this can be accomplished by quantitatively measuring the critical parameters that determine load-bearing capacity (denominator in equation [1.1]) using non-invasive imaging and simple engineering principles.

The technique proposed in this thesis is detailed as the preferred method in Figure 1.2. A limb with a defect is examined by one of a number of non-invasive imaging techniques, including magnetic resonance imaging (MRI), dual-energy x-ray

absorptiometry (DXA), quantitative computed tomography (QCT), and quantitative ultrasonic attenuation (QUA). From the imaging data, the specimen is discretized into multiple cross-sections, and the material and geometric properties of each cross-section are calculated. The weakest cross-section of the specimen is determined for a variety of loads (tension/compression, torsion, bending, and combinations of the three) that correspond to those experienced in daily activities.

A calculated property (structural rigidity, in particular) of the weakest cross-section may then be incorporated into a measure of fracture risk, such as the denominator in equation [1.1]. The numerator must be found from studies of the load bearing requirements for common activities of daily living. These are available for both the femur[24,25,26] and the spine[27,28] from a number of theoretical and *in-vivo* studies.
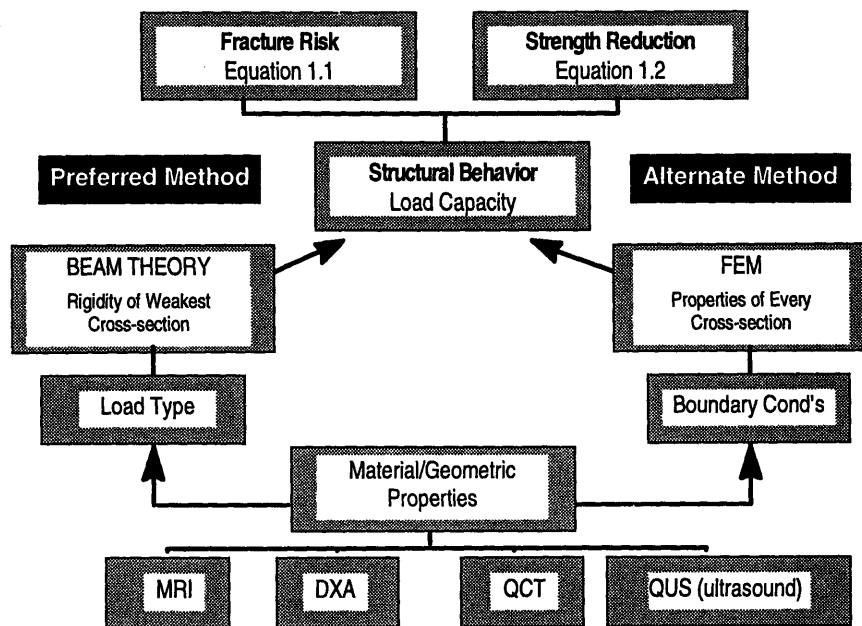


Figure 3.2 - Cross-sectional material and geometric properties of a bone with a defect and the healthy contralateral bone are measured using a non-invasive imaging technique. These properties and appropriate loading conditions are then used by either finite element models or composite beam theory to estimate the load capacity of the two bones. The ratio of the two load capacities (defect to healthy) is one way to measure the fracture risk due to a defect.

Even in the absence of a reliable model to determine the numerator in the factor of risk, a quantitative measure of a bone's strength reduction can be arrived at by comparing the load bearing capacity of a bone with a defect to the load-bearing capacity of the healthy contralateral limb:

$$\% \text{ Stg. Reduction} = \frac{\text{Load bearing capacity (rigidity) of bone with defect}}{\text{Load bearing capactiy (rigidity) of contralateral bone}} \qquad [3.2]$$

Equation [1.2] additionally requires properties of the matching cross-section from the healthy contralateral limb. However, it offers certain simplifications over equation [1.1]. It only requires knowing the *type* rather than the magnitude of expected loads and only requires that the imaging technique provide a *relative*, rather than absolute, measure of bone properties since the measurements are normalized to the contralateral "control."

An alternate method shown in Figure 1.2 is to use finite element models specifically developed for each patient. Although this analysis is potentially more powerful, it has a number of drawbacks, including:

1) Current state of the art makes development of patient specific finite element models extremely expensive and time-consuming, limiting the clinical applicability of the method.
2) Finite element models would require scans of the entire limb and are generally created from QCT scans. However, QCT is radiative and therefore limits the number of scans (and cross-sections) that may be made.
3) Finite element models require detailed loading and fixation boundary conditions that are not currently available in the literature.
4) Bone may not behave exactly like a continuum such as steel, causing finite element models to potentially overestimate stiffness and incorrectly measure the effects of stress concentrators.

An additional option is to use closed-form solutions based on continuum mechanics that exist for holes in porous materials [29], but they are extremely limited in the hole shapes, material complexity, and loading conditions to which they may be applied.

*THEORY BEHIND THE METHOD.* The preferred method of Figure 1.2 relies on the validity of a few important assumptions. Since this method uses measurements of structural rigidity, the first and most important assumption is that there exists a linear relation between structural rigidity (or some alternate easily-measured property) and the load capacity of a bone. This has been shown to be true when testing trabecular bone cylinders[30] in the past. The method also assumes failure behavior according to Bernoulli-Euler theory by calculating strength based solely on information from the weakest cross-section. That is, it does not account for stress flow affected by the geometry of a defect, which may affect where and how failure initiates. Fortunately, bone (trabecular bone in particular) may not behave exactly like a continuum. Its porous and lamellar structure may somewhat alleviate the stress concentration factors induced by geometric and material irregularities.

Provided Bernoulli-Euler beam theory adequately models the stress state and load capacity varies linearly with structural rigidity, then it remains to determine a non-invasive technique of measuring the structural rigidity of a bone. Since the modulus and spatial distribution of the material determine a specimen's rigidity, a non-invasive imaging technique must somehow measure these two properties.

It has been shown that trabecular bone can be modeled as a rigid, porous foam composed of a mineral (calcium hydroxyapatite) suspended in an organic matrix [31]. For a given mineral content, variations in the organic phase and the internal soft tissue (e.g. marrow) do not significantly affect structural properties of non-pathologic bone. Therefore, in trabecular bone, the mineral phase is the material which primarily governs a specimen's rigidity. In fact, a number of studies have shown ash density to have a very strong relationship to the modulus of trabecular bone[32]. The ash density is the mass of the mineral phase divided by the specimen volume and may be found from apparent dry density from the following relation:

$$\rho_\alpha = \rho_{apparent} \left( \frac{dry\ weight}{ash\ weight} \right) \qquad\qquad [\ 3.3\ ]$$

Therefore, an instrument which is able to measure a specimen's ash density and cross-sectional geometry should give an excellent approximation of the specimen's structural rigidity. QCT accomplishes this by measuring the energy attenuation of an electromagnetic wave, which depends on the molecular composition and density of a bone's mineral phase. The spatial distribution of the mineral phase may be determined by measuring attenuation through a cross-section from a number of orientations. From this measure of density and spatial distribution, geometric, material, and structural properties of the bone can be calculated. The load capacity of the specimen may then determined as a linear function of the structural rigidity of its weakest cross-section.

## 3.4 OUTLINE OF STUDY - EVALUATING THE SOLUTION

To evaluate the non-invasive fracture risk prediction technique described in the previous section, the long-term goal is to test the following hypothesis:

> *Hypothesis. There exists a strong correlation between the failure load of an entire bone with a defect and material and geometric properties (derived from non-invasive imaging data) of the weakest cross-section containing the defect.*

This hypothesis is first tested for simple beams of trabecular and cortical bone before studying whole bones as they appear in vivo.

## 3.4.1  RESEARCH QUESTIONS

The research for this thesis focused on four questions pertaining to the hypothesis above. The assumption that composite beam theory can be used to predict load capacity was investigated with simple mechanical tests and led to the question:

> *Research Question 1.  Is the elastic behavior of trabecular bone with a defect related to its load bearing capacity?*

In answering Question 1, elastic structural properties, the rigidity in particular, were measured using mechanical tests. However, composite beam theory analysis using data from non-invasive imaging techniques may be limited by the ability of the imaging technique to accurately measure structural properties of bone, which led to the question:

> *Research Question 2.  Can the elastic mechanical behavior of trabecular bone with defects be predicted by non-invasive imaging techniques?*

Although rigidity may be an elastic property that correlates to load capacity, this correlation assumes one of many possible failure criteria. It may be that another failure criterion is more appropriate, meaning that a different elastic property would correlate more highly with load capacity. If non-invasive techniques do effectively measure the elastic properties of a bone with a defect, they may be used to isolate various material, geometrical, and structural properties to answer the question:

> *Research Question 3.  Which non-invasive imaging measurement best predicts the load capacity of trabecular bone with defects?*

Finally, the primary hypothesis assumes that elastic properties alone are sufficient to predict the load capacity of trabecular bone.  However, other factors, particularly geometrically-sensitive stress risers, may also affect the load capacity of trabecular bone when defects are introduced.  It is important to determine if their effect is significant, which led to the final research question:

> **Research Question 4.** *How do certain other factors affect the biomechanical properties of trabecular bone with defects?*

## 3.4.2 TEST METHOD

A series of parametric tests were conducted to answer the research questions for trabecular bone, idealized as a relatively homogeneous cylinder with a regularly shaped hole extending through its middle cross-section, as shown in Figure 1.3. Since we assumed the mechanical behavior of a beam with a hole is primarily governed by its modulus and geometry, those were the two parameters which were varied in this study. Specimens from a variety of animals and anatomic sites resulted in a continuous variation of modulus, whereas defects were limited to six discrete geometries.
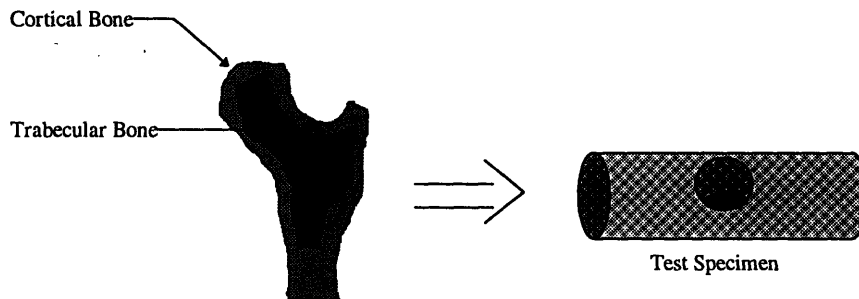


Figure 3.3 - Whole bone is composed of both cortical and trabecular bone. This thesis focuses on predicting fracture risk in only trabecular bone shaped as homogeneous cylinders with a transverse hole.

The important variables in the experiment were as follows:

- *FIXED VARIABLES*:  homogeneity of specimen
  anisotropy of specimen
  specimen size
  sharpness of defect (rounded)
- *PARAMETRIC VARIABLES*:  density of specimen
  defect size
  defect shape (circular or rounded slot)
- *INDEPENDENT VARIABLE*:  structural rigidity (EI, EA, GJ)
- *DEPENDENT VARIABLES*:  slope of load vs. displacement curve
  yield (ultimate) load

Tests were conducted on 115 cylindrical cores of cancellous bone taken from the vertebrae of four bowhead, one immature sperm, and one pygmy sperm whale.

Specimens were screened for longitudinal orientation of trabeculae and material homogeneity based on plane radiographs.

Lytic bone lesions were simulated by drilling circular holes with diameters 28%, 47%, and 56% of the nominal cross-sectional diameter and rounded slots of the same diameters and twice the length into the rods of cancellous bone. In all cases, the long axis of the slot was parallel to the long axis of the specimen. Specimens were randomly assigned their defect size and shape. A control group with no holes was also included in the testing. The experimental design, therefore, included seven groups: three hole sizes multiplied by two shapes (circular and elongated), plus one group with no holes. Prior to creating the defects, the specimens were scanned using clinical QCT. After the defects were created, the specimens were again scanned at the defect site with clinical QCT.

The specimens were then subjected to simple modes of failure by uniaxial tension, bending, and torsional loads. Yield load was taken as the point where the tangent slope of the curve deviated from the slope of the linear portion of the curve. This corresponded to approximately 0.2% strain offset. The specimen's apparent structural (global) rigidity was taken as the slope of the load vs. normalized deflection. Outer fiber strain of the cross-section at the defect was determined in the case of bending by fitting a parabola to five digitized points on the bone, and calculating the strain at the defect from the radius of curvature of the parabola at that point.

The first research question was answered by correlating the mechanically measured rigidity with failure load of the trabecular cores. The second question was answered by correlating QCT measurements of rigidity to the mechanically measured rigidity of each specimen. The third research question was answered by determining which of a number of QCT measurements was correlated most highly with specimens' failure loads. The final question was answered by comparing trends in failure loads from the mechanical tests to trends predicted by finite element models, and by analysis of variance (ANOVA) tests, where the groupings were based on hole size and shape.

## 3.5 SCOPE AND LIMITATIONS

In order to answer basic questions about the mechanical behavior and imaging characteristics of bones with defects, it was necessary to isolate certain parameters and make a number of simplifications that limit the extent to which conclusions may be applied to in-vivo conditions. Whole bones are composite structures, composed of both cortical and trabecular bone tissue, with an irregular shape and heterogeneous density and microstructure. They are surrounded by soft tissue which affects loading conditions and imaging characteristics. Also, the various pathologic defects which may afflict it typically have irregular shape, composition, and size.

However, a number of simplifications in the specimens were necessary in order to isolate density and hole size as independent variables. The specimens were chosen to be regularly-shaped cylinders composed entirely of trabecular bone, from which all soft tissue was removed. Each specimen had relatively homogeneous density, transverse isotropy, and similar orientations of the major trabecular axis so that variations in these parameters did not affect experimental results. Also, the defects were regularly-shaped circular holes or slots extending through the cross-section at the specimen's mid-span.

Cores from whale vertebrae, rather than human bone, were tested in order to secure sufficiently large specimens. Since whale bone was shown to be a good model for human trabecular bone[33] the results of this study are intended to be generally applicable to human trabecular bone. However, the 25 mm x 75 mm specimens and hole sizes are smaller than *in-vivo*, while the trabecular microstructure is not. Therefore, the microstructural rather than continuum behavior of the tissue may have been exaggerated somewhat in this study. Bending, tension, and torsion tests covered the predominant modes of loading and failure expected *in-vivo*; however, conclusions from these tests may have only limited quantitative applicability to combined loading states, since stress flow around a defect depends somewhat on the type of loads. This dependence may also be magnified by non-circular hole shapes, which were not tested in these experiments.

Therefore, the following parameters, which may affect both mechanical behavior and imaging characteristics of trabecular bone were not addressed in this study:

1) shape of the specimen
2) heterogeneity of the specimen
3) orientation of planes of isotropy
4) interaction between cortical and trabecular bone, affecting both mechanical behavior and imaging characteristics
5) effects of soft tissue on mechanical behavior and imaging characteristics
6) material composition of the defect
7) sharpness of the defect and its effect on stress concentrations; interaction of multicameral defects
8) anatomical site of the defect.

## References

[1]   Silverman, "Essentials of Caffeys pediatric x-ray diagnosis," *Pediatric Radiology*, 1989, pg. 1216.

[2]   H.J. Mankin, M.C. Gebhardt, and D.S. Springfield, "Orthopaedic oncology service tumor database" [Abstract], 1996.

[3]   J. Body, "Metastatic bone disease: clinical and therapeutic aspects," *Bone*, Vol. 13, 1992.

[4]   C. Boring, T. Squires, and T. Tong, "Cancer statistics," *Cancer J Clin* 43:7, 1993.

[5]   B. Berrettoni and J. Carter, "Current concepts in review: mechanisms of cancer metastasis to bone," *J Bone Joint Surgery* 68A:308, 1986.

[6]   J. Walls, N. Bundred, and A. Howell, "Hypercaclemia and bone resoprtion in malignancy," *Clin Orthop* 312:51, 1995.

[7]   M. Fidler, "Prophylactic internal fixation of secondary neoplastic deposits in long bones," *British Medical J*, Vol. 10:341, 1973.

[8]   R.K. Beals, , G.D. Lawton, and W.E. Snell, "Prophylactic internal fixation of the femur in metastatic breast cancer," *Cancer* 28:1350, 1971.

[9]   F.F. Parish and J.A. Murray, "Surgical treatment for secondary neoplastic fractures:  a retrospective study of ninety-six patients," *J Bone Joint Surg* 52A:665, 1970

[10]   J.S. Keene, D.S. Seelinger, A.A. McBeath, and W.D. Engber, "Metastatic breast cancer in the femur: a search for the lesion at risk of fracture," *Clin Orthop* 203:282, 1986.

[11]   R.E. Zickel, and W.H. Mouradian, "Intramedullary fixation of pathological fractures and lesions of th subtrochanteric region of the femur," *J Bone Joint Surg* 58-A-8:1061, 1976.

[12]   J. Haler, M.P. Andre, D. Resnick, C. Miller, B.A. Howard, J.P. Shils, D.J. Satoris, and D. Trudell, "Detection of thoracolumbar vertebral body destruction with lateral spine radiography," *Investigative Radiology* 25:517, 1990.

[13]   J.A. Hipp, B.C. Edgerton, K.N. An, and W.C. Hayes, "Structural consequences of transcortical holes in long bones loaded in torsion," *J Biomech* 23:1261, 1990.

[14]   J.A. Hipp, G. Katz, and W.C. Hayes, "Local demineralization as a model for bone strength reductions in lytic transcortical metastatic lesions," *Investigative Radiology* 26:934, 1991.

[15]   J.A. Hipp, R.J. McBroom, E.J. Cheal, and W.C. Hayes, "Structural consequences of endosteal metastatic lesions in long bones," J Orthop Res 7:828, 1989.

[16] R.J. McBroom, E.J. Cheal, and W.C. Hayes, "Strength reductions frommetastatic cortical defects in long bones," *J Orthop Res* 6:369, 1988.

[17] V.C. Mow and W.C. Hayes, Basic Orthopedic Biomechanics, Raven press Ltd., New York, 1991, Chapter 3, "Biomechanics of cortical and trabecular bone: implications for assessment of fracture risk," pp. 93-141.

[18] M. Fidler, "Incidence of fracture of metastases in long bones," *Acta Orthop Scand* 52:623, 1981.

[19] K. Mase, T. Fukumura, J. Toriwaki, "Modified Digital Voronoi Diagram and its Applications to Image Processing," *Systems Computer Controls* 12:6, 1981.

[20] R. Capanna, A. Dal Monte, S. Gitelis, and M. Campanacci, "The natural history of unicameral bone cysts after steroid injection, *Clinical Orthopaedics and Related Research*, 1982, pp. 204-211.

[21] R. Bunting, W. Lamont-Havers, D. Schweon, and Akliman, " Pathologic fracture risk in rehabilitation of patients with boney metastases," *Clinical Orthopedic and Related Research*, 1985, 192:222-227.

[22] D.S. Cheng, C.B. Seitz, and H.J. Eyre, "Nonoperative management of femoral, humeral, and acetabular metastasis in patients with breast carcinoma," *Cancer* 45:1533, 1980

[23] H. Mirels, "Metastatic disease in long bones," *Clin Orthop Rel Res* 249:256, 1989.

[24] R.D. Crowindshield, R.C. Johnson, J.G. Andrews, and R.A. Brand, "A biomechanical investigation of the human hip," *J Biomech* 11:75, 1978.

[25] A.G. Patriarco, R.W. Mann, S.R. Simon, and J.M. Mansour, "An evaluation of the approaches of optimization models in the prediction of muscle forces during human gait," *J Biomech* 14:513, 1981.

[26] G. Bergmann, F. Graichen, and A. Rohlmann, "Hip Joint loading during walking and running, measured in two patients," *J Biomech* 26:969, 1993.

[27] A.L. Nachemson, "Disc pressure measurements," *Spine* 6:93, 1981.

[28] A. Schultz, K. Haderspeck, D. Warwick, and D. Portillo, "Use of lumbar trunk muscles in isometric performance of mechanically complex standing tasks," *J Ortho Res* 1:77, 1983.

[29]   S.C. Cowin, "The stresses around a hole in a linear elastic material with voids," *Q. Jl Mech. Appl. Math.*, 37:441-466, 1984

[30]   S.A. Goldstein, "The mechanical properties of trabecular bone dependence on anatomic location and function," *Journal of Biomechanics*, 20:1055-1061, 1987

[31]   L.J. Gibson, "The mechanical behavior of cancellous bone," *Journal of Biomechanics*, 18:317-328, 1985.

[32]   J.C. Rice, S.C. Cowin, and J.A. Bowman, "On the dependence of the elasticity and strength of cancellous bone on apparent density," *Journal of Biomechanics*, 21:155-168, 1988.

[33]   J. Hong, "Noninvasive Prediction of Failure in Trabecular Bone with Simulated Osteolytic Defects," Massachusetts Institute Technology, 1997.

# Chapter 2

# Materials

## 2.1 DESCRIPTION OF TRABECULAR BONE

Bones serve as the most important structural elements in the human body, protecting internal organs and providing the kinematic links necessary for muscle action. They are composed of an external shell of dense cortical tissue and a core which in many places is filled with a porous, mineralized tissue designated as cancellous, or trabecular, bone, shown in Figure 2.1. Trabecular bone is an interconnected three-dimensional network of thin rods and plates of bone called trabeculae. Its mean (SD) apparent density in humans is 0.30 $g/cm^3$ (0.10 $g/cm^3$), and the accepted range is from 0.10 to 0.90 $g/cm^3$ [1]. Trabecular bone is most prevalent in the following locations:

1) at the ends of long bones, under synovial joints
2) in the core of short bones
3) in the core of flat bones
4) under pretuberances to which tendons are attached

This research focuses on trabecular bone as a structural component of long bones, where it transmits and gradually concentrates the large loads from the cartilaginous joint surfaces into the compact bone of the shaft [2].

Biomechanically, trabecular bone may be regarded as a bi-phasic composite of hydroxyapatite $(CA_{10}(PO_4)_6(OH)_2)$-like crystals embedded in a collagen matrix. On the continuum level, it is generally characterized as a heterogeneous, anisotropic, cellular solid [3,4,5].

Most research indicates that the both the modulus and strength of trabecular bone are linearly related to the square of its apparent density [6,7], and modulus can vary by more than 100-fold from one location to another within the same metaphysis [8]. Also, numerous studies have demonstrated a sensitivity of modulus and strength to loading direction (anisotropy) [5,9,10,11], indicating that both elastic and failure properties must take into account architecture as well as tissue density.

A linear relationship between strength and modulus [5,12] and a weak dependence of yield and ultimate strain on apparent density and modulus [12,13,14,15] imply that bone may fail at a maximum principle strain. Linde et al reported mean (SD) ultimate strains in human proximal tibial bone of 2.02% (0.43). Turner reported yield strain of 0.74%

(0.14%) for bovine distal femoral bone, and Keaveny reported yield strain of 0.78% (0.03%) in tension and 1.09% (0.09%) in compression for bone from the bovine proximal tibia[16].
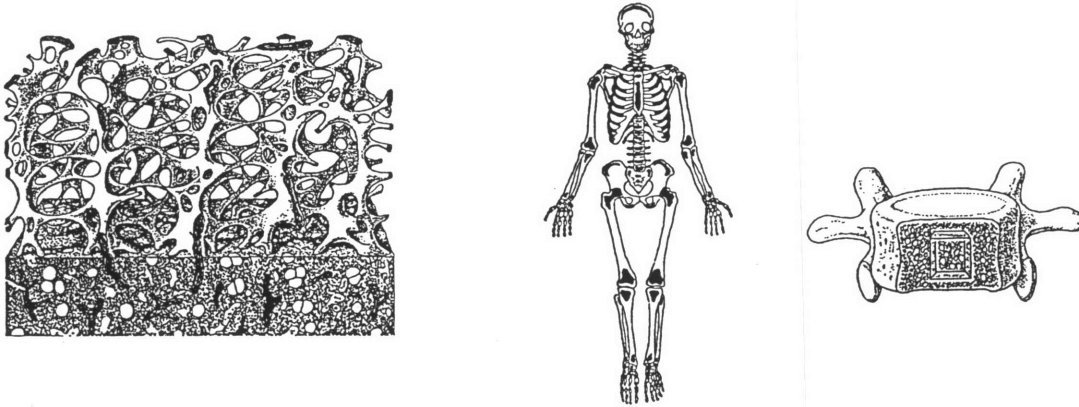


Figure 2.1 - Distribution of trabecular bone within the human skeleton.

## 2.2 WHALE BONE AS A MODEL FOR HUMAN BONE

In this study, trabecular bone extracted from the vertebrae of whales was used as the model for human trabecular bone because it provided very large regions of homogeneous, uniformly-oriented tissue. Whale vertebrae were chosen as the specimen source because they could provide homogeneous samples large enough to be considered a continuum even with the presence of a large defect and could be machined into homogeneous test cylinders with a reasonably-large gage section. Homogeneous specimens of sufficient size could not be obtained from human or bovine tissue, which are typically used for biomechanical testing.

A small experiment was conducted to validate whale vertebral trabecular bone as an experimental model for human trabecular bone by comparing its uniaxial compressive behavior to that of human trabecular bone. Vertebrae were harvested from three of the whales used in the main study, and twenty-two (22) cylindrical samples were extracted from the vertebrae using the same techniques as were used in the main study. Specimens were sectioned using a rotary diamond blade (EXTEC labcut 1010 and 15HC series blade) into cylinders 12.7 mm in diameter and 15 mm in height, and their bulk dimensions were measured using a Mitutoyo digimatic caliper.

After cyclic preconditioning at 0.5 Hz, the specimens were loaded compressively to failure under displacement control at an average strain rate of 1.88% $s^{-1}$ in order to determine their moduli and strengths. Subsequent to testing, marrow and fat were removed from the specimens with a water jet and ultrasonic baths of 20% concentration chlorine bleach, and water was removed from the pores in a centrifuge at 1000 rpm for 15 minutes. Wet weights were immediately measured in a closed-chamber digital balance. Dry and ash weights were measured after dehydrating the specimens for 120 hours at 75°C and ashing for 24 hours at 600°C, respectively. Densities were determined using the following relations:

$$\text{Apparent Density} = \frac{\text{wet weight}}{\text{bulk volume}}$$     [ 2.1 ]

$$\text{Ash Density} = \frac{\text{ash weight}}{\text{dry weight}} \times \text{apparent density}$$     [ 2.2 ]

In order to establish that trabecular bone from whales serves as an adequate model for human bone, the compressive behaviors of the specimens were compared to models developed by Keller based on compressive tests of 259 specimens from human femurs[17]. Figures 2.2 and 2.3 show that the relations between modulus (strength) and ash density for whale bone qualitatively match those that Keller found for human bone.



**Modulus vs. Ash Density**
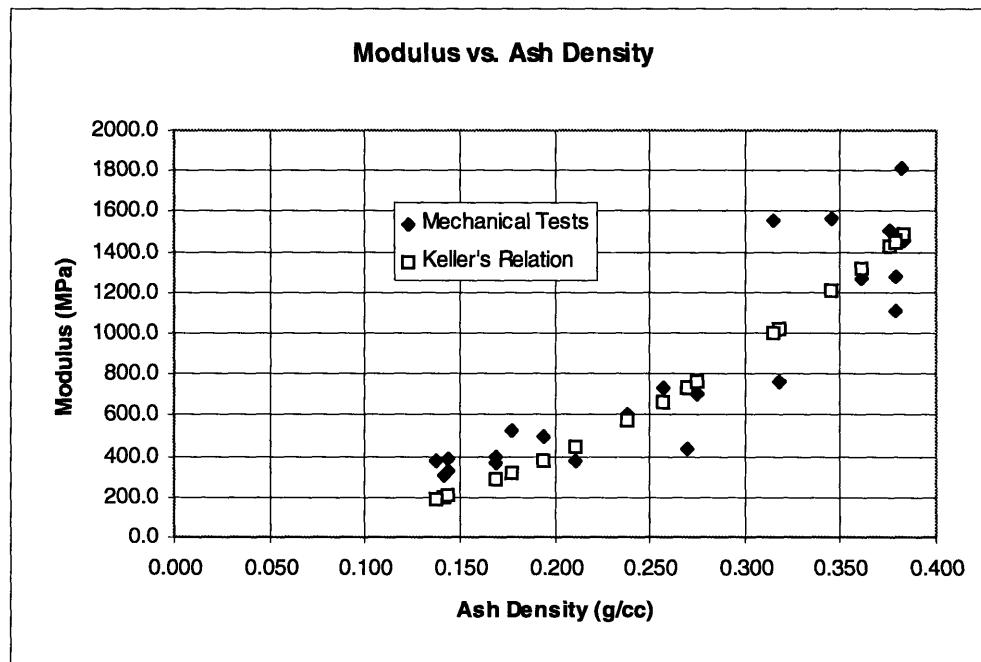
Figure 2.2 - The relation between compressive modulus and ash density of whale bone is similar to the relation between modulus and ash density found by Keller for human trabecular bone.

The relations found by Keller and plotted in the figures are as follows:

$$E = 10.2(\rho_\alpha)^{2.01} \quad , r^2 = 0.67 \qquad\qquad [\,2.3\,]$$

$$S = 114\ (\rho_\alpha)^{1.72} \quad , r^2 = 0.88 \qquad\qquad [\,2.4\,]$$

where

- $E$ = Young's modulus (GPa)
- $S$ = ultimate strength (MPa)
- $\rho_\alpha$ = ash density (g/cc).

A quadratic relation was fit to the modulus vs. ash density curve for the whale bone ($r^2 = 0.82$). This function was used throughout the study to predict modulus based on non-invasive measurement of density from QCT:

$$E\ (GPa) = 7.584\ (\rho_\alpha)^2 + 0.940\ (\rho_\alpha),\ \rho_\alpha\ \text{in g/cc} \qquad\qquad [\,2.5\,]$$
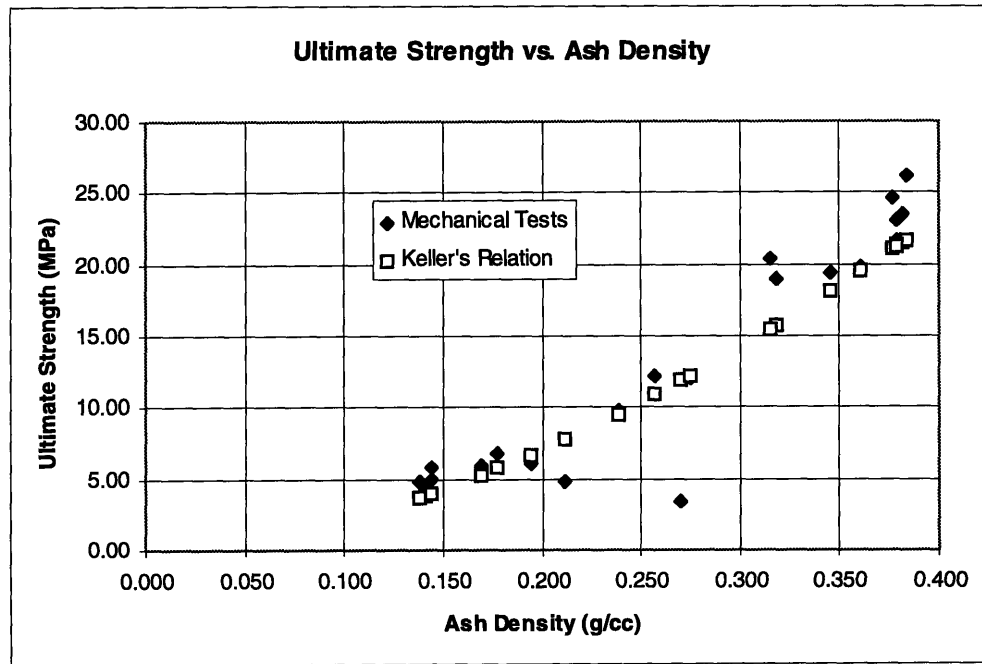


Figure 2.3 - The relation between compressive strength and ash density of whale bone is similar to the relation between strength and ash density found by Keller for human trabecular bone.

## 2.3 TEST SPECIMENS

One hundred fifteen (115) cylindrical cores of cancellous bone were taken from the vertebrae of four bowhead whales (Balaena mysticetus) ranging in age from adolescent to elderly, one immature sperm whale (Physeter macrorynchus), and one mature pigmy sperm whale (Kogia breviceps). Specimens were acquired from recently deceased whales at the National Marine Fisheries Service in Miami, Florida and the Department of Wildlife Management in Barrow, Alaska under research authorization from the National Oceanic and Atmospheric Administration. The tissue was harvested within 24 hours of the death of each animal and maintained below 0°C for a period of approximately 48 hours until it was shipped to the Lab at Beth Israel.

Cylindrical cores were extracted from each vertebrae in the superior to inferior direction with the longitudinal axis of the core oriented along the principle trabecular axis by designating the distal endplate as the orthogonal-zero reference surface. Coring regions were selected based on radiographs (Hewlett Packard Faxitron Series, model 43855A) and QCT scans (GE High Speed Advantage Helical Scanner, 3 mm slices and 0.9375 mm$^2$/pixel resolution) of each vertebrae. The vertebrae were placed in an iced saline bath, and cores were extracted using a drill press at 360 rpm and a 12.7 mm diamond tip coring tool. Each core was then radiographed at 75 kV for 65 seconds and visually inspected to select specimens in which the trabecular structure was homogeneous, free of discontinuities (e.g. vascular channels), and uniformly oriented along the long axis of each specimen ( <10° off axis).
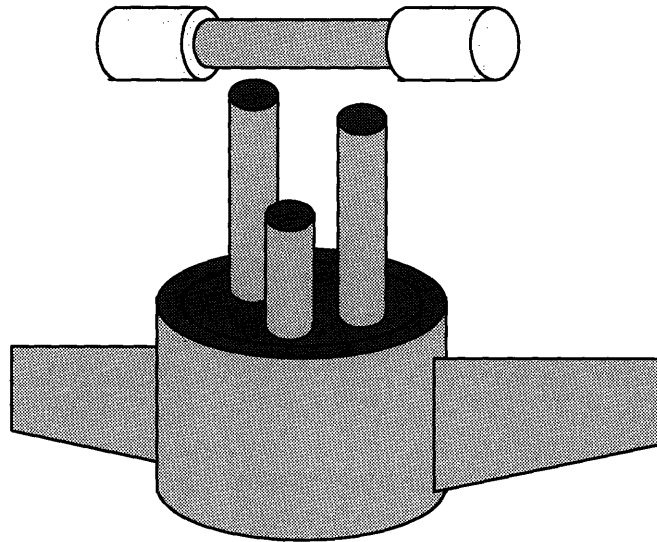


Figure 2.4 - Coring cylindrical cores of trabecular bone from whale vertebrae

As part of the test protocol, cores which passed the screening were imaged before and after defects were introduced using QCT in 3 mm slices and 0.234 mm$^2$/pixel

resolution. Their cross-sectional properties were calculated from the CT images using a Unix workstation. The variation in important cross-sectional properties throughout the specimen lot is shown in Table 2.1.

Table 2.1 - Cross-sectional Properties of Specimens Selected for Testing in Four-point Bending, Torsion, and Tension (variables defined in Appendix D).

|  | Density (g/cc) | A (mm$^2$) | EA (MN) | Ix (cm$^4$) | EIx (Nm$^2$) | J (cm$^4$) | GJ (Nm$^2$) |
|---|---|---|---|---|---|---|---|
| Mean | 0.37 | 84 | 0.14 | 0.078 | 1.24 | 0.21 | 3.4 |
| Std. Dev. | 0.18 | 33 | 0.15 | 0.045 | 1.47 | 0.06 | 3.2 |
| Min | 0.17 | 41 | 0.02 | 0.025 | 0.10 | 0.12 | 0.5 |
| Max | 1.03 | 143 | 0.95 | 0.165 | 9.55 | 0.33 | 19.1 |

In order to justify the continuum assumption, cross-sections from four cylindrical samples were analyzed under a stereo microscope at 20 times magnification. Figure 2.5 shows a stereo microscope view of one of the samples. The number of trabeculae per centimeter were measured in five directions across each circular cross-section, resulting in a mean (SD) over the twenty measurements of 14.3 (2.05) trabeculae per centimeter. Analysis by Harrigan concluded that at least three to five trabeculae are necessary to obtain average continuum behavior [18]. Given test specimens 1.27 centimeters in diameter, the average number of trabeculae per diameter (18.2) was more than sufficient to meet the continuum assumption. The largest hole (56%) tested would leave an average of 4 trabeculae on either side of the hole, which is on the margin of the continuum assumption. However, 1.27 cm diameter specimens were the largest possible given the aspect ratio (length to diameter) required by the mechanical tests and the size of vertebrae from which the specimens were harvested.
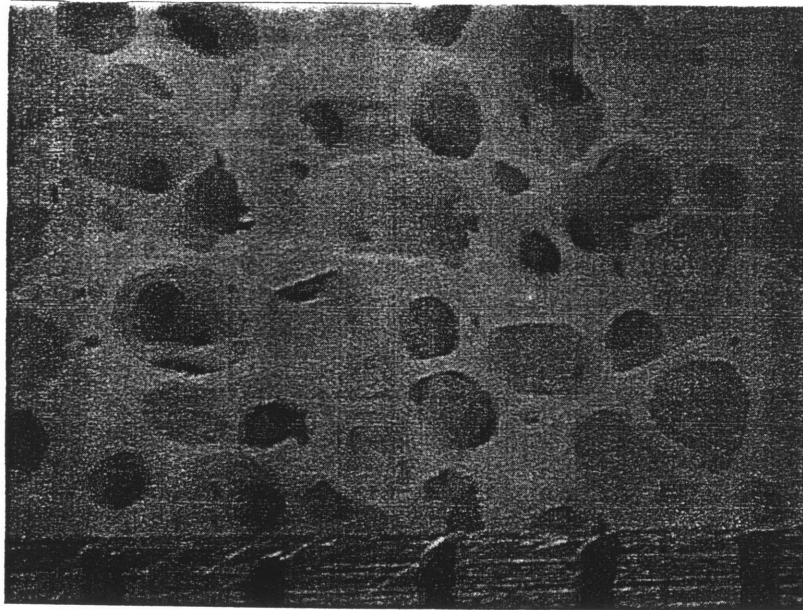


Figure 2.5 - Cross-section of a trabecular sample viewed at 20x magnification.

Trabecular rod thickness and trabecular plate width were measured to be on the order of 0.1 - 0.5 mm and 0.5 - 3.0 mm, respectively. Snyder and Hayes reported similar trabecular thicknesses for human proximal femurs in the same density range as the test specimens for this experiment [19]. Although they only found on the order of 6 trabeculae per centimeter (we found 14.2 per cm), their specimens may have been somewhat osteoporotic since they were from a population with a mean age of 66. The similarity in trabecular spacing and thickness was a further justification for whale trabecular bone as a model for human trabecular bone.

## 2.4 SPECIMEN PREPARATION

Specimen preparation included coring, potting, introducing defects, and instrumenting for mechanical tests. The coring methods were discussed previously.

### 2.4.1 SPECIMEN POTTING

Cored specimens were 12.7 mm in diameter and approximately 50 mm in length. Approximately, six millimeters at each end of a specimen were potted in Polymethylmethacrylate (PMMA) endcaps for mechanical testing, leaving a gage section of 38 mm. The potted ends of the bone were scored, providing a rough surface on which the PMMA could grab the bone during the tension and torsion tests.

Specimens were potted in a precisely-machine aluminum jig, shown in Figure 2.6, in order to assure that they were properly aligned with their endcaps. An aligning sleeve was fitted over the cylindrical core and inserted into the aluminum potting jig. Liquid PMMA was prepared by mixing 2.25 parts of powdered monomer with 1 part liquid Fastray catalyst and poured into a well at the top of the jig, enveloping the end of the specimen that extended into the well. A rubber O-ring around the bone core served as a bottom for the mold well. The curvature of the ring molded a fillet into the PMMA endcap, reducing stress concentrations at the interface of the endcap and the specimen, as shown in the figure.

After 25 minutes the endcap was cured, and the other end of the specimen was potted. During potting, the specimen was wrapped in moist gauze to prevent drying. The polymerization of PMMA is an exothermic reaction, and heating of the specimen was a concern. Therefore a large block of aluminum was used as the potting jig to conduct heat away from the specimen and maintain a low average temperature. A thermocouple was used to trace the temperature profile throughout the reaction, and the profile is shown in Figure 2.7. The profile shows that the temperature spikes over a short period of time and does not even reach body temperature.
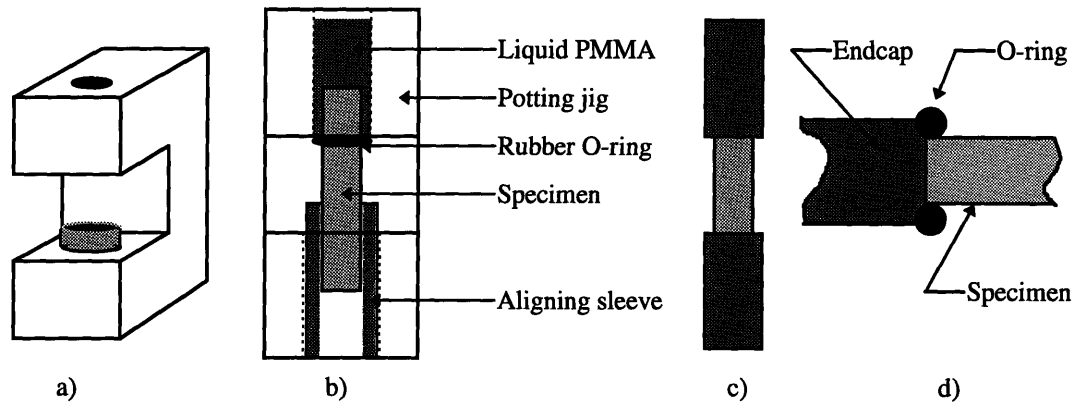
Figure 2.6 - a) Aluminum potting jig with aligning sleeve; b) configuration for molding PMMA endcaps around a specimen; c) a specimen with endcaps after potting is complete; d) A rubber O-ring moulded a rounded fillet at the specimen-endcap interface.
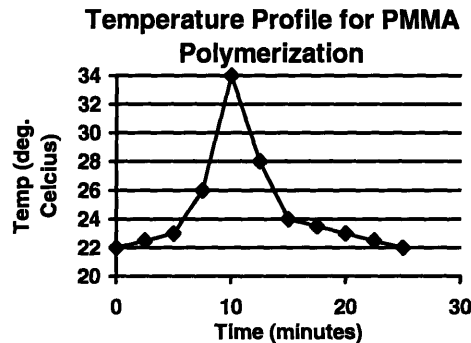


Figure 2.7 - The temperature profile during polymerization of PMMA.

## 2.4.2 INTRODUCTION OF DEFECTS

Specimens were randomly assigned a defect shaped as a circular hole or elongated slot with a diameter 28%, 47%, or 56% of the nominal specimen diameter, as shown in Figure 2.8. Defects were drilled or milled into the specimens. Slots were twice as long as they were wide, and had the same radius as the corresponding circular hole. These shapes and relative diameters were chosen because they roughly represent the geometry range most commonly encountered in pediatric defects and they produced reasonable steps in predicted specimen properties, as listed in Table 2.2. Specimens without a hole were assigned a value of 1.00 for each property in the table, and the relative value of a given property was calculated for each hole size based on the geometric reduction in cross-section, assuming a solid, not porous, material.
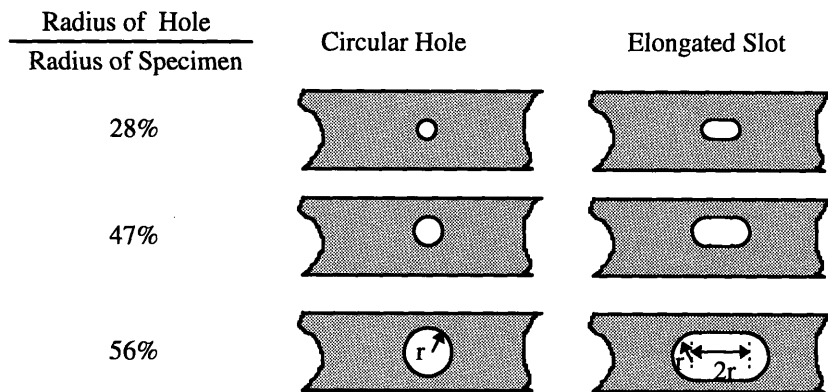
Figure 2.8 - Hole and slot sizes used for specimen testing.

Table 2.2 - Relative Geometric Properties for Different Hole Sizes

| Hole/Slot Size | Drill/Mill Bit inches (mm) | Area | Bending Moment of Inertia | Torsional Moment of Inertia |
|---|---|---|---|---|
| No Hole | | 1.00 | 1.00 | 1.00 |
| 28% | 9/64   (3.57) | 0.65 | 0.54 | 0.75 |
| 47% | 15/64  (5.95) | 0.42 | 0.29 | 0.56 |
| 56% | 9/32   (7.14) | 0.33 | 0.19 | 0.46 |

Defects were milled or drilled into specimens on a Bridgeport milling machine at speeds between 400 and 1200 rpm, depending of the size of the hole. Each specimen was clamped snugly into a Delrin support jig, shown in Figure 2.9. A stiff lower base supported the specimen from bending, and more flexible top clamp held the specimen in alignment without damaging it. A well beneath the defect collected material that was removed and held water to keep the specimen cool from the bottom. Specimens were also cooled with a water spray from the top.
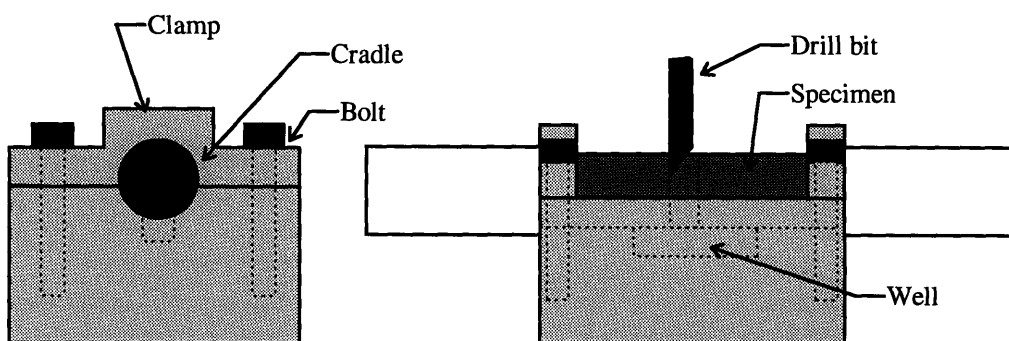


Figure 2.9 - Delrin jig for milling/drilling defects into specimens.

Titanium-coated drill bits were used to drill the circular holes. Four-fluted, end-cutting, carbide-tipped mill bits were used to mill the slots. Slots were milled with two 6.8 mm deep passes of the mill bit along the length of the slot. Stereo-microscopic

images of the specimens at 75 times magnification showed that the drill and mill bits cut smooth surfaces and did not damage trabeculae beyond the surface of the defect.

## 2.4.3 Marking for Testing

Immediately before testing, each specimen was coated with a water based, black ink using a paint brush. The ink provided contrast for optical markers used to track specimen deformation with a non-contacting displacement measurement system (MacReflex) during testing. Diamond-shaped markers of Scotchlite reflective tape approximately 1 mm on a side were fixed to the specimens with a pin-tip-sized drop of cyanoacrylate in the patterns shown in Figure 2.10. A grid was optically projected onto the specimen to align the placement of markers. Markers were placed on two opposite sides of only the specimens tested in tension.
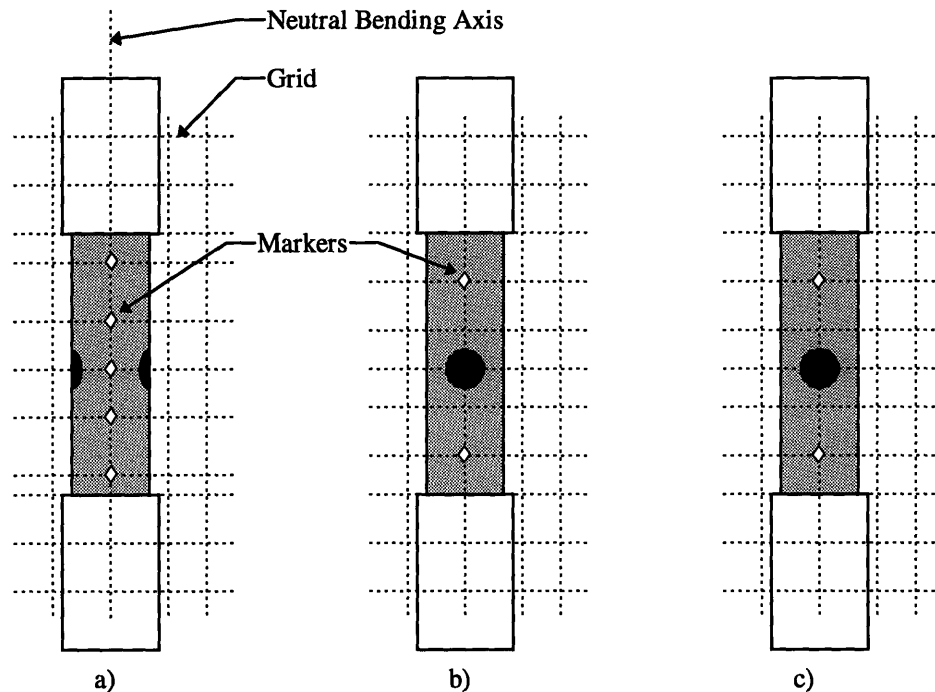
Figure 2.10 - Specimens with markers for a) bending b) torsion c) and tension. Tension specimens had two identical sets of markers on opposite sides of the specimens. The superimposed grid size shown here is approximately 0.5 cm.

The shape, size, and material of the markers were all selected based on informal tests to provide the maximum resolution for the optical measurement system. The cyanoacrylate used to affix the markers was small enough that it was not likely to have affected the specimens' mechanical behavior.

## 2.5 CONSIDERATIONS FOR SPECIMEN SIZE

Selection of the specimen size was based on a number of considerations, including the nature of bending, tension, and torsion tests, the availability of bone material, and data from finite element models of specimens with holes and slots.

The specimen diameter (12.7 mm) was driven by the size required to consider the material a continuum, as discussed above. The cross-section was chosen to be circular because that shape was easiest to machine precisely, most nearly represented the gentle curvatures of trabecular bone *in vivo*, provided a more even load distribution in torsion, and was less prone to parasitic loads due to overconstraints and mismatches in geometry at the grips in bending, tension, and torsion.

The aspect ratio of the specimen's length to its diameter was limited to 3 by the size of the vertebrae from which the specimens were cored. The smallest vertebrae could only yield about 38 mm of bone between the endcaps, and dividing by a diameter of 12.7 mm resulted in an aspect ratio of 3. However, a minimum aspect ratio is recommended to obtain regions of constant stress field and to maintain a pure type of loading in bending and torsion tests. In order to minimize the contribution of shear to the bending test and limit the effect of stress concentrations at the load points on rigidity and strength, an aspect ratio of 6 to 12 is recommended [20]. For torsion, an aspect ratio of at least 5 is recommended. The addition of PMMA endcaps added a pseudo length to the specimen, increasing the aspect to 9.5 for bending specimens and to about 4 for the torsion specimens.

For specimens with holes, it is even more important to ensure that stress concentrations at the interface between the endcap and specimen gage length do not affect the rigidity or strength in the region where data is being collected. In order to determine if the specimens had a gage length long enough to satisfy this requirement, maximum principle strain contours were analyzed using finite element models of the candidate specimen geometry for tension, torsion, and four-point bending of a specimen with a hole. The minimum necessary aspect ratio for the specimen gage length was calculated by dividing the minimum necessary length for a model by the diameter of the model. The minimum necessary length was defined as the length required to prevent stress concentrations at the endcap from overlapping with stress concentrations due to the hole.

The finite element models were of a cylindrical specimen 4 cm long, 1 cm in diameter, imbedded in endcaps 1.5 cm long and 0.1 cm thick (cm are specified as the units only to clarify that we are speaking of a distance). The models were homogeneous and isotropic. Models were run for the largest hole size - a slot 60% the diameter of the specimen with an eccentricity of 200%. Smaller hole sizes would have less stringent minimum gage length requirements.

The strain distribution was resolved into 12 iso-strains in equal strain increments. The minimum strain gradient around the hole is listed in Table 2.1 for each model along with the maximum gradient. Also listed are the size of the region that contains 95% of the strain gradients around the hole and the region that contains 95% of the strain gradients emanating from the endcap interface. Figure 2.11 shows the regions qualitatively. The minimum gage length necessary to prevent the strain gradients in the two regions from interacting was the length of the hole region plus two times the length of the endcap region (since there were endcaps on both sides of the specimen). The minimum necessary aspect ratio was the minimum required gage length divided by the diameter of the specimen (1 cm).

Table 2.1 - Results of finite element modeling to determine minimum necessary aspect ratio of specimen gage length

| | Min. Gradient (iso-strains per cm) | Max. Gradient (iso-strains per cm) | Hole Region (cm) | Endcap Region (cm) | Required Length (cm) | Required Aspect Ratio |
|---|---|---|---|---|---|---|
| Bending | 0.198 / cm | 5.80 / cm | 2.20 cm | 0.12 cm | 2.44 cm | 2.44 |
| Torsion | 0.280 / cm | 11.6 / cm | 2.30 cm | < 0.05 cm | 2.30 cm | 2.30 |
| Tension | 0.202 / cm | 6.12 / cm | 2.37 cm | 0.10 cm | 2.57 cm | 2.57 |



Region B: 95% of strain gradients near endcap    Region A: 95% of strain gradients around hole    Region B: 95% of strain gradients near endcap

Gage length of specimen
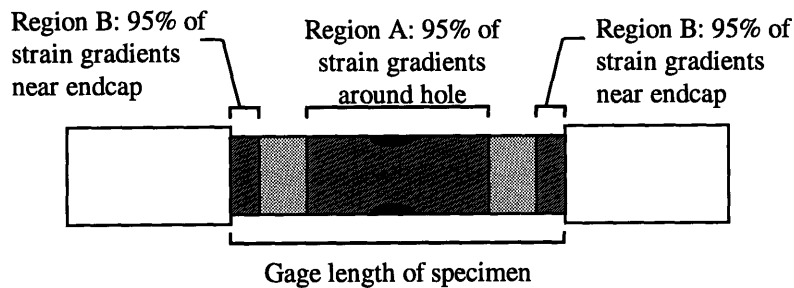
Figure 2.11 - The gage length of the specimen had to be long enough that regions A and B did not overlap.

These relative dimensions and aspect ratios represent the minimum necessary to prevent interaction or overlapping of stress concentrations from different sources. While inhomogeneities and anisotropy in the actual specimens increase the distance over which stress concentrations may interact, it was assumed that the stringent criteria described above were sufficient to exclude *significant* interaction even in actual bone specimens. Also, the actual specimens were screened for homogeneity, and the maximum hole diameter was 56%, rather 60%, of the specimen's nominal diameter. Therefore, the actual specimen ratio of 3 was considered sufficiently large

---

[1]  S.R. Simon, Orthopaedic Basic Science, American Academy of Orthopaedic Surgeons, 1994, Chapter 4, pg. 146.

[2]   W.C. Hayes, L.W. Swenson, and D.R. Schurman. "Axisymmetric finite element analysis of the lateral tibial plateau." *Journal of Biomechanics*, 11:21-23, 1978.

[3]   L.J. Gibson, "The Mechanical Behavior of Cancellous Bone," *Journal of Biomechanics*, 18:317-328, 1985.

[4]   J.W. Pugh, R.M. Rose, and E.L. Radin, "A structural model for the mechanical behavior of trabecular bone," *Journal of Biomechanics*, 6:657-670, 1973

[5]   J.L. Williams and J.L. Lewis, "Properties and an anisotropic model of cancellous bone from the proximal tibial epiphysis," *Journal of Biomechanical Engineering*, 104:50-56, 1982.

[6]   D.R. Carter and W.C. Hayes, "The compressive behavior of bone as a two-phase porous structure," *Journal of Bone and Joint Surgery*, 59:954-962, 1977.

[7]   J.C. Rice, S.C. Cowin, and J.A. Bowman, "On the dependence of the elasticity and strength of cancellous bone on apparent density," *Journal of Biomechanics*, 24: 1143-1149, 1991.

[8]   S.A. Goldstein, D.L. Wilson, D.A. Sonstegard, and L.S. Matthews, "The mechanical properties of human tibial trabecular bone as a function of metaphyseal location," *Journal of Biomechanics*, 16:965-969, 1983.

[9]   T.D. Brown, and A.B. Ferguson, "Mechanical property distributions in the cancellous bone of the human proximal femur," *Acta Orthop. Scand.*, 51:429-437, 1980.

[10]  J. Galante, W. Rostoker, and R.D. Ray, "Physical properties of trabecular bone," *Calcified Tissue Research*, 5:236-246, 1970.

[11]  F. Linde, B. Pongsoipetch, L.H. Frich, and I. Hvid, "Three-axial strain controlled testing applied to bone specimens from the proximal tibial epiphysis," *Journal of Biomechanics*, 23:1167-1172, 1990.

[12]  C.H. Turner, "Yield Behavior of Bovine Cancellous Bone," *Journal of Biomechanical Engineering*, 111: 256-260, 1989

[13]  I. Hvid, S.M. Bentzen, F. Linde, L. Mosekilde, and B. Pngsoipetch, "X-Ray quantitative computed tomography: the relations to physical properties of proximal tibial trabecular bone specimens," *Journal of Biomechanics*, 22:837-844, 1989

[14] J. Hvid, N.C. Jensen, C. Bunger, K. Solund, and J.C. Djurhuus, "Bone mineral assay: its relation to the mechanical strength of cancellous bone," *Engineering in Medicine*, 14:79-83, 1985.

[15] L. Rohl, E. Larsen, A Odgaard, and J. Jorgensen, "Tensile and compressive properties of cancellous bone," *Journal of Biomechanics*, 24:1143-1149, 1991.

[16] T.M. Keaveny, E.F. Wachtel, M.J. Cutler, and T.P. Pinilla, "Yield strains for bovine trabecular bone are isotropic but asymmetric," 40th Annual meeting of Orthopaedic Research Society, Feb 21-24, 1994, p 428.

[17] T.S. Keller, "Predicting the compressive mechanical behavior of trabecular bone," submitted to *Journal of Biomechanics*, 27(9): 1159-68, 1994.

[18] T.P. Harrigan, M.Jatsy, R.W. Mann, and W.H. Harris, "Limitations of the continuum assumption in cancellous bone," *Journal of Biomechanics*, 21:269-275, 1988.

[19] V.C. Mow, A. Ratcliffe, and SL-Y Woo, Biomechanics of Diarthrodial Joints, Vol. II, Springer-Verlag, New York, 1990, Chapter 18, pp. 31-59.

[20] H.E. Davis, The Testing and insepction of Engineering Materials, 3d ed., McGraw Hill, New York, 1964.

# Chapter 3
# Methods

This chapter describes the test methods used in the study. First, a summary of the materials, methods, and measurements is presented. Then each mechanical test is individually discussed in detail.

## 3.1 SPECIMENS

Tests were conducted on 115 cylindrical cores of cancellous bone removed from the vertebrae of four bowhead, one immature sperm, and one pygmy sperm whale using a diamond-tipped core drill with an inner diameter of 12.7 mm. The cores were screened to select specimens with trabecular structure that was homogeneous, free of discontinuities, and uniformly oriented along the long axis of the specimen. The cores were potted in cylindrical PMMA endcaps. After specimens were cored, screened, and potted, each was randomly assigned one of seven defect sizes and shapes (including no defect). Lytic bone defects were simulated by drilling or milling circular holes 28%, 47%, and 56% of the nominal cross-sectional diameter and rounded slots of the same diameter and twice the length into the specimens, as described earlier.

To preserve the mechanical properties of the bone, all machining took place under continuous water cooling, and specimens were wrapped in saline-soaked gauze during potting. While not being machined, imaged, or tested, specimens were stored wrapped in gauze and frozen at -20°C, which is recommended as a storage technique that results in negligible degradation of bone properties over an extended length of time [1].

Within each hole size, specimens were randomly assigned one of three mechanical test modes: four-point bending, tension, or torsion. The resulting testing lot is shown in Figure 3.1, and the number of specimens tested in each mode is shown in Table 3.1. In parenthesis is the number of specimens for which data was actually used. Eleven specimens were excluded because they broke during setup or broke at the endcaps rather than within the gage length.
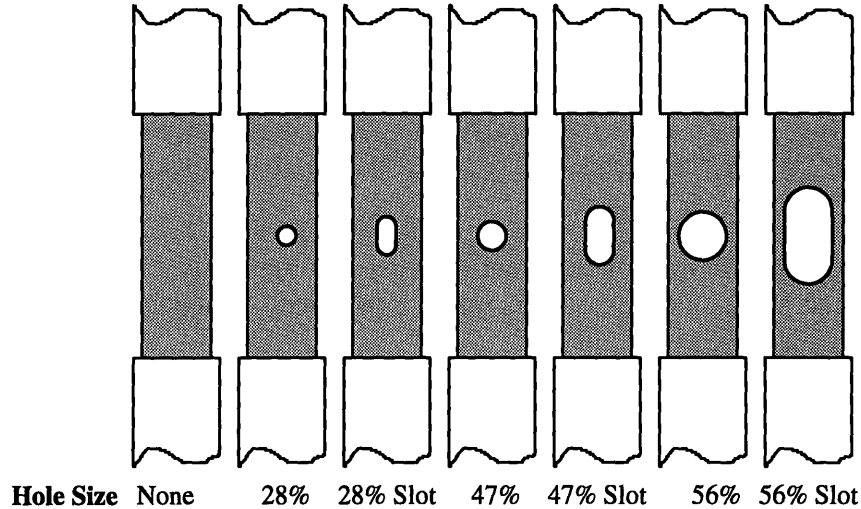
Figure 3.1 - Seven different groups of holes were tested, including no hole. A slot was paired with a circle for each diameter. The hole size is the ratio of the maximum width of the hole to the nominal diameter of the specimen.

Table 3.1 - Number of Specimens Tested in Each Mechanical Mode

| Hole Size | No Hole | 28% | 28% Slot | 47% | 47% Slot | 56% | 56% Slot |
|-----------|---------|-----|----------|-----|----------|-----|----------|
| Bending | 7  (6) | 5 (5) | 5 (5) | 5 (5) | 5 (5) | 5 (5) | 5 (5) |
| Tension | 6  (5) | 5 (5) | 5 (5) | 5 (3) | 5 (5) | 5 (4) | 5 (5) |
| Torsion | 12 (10) | 5 (5) | 5 (5) | 5 (3) | 5 (3) | 6 (5) | 5 (5) |

## 3.2 QUANTITATIVE COMPUTED TOMOGRAPHY SCANNING

The specimens were degassed for 45 minutes and scanned in a water bath with a GE High Speed Helical QCT Scanner both before and after defects were introduced. QCT scans were taken of the cross-section at the center of the defect (at its maximum width) for each specimen. QCT attenuation values were converted from Hounsfield units to density (g/cc) based on relations derived from solid hydroxyapatite phantom rods of known density, which were included in each scan. Cross-sectional properties were calculated based on the density and spatial distribution of bone mineral recorded in each QCT image. The protocol for QCT scanning and data reduction is described in detail in Chapter 5.

Descriptive statistics for the properties of the specimens in each of the mechanical testing groups are presented in Table 3.2. Comparing Table 3.2 to Table 2.1, which includes statistics for the entire lot of test specimens, shows that the distribution of specimens in each test was very similar to the overall distribution within the entire lot of 115 specimens.

Table 3.2 - Cross-Sectional Properties of Test Specimens as Measured by QCT

|  | All Tests | Tension | Specimens | Bending | Specimens | Torsion | Specimens |
|---|---|---|---|---|---|---|---|
|  | Density (g/cc) | A (mm$^2$) | EA (MN) | Ix (cm$^4$) | EIx (Nm$^2$) | J (cm$^4$) | GJ (Nm$^2$) |
| n | 104 | 36 | 36 | 32 | 32 | 36 | 36 |
| Mean | 0.37 | 82 | 0.14 | 0.078 | 1.20 | 0.21 | 3.5 |
| Std. Dev. | 0.18 | 33 | 0.17 | 0.045 | 1.13 | 0.06 | 3.4 |
| Min | 0.17 | 41 | 0.02 | 0.026 | 0.13 | 0.12 | 0.6 |
| Max | 1.03 | 141 | 0.95 | 0.165 | 4.27 | 0.33 | 12.9 |

## 3.3 FINITE ELEMENT MODELING

Linear, elastic finite element models were used to predict the stress, strain, and strain energy concentration factors for the specimens. Models of tension, torsion, and four-point bending of the specimens for each hole size and shape were created using Patran (PDA Engineering, Costa Mesa, Ca). The models included both the bone and rigidly attached metal endcaps through which the loads were applied. Twenty-node, quadratic, isoparametric elements were chosen to provide an accurate representation of the geometry of a circular defect in a cylinder and of large strain gradients. In addition, the mesh was significantly refined in the neighborhood of the defect. The models had approximately 1500 elements and 8500 degrees of freedom, depending on the defect size. The models were tested for convergence and validated against experimental studies of cylinders with holes.

Boundary conditions exactly modeled the constraints in the actual mechanical tests. Unit loads were applied to the models, and the maximum stress, strain, and strain energy in each model was recorded. Stress concentration factors were calculated for each hole size by dividing the maximum stress recorded in the finite element model by the stress predicted using Bernoulli-Euler solid mechanics theory. The "Bernoulli-Euler" stress was calculated at the specimen's most-reduced cross-section. Concentration factors were also calculated for strain and strain energy. Details of the finite element models and the their results are discussed in Chapter 6; however, the stress resulting concentration factors calculated for each hole size are presented here in Table 3.3. The Patran script files used to generate the models and sample plots are shown in Appendix C.

Table 3.3 - Stress Concentration Factors from Different Hole and Loading Models

| Hole Size | None | 28% | 28% Slot | 47% | 47% Slot | 56% | 56% Slot |
|---|---|---|---|---|---|---|---|
| Bending | 1.00 | 1.88 | 1.58 | 1.55 | 1.45 | 1.41 | 2.54 |
| Tension | 1.00 | 2.46 | 3.82 | 2.28 | 4.34 | 2.32 | 7.49 |
| Torsion | 1.00 | 2.19 | 2.85 | 2.08 | 3.70 | 2.05 | 9.19 |

The results of the model for four point bending of a 56% slot are shown in Figure 3.2. They show quantitatively the areas of high stress/strain concentration in the specimen.
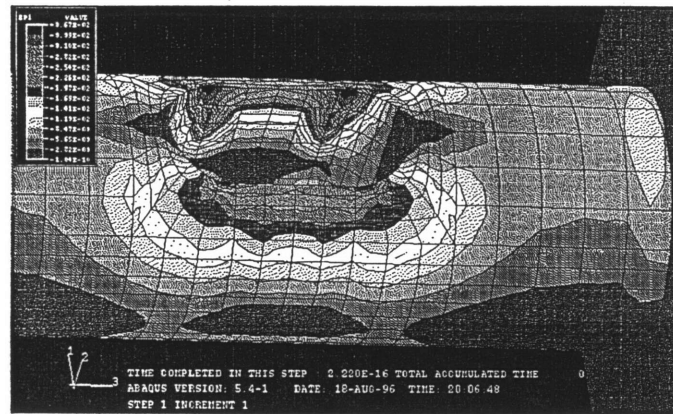


Figure 3.2 - Strain contours for a specimen with a 56% slot subjected to four-point bending.

## 3.4 MECHANICAL TESTING

After the QCT examinations, specimens were tested to destruction in either four-point bending, tension, or torsion. These failure modes were chosen because they represent the primary modes in which long bones typically fail, and because they are not as susceptible to measurement error as compression tests can be [2].

Specimens were thawed in physiological saline before testing and kept moist during testing, which was undertaken at room temperature (21° C, 63% humidity). At this temperature, the modulus has been shown to increase by only 2-4% above that at body temperature (37°C) [1]. Specimens were tested at a constant displacement rate to complete fracture using an *INSTRON* model 1331 universal test machine for bending and tension and an Interlaken model 3300 test frame for torsion. The specimen's PMMA endcaps were secured in aluminum sleeves with set screws during testing in order to give an even load distribution and to avoid damaging the bone.

Because bone is a viscoelastic material, it exhibits a strain rate sensitivity in testing, and can be as much as 50% stiffer at high strain rates than low [3]. Strain rates in daily activities are typically around 0.1% per second [4]. Therefore, the displacement rate was adjusted for each specimen so that its predicted strain rate was between 0.01% $s^{-1}$ and 0.1% $s^{-1}$ based on its rigidity as measured by QCT and assuming a failure strain of 1.0%.

The applied load, test frame actuator displacement, and specimen deformation were all sampled at 12 Hz, and data acquisition was synchronized using the Biopac Data Acquisition System. A load cell was used to measure the load applied to each specimen.

The displacement of the test frame actuator was measured with a linear variable displacement transducer (LVDT). The MacReflex Position Sensor measured specimen deformation by tracking the displacement of small optical markers attached at specific points along the specimen.

The MacReflex Position Sensor is a charged coupled device (CCD) camera system capable of tracking markers which reflect infrared light emitted from an light-emitting diode (LED) array attached to each camera. Each camera employs a 604 × 294 pixel CCD, a strobing infra-red LED array centered at 885 nm, and an electronic shutter that samples an object's position for 1/4000 seconds at a rate of 60 Hz. Proprietary hardware and software resolve images from the cameras into a 27,000 × 19,400 pixel grid with a standard deviation in pixel position of 0.003% of the field of view (FOV) due to spatio-temporal noise. Markers can be tracked in three dimensions by triangulation of images from multiple cameras, and the cameras' coordinate systems are scaled using a three-dimensional calibration frame with seven markers of known positions.

Fifty millimeter lenses and spacing rings were used with the MacReflex cameras in these experiments to give a 70 mm FOV (defined as the diagonal of the rectangular image), resulting in a spatial resolution of about 2 microns. Diamond shaped markers 1 mm on a side were used for maximum resolution. Validation of the MacReflex system and its markers are discussed in Appendix A, along with the protocol for using the system. Appendix A also discusses validation of the four-point bending and tension test apparati. The validation of the torsional apparatus is discussed in another thesis[5].

Data were filtered using a low pass Blackman filter at -67dB with a cutoff frequency of 1.5 Hz, and a plot of load vs. normalized displacement (a calculation of average strain) was generated for each specimen. Deflection was normalized so that the slope of the plot would give units consistent with rigidity and in order to compensate for any variation in the distances between markers from one specimen to the next. The following properties were determined from this plot for each specimen:

- *GLOBAL RIGIDITY.* Global rigidity of the specimen was taken as the slope of a least-squares fit to the obviously linear portion (as determined by eye) of the plot of load vs. normalized deflection. The fit was not forced through a zero y-intercept; however, most plots naturally produced a y-intercept very near zero.

- *YIELD LOAD.* Yield load was taken as the point where the tangent slope of the curve deviated from the slope of the linear portion of the curve by 30%, as shown in Figure 3.3 for the case of bending. This is approximately the same as the 0.2% strain offset for the plot in Figure 3.3. Approximately 10% of the linear portion of the curve was sampled on either side of a point to determine its tangent modulus.

- *YIELD STRAIN.* Outer fiber yield strain was taken as the strain that occurred simultaneously with the yield load. Strain was calculated from marker displacements.

- **ULTIMATE LOAD.** Ultimate load was taken as the maximum load supported by the specimen before failure.
- **ULTIMATE STRAIN.** Outer fiber ultimate strain was taken as the strain that occurred simultaneously with the ultimate load. Again, strain was calculated from marker displacements.
- **FRACTURE PATTERN.** The location and pattern of fracture for each specimen were drawn to compare with the fracture location predicted by finite element models.
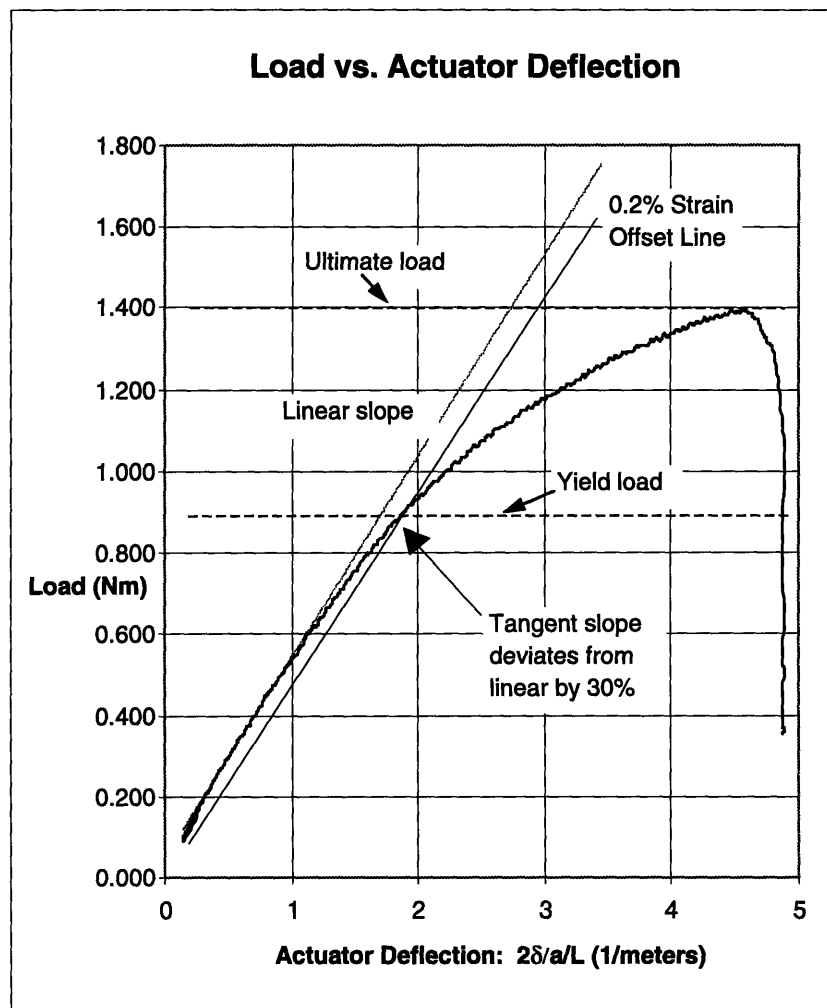


Figure 3.3 - Typical load vs. normalized deflection plot shows that 30% deviation in slope is approximately the same as a 0.2% strain offset. The specimen used in this plot had no defect. Strain was calculated using simple solid mechanics assuming a two-section beam of PMMA and bone.

The yield criterion was chosen because it corresponded to the 0.2% strain offset in an intact specimen and because it could be easily measured and was consistent from one specimen to the next, regardless of defect size. Other researches have used various offsets, such as 0.2% offset [6], 0.03% offset [7], as well as the point where the slope of the stress-strain curve began to decrease [8]. However, a study by Turner [7], while concluding that the definition of yield had very little effect on the resulting relationship between

yield strain and cross-sectional properties, found that the standard deviation of yield strain measured at the point where slope began to decrease was as much as 22% less than that measured using the other criteria, further supporting the choice of the 30% deviation in slope as a valid choice for a yield criterion. It should be noted that the study also found that changing the definition of the point of zero strain did not affect the results.

### 3.4.1 4-POINT BENDING TEST

The basic test setup for the four-point bending test is shown in Figure 3.4. Marker and camera placements for four-point bending specimens are shown in Figures 3.5 and 3.6. The four-point bending jig used four load points spaced symmetrically about the center of the specimen to apply a constant moment throughout the gage length of the specimen. The moment arm on each side of the specimen was 38 mm. The lower left load point was fixed, and the other three load points were roller bearings, allowing axial deformation (which occurs during bending) without introduction of undesired axial loads. The top half of the four-point bending mount was rigidly fixed to the load cell of an INSTRON 1331 test frame and was free to rotate on a roller bearing about an axis perpendicular to the page. This rotational freedom insured identical loads, rather than identical displacements, at all load points. Load was applied through a hydraulic actuator to which the bottom half of the four-point contact mount was attached.
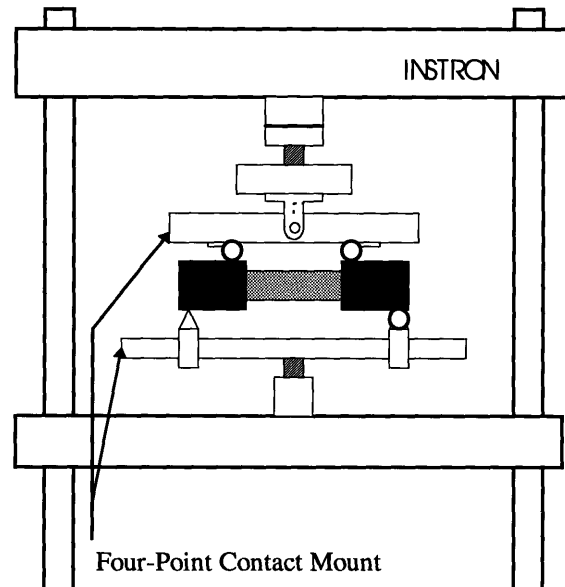


Figure 3.4 - Basic setup for four-point bending test.

Infra-red reflecting markers were placed symmetrically about the hole in 8 mm increments, with one marker directly at the center of the hole. Cameras were placed level with the specimen at a 20° angle from the specimen's normal, providing excellent

resolution in the plane of bending. They recorded displacement in three dimensions, but bending was calculated only in the plane of the actuator movement.
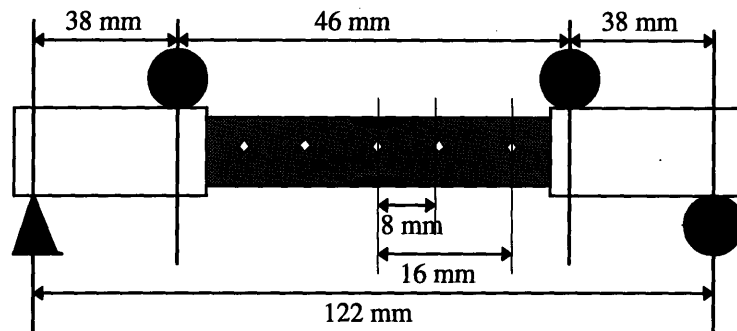


Figure 3.5 - Dimensions of test setup and marker placement for four-point bend test.
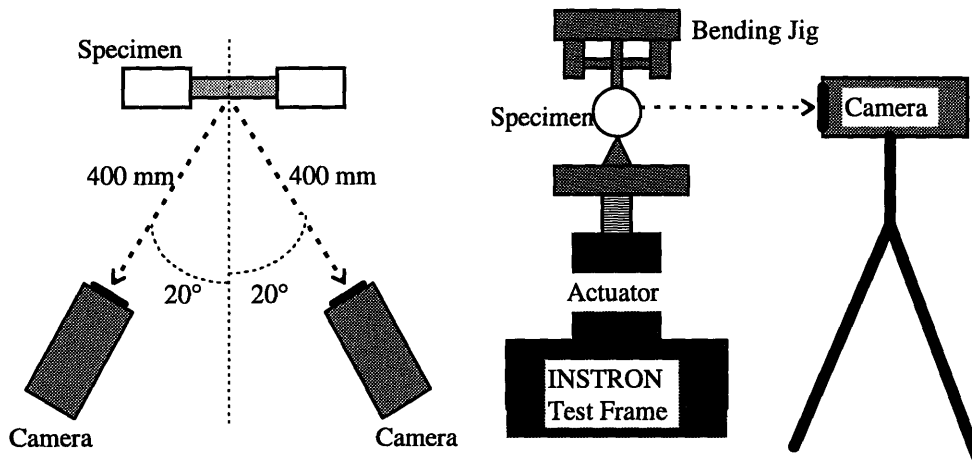


Figure 3.6 - Placement of cameras relative to the specimen.

Four point bend testing was performed on an *INSTRON* model 1331 test frame and load was measured in Newtons with a Sensotec 100 lb load cell. The applied moment was plotted vs. a normalized midspan deflection, as shown previously in Figure 3.3. The applied moment was calculated from the load cell measurements and moment arm (0.0381 m) using the relation:

$$M = \frac{0.0381 \text{ m} \times \text{Load}}{2} \qquad [3.1]$$

The calculation of normalized deflection required a few assumptions. The first deals with the relation between strain and the applied moment. The strain at a given coordinate (x,y) relative to the section centroid is given by the general relation

$$\varepsilon = \frac{(M_X I_Y + M_Y H_{XY})y - (M_Y I_X + M_X H_{XY})x}{E(I_X I_Y - H^2_{XY})}$$  [ 3.2 ]

assuming equal compressive and tensile moduli. When the bending is applied purely about the x-axis, the y-component drops out. Also, since the orientation of the defects causes the x-axis to coincide with a principle axis of the specimen, $H_{XY} = 0$, further simplifying the relation to

$$\varepsilon = \frac{Mc}{EI_X}$$  [ 3.3 ]

Given the simplified relation between load and strain, the relation between load and midspan deflection was derived using elementary solid mechanics and assuming a specimen composed of two homogeneous endcaps and a single section of bone. The rigidity of such a specimen in terms of its midspan deflection may be written as

$$EI = \frac{M}{(2\delta) / (aL)}$$  [ 3.4 ]

where

- $M$ = applied moment
- $\delta$ = midspan deflection, measured by actuator displacment
- $a$ = length of moment arm
- $L$ = gage length of specimen (length between the inner two load points).

The normalized deflection was taken as the denominator in equation 3.4. Calculation of the specimen's rigidity, yield load, and ultimate load were described earlier. Yield and ultimate strain were derived from the five markers' digitized positions at the time of yield and ultimate load. The displacement of each marker from its original position at the beginning of the test was plotted in two dimensions in the plane of bending to give the current shape of the gage length relative to its unloaded shape. The y-axis was chosen to be coincident with the center marker. The equation for a parabola ($y = ax^2 + bx + c$) was fit with a least squares method to the five points, and the strain at the bottom exterior of the specimen was calculated from that fit using the following relations [9]:

$$P = \frac{1}{2 |a|}$$  [ 3.5 ]

$$\rho(x) = \frac{(P + 2x)^{3/2}}{\sqrt{P}}$$  [ 3.6 ]

$$\varepsilon(x) = \frac{c}{\rho(x)}$$  [ 3.7 ]

where

- a        = coefficient of the quadratic term in the parabola equation
- P        = the parameter of the parabola
- $\rho(x)$    = the radius of curvature of the parabola at point x
- $\epsilon(x)$     = outer fiber strain at point x in the parabola
- c        = distance from the specimen's centroid to its outer fiber (assumed to be approximately 6.35 mm).

## 3.4.2 TORSION

In the torsion test, force from a uniaxial test frame was converted to torque applied about the specimen's long axis through a system of cables and pulleys. This technique allowed the specimen to warp and deform axially while still maintaining a pure torsional load about its centroid and not inducing uncontrolled axial or bending restoring forces. The technique has been demonstrated in other biomechanical studies [10]. The basic setup is shown in Figure 3.7. Two markers were placed symmetrically on either side of the defect, approximately 12.5 mm from its center, and the cameras were positioned in a manner similar to the setup for four-point bending, as shown in Figure 3.8.

Interlaken load frame
Aluminum interface plate
Six axis load cell
Steel collet
Specimen
Aluminum endcap
with steel cable

Aluminum
support plate

Rolling/sliding
bearing

Steel cable

Aluminum base
plate

Interlaken
actuator

SIDE VIEW
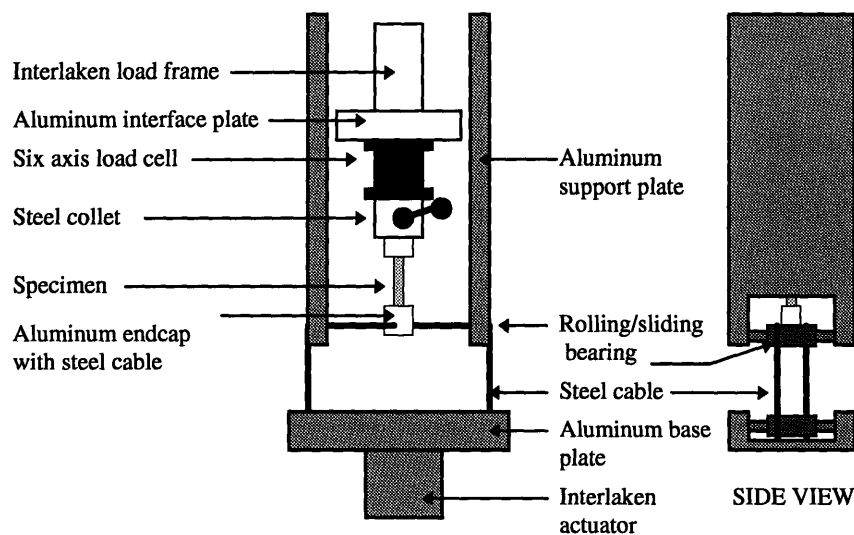
Figure 3.7 - Torsion testing jig setup.
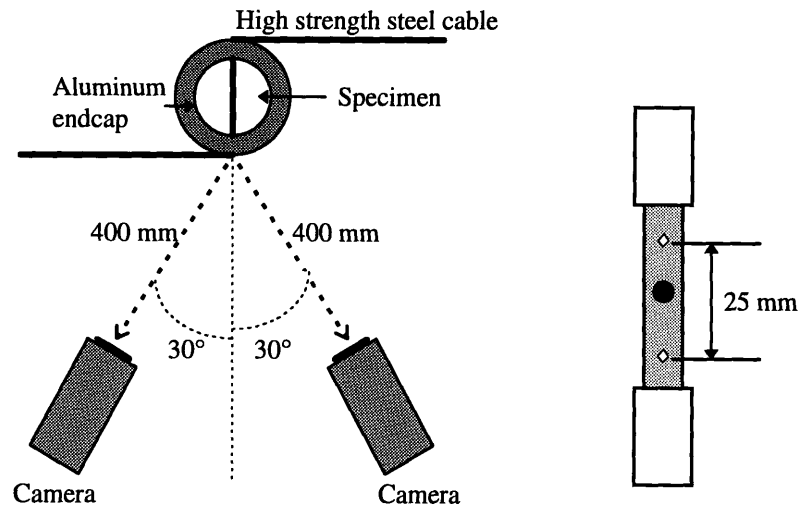
Figure 3.8 - Top view of camera positions and front view of specimen with markers.

The torsion tests were performed on an Interlaken model 3300 test frame, and the applied torque was measured with an AMTI model MC-3A-6-1000 six-axis load cell. The MacReflex cameras recorded the movement of the markers in three dimensions.

For torsion, the applied torque measured by the load cell was plotted versus the normalized deflection. A small pre-load was necessary to straighten the cables in each test. This did not significantly load the specimen, so the load measurement was tared after this pre-loading. The normalized deflection, called twist in the case of torsion, was calculated from the relative displacements of the two markers in three dimensions. The calculation assumed rotation about the geometric center of the specimen and assumed the instantaneous axis of rotation was perpendicular to the plane of motion of the marker. This allowed for relative twist between the markers to be calculated even though the markers were not necessarily rotating in the same plane, as would be the case if the specimen warped out of plane. However, the calculation implicitly assumed that out of plane motion of each marker was small compared to rotational motion. It turned out in the tests that this assumption was valid.

First, the motion of each marker relative to its unloaded position was calculated:

$$\Delta = \sqrt{(x-x_0)^2+(y-y_0)^2+(z-z_0)^2}$$

[ 3.8 ]

The rotation of the marker about the specimen's geometric center was then calculated by taking $\Delta$ as the chord of the arc segment swept out by each marker:

$$\theta = 2 \ asin \ (\frac{\Delta}{2r})$$

[ 3.9 ]

where r is the radius of the specimen. Then the twist of the gage length between the markers was calculated by  dividing the relative rotation of the two markers by the original gage length.

$$\text{Twist} = \frac{\delta\theta}{L_0} = \frac{\theta(\text{marker 2}) - \theta(\text{marker 1})}{L_0} \qquad\qquad [\,3.10\,]$$

The original gage length, $L_0$, was taken as the distance between the two markers before a load was applied.  Twist was measured in radians/meter.  Global rigidity, yield load, ultimate load, yield strain, and ultimate strain were calculated as discussed previously, with strain measured as the twist.  However, in order to give the proper units, yield (ultimate) twist was multiplied by the specimen radius (6.35 mm) to give yield (ultimate) strain:

$$\gamma = \frac{r\theta}{L_0} \qquad\qquad [\,3.11\,]$$

### 3.4.3 TENSION

Tension is a mode of testing in which undesired loads can be very difficult to eliminate.  For instance, take a cylindrical specimen 12.7 mm in diameter by 45 mm long, loaded in tension by rigid grips at both ends. If the specimen's long axis was misaligned with the axis of the grips by only 0.66°, it would experience twice the load on one side as the other due to undesired bending.

Therefore, the tension apparatus used in this test was designed to reduce undesired loads as much as possible by allowing to system to self-align and the specimen to twist and bend freely.  The system, shown in Figure 3.9, consisted of three-link chains connecting each end of the specimen to an *INSTRON* test frame.  The test frame actuator was on the bottom of the specimen, and the fixed portion of the frame, on the top.  The specimen's PMMA endcaps were set screwed into aluminum endcaps through which the applied load could be evenly distributed.  Alignment freedom was enhanced through a greased universal ball joint and high strength, low-twist cable which connected each aluminum endcap to the three-link assembly.
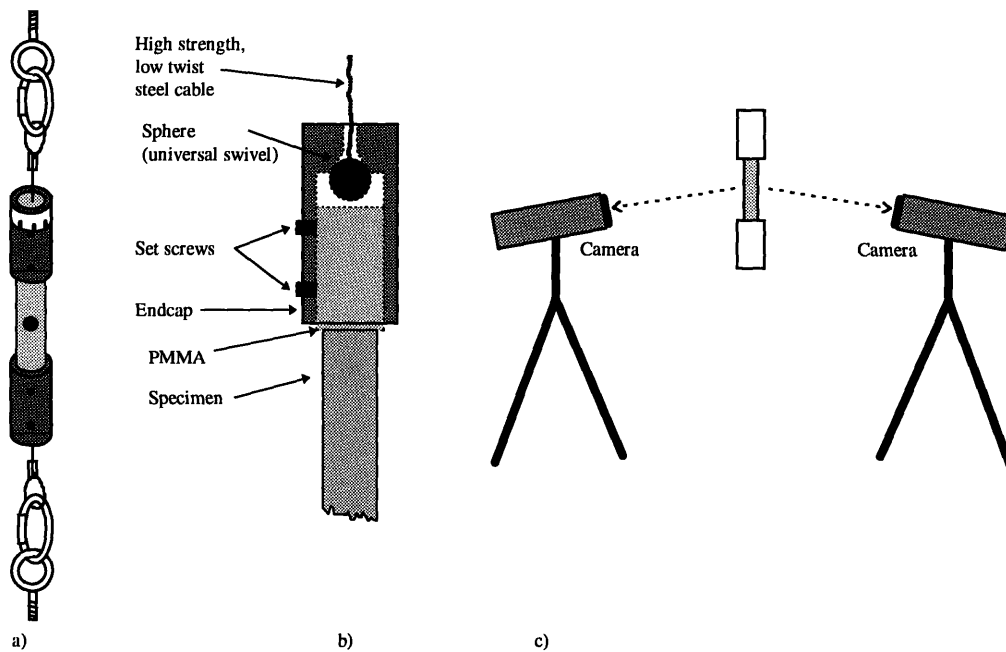
Figure 3.9 - a) Tension test setup; b) close-up view of endcap; c) cameras tracked marker
displacements on opposite sides of the specimen.

Tests were performed on an *INSTRON* model 1331 test frame, and load was
measured in Newtons with a Sensotec 2000 lb load cell, model 41/572-01. MacReflex
was used to track marker displacement. Specimens were marked in the same manner as
the torsion specimens, except that a set of markers was placed on two sides, rather than
just one. The opposing markers were used to check and correct the uneven strain.
Cameras were placed slightly below level with the specimen and angled up so that the
LED strobes would not interfere with one another. Cameras were opposite each marker
set so that one camera tracked the displacement of each marker set and marker motion
was recorded in only two dimensions. Marker displacements were normalized to the
initial distance between the markers, giving a unitless measurement. Therefore, marker
displacement did not need to be calibrated to any particular unit of measure.

For tension, the applied load measured by the load cell was plotted versus a
normalized displacement. The displacement between markers was divided by the
initial distance between the makers for each set, to give a strain averaged over the
length between the markers. The strains of the two marker sets were averaged, and this
average was used for the plot of load vs. normalized displacement, as well as
calculations of yield and ultimate strain.

---

[1]  C.H. Turner and D.B. Burr, "Basic biomechanical measurements of bone: a tutorial," *Bone*,
     14:595-608, 1993.

[2]   T.M. Keaveny, W.C. Hayes, "A 20-year perspective on the mechanical properties of trabecular bone," *Journal of Biomechanical Engineering*, 115:534-542, 1993.

[3]   G.J. Sammarco, A.H. Burstein, W.L. Davis, and V.H. Frankel, "The biomechanics of torsional fractures: the effect of loading on ultimate properties," *Journal of Biomechanics*, 4:113-117, 1971.

[4]   S.R. Simon, Orthopaedic Basic Science, American Academy of Orthopaedic Surgeons, 1994, Chapter 4.

[5]   J. Hong, "Noninvasive Prediction of Failure in Trabecular Bone with Simulated Osteolytic Defects," Massachusetts Institute Technology, 1997.

[6]   J.W. Vahey, J.L Lewis, and R. Vanderby, "Elastic moduli, yield stress, and ultimate stress of cancellous bone in the canine proximal femur," *J. Biomechanics*, 20: 29-33, 1987.

[7]   C.H Turner, "Yield behavior of bovine cancellous bone," *J. Biomechanics*, 111: 256-260, 1989.

[8]   I. Hvid, "Cancellous bone at the knee: a comparison of two methods of strength measurement," *Arch. Orthop. Trauma Surg.*, 104: 211-217, 1985.

[9]   I.N. Bronshtein and K.A. Semendyayev, Handbook of Mathematics, Van Nostrand Reinhold Co., New York, 1985, Chapter 2.

[10]  N.R. Crawford, A.G.U. Brantley, C.A. Dickman, and E.J. Koeneman, "An apparatus for applying pure nonconstraining moments to spine segments in vitro," *Spine*, 20:2097-2100, 1995.

# Chapter 4
# Results and Discussion

This chapter presents descriptive statistics of the test results and shows typical plots of load vs. normalized deflections for each type of test. Then each of the research questions is addressed by discussing the results of statistical analyses of the test data. A typical data sheet for each type of test and a table of the raw QCT and mechanical test data are shown in Appendix B.

## 4.1  TEST RESULTS

All but eleven specimens failed within the gage length of the bone. These eleven specimens were excluded because they broke at the endcaps or were inadvertently damaged before the test began. Load vs. normalized deflection was plotted for every specimen, and mechanical behavior characteristics were determined according to the equations described in the previous Chapter. In addition, the fracture pattern on each specimen was carefully sketched. Copies of these sketches are also included in Appendix B.

Figure 4.1 shows a typical load vs. normalized deflection for the four-point bending test. In general most specimens displayed a large region of nonlinear deflection after yield, and a progressively decreasing load capacity after ultimate load. Fracture appeared to occur by intermittent crack growth. Some specimens immediately fractured once ultimate load was reached. In others, load capacity dropped sharply over a series of "steps", in which a crack would propagate, arrest, and then propagate again in fast fractures. Analysis of the failed specimens showed cases where the crack would displace from its initial path, presumably at the site of a crack-arrest. In general, cracks initiated between the corners and center of the defect, and initiated at the same location on both sides of the defect. They propagated in straight, parallel lines perpendicular to the long axis of the specimen (see sketches in Appendix B).

Figure 4.2 shows two typical plots of curvature at yield in four-point bending, defined by the displacement of five markers placed along the neutral axis of each specimen. The maximum deflection of most specimens was at the site of the center marker, since it was placed at the center of the defect. However, maximum deflection was not at the center of some specimens, typically those without a defect.

**Load vs. Actuator Deflection**
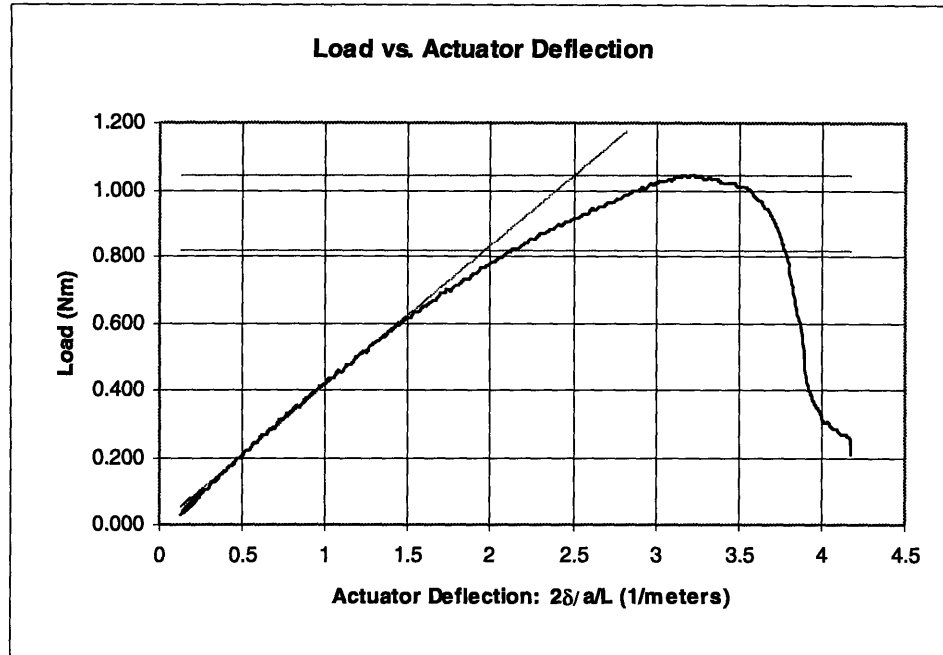
Figure 4.1 - Typical plot of load vs. normalized deflection for four-point bending

**Curvature at Yield**

$y = -1.27E\text{-}06x^2 + 1.77E\text{-}04x + 4.30E\text{+}02$
$R^2 = 9.64E\text{-}01$

**Curvature at Yield**

$y = -7.21E\text{-}07x^2 - 3.14E\text{-}03x + 2.51E\text{+}02$
$R^2 = 9.88E\text{-}01$
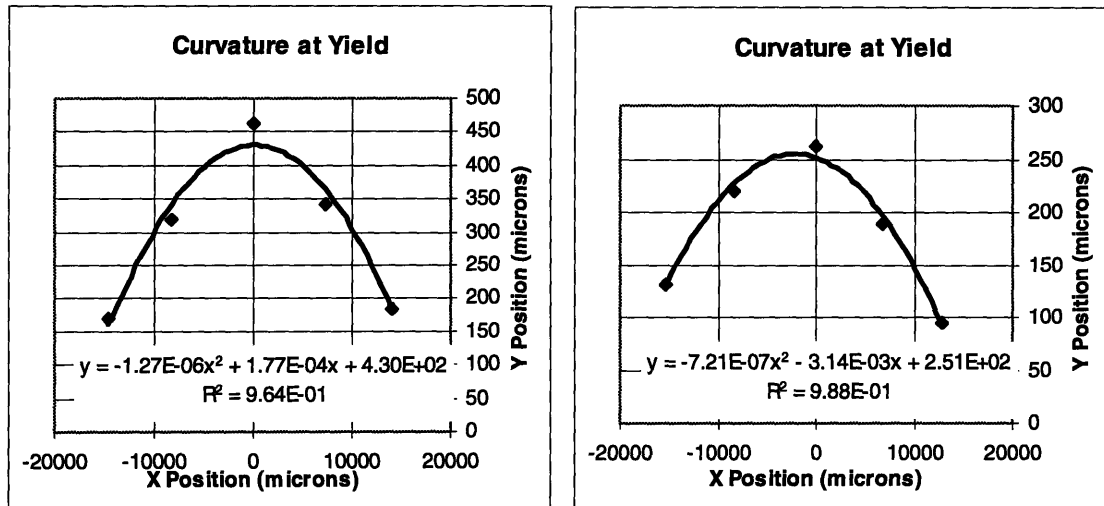
Figure 4.2 - Two typical plots of deflection at digitized points along the length of a specimen at yield. The first plot has the curvature centered at the center marker. Curvature in the second plot is centered to the left of the center marker.

Figure 4.3 shows a typical plot of load vs. normalized deflection for torsion. Most torsion specimens, like the bending specimens, showed significant nonlinear deformation after yield and appeared evenly divided between specimens which slowly lost load carrying capacity and those that instantly fractured after ultimate load. Fractures were in general spirals, initiating at the corners of the defect. However, in some of the specimens with circular defects, the crack propagated in a straight line perpendicular to the specimen's long axis, like the four-point bending cracks.

Figure 4.4 shows a typical plot of load vs. normalized deflection for the tension test. Tension displayed post-yield behavior similar to that of bending and torsion. However, a small, but significant, number of specimens failed in a more brittle manner, in which yield and ultimate loads were very close in magnitude. Tensile fracture patterns were similar to the four-point bending patterns; however, cracks predominantly initiated at the center of the defect rather than the corners.
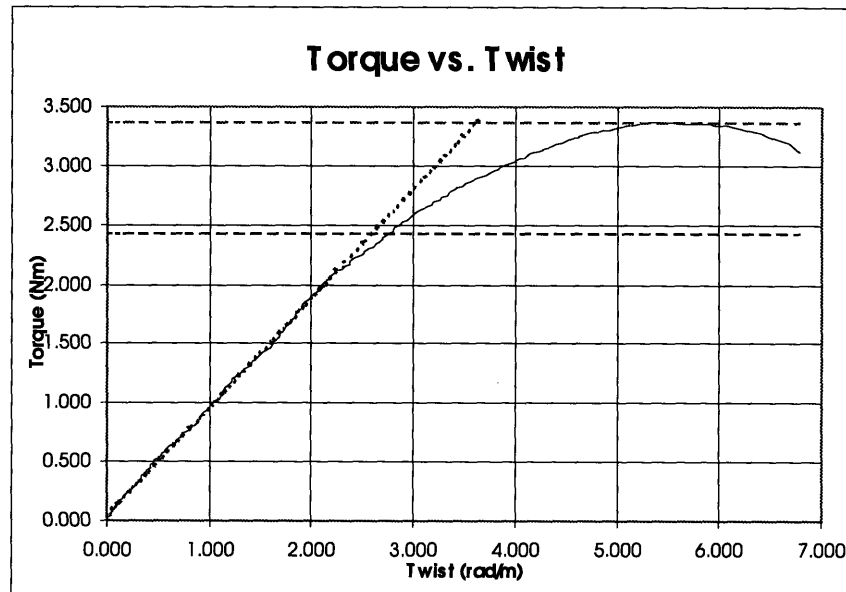


Figure 4.3 - Typical plot of load vs. normalized deflection (twist) for the torsion test.
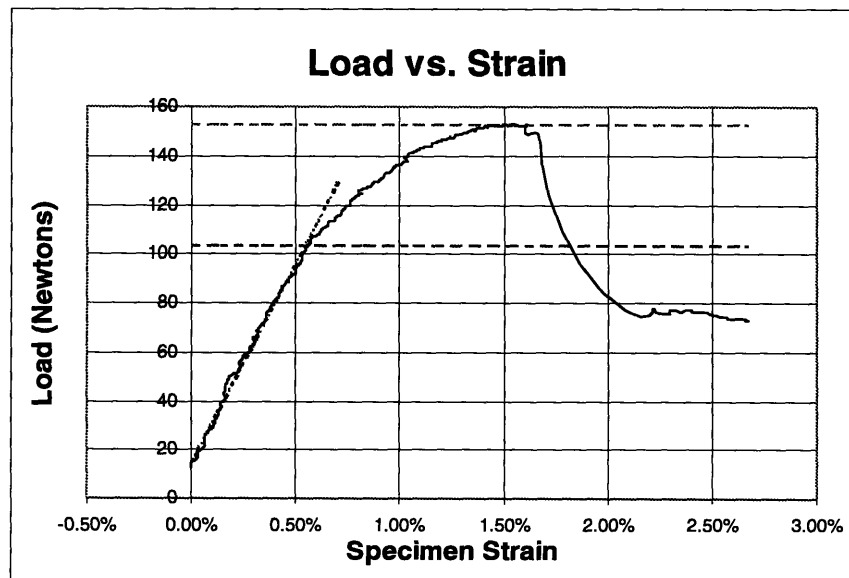


Figure 4.4 - Typical plot of load vs. normalized deflection (strain) for the tension test.

Table 4.1 lists descriptive statistics for the results of the four-point bending tests, Table 4.2 of torsion tests, and Table 4.3 of tension tests. The tables show a wide range of rigidities, yield loads, and ultimate loads within each test. The average coefficient of variation for these properties (standard deviation divided by the mean) was 87% and was very consistent from one type of test to the next. It should be noted, however, that yield strain does not vary as widely as the loads or rigidity.

Table 4.1 - Descriptive Statistics of Four-Point Bending Tests

|        | Yield Strain | Ultimate Strain | Rigidity Nm^2 | Yield Load Nm | Ultimate Load Nm |
|--------|--------------|-----------------|---------------|---------------|------------------|
| **Mean**  | 1.10% | 2.17% | 0.91 | 1.22 | 1.56 |
| **Stdev** | 0.40% | 0.96% | 0.64 | 1.09 | 1.42 |
| **Max**   | 2.08% | 4.13% | 2.05 | 3.82 | 5.50 |
| **Min**   | 0.46% | 0.90% | 0.11 | 0.18 | 0.21 |

Table 4.2 - Descriptive Statistics of Torsion Tests

|        | Yield Strain | Ultimate Strain | Rigidity Nm^2 | Yield Load Nm | Ultimate Load Nm |
|--------|--------------|-----------------|---------------|---------------|------------------|
| **Mean**  | 1.15% | 3.27% | 0.43 | 1.12 | 1.70 |
| **Stdev** | 0.40% | 1.47% | 0.34 | 0.98 | 1.50 |
| **Max**   | 2.01% | 8.21% | 1.43 | 3.65 | 6.23 |
| **Min**   | 0.12% | 1.18% | 0.03 | 0.10 | 0.17 |

Table 4.3 - Descriptive Statistics of Tension Tests

|        | Yield Strain | Ultimate Strain | Rigidity KN | Yield Load Newtons | Ultimate Load Newtons |
|--------|--------------|-----------------|-------------|--------------------|-----------------------|
| **Mean**  | 0.51% | 1.20% | 80.7  | 401  | 556  |
| **Stdev** | 0.13% | 0.44% | 78.2  | 379  | 486  |
| **Max**   | 0.87% | 2.56% | 275.4 | 1317 | 1734 |
| **Min**   | 0.28% | 0.57% | 8.48  | 64   | 89   |

## 4.2 CAN THE ELASTIC BEHAVIOR OF TRABECULAR BONE WITH DEFECTS BE USED TO PREDICT ITS LOAD CAPACITY?

To answer the first research question, relations between rigidities and yield load were investigated. Yield load correlated very strongly with ultimate load ($r^2 = 0.98$ for bending, $r^2 = 0.97$ for torsion, $r^2 = 0.97$ for tension) . Therefore, conclusions drawn from statistical analysis of the yield load should apply equally well to ultimate load.

The yield load was correlated with mechanically measured rigidity first, since rigidity was the only elastic property that could be directly measured mechanically. Global rigidity, taken as the linear portion of the load vs. normalized deflection curve, correlated well with yield load for bending ($r^2$ = 0.84) , torsion ($r^2$ = 0.89), and tension ($r^2$ = 0.88). The regressions are shown in Figures 4.5-4.7.

In bending, we were also able to measure cross-sectional rigidity local to the defect by calculating the outer fiber strain of the specimen at the defect. Derivation of this strain from five marked points along the neutral axis of the specimen was discussed earlier for the case of measuring yield strain. Rigidity was calculated as the slope of the linear portion of the load vs. strain curve. By using the curvature specifically at the defect to calculate strain, the local rigidity could be measured directly at the defect, rather than averaging over the entire length of the specimen. This local rigidity had an even stronger correlation with yield load ($r^2$ = 0.93). Our observation that yield load correlates more highly with local rigidity than global rigidity suggests that failure is a local phenomenon. It depends more on the mechanical properties and the load state of the cross-section where failure occurs and cross-sections local to the failure site than cross-sections far away. Global rigidity probably correlated less highly because it represented properties averaged over a wide range of cross-sections beyond the area local to the defect.
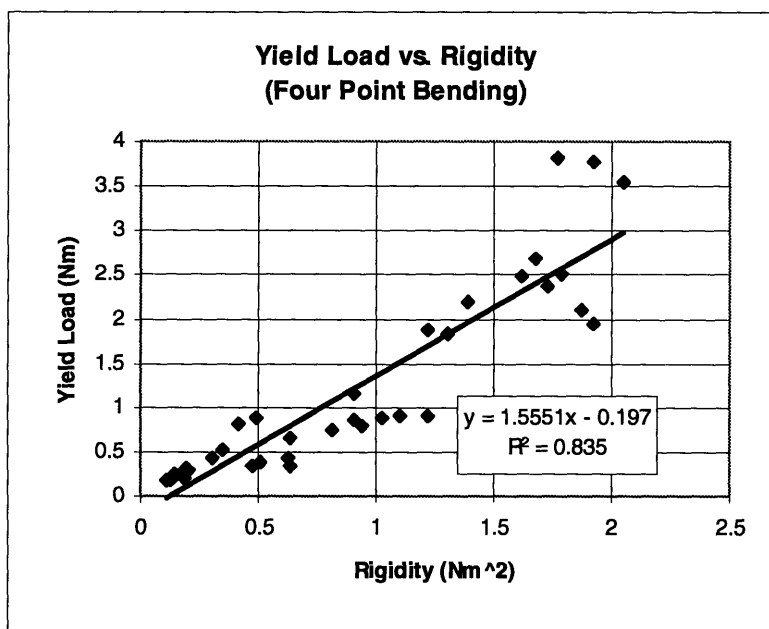


Figure 4.5 - Regression between yield load and global rigidity for four-point bending.

**Yield Load vs. Rigidity (Torsion)**

$y = 2.3165x + 0.0424$
$R^2 = 0.8869$
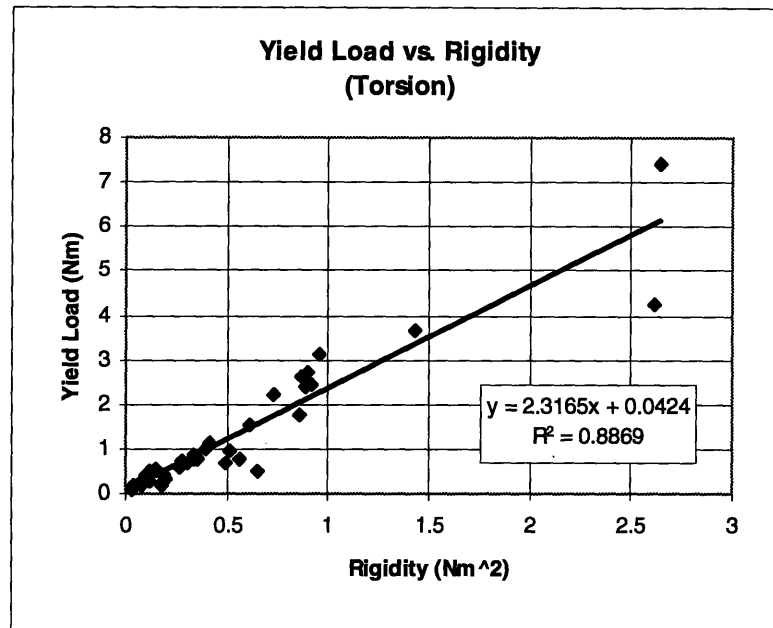
Figure 4.6 - Regression between yield load and global rigidity for torsion.

**Yield Load vs. Rigidity (Tension)**

$y = 0.0046x + 33.203$
$R^2 = 0.8846$
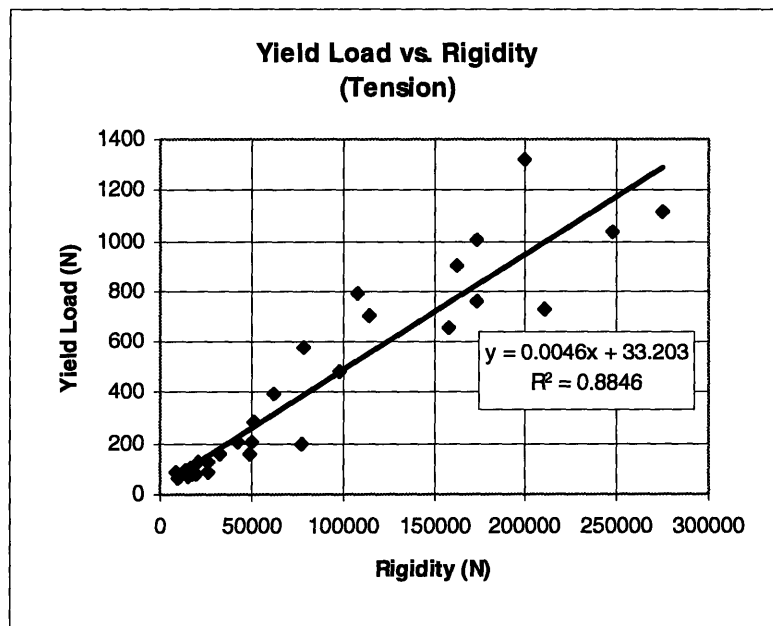
Figure 4.7 - Regression between yield load and global rigidity for tension.

## 4.3 CAN THE ELASTIC MECHANICAL BEHAVIOR OF TRABECULAR BONE WITH DEFECTS BE PREDICTED BY NON-INVASIVE IMAGING TECHNIQUES?

This question was answered in a simple form by correlating QCT estimates of the rigidity at the defect cross-section to the mechanically measured bending rigidity. The correlation between QCT GJ and torsional rigidity was $r^2 = 0.94$, and the correlation between QCT EA and axial rigidity was $r^2 = 0.87$. In bending, QCT EI min correlated to mechanically-measured global rigidity ($r^2 = 0.77$), but correlated more highly to the local rigidity of the defect cross-section as determined by outer-fiber strain calculations ($r^2 = 0.92$). It should be noted that in the case of local rigidity, the slope of the regression (shown in Figure 4.8) was not statistically different from one ($p > 0.5$) and the intercept was near zero. This indicates that QCT not only correlates to, but also accurately measures, the mechanical rigidity of a cross-section. Since a strictly local rigidity was not measured for torsion or tension, this conclusion could not be confirmed by experiment for those two modes of testing.
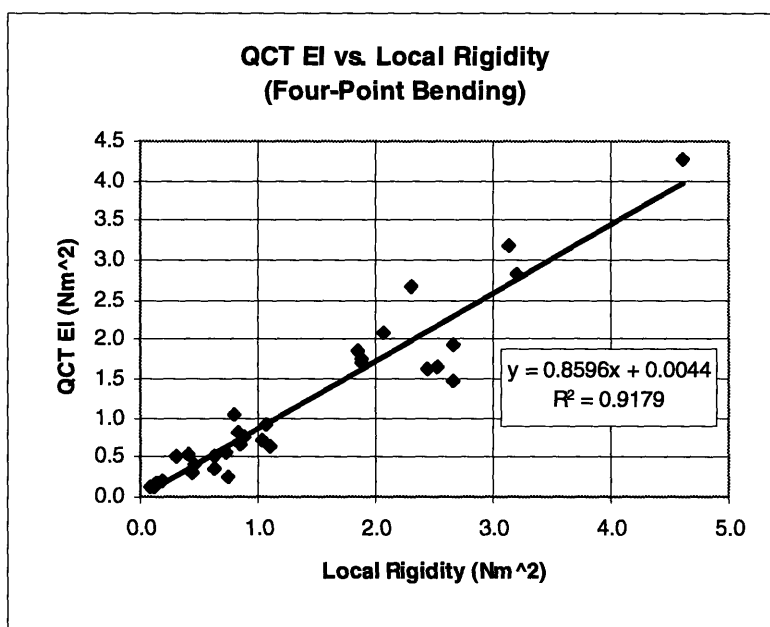


Figure 4.8 - Correlation of QCT EI to the cross-sectional rigidity at the center of the defect..

An analysis of covariance was performed to determine whether or not different hole sizes had different relations between QCT rigidity (AE, EI, and GJ) and mechanically-measured rigidity. The regressions of QCT measured rigidity vs. mechanically measured rigidity (discussed above) were grouped with hole size as the concomitant variable, and the slopes of the grouped regressions were compared. No significant difference was detected between groups for tension ($p > 0.20$) or torsion ($p > 0.20$).

The only group which was significantly different than others in bending was the 56% hole group (p = 0.03). Ideally, to validate the method proposed by this thesis to non-invasively measure load capacity, the relationship between QCT measurements of rigidity and actual mechanical rigidity should be the same for every hole size. However, stress concentrations around the hole may further reduce the rigidity of a specimen with a defect beyond what would be calculated from a QCT image alone. Accordingly, the slope of Figure 4.9 would be multiplied by a factor equal to the stress-concentration factor. Table 3.3 showed that finite element models predicted different stress concentration factors for each hole, and that the factors for the 56% hole in bending were, on average, larger than those of other hole sizes, which is consistent with the graph in Figure 4.9.
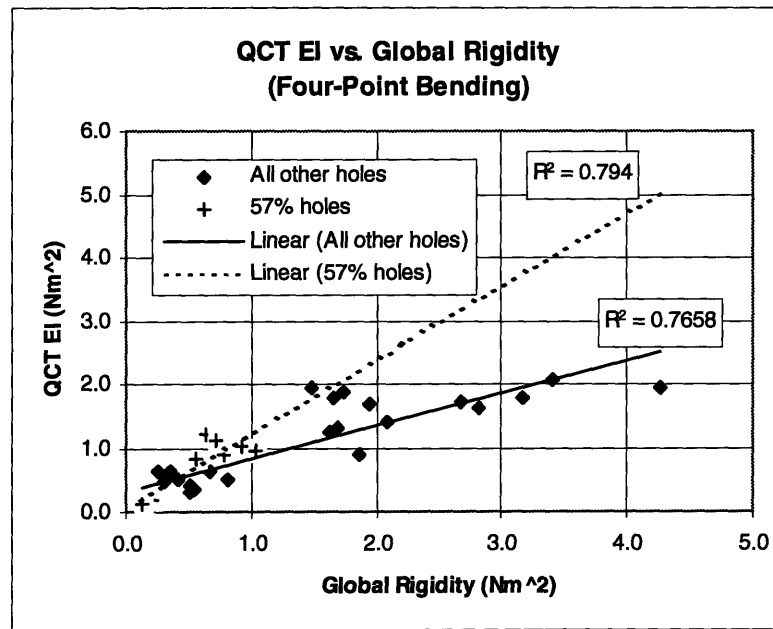


Figure 4.9 - QCT EI vs. global rigidity in four-point bending. Data is grouped according to hole size.

However, it should be noted that the significant difference detected when comparing QCT EI with global rigidity was not apparent when comparing QCT EI to local rigidity. Given the facts that global rigidity is not a great measure of local rigidity, a smaller range of rigidities is represented for the 56% group than the rest of the groups, and no statistical difference was detected between groups in tension, torsion, or bending using local rigidity, the statistical difference shown in Figure 4.9 was not taken as convincing evidence that hole size is a significant concomitant variable affecting a specimen's rigidity.

## 4.4 CAN NON-INVASIVE MEASUREMENTS OF THE ELASTIC PROPERTIES OF BONES WITH DEFECTS BE USED TO PREDICT THE BONES' LOAD CAPACITY?

In order to determine which elastic property best predicts failure (yield load), different properties were isolated using QCT. In the case of bending they were density, hole size ratio, moment of inertia (I), rigidity (EI), and $I\sqrt{E}$. QCT was used to measure the elastic properties of the specimens because, as discussed in the previous section, it is a good measure of elastic properties and unlike mechanical tests can be used to measure various geometric and material properties independently. The mechanical tests in this experiment could only measure the rigidity. The coefficients of determination of the linear relation between each property and yield load are shown in Table 4.4. Each property corresponds to a particular failure criterion, listed in the table. The "Current Clinical" criterion is not a criterion for yield, but rather the criterion currently cited to indicate the need for surgical intervention to prevent pathologic fracture.

Table 4.4 - Coefficients of Determination for the Regression Between Various Elastic Properties and Yield Load

| Elastic Property | Failure Theory | Bending | Torsion | Tension |
|---|---|---|---|---|
| Hole Diameter Ratio (d/D) | Current Clinical | 0.32 | 0.22 | 0.25 |
| Material: Density | Material | 0.55 | 0.81 | 0.72 |
| Geometry: A / I min / J | Constant Stress | 0.33 | 0.40 | 0.38 |
| Structure: EA / EI min / GJ | Constant Strain | **0.92** | **0.89** | **0.95** |
| Structure: $A\sqrt{E}$ / $I\sqrt{E}$ / $J\sqrt{G}$ | Constant Strain Energy | 0.86 | 0.90 | 0.89 |

Yield load typically correlated most highly with the specimen's rigidity, and it was statistically more highly correlated than with other elastic properties (p=0.001) except for $I\sqrt{E}$ (p=0.2) in all three modes of testing. There was also a very strong correlation between rigidity and ultimate load in bending ($r^2 = 0.95$), torsion ($r^2 = 0.83$), and tension ($r^2 = 0.95$). The regressions between rigidity and yield load for each mode of failure are shown in Figures 4.10-4.12.

**Yield Load vs. QCT EI**
**(Four-Point Bending)**

$y = 0.9782x + 0.1177$
$R^2 = 0.9233$
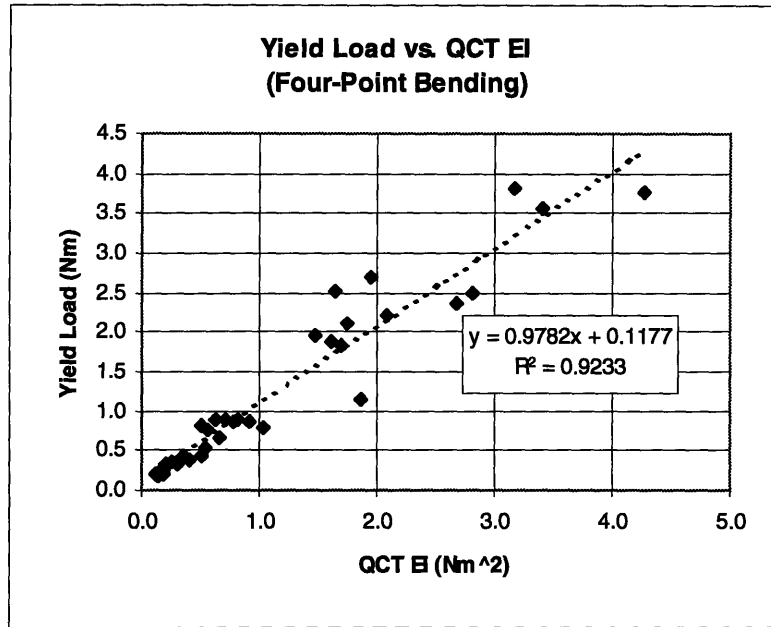
Figure 4.10 - Yield load vs. QCT measurement of bending rigidity.



**Yield Load vs. QCT GJ**
**(Torsion)**

$y = 0.2478x + 0.2047$
$R^2 = 0.8901$
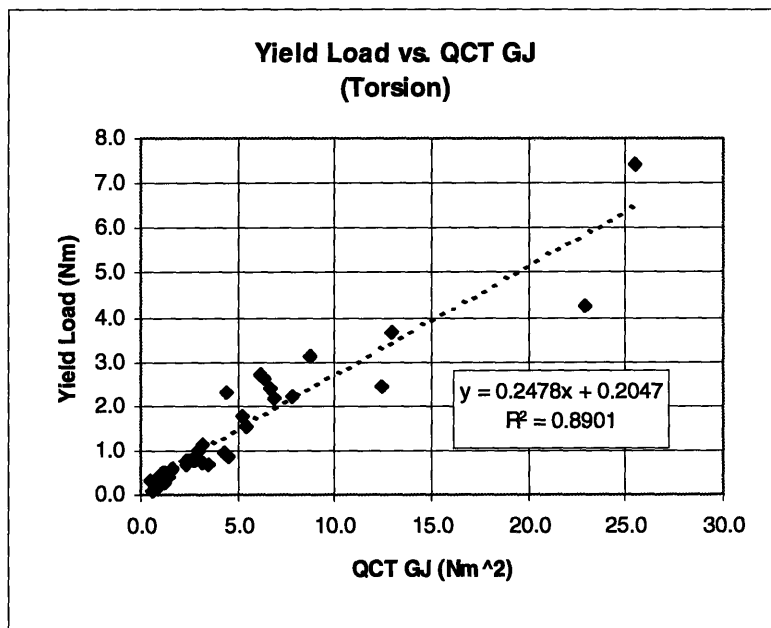
Figure 4.11 - Yield load vs. QCT measurement of torsional rigidity.
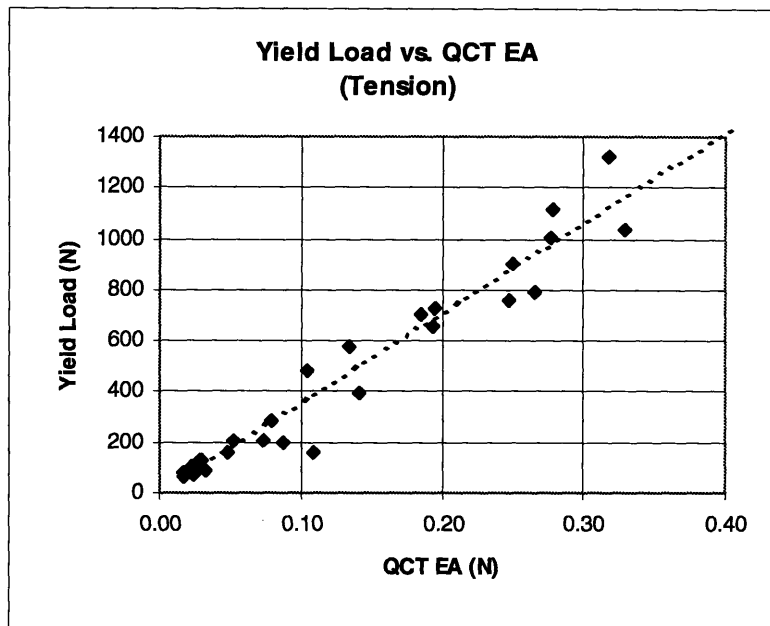
Figure 4.12 - Yield load vs. QCT measurement of axial rigidity.

The high correlation between rigidity and yield load suggests that yield strain is a constant throughout all specimens. The average yield strain was 1.10% in bending, 1.15% in torsion, and 0.51% in tension. These values are consistent with yield strains between 0.74% and 2.0% found in studies of human and bovine bone [1][2][3]. The fact that the yield strain for tension was lower than those for torsion and bending may be due to the fact that an average strain was reported for tension. Since failure undoubtedly initiated on the side with the higher strain, an average of a high and low strain would consistently underreport the actual failure strain.

In order to determine if yield strain was indeed invariant across specimens of different strengths, it was plotted versus yield load. No significant correlation was found in bending, torsion, or tension. The plot for bending is shown in Figure 4.13. A number of groupings were investigated by analysis of covariance to explain the spread in yield strains. Grouping by species indicated statistically significant differences between groups (p < 0.05 for bending), despite the fact that the bowhead group spanned a large range of densities and ages (from mature to geriatric). The results for torsion displayed the same grouping as those for bending; however, the groupings in tension were not significant. Additionally, it should be noted that there was a larger standard deviation in yield strain for the sperm and pigmy sperm whale specimens than in the bowhead specimens for all three types of tests.

We hypothesize that different mineralization of the tissue may be what leads to the different yield strain values in each group. This would explain why the yield strains group somewhat by species and why one species (with more consistent mineralization) might display a tighter grouping in yield strains.
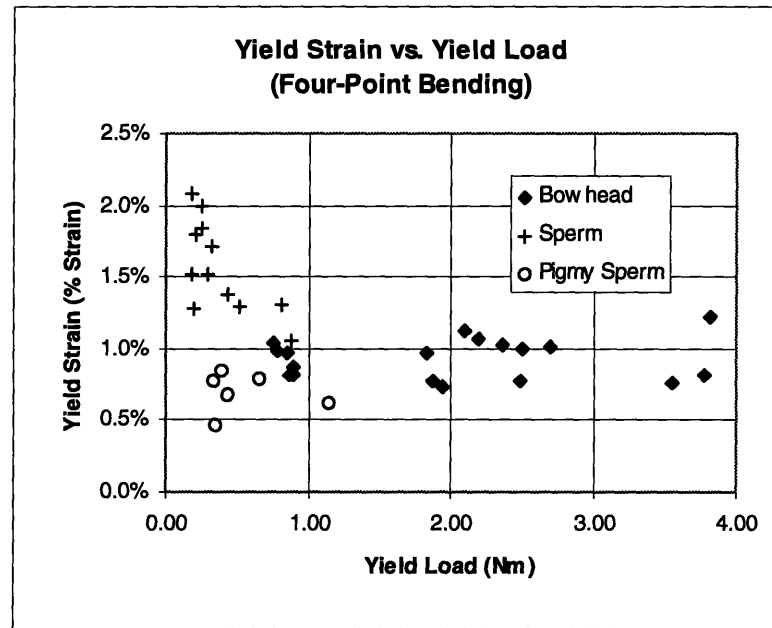
Figure 4.13 - A plot of yield strain vs. yield load shows a grouping of yield strain according to species. This grouping may be linked to different mineralizations characteristic of each specie.

## 4.5 HOW DO CERTAIN FACTORS AFFECT THE BIOMECHANICAL PROPERTIES OF TRABECULAR BONES WITH DEFECTS?

Comparison of coefficients of determination revealed the correct material and structural characteristics necessary to predict yield load. However, other factors which could possibly affect load capacity were also investigated using analysis of covariance on the regression of yield load vs. rigidity:

- Hole size
- Hole shape (eccentricity)
- Stress concentration factor

An analysis of covariance was first performed on the regression between yield load and QCT measurements of rigidity, using hole size as the concomitant variable. In contrast to the difference found in the slope of QCT EI and measured rigidity , there was no difference for bending (p=0.58) between QCT EI and yield load. There was also no statistical difference in slope from one hole size to the next for tension (p=0.1) or torsion (p=0.48). In addition, the relative values of the slopes from one hole-size group to the next were not ranked in the order that finite element analyses would predict. The slopes and standard errors of regression in bending for each hole size are listed in Table 4.5, and the corresponding plot is shown in Figure 4.14.

Table 4.5 - Grouping of Slopes for Regression of Yield Moment vs. Bending Rigidity Based on Hole Size.

| Hole Size | N | Slope | Std. Error of Reg. |
|---|---|---|---|
| No hole | 7 | 0.97 | 0.14 |
| 28% | 10 | 1.08 | 0.11 |
| 47% | 10 | 1.10 | 0.10 |
| 56% | 11 | 0.90 | 0.12 |
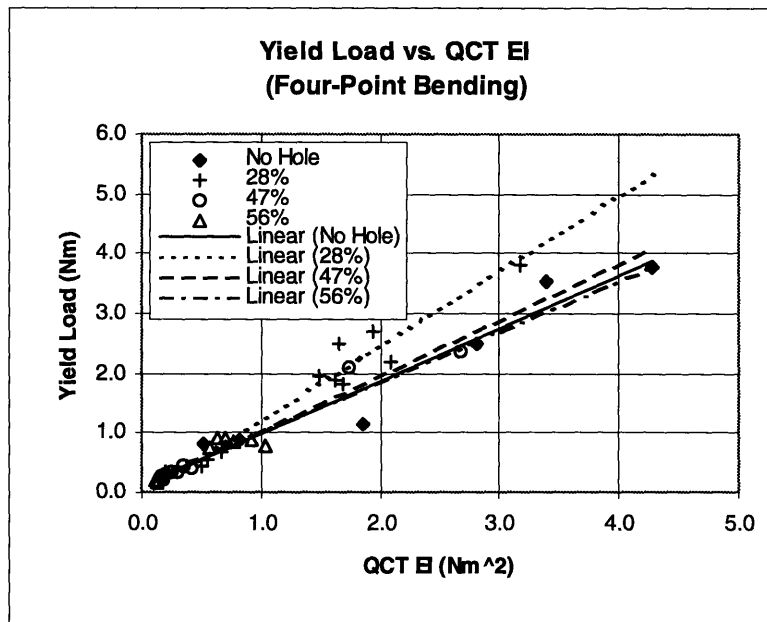


Figure 4.14 - Yield load vs. QCT EI in four-point bending grouped according to hole size. There is no statistical difference between the different groups, and relatives values of slopes do not agree with predictions based on finite element models.

Analysis of covariance was also performed using eccentricity (slot vs. circular hole) as the concomitant variable. It showed that there was a statistically significant difference between the slopes for different hole shapes in bending (p=0.034), torsion (p=0.008), and tension (p=0.018), with the slots about 25% weaker than the circular holes. Figure 4.15 shows the grouping for bending. This is in agreement with the predictions by finite element models and results of studies on cortical bone, although the effect of a slotted defect was greater in cortical bone [4].

**Yield Load vs. QCT EI**
**(Four-Point Bending)**
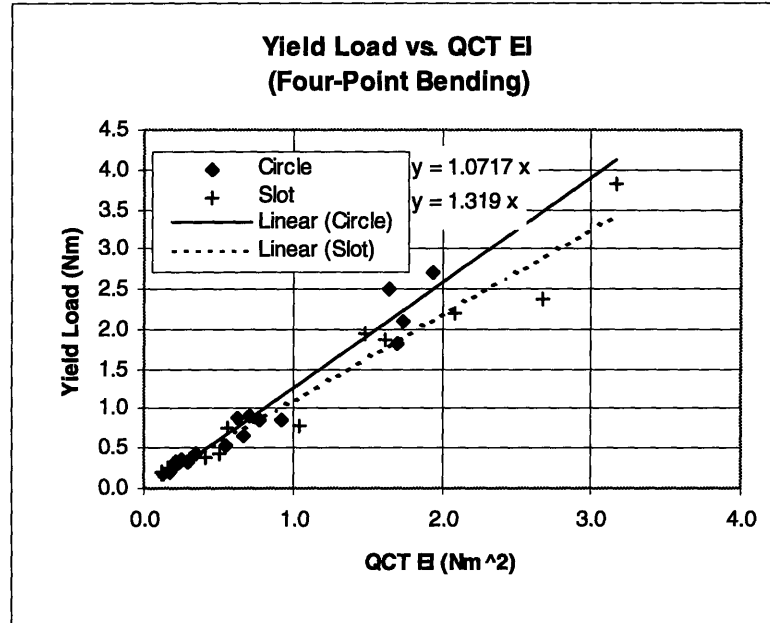


Figure 4.15 - Yield load vs. QCT EI in four-point bending grouped according to hole shape. The specimens with slotted holes were weaker than the specimens with the same defect width but circular holes by about 25%.

The final factor studied was grouping by stress concentration factor. Linear elastic continuum theory predicts the existence of stress-concentration factors that depend on the load condition and defect geometry. The grouping of specimens according to predicted stress-concentration factors would be different than the grouping by hole size or shape alone, so the two types of grouping were investigated independently. Finite element models were used to determine the stress concentration factors for each loading condition, hole size, and hole shape.

One way to determine the presence of stress concentrations is to analyze the location where fracture initiated. A 2x2 contingency table was made for each mechanical testing mode, based on the fact that finite element models would predict failure initiation either in the corner or the middle of a defect. These tables are shown below.

Chi-squared analysis indicated that the theoretical models correctly predict the location of the onset of fracture for bending (p=0.025), tension (p=0.10), and torsion (p=0.025). However, a heterogeneity chi-square analysis indicated that the three sets of data could not be pooled (p=0.5), suggesting that the behavior may not be exactly the same for tension as for bending and torsion.

Table 4.6 - Contingency Table for Fracture Location in Bending

| Theory/Experiment | Corner | Middle | Total |
|---|---|---|---|
| Corner | 11 | 4 | 15 |
| Middle | 3 | 12 | 15 |
| Total | 14 | 16 | 30 |

Table 4.7 - Contingency Table for Fracture Location in Torsion

| Theory/Experiment | Corner | Middle | Total |
|---|---|---|---|
| Corner | 11 | 2 | 13 |
| Middle | 4 | 9 | 13 |
| Total | 15 | 11 | 26 |

Table 4.8 - Contingency Table for Fracture Location in Tension

| Theory/Experiment | Corner | Middle | Total |
|---|---|---|---|
| Corner | 7 | 8 | 15 |
| Middle | 2 | 10 | 12 |
| Total | 9 | 18 | 27 |

Next, stress-concentrations were incorporated into the yield load vs. QCT rigidity regression by multiplying the measured yield load by the appropriate stress concentration factor. The following argument describes this approach as appplied to bending, and similar arguments apply to torsion and tension. Based on elementary solid mechanics and the finding in Section 4.3 that QCT EI correlates highly with mechanically-measured rigidity,

$$\varepsilon = \frac{M \times c}{EI} \propto \frac{M \times c}{(EI) \text{ based on QCT}} \qquad [4.1]$$

and at yield

$$\varepsilon(\text{yield}) \propto \frac{M(\text{yield}) \times c}{(EI) \text{ based on QCT}} \qquad [4.2]$$

As discussed in section 4.4, yield strain was basically invariant. Also, c (the distance from the neutral axis to the surface of the specimen) is approximately a constant. Therefore, equation 4.2 becomes:

$$\frac{M(\text{yield})}{(EI) \text{ based on QCT}} = \text{constant} \qquad [4.3]$$

or

(EI) based on QCT $\propto$ M(yield)                                    [ 4.4 ]

Equation 4.4 describes the linear regression of the plot in Figure 4.10. However, stress concentrations would theoretically increase the local stress and strain beyond that predicted by elementary solid mechanics. Therefore, equation 4.2 would need to be modified by the net stress concentration factor as follows:

$$\epsilon(\text{yield}) \propto \frac{\text{M(yield)} \times c}{\text{(EI) based on QCT}} \times K_{net}$$                                    [ 4.5 ]

so that

(EI) based on QCT $\propto$ M(yield) $\times$ $K_{net}$                                    [ 4.6 ]

Therefore, the plots in Figures 4.10 through 4.12 were modified according to equation 4.6 by multiplying the measured yield load by the net stress concentration factor based on finite element models for each specimen. The coefficients of determination for the regressions actually worsened, rather than improved, for all three load cases when the net stress concentration factors were incorporated. The reduction in $r^2$ and the significance level of the difference between $r^2$ before and after stress concentrations were introduced are shown in Table 4.9. The plots of yield load vs. QCT rigidity summarized in Table 4.9 only included the specimens with holes. Including specimen's without holes in the regression worsened the correlations even further.

Table 4.9 - Reduction in the Coefficient of Determination of Yield Load vs. Rigidity When Stress Concentrations Are Incorporated.

|            | Without Stress Conc. | With Stress Conc. | $\Delta r^2$ | Significance Level (p<) |
|------------|----------------------|-------------------|--------------|-------------------------|
| Bending    | 0.91                 | 0.83              | -0.08        | 0.10                    |
| Tension    | 0.95                 | 0.74              | -0.21        | 0.05                    |
| Torsion    | 0.91                 | 0.60              | -0.31        | 0.05                    |

Fracture initiated where linear elastic continuum theory predicted it would in most cases, but incorporation of theoretical stress concentration factors actually worsened correlations of rigidity with yield load. These two facts suggest that while stress concentrations are present to some degree, they do not exist to the extent that the assumptions of a linear elastic continuum would suggest. This may be due in part to the structural nature of trabecular bone as well as to masking of stress concentrations at the onset of plasticity. Studies of cortical bones with defects [5][6][7] have had similar results, in that small holes (< 20%) did not have as great an effect on load capacity as

theoretically derived stress concentration factors would predict and load capacity tended to vary linearly with hole size.

However, it is interesting to note that closed-form solutions of a flat plate of a linear elastic material with voids subjected to uniaxial tension far away from the hole predict stress concentration factors even greater than those present in a material without voids (greater than 3) [8]. If these large stress concentrations had been present in this study, the slope in Figure 4.14 of specimens with holes would have been very significantly less than that of specimens without holes.

## 4.6 COMBINING SPECIMEN GROUPS FROM DIFFERENT ANIMALS

As a "housekeeping" measure, analysis of covariance was performed on the regression between yield load and QCT measurements of rigidity, using the animal from which the specimens were taken as the concomitant variable. There was no significance difference in the slope of the plot from one animal to the next for bending (p=0.73) or tension (p=0.53), although a significant difference was detected for torsion between specimens from animals A, B, and C and animals D, E, and F. However, the standard errors of the regressions overlapped noticeably, as shown in the table below.

Table 4.10 - Grouping of Slopes for Regression of Yield Torque vs. Torsional Rigidity Based on Animal.

| Animal | N | Slope of Regression | Std Error of Reg. |
|--------|---|--------------------|--------------------|
| A | 12 | 0.43 | 0.15 |
| B | 9 | 0.41 | 0.16 |
| C | 6 | 0.32 | 0.18 |
| D | 5 | 0.28 | 0.20 |
| E/F | 4 | 0.12 | 0.28 |

It should be noted for the analyses of covariance based on animal, although the population means all lay on straight lines ($r^2$s were high), small sample sizes (particularly for animals D, E, and F) may have reduced the power of the analysis and possibly violated the assumption that the regression coefficients had normal distributions. Considering the small sample size, the lack of a statistical difference in bending and tension, and the large standard error of regression in torsion, the specimens were all considered to be statistically from the same population.

## 4.7 CONCLUSIONS

There are two broad conclusions which encompass most of the results from this experiment. The first is that a simple elastic property (rigidity) of a single, weakest cross-section is an excellent measure of the load capacity of trabecular bone, regardless of the size or shape of any defects present. The second broad conclusion is that relative rigidity, and hence, relative load capacity of trabecular bone can be easily measured non-invasively, particularly using quantitative computed tomography. Together, these conclusions suggest that the preferred method of non-invasive imaging in Figure 1.2 can be used to accurately estimate fracture risk for trabecular bone, providing physicians with an objective, quantitative method of assessing bone tumors.

The most important take-home message is that stress concentration factors are sufficiently insignificant in trabecular bone with rounded holes that they do not confound simple Bernoulli-Euler models in the prediction of load capacity. The consistently high correlations between yield load and non-invasively measured elastic rigidity for all three fundamental types of loading further indicates that, assuming the type loading (though not the load magnitude), the rigidity of the weakest cross-section of a region of trabecular bone with a defect is sufficient to determine the load capacity of the entire trabecular region. Therefore, comparison of the minimum rigidity at the defect site to the rigidity of a corresponding cross-section on a healthy contra-lateral limb should give an excellent estimate of the reduction in load capacity of the bone with the defect. It should be noted that the correlation of rigidity to yield load and other results in the experiment indicate a strain-based yield criterion for trabecular bone, which is consistent with other investigations.

The specimens in the study displayed a significant non-linear region before they reached ultimate load, and it is reasonable to assume that *in vivo* bones are capable of supporting significant loads even after they have initially yielded. However, although yield load was used in this experiment primarily in order to accommodate the linear finite element models, the high correlation between yield and ultimate loads extends the power of the prediction to include ultimate load capacity as well. Comparing the rigidity of bone with a defect to that of a healthy contralateral limb should provide an excellent measure of the reduction in ultimate as well as yield load.

Both in theory (see Table 2.2) and experiment, as hole size increased it reduced the load capacity in bending more significantly than in tension or torsion. However, this experiment tested bending about the weakest axis. If the specimens were bent about the y- rather than the x-axis, the hole would, theoretically, have had less of an effect. The different effects of hole size on different modes of mechanical testing serves to point out that, regardless of the fracture risk prediction technique used, one still needs to know to some degree the types of loading expected on a weakened limb.

As a final note, although little research has been done on defects in trabecular bone, more has been done for cortical bone, and researchers have found strong correlations between hole size (width) and load capacity. However, most studies focused on specimens within a small density range and on *in-vitro* experiments where bone did not remodel in response to the defect. This study demonstrated that, at least for trabecular bone, material as well as geometric properties are required to predict load capacity. This is particularly important in trabecular bone, where density can vary from region to region, and in bone where remodeling in response to a defect can change the material properties of the tissue.

Although this study was conducted on a controlled set of tissue from whales, its conclusions should apply equally-well to a wide range of human trabecular bone. Homogeneous specimens of trabecular bone that adequately modeled human trabecular bone were tested in all three principle loading conditions: axial, bending, and torsion. The specimens in each mechanical test spanned a similar, wide range of material and geometric properties, representative of the spectrum of human trabecular bone. Defect sizes and shapes were parametrically controlled, and resembled those typically found in pediatric lesions. Furthermore, the conclusions focus on general characteristics of all trabecular bone and on the *relative* mechanical behavior of bones with various sizes and shapes of defects. The particular equations relating one property to another or describing a particular property of specimens used in this test are not intended to apply to human bone and, in fact, are irrelevant to proving the technique which was the subject of this thesis. Therefore, the conclusions of this study should be applicable to human trabecular bone, and the validity of this technique should extend to human bone as well.

The most important limitations of the study are that the strength prediction technique has not been proven to extend to highly inhomogeneous trabecular bone or regions in which trabecular orientation is highly variable. It also does not address cortical or combined cortical-trabecular bones, or bones in soft tissue. It does, however, provide a fundamental assessment of the behavior of trabecular bone from a controlled, parametric investigation, upon which the more clinically-applicable whole bone tests can be based.

---

[1]  F. Linde, B. Pongsoipetch, L.H. Frich, and I. Hvid, "Three-axial strain controlled testing applied to bone specimens from the proximal tibial epiphysis," *Journal of Biomechanics*, 23:1167-1172, 1990.

[2]  C.H. Turner, "Yield Behavior of Bovine Cancellous Bone," *Journal of Biomechanical Engineering*, 111: 256-260, 1989

[3]  T.M. Keaveny, E.F. Wachtel, M.J. Cutler, and T.P. Pinilla, "Yield strains for bovine trabecular bone are isotropic but asymmetric," 40th Annual meeting of Orthopaedic Research Society, Feb 21-24, 1994, p 428.

[4]  M.L. DeSouza, K.N. An, B.F. Morrey, and E.Y.S. Chao, "Strength reduction of rectangular cortical defects in diaphyseal bone," 35th Annual Meeting of ORS, p. 113, 1989.

[5]  B.C. Edgerton, K.N.An, and B.F. Morrey, "Torsional strength reduction due to cortical defects in bone", *Journal of Orthopaedic Research*, 8:851-855, 1990.

[6]  R.J McBroom, E.J. Cheal, and W.C. Hayes, "Strength reductions from metastatic cortical defects in long bones", *Journal of Orthopaedic Research*, 6:369-378, 1988.

[7]  J.A. Hipp, B.C. Edgerton, K.N. An, and W.C. Hayes, "Structural consequences of transcortical holes in long bones loaded under torsion", *Journal of Biomechanics*, 23(12): 1261-1268, 1990.

[8]  S.C. Cowin, "The stresses around a hole in a linear elastic material with voids, " *Q. Journal Mech. Appl. Math.*, 37: 441-465, 1984.

# Chapter 5
# Quantitative Computed Tomography Scans

## 5.1 OVERVIEW

Quantitative Computed Tomography (QCT) was used to non-invasively measure cross-sectional properties of the specimens. QCT scanners are powerful tools for measuring the geometric and material properties of bone cross-sections and as such, represent a reliable means of supplying the structural data necessary to calculate a factor of risk. QCT measurements have demonstrated precision of 3%-4% for measurements between scanners and 1-3% for multiple scans on a single scanner [1]. However, although its measurements are very accurate and precise, it should be noted that QCT produces at least 30 times higher radiation than dual-energy X-ray absorptiometry, which only measures projected attenuations of a cross-section [2]. Other techniques that produce no radiation at all, such as ultrasound and MRI, may also be used to measure structural properties of a bone cross-section. QCT was chosen for this experiment as a "gold standard" of imaging since it provides such excellent accuracy and precision.

A QCT scanner consists of source and detector arrays mounted on a circular gantry that rotates 360° around a specimen, at each point measuring the attenuation of x-ray energy emitted from the source. The attenuation values are continuously calibrated for changes in the surrounding medium (air) by measuring attenuation of an X-ray beam through the surrounding medium to a detector outside of the specimen's width. The attenuations measured at all of the angles around the specimen are convolved into a two-dimensional image of its cross-section. Each pixel in the 2-D image represents the calculated attenuation of the corresponding location in the specimen's cross-section. After each full rotation, the circular x-ray gantry translates along the length of the specimen and produces an image of the next cross-section, and so on.

The QCT value is measured in dimensionless Hounsfield units, H, which are defined by the relation

$$H = 1000 \, (\mu \, / \, \mu_0 - 1)$$ [ 5.1 ]

where $\mu$ is the linear attenuation coefficient of the matter being measured and $\mu_0$ is the linear attenuation coefficient of water measured on the specific scanner [3]. QCT

density is linearly related to calcium concentration [4], and numerous studies have found a strong linear relationship between QCT-density and apparent density[5 6 7]. Since QCT images present the spatial distribution of mass within the cross-section, material, geometric, and structural properties of the cross-section can easily be calculated from the image.

## 5.2 SCAN PROTOCOL

QCT scans were performed using a General Electric High Speed Advantage Helical Scanner at Beth Israel Hospital, Boston, MA. Specimens were degassed in saline and sealed in water-filled acrylic tubes, and the tubes were positioned in a wooden gantry along with four solid hydroxyapatite phantom rods of known densities, as shown in Figure 5.1. The specimens and phantoms were scanned serially in 3 mm thick slices and spaced at 3 mm intervals, since these are typical of clinical studies. They were scanned at 120 kV and 220 mA, and attenuation values were filtered through a bone algorithm on the CT scanner. The image resolution was 0.234 mm/pixel (in both the X and Y directions). Two specimens were scanned in each image, along with the phantoms, which were used to calibrate the Houndsfield units with bone mineral density. The scanning protocol, along with the data reduction protocol and computer programs, is in Appendix D.
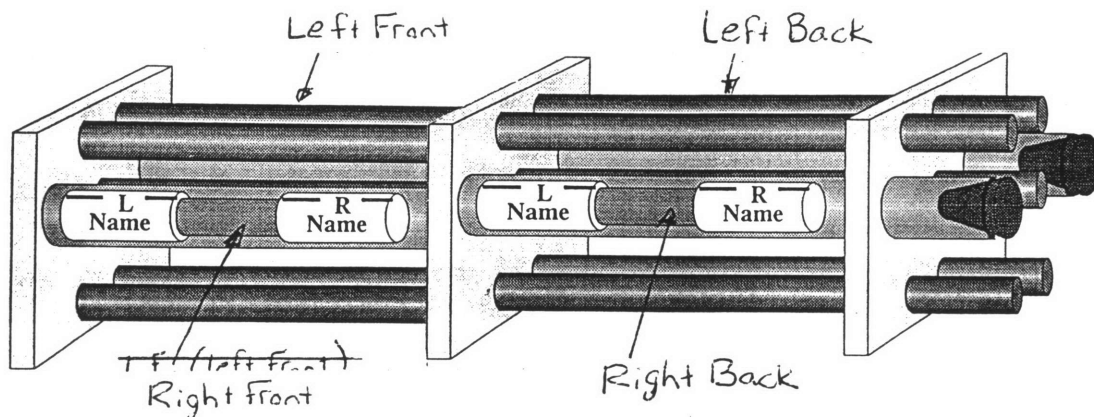


Figure 5.1 - Gantry for holding specimens during QCT scans.

## 5.3 CALCULATIONS

The images produced by each QCT scan were a series of two-dimensional arrays of x-ray attenuation values, one array per cross-section (or "slice"). These attenuation values were converted into true densities, measured in g/cc. All the pixels in a slice were filtered based on a density threshold to distinguish between water, trabecular

bone, and material more dense than trabecular bone. The density values and spatial distribution of thresholded pixels in a cross-section were then used to calculate material, geometric, and structural properties of the cross-section.

*CONVERSION FROM HOUNDSFIELD UNITS TO DENSITY.* A computer program sampled attenuation values for the five hydroxyapatite phantoms included in each scan slice. Using the known densities of the phantoms, it then calculated a linear relation to convert QCT attenuation values into ash density, measured in g/cc. Since the true ash density of the phantoms tended to vary slightly from one slice to the next, the regressions for all slices in a scan set were averaged, and this average was used as the conversion equation for every slice in the set. The coefficient of variation of the regression equation between 30 slices in a single scan set was measured for 29 scan sets. The mean coefficient of variation within a group was 2%, and the maximum was 3%. The maximum variation between the means of six groups was only 5%.

*THRESHOLDING.* The program which calculated cross-sectional properties relied on a threshold value to eliminate pixels which were not trabecular bone. The upper threshold was set at 1,500 mg/cc. The lower threshold was chosen to be a value which excluded water and reduced the effect of volume averaging of water and bone at the periphery of the specimen. Using image analysis software (Advanced Visual Systems, Waltham, Mass.) on a Sun workstation, the measured density value for water was sampled for seven scan sets. The average (max) density for the water was 54 (69) mg/cc. This established a minimum threshold of 69 mg/cc.

Next, the density and area within a circular region of the bone in a specimen were sampled for three specimens as the density threshold was increased. Based on the plot of area shown in Figure 5.2, the threshold began to eliminate bone when set above 0.13 g/cc. Density, area, and polar moment of inertia were also measured for the three regions shown in Figure 5.3 as the density threshold was varied. Analysis of the variation in cross-sectional properties from one region to the next indicated that below 0.9 g/cc, volume averaging at the water/bone interface may have begun to affect measurements adversely. Therefore, 0.11 g/cc was chosen as the water/bone threshold.
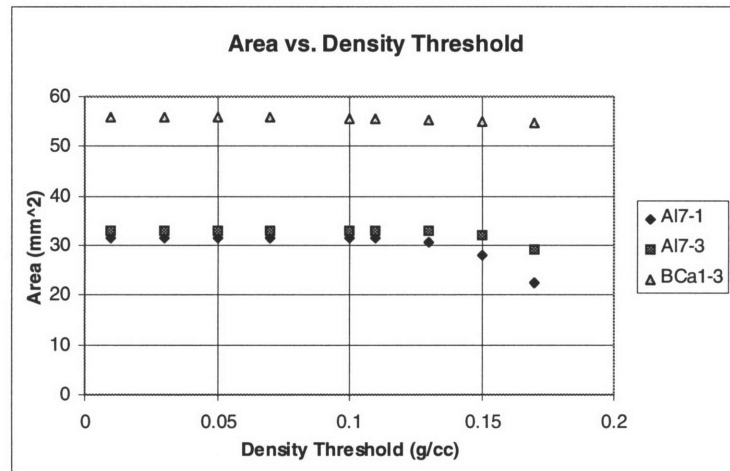
Figure 5.2 - Change in area as density threshold was increased.
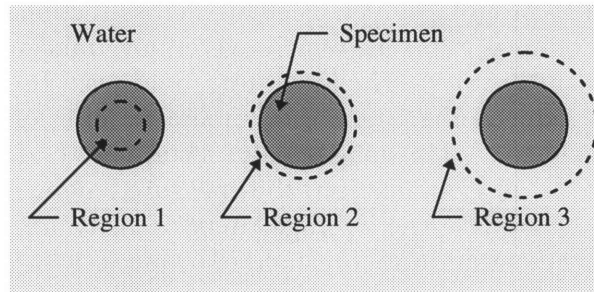


Figure 5.3 - Cross-sectional properties were measured in three increasingly larger regions with respect to the specimen cross section.

*CALCULATION OF PROPERTIES.*   The cross-sectional properties of each image were calculated using a C program listed in Appendix D.   Each image was a 2-D array of attenuation values, one value for each pixel.   The size of each pixel (0.234 mm) was input to the program based on the specifications of the scan.   The density, $\rho_i$, of each pixel in the cross-section was calculated using the phantom regressions discussed earlier, and the modulus, $E_i$, of each pixel was calculated using equation 2.5.

Area, geometric moments of inertia, and rigidities were calculated for each pixel above the threshold density of 0.11 g/cc and summed over all of the pixels to give the properties of the total cross-section. Properties were calculated using the standard engineering formulas below, and are detailed further in the code in Appendix D.  The density (modulus) reported for a cross-section was the average density (modulus) over all "bone" pixels in the cross-section. The shear modulus, G, was assumed to be linearly related to E.  Therefore E was used in the calculation of the torsional rigidity, rather than conducting a separate study to determine G.  Geometric moments of inertia were calculated about the geometric centroid of the cross-section, and rigidities were calculated about the mass centroid of the cross-section.  The following formulas, where

summation implies over all thresholded pixels, were used to calculate cross-sectional properties:

$$A = \Sigma \, da \qquad\qquad\qquad\qquad\qquad\qquad\qquad\qquad [5.2]$$

$$Ix = \Sigma \, (x^2 \, da) - Ax' \qquad\qquad\qquad\qquad\qquad\qquad [5.3]$$

$$J = Ix + Iy \qquad\qquad\qquad\qquad\qquad\qquad\qquad\qquad [5.4]$$

$$\rho = \frac{\Sigma \, (da \times \rho_i)}{\Sigma \, da} \qquad\qquad\qquad\qquad\qquad\qquad\qquad [5.5]$$

$$E = \frac{\Sigma \, (da \times E_i)}{\Sigma \, da} \qquad\qquad\qquad\qquad\qquad\qquad\qquad [5.6]$$

$$EA = \Sigma \, (da \times E_i) \qquad\qquad\qquad\qquad\qquad\qquad\quad [5.7]$$

$$EIx = \Sigma \, (x^2 \, da \times E_i) - AEx'' \qquad\qquad\qquad\qquad [5.8]$$

$$GJ = EIx + EIy \qquad\qquad\qquad\qquad\qquad\qquad\qquad [5.9]$$

where

| | |
|---|---|
| da | $= 0.234 \text{ mm}^2$ |
| x' | = x coordinate of the geometric centroid |
| x'' | = x coordinate of the mass-weighted centroid |
| $\rho_i$ | = density of pixel i, calculated from phantom regression |
| $E_i$ | = modulus of pixel i, calculated from $\rho_i$ using equation 2.5. |

The cross-sectional properties of the slice at the largest diameter of each hole were used in comparing non-invasive image analysis with mechanical tests.

## 5.4 VALIDITY OF SCANS OF SPECIMENS WITH DEFECTS

The low coefficient of variation in measuring density of the phantom rods within a scan and between scans served as one measure of validating the consistency of the QCT scanning protocol. However, there was also concern that the introduction of a hole might affect the QCT measurements, and this would not be reflected in measurements of the solid phantoms.

Therefore, in order to validate that QCT correctly measured the cross-sectional properties near the hole, QCT measurements of the post-defect specimens were

compared to expected values based on the QCT scans of intact specimens using the following relations:

$$EA_{expected} = EA(intact) \times \left(1 - \frac{A(hole)}{A(intact)}\right)$$  [ 5.10 ]

$$EI_{expected} = EI(intact) \times \left(1 - \frac{I(hole)}{I(intact)}\right)$$  [ 5.11 ]

$$GJ_{expected} = GJ(intact) \times \left(1 - \frac{J(hole)}{J(intact)}\right)$$  [ 5.12 ]

where intact rigidities were the values from QCT scans of intact specimens, and the ratios (hole to intact) of area, bending moment of inertia, and polar moment of inertia were calculated from the known nominal diameter of the intact specimens and the known diameters of the holes. Values from the actual scans of post-defect specimens correlated extremely well with the expected values, as shown in Table 5.1.

Table 5.1 - Post-defect QCT measurements compared to expected measurements based on QCT scans of intact specimens.

| Cross-sectional Property | Correl. Coeff. ($r^2$) | Slope | Y-intercept |
|---|---|---|---|
| Axial Rigidity (EA) | 0.99 | 0.99 | 0.00 |
| Bending Rigidity (EI) | 0.99 | 0.98 | 0.013 |
| Torsional Rigidity (GJ) | 0.99 | 0.98 | 0.015 |
| Density | 0.98 | 0.89 | 0.015 |

The fact that the slope for density is less than one may be explained by noting that volume averaging of pixels on the boundary of the specimen and its water bath effectively lowers the average density of the specimen. By introducing a hole, the length of the specimen-water boundary is increased, resulting in more volume averaging and a reduced average density.

---

[1]   P. Steiger, J.E. Block, S. Steiger, et al, "Spinal bone mineral density by quantitative computed tomography: effect of region of interest, vertebral level, and technique," *Radiology*, 175: 537-43, 1990.

[2]   H.W. Wahner, I. Fogelman, The Evaluation of Osteoporosis: Dual Energy X-ray Absorptiometry in Clinical Practice, Martin Dunitz, London, 1994.

[3]   S.M. Bentzen, I. Hvid, and J. Jorgensen, "Mechanical strength of tibial trabecular bone evaluated by x-ray computed tomography, *Journal of Biomechanics*, 20:743-752, 1987.

[4] J.G. Benterud, A. Alho, J.H. Stromme, and A. Hoiseth, "Calcium equivalence of bone mineral measured by single-energy computed tomography - An autopsy study of femur," *Trans. European Society of Orthopedic Research*, 1:1, 1991.

[5] R. J. McBroom, W.C. Hayes, W.T. Edwards, R.P. Goldberg, and A.A. White, "Prediction of vertebral body compressive fracture using quantitative computed tomography," *Journal of Bone and Joint Surgery*, 67:1206-1214, 1985.

[6] I. Hvid, N.C. Jensen, C. Bunger, K. Solund, and J.C. Djurhuus, "X-ray quantitative computed tomography: the relations to physical properties of proximal tibial trabecular bone specimens," *Journal of Biomechanics*, 22:837-844, 1989.

[7] M.J. Cirelli, S.A. Goldstein, J.L. Kuhn, D.D. Cody, and M.B. Brown, "Evaluation of orthogonal mechanical properties and density of human trabecular bone from the major metaphyseal regions with materials testing and computed tomography," *Journal of Orthopedic Research*, 9:674-682, 1991.

# Chapter 6
# Finite Element Modeling

As mentioned in Chapter 3, linear, elastic finite element models were used to predict the stress, strain, and strain energy concentration factors for the specimens. Models of tension, torsion, and four-point bending of the specimens for each hole size and shape were created using Patran (PDA Engineering, Costa Mesa, Ca). The models included both the bone and rigidly attached metal endcaps through which the loads were applied. Twenty-node, quadratic, isoparametric elements were chosen to provide an accurate representation of the geometry of a circular defect in a cylinder and of large strain gradients. In addition, the mesh was significantly refined in the neighborhood of the defect. The models had approximately 1500 elements and 8500 degrees of freedom, depending on the defect size. The models were tested for convergence and validated against experimental studies of cylinders with holes.

Boundary conditions exactly modeled the constraints in the actual mechanical tests. Unit loads were applied to the models, and the maximum stress, strain, and strain energy in each model was recorded. Stress concentration factors were calculated for each hole size by dividing the maximum stress recorded in the finite element model by the stress predicted using Bernoulli-Euler solid mechanics theory. The "Bernoulli-Euler" stress was calculated at the specimen's most-reduced cross-section. Concentration factors were also calculated for strain and strain energy.

The models could have included only one quarter (one half in the case of torsion) of the geometry of the specimens by applying appropriate boundary conditions. However, full models were developed in order to allow for future incorporation of different bone material properties for each element, mapped from QCT scans of actual specimens.

Throughout this chapter, two measures of the stress concentration factor are discussed: the gross and net stress concentration factors

$$\text{Gross stress concentration:} \qquad K_g = \frac{\sigma max}{\sigma gross} \qquad\qquad [\,6.1\,]$$

$$\text{Net stress concentration:} \qquad K_n = \frac{\sigma max}{\sigma net} \qquad\qquad [\,6.2\,]$$

where $\sigma_{net}$ is the stress calculated using the net cross-section after the hole is introduced and $\sigma_{gross}$ is calculated using the intact, or gross, cross-section without including the hole.

## 6.1  MODEL DESCRIPTIONS

Each finite element model was composed of three material types: trabecular bone (E = 1 GPa), endcaps (E = 50 GPa), and an extremely stiff ring (E = 200,000 GPa) through which the loads in tensile and torsional models were applied. The high modulus of the ring compensated for its small dimensions to produce a stiffness which simulated that of the actual jigs through which loads were applied. More importantly, it provided an even load distribution into the endcaps. The material types are identified by the italic text in Figure 6.1. The bone was a solid section which extended through the endcaps and contained a hole at its midspan. The endcaps were thin cylinders around the ends of the bone, and the stiff ring attached directly to an endcap.

The model geometries, meshes, and loading conditions were developed in Patran session files and contained parameters that were modified to change the hole shape and size, as appropriate to each specimen. The Patran session files were written and commented such that a new model could be easily generated by altering certain specimen dimensions, including:

- Radius of specimen
- Length of specimen
- Hole radius
- Hole shape
- Thickness of endcaps
- Length of endcaps
- Length of bone potted in endcaps
- Boundary conditions.

The finite element models assumed that the bone extended entirely through the endcaps and that the endcaps were rigidly fixed to the bone (there was no slip at the interface). The models' coordinate system oriented the x-axis transverse to the hole and the long axis of the bone, the y-axis coincident with the hole's long axis, and the z-axis coincident with the long axis of the specimen, as shown in Figure 6.1.

The model was divided into separate segments, shown in normal text in Figure 6.1, that were meshed somewhat independently:

1) a rectangular region in the neighborhood of the hole, which had the most refined mesh
2) regions on either lateral side of the first, which had a less refined mesh

3) the gage length of the bone surrounding the hole
4) the segment of bone extending through the endcaps
5) the endcaps.
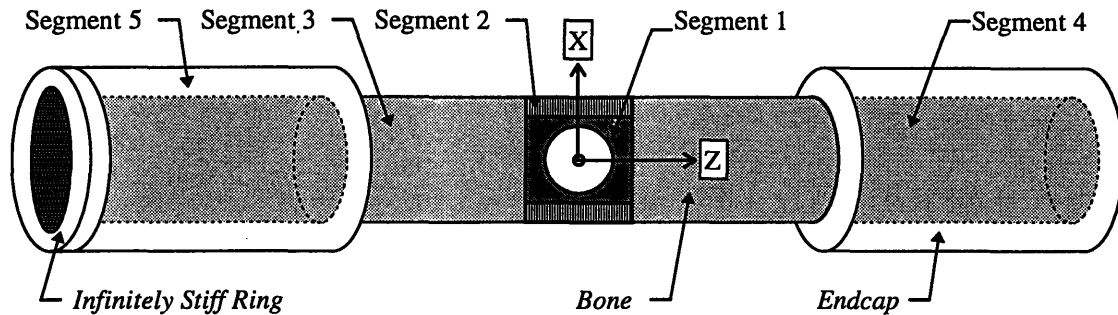


Figure 6.1 - Different meshes were applied to different segments of each model.

The mesh was developed to be refined near local concentrations of stress/strain gradients predicted by theory. The gradients were assessed quantitatively using iso-contours of a number of different hole-size models. Gradients were highest at load and displacement constraints in the endcaps, along the y-axis for bending, and in the region immediately surrounding the hole, particularly on the sides of the hole. Therefore the endcaps were meshed two elements thick. The y-axis had a tighter mesh than the z-axis. Also, the region surrounding the hole had a tight mesh which was progressively refined towards the hole, and the near-hole region with the tight mesh (segments 2 and 3) was sized to engulf local concentration of gradients. Figures 6.2 - 6.5 show the bending models for each hole size. The meshes for the slots were very similar to the meshes for circular holes, and the meshes for tension and torsion were identical to those for bending.
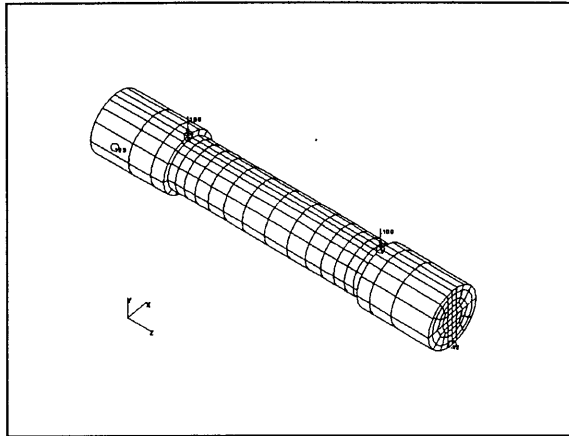
Figure 6.2 - Bending model with no hole.          Figure 6.4 - Bending model with 47% hole.
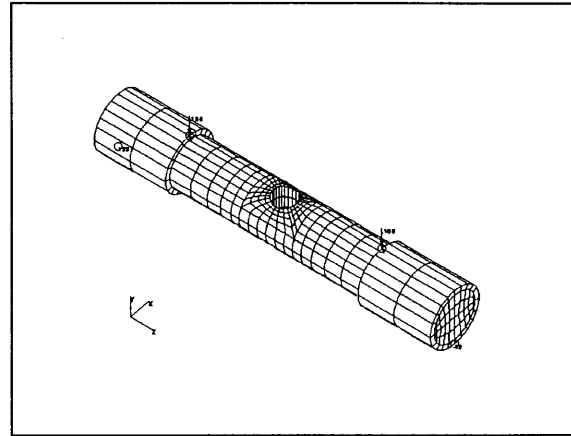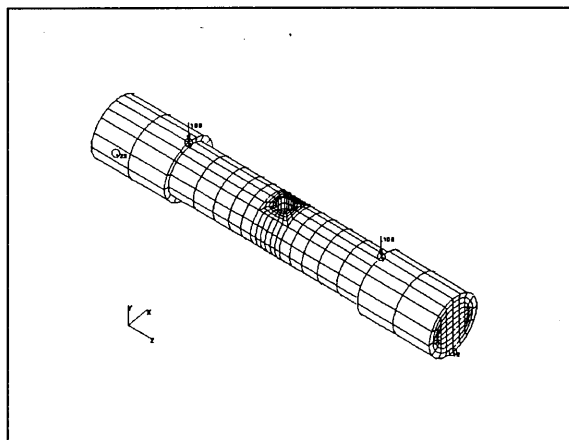
Figure 6.3 - Bending model with 28% hole          Figure 6.5- Bending model with 56% hole.
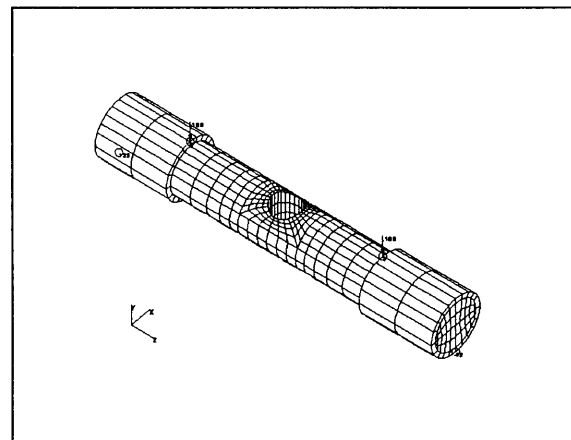
*FOUR-POINT BENDING:* The boundary conditions simulated a pin and z-axis roller on the bottom outside of the endcaps and two z-axis rollers on the top inside of the endcaps, with point-loads applied through the two top rollers. The bottom left node of the left endcap was constrained in all three degrees of freedom. The bottom right node of the right endcap was constrained in x and y but free to translate along the z-axis. The two loads were two concentrated forces in the y-axis, applied at two individual nodes on the exact top of the endcaps. The motions of the two nodes were constrained to zero in the x-axis but free in the y- and z-axes.

*TENSION:* The boundary conditions simulated uniaxial tension by fixing all nodes on the bottom surface of one endcap from motion in the z-axis and applying a uniformly-distributed pressure load on the nodes of the top surface of the stiff ring, as shown in Figure 6.6. Applying a load rather than set displacements at the ring freed the

model to twist or bend once inhomogeneous material properties were applied from QCT maps.

*TORSION*: The boundary conditions simulated applying a pure torque by fixing all nodes on the bottom surface of one endcap from motion in the x-axis and y-axis and applying four point loads in pairs of equal and opposite directions on nodes of the top surface of the stiff ring, as shown in Figure 6.6. Because the ring was extremely stiff compared to the rest of the model and the applied load, an evenly-distributed torque was transmitted to the specimen, and it was free of shear that might have been introduced by applying point, rather than distributed load conditions. As in tension, applying a load rather than set displacements at the ring freed the model to bend and deform axially if inhomogeneous material properties were applied from QCT maps.



Distributed load applied to ring
for tension

Fixed displacement in Z for tension
Fixed displacement in X, Y for torsion

Four point loads applied to ring
for torsion
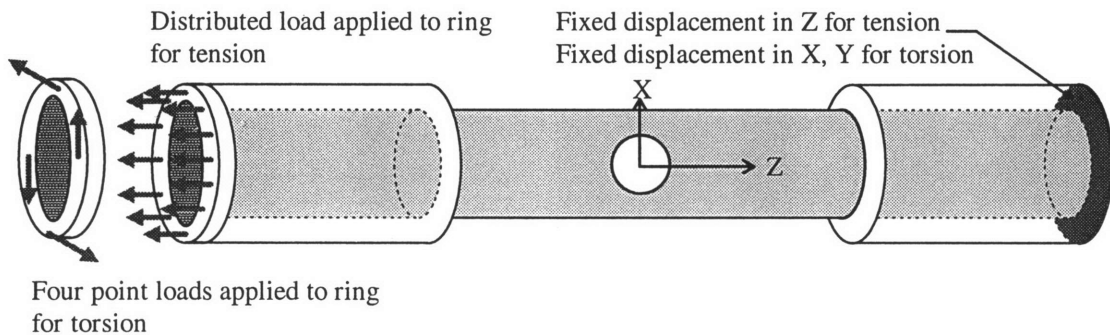
Figure 6.6 - In the tension model, one endcap was constrained from motion in Z, and a distributed pressure load was applied to the stiff ring. Four point loads were applied to the ring in the torsion model to result in a couple, and motion of one end was constrained in X and Y.

## 6.2 CONVERGENCE TESTING

The four-point bending model with a 20% circular hole was used to verify the mesh with a convergence test of eight mesh densities. All eight models were identical except for changes in the mesh, and the same load was applied to every model. The models used in the convergence test had the following parameters in common:

- Bone radius =        0.5          Endcap thickness =    0.1
- Bone length =        2.0          Endcap length =       1.5
- Bone modulus =       25e+3        Endcap modulus =      20e+6
- Hole Size =          20%
- Force =              -50
- Moment Arm =         1.5
- (Resulting mid-span displacement = 0.32)

The bone extended entirely through the endcap, and the loads were applied in the y-axis at the edges of the endcap. The series of meshes tested for convergence are shown and described in Figures 6.7 through 6.14.
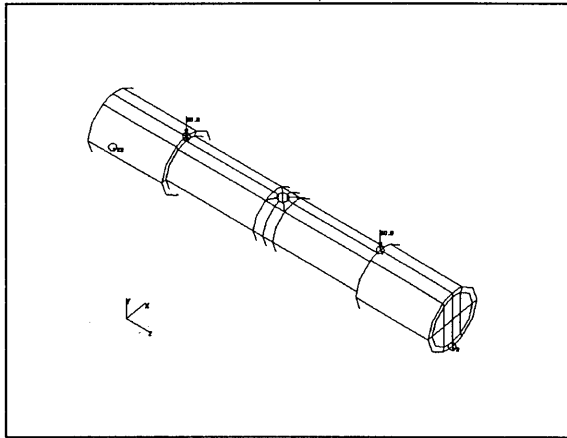


Figure 6.7 - Mesh A2: (452 nodes) This was the coarsest mesh possible and included wedge elements along both sides of the hole. Wedge elements are typically stiffer than quadrilateral elements.
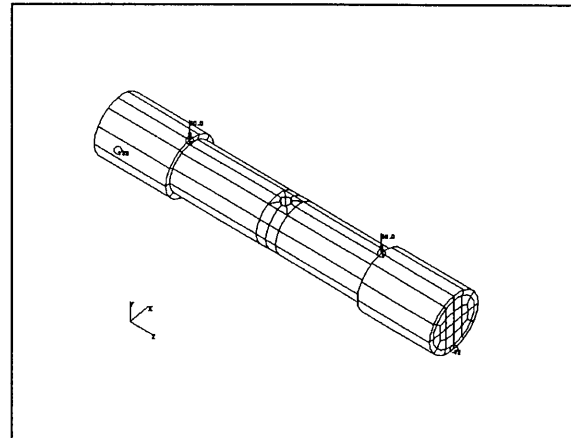


Figure 6.9 - Mesh A1 - (964 nodes) The mesh density of the entire model was doubled in the x and y (radial) directions.
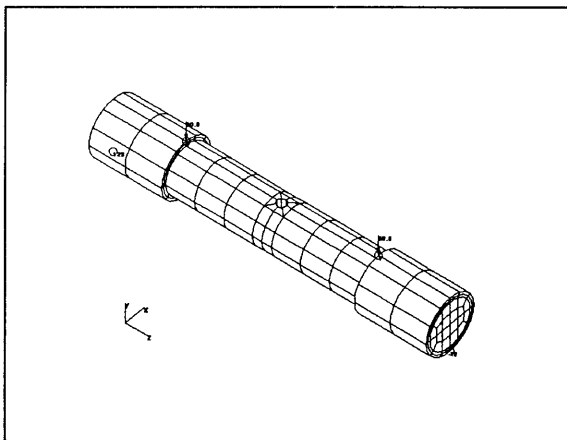


Figure 6.8 - Mesh 1: (1924 nodes) The endcap mesh was doubled in the z and y directions, and the gage length mesh was tripled in the z direction
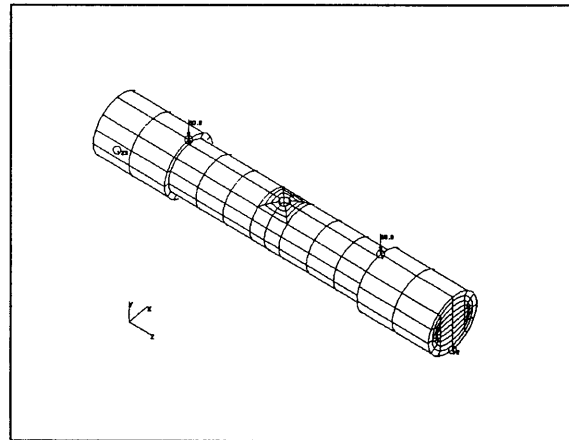


Figure 6.10 - Mesh 2: (3572 nodes) The mesh extending radially outward from the hole was doubled. The mesh density of the entire model was doubled in the y direction. This particular model increased mesh densities specifically in the directions where stress/strain gradients were most concentrated.
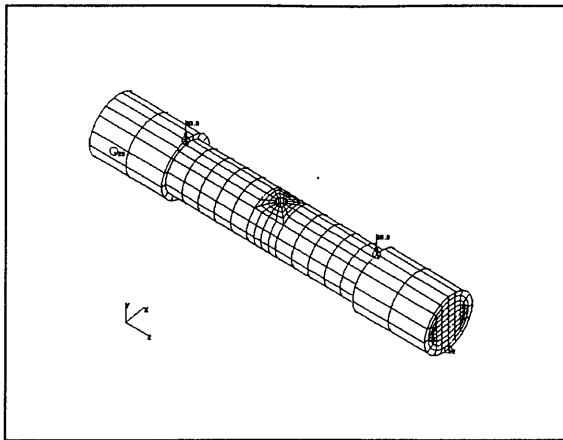
Figure 6.11 - Mesh 3: (6984 nodes) The
number of elements in the neighborhood of
the hole was doubled. This effectively
increased the mesh density in the x direction
for much of the model. The mesh density
along the z-axis was increased by a ratio of
5:3.
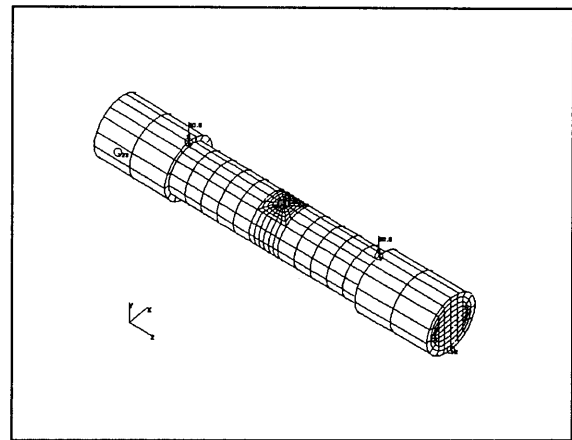


Figure 6.13 - Mesh 4: (8404 nodes) The mesh
density both around the hole and extending
radially outward from the hole was increased.
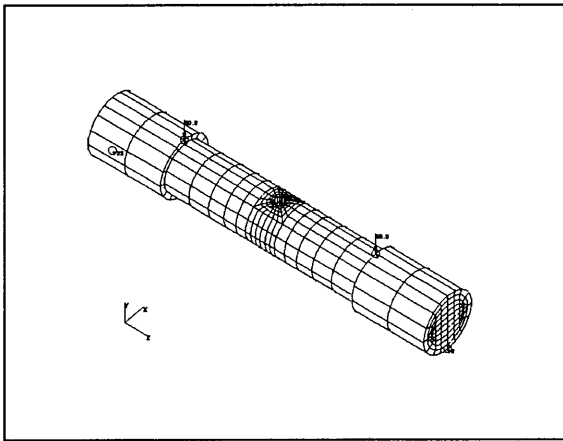


Figure 6.12 - Mesh 5: (8404 nodes) This mesh
had the same number of elements as mesh 4,
but they were proportioned so the mesh was
more refined towards the hole.
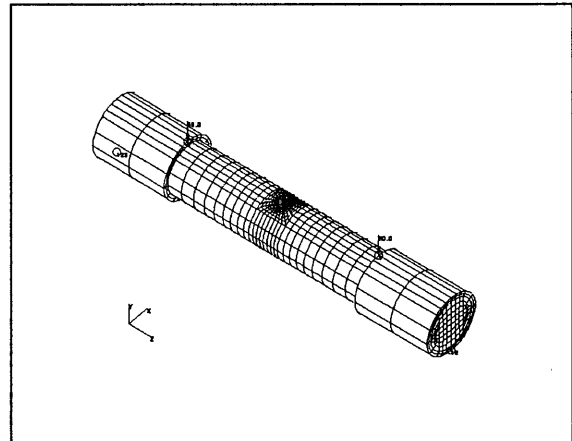


Figure 6.14 - Mesh 6: (16248 nodes) This mesh
provided the severest test of convergence by
significantly increasing mesh density
everywhere: in the x and z directions, radially
outward from the hole, around the hole and
through the thickness of the endcaps. Note
that long, distorted elements in this mesh may
cause the model to be excessively stiff.

## 6.2.1 ANALYSIS

Displacements, stresses, and strains were studied at four different sites, as shown in Figure 6.15. The circle represents the side-exterior; the triangle, the side-interior; the square, the front-exterior; and the front-interior is not shown but can be inferred. Stresses should be highest at the two points on the sides and near zero at the square. Points on the interior of the hole were chosen to study the stress convergence and were selected in a region of large stress gradients.
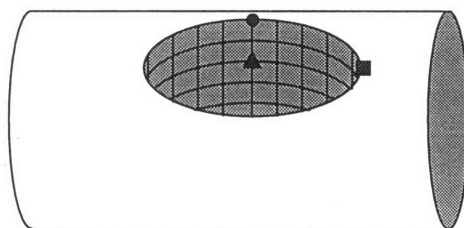


Figure 6.15 - Locations studied for convergence test.

## 6.2.2 RESULTS

The displacement convergence and the strain energy convergence for the side- and front-exterior nodes are shown in the Figures 6.16 through 6.21. Displacements converged nicely at all four selected sites. The stress and strain converged as expected for the points on the side (where stresses are high) and oscillated about zero for the location of the square in Figure 6.15. The study indicated that models had converged by Mesh 4. Mesh 5 was used for the models referenced in this thesis.
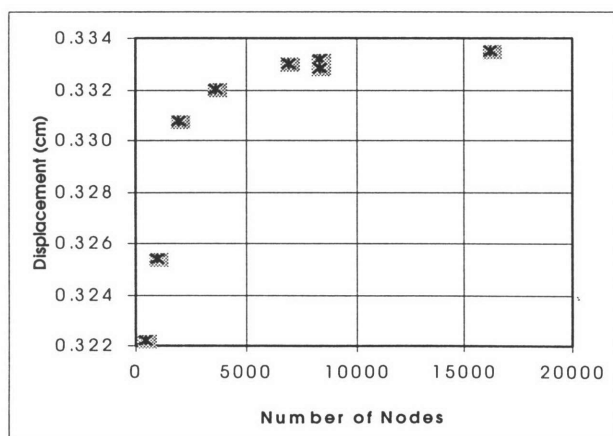


Figure 6.16 - Convergence of displacement of side-exterior point.
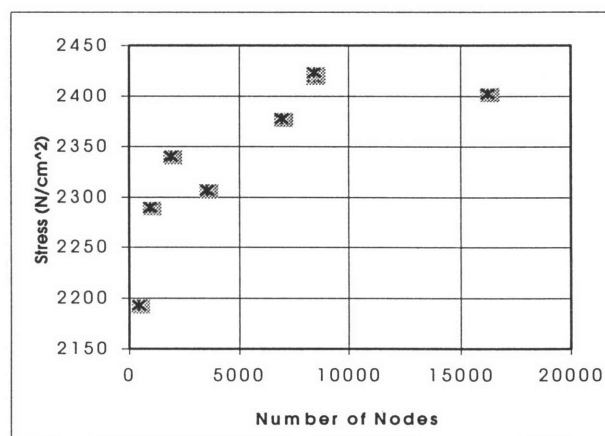
Figure 6.17 - Convergence of stress of side-exterior point.
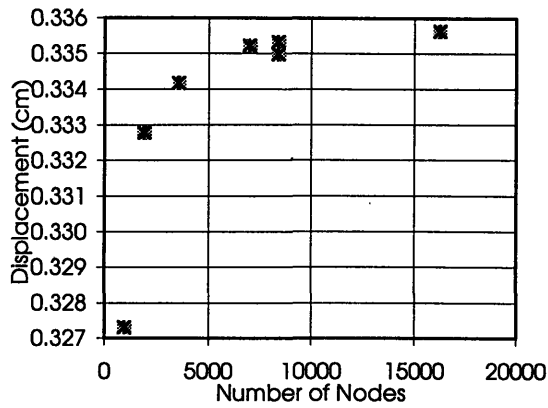
Figure 6.18 - Convergence of displacement of side-interior point.
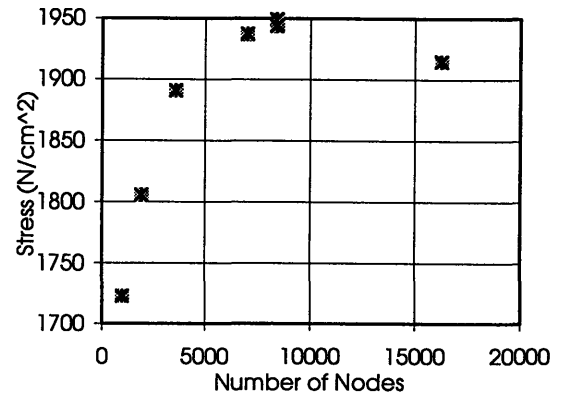


Figure 6.20 - Convergence of stress of side-interior point.
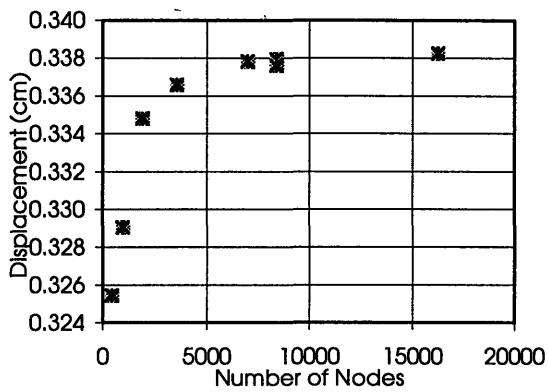


Figure 6.19 - Convergence of displacement of front-exterior point.
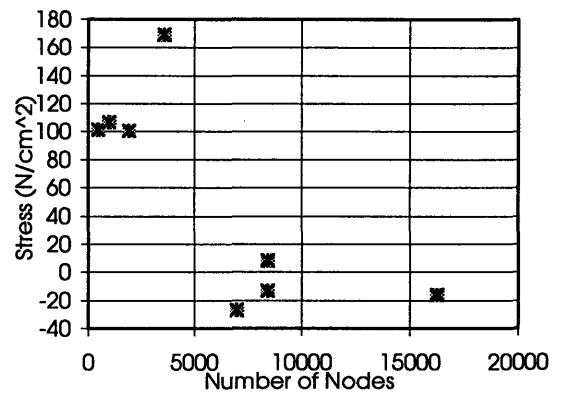


Figure 6.21 - Convergence of stress of front-exterior point.

The following figure shows the converged axial stress contours. A model with a 40% hole is displayed in order for the contours to be large enough to be visible.
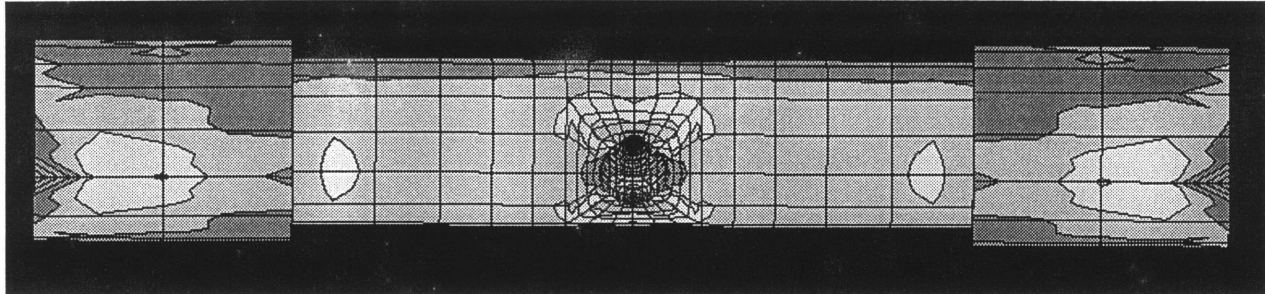


Figure 6.22 - Axial stress contours of converged bending model with 40% hole.

## 6.3 VALIDATION OF MODELS

After determining the mesh density required for a converged solution, it was still important to validate the bending, tension, and torsion models against existing data. There exist published stress concentration factors for round bars with circular transverse holes in bending, tension, and torsion. Therefore, maximum stress concentration factors from the finite element models were compared to these existing data for 20% holes. In addition, maximum stress in bending was compared to existing data for holes from 6% to 60% in order to verify that the models would remain valid over a range of geometries.

### 6.3.1 VALIDATION OF BENDING, TENSION, AND TORSION

First, stress concentration factors were calculated for models of bending, tension, and torsion of specimens with 20% holes based on the converged mesh (Mesh 5). For each type of loading, the maximum principle stress in the finite element model was determined for models with no hole, a 20% circular hole, and a 20% slot. Then the gross stress concentration factors ($K_g$) were calculated by dividing the stress in the models with holes by the stress in the model without a hole. The published stress concentration factors were determined from graphs of $K_g$ versus hole size as a percentage of nominal specimen diameter. These graphs were developed by Thum and Kirmser[1], by Jessop, Snell, and Allison[2], and by Fessler and Roberts[3], using data from tests of actual specimens of different materials.

The maximum stress in the finite element model did not occur on the surface of the specimen but at a small distance inside the hole on the surface of the hole. This was in agreement with experimental findings[1, 2, 4, 5] and was the stress used to calculate the published stress concentration factors.

Table 6.1 shows the gross stress concentration factors for the finite element models and for the published experimental data. The finite element models were in good agreement with the published data. The stress concentration factors for the models with slots are shown for reference, although experimental data does not exist for slots.

Table 6.1 - Theoretical and Experimental Stress Concentration Factors

| Model | Hole | Node | Modulus | Max Stress | Kg (FEM) | Kg (published) |
|---|---|---|---|---|---|---|
| ben0 | none | 41 | 25 | 761 | | |
| ben20e1 | 20% | 1062 | 25 | 2424 | 3.18 | 3.05 |
| ben20e2 | 20% slot | 14421 | 25 | 2358 | 3.10 | |
| ten0 | none | 109 | 25 | 64 | | |
| ten20e1 | 20% | 1057 | 25 | 228 | 3.59 | 3.64 |
| ten20e2 | 20% slot | 14327 | 25 | 716 | 11.24 | |
| tor0 | none | 1640 | 25 | 122 | | |
| tor20e1 | 20% | 1327 | 25 | 452 | 3.71 | 3.75 |
| tor20e2 | 20% slot | 1237 | 25 | 762 | 6.25 | |

## 6.3.2 VALIDATION OF BENDING FOR VARIOUS HOLE SIZES

Four-point bending models were made of specimens with circular holes 0%, 6%, 14%, 20%, 30%, 40%, 50%, and 60% of the specimen's nominal cross-sectional diameter. The meshes were based on the converged mesh (Mesh 5) from the convergence study discussed previously. The maximum axial stress in each finite element model was compared with maximum stress predictions using formulas developed by Roark[6] and using graphs developed by Thum and Kirmser[1].

The Roark data come from formulas based on a compilation of data from multiple researchers. The Roark formulas are only applicable for holes smaller than 45% and were, therefore, not included in analysis of the 50% and 60% models. The graph developed by Thum and Kirmser is shown in Figure 6.23. As discussed earlier, $K_n$ represents the stress concentration factor based on nominal stress (stress accounting for the reduced cross-section) and $K_g$ represents the stress concentration factor based on gross stress (calculated for the intact cross-section). These two concentration factors were used to calculate the $K_n$ and the $K_g$ stresses, shown in Table 6.2.

STRESS CONCENTRATION FACTOR
FOR BENDING OF A
ROUND BAR OR TUBE
WITH A
TRANSVERSE HOLE
Jessop, Snell, Allison (Brit. Eng. Sci. Data)
and Thum and Kirmser (Solid Round Bar)
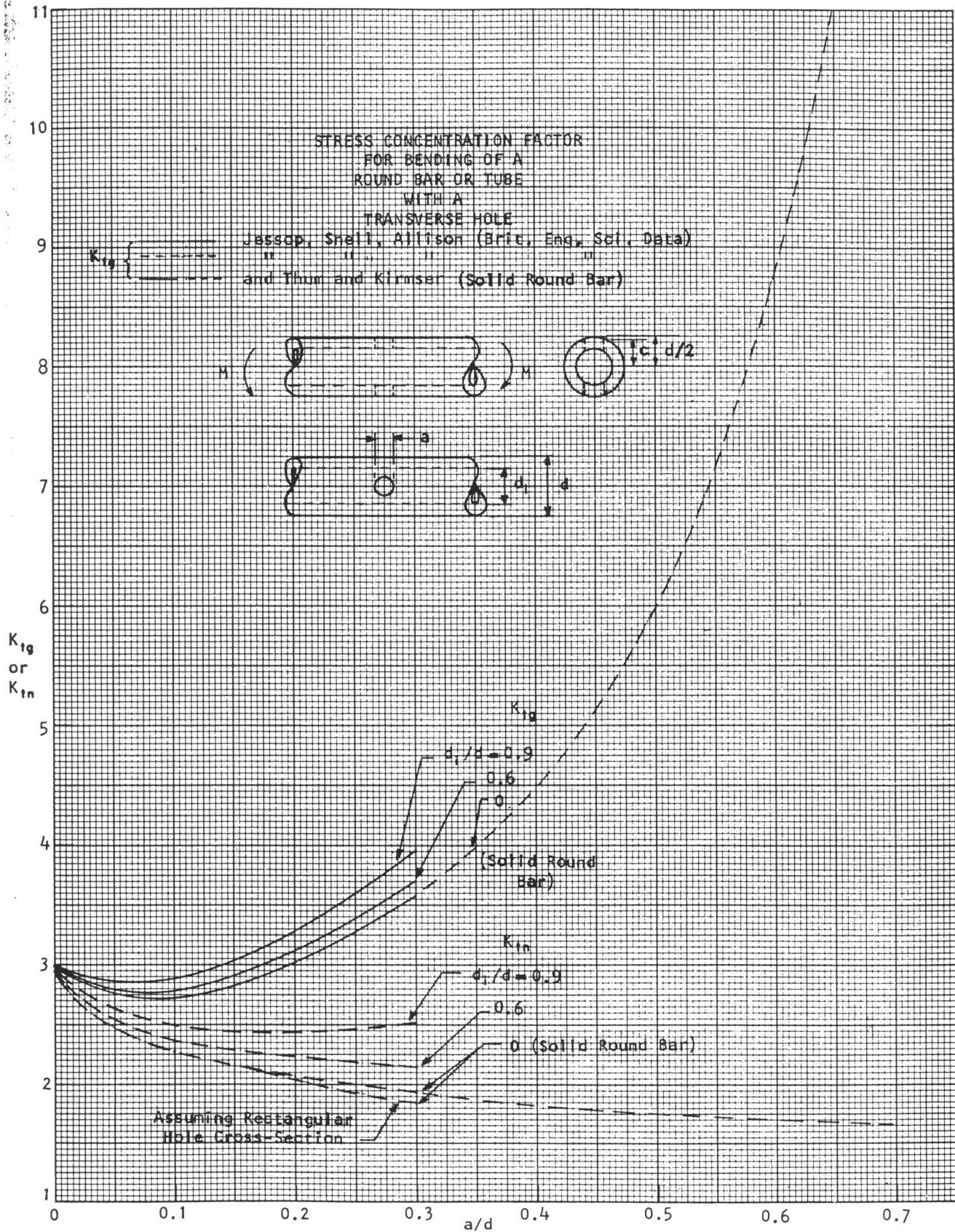
Table 6.2 compares the finite element data and the empirical data. S33 represents the maximum axial stress. Figure 6.24 shows the maximum stress predicted by the FEM vs. the maximum stress predicted by the three empirical relations. Both demonstrate how accurately the FEM predicted maximum stress as hole size changes. The correlations were all above $r^2 = 0.99$ and the slopes were all close to 1.0 with small y-intercepts. The lower correlation with Roark and the associated greater deviation from a slope of 1.0 may be explained by the fact that Roark's equations were developed with data compiled from a number of different sources, whereas the Thum and Kirmser data specifically represent stress concentration factors for a single study of solid cylinders with transverse circular holes.

Table 6.2 - Theoretical and Experimental Stresses Calculated from Different Stress Concentration Factors. (S33 = maximum axial stress)

| Model | Node # | Hole Size | S33 | S33 (Roark) | S33 (Kn) | S33 (Kg) |
|---|---|---|---|---|---|---|
| | Finite Elements | | | Stress Calculated Using Experimental Data | | |
| bh00vA | 1091 | 0% | 402 | 402 | 403 | 403 |
| bh06v5 | 772 | 6% | 1223 | 1114 | 1080 | 1114 |
| bh14v5 | 1056 | 14% | 1207 | 1116 | 1124 | 1117 |
| bh20v5 | 1056 | 20% | 1240 | 1182 | 1190 | 1171 |
| bh30v5 | 1056 | 30% | 1329 | 1115 | 1264 | 1326 |
| bh40v5 | 1056 | 40% | 1495 | 1202 | 1500 | 1510 |
| bh50v7 | 630 | 50% | 1751 | | 1737 | 1745 |
| bh60v7 | 630 | 60% | 2009 | | 2011 | 2004 |

Since the models converged, agreed with experimental data for circular holes in all three types of loading, and agreed with experimental data for a range of hole sizes in bending, it was assumed that models would be equally appropriate for elliptical holes of various sizes in all modes of loading.
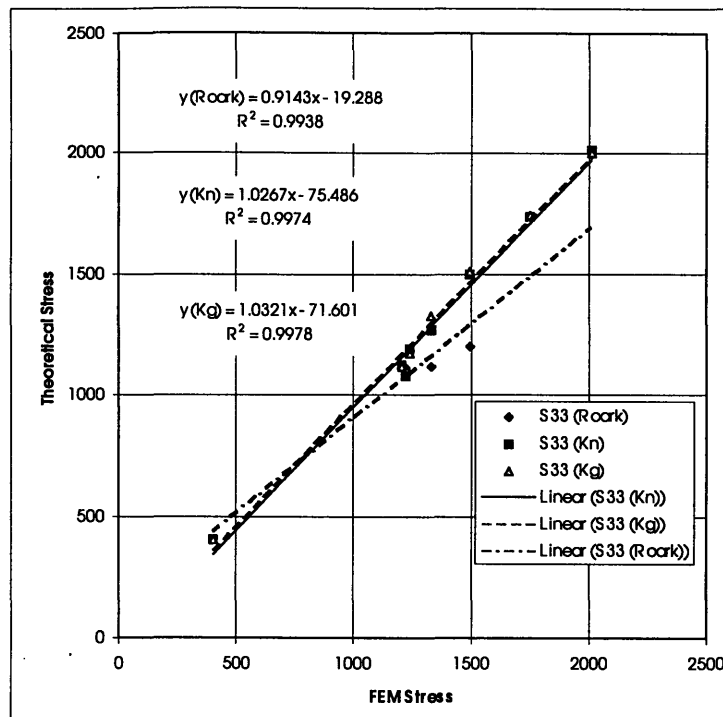
Figure 6.24 - Finite element models predicted stress concentrations very accurately over a range of hole sizes.

## 6.4 CALCULATION OF STRESS CONCENTRATION FACTORS

The stress concentration factors shown in Table 3.3 of Chapter 3 were net stress concentration factors, calculated using the same equation as 6.2:

Net stress concentration factor:  $K_n = \dfrac{\sigma max}{\sigma net}$ 　　　　　　　　[ 6.3 ]

The numerator, $\sigma_{max}$, was taken as the maximum stress in a finite element model of each specimen. The models, discussed in section 6.1, used the converged mesh, Mesh 5. Since the study compared various properties to a mechanically-measured load (yield load), a unit load (rather than displacement) was applied in every model. The denominator, $\sigma_{net}$, was based on the elementary Bernoulli-Euler formulas shown below:

tension:　　$\sigma\, net = \dfrac{P}{A\, net} = \dfrac{P}{A\, no\, hole} \times \dfrac{A\, no\, hole}{A\, net} = \sigma\, no\, hole \times \dfrac{A\, no\, hole}{A\, net}$ 　　[ 6.4 ]

bending:　　$\sigma\, net = \dfrac{Mc}{I\, net} = \sigma\, no\, hole \times \dfrac{I\, no\, hole}{I\, net}$ 　　　　　　[ 6.5 ]

torsion:      $\sigma \text{ net} = \dfrac{T}{J \text{ net}} = \sigma \text{ no hole} \times \dfrac{J \text{ no hole}}{J \text{ net}}$                    [ 6.6 ]

where $\sigma_{no\ hole}$ was taken from the finite element models as the uniform stress throughout the gage section measured in specimens without a defect. The geometric properties, A, I, and J, were calculated based on the width of the defect at the location of the maximum stress in the finite element model. This location was in general at the widest point in the defect. The defect's width may be given by the equation:

$$W_{hole} = \sqrt{(r_{hole})^2 - (X - r_{hole})^2}$$                    [ 6.7 ]

where $r_{hole}$ is the maximum width of the defect, and X is measured according to the coordinate system in Figure 6.25. Since the height, $H_{Hole}$, changes with the width, the height is also a function of X.
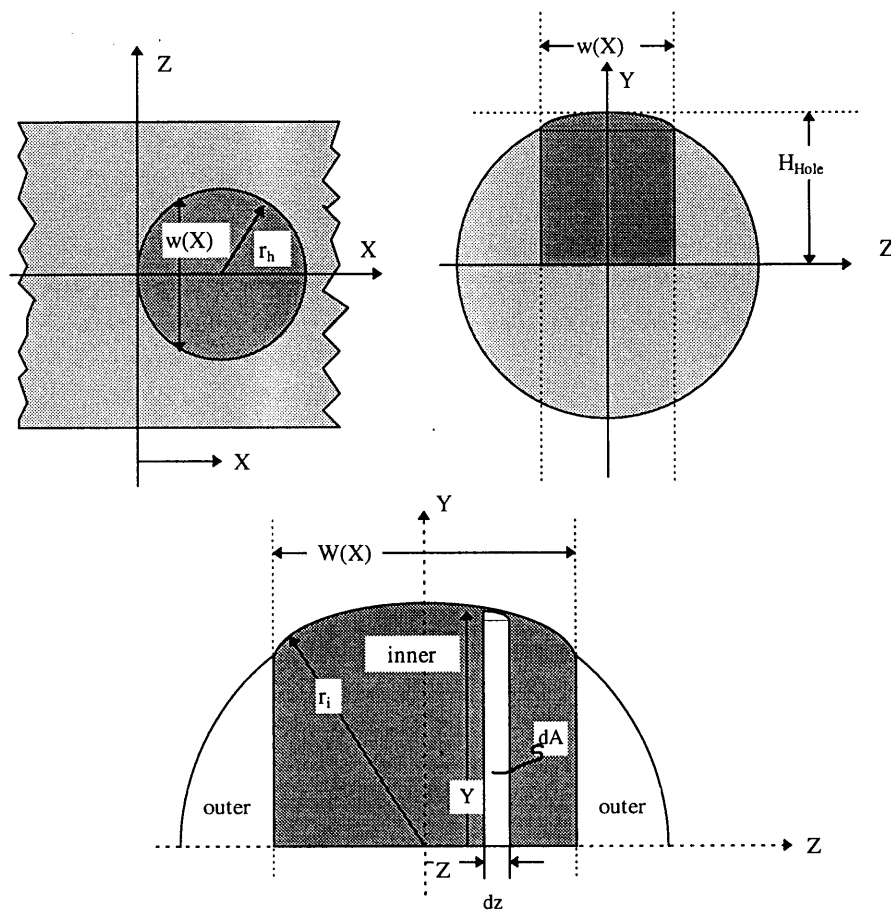


Figure 6.25 - Measurement of geometry of the defect along the length of the specimen.

The area, centroid, and moment of inertia of the hole at each cross-section were found by integrating along Z according to the convention shown in Figure 6.25. The differential element used for the integration is also shown in Figure 6.25:

$$dA = YdZ. \qquad\qquad [ 6.8 ]$$

To integrate across Z, Y and $dA$ were written in terms of Z:

$$Y_i = \sqrt{r_i^2 - Z^2}, \qquad dA_i = \sqrt{r_i^2 - Z^2}\, dZ \qquad\qquad [ 6.9 ]$$

The subscript $i$ indicates the inner portion (hole) in Figure 6.25. The area of the segment was given by

$$A_i = \int dA_i = \int_{-W(x)/2}^{W(x)/2} \sqrt{r_i^2 - Z_i^2}\, dZ = \tfrac{1}{2}\left[ Z\sqrt{r_i^2 - Z_i^2} + r_i^2 \sin^{-1}\!\left(\frac{Z}{r_i}\right) \right]_{-W(x)/2}^{W(x)/2}. \qquad [ 6.10 ]$$

The area moment of inertia of the differential rectangular element $dA$ about its base was

$$dI_i = \tfrac{1}{3} Y^3 dZ. \qquad\qquad [ 6.11 ]$$

Therefore, the area moment of inertia of the entire segment about the Z-axis was

$$I_i = \int dI_i = \int_{-W(x)/2}^{W(x)/2} \tfrac{1}{3} Y^3 dZ = \int_{-W(x)/2}^{W(x)/2} \tfrac{1}{3} \sqrt{\left(r_i^2 - Z_i^2\right)^3}\, dZ$$

$$= \tfrac{1}{12}\left[ Z\sqrt{(r_i^2 - Z_i^2)^3} + \frac{3r_i^2 Z}{2}\sqrt{r_i^2 - Z_i^2} + \frac{3r_i^4}{2}\sin^{-1}\!\left(\frac{Z}{r_i}\right) \right]_{-W(x)/2}^{W(x)/2}. \qquad [ 6.12 ]$$

The moment of inertia about the y axis in Figure 6.25 was calculated in a similar manner, integrating along the z-axis, with a differential element da=Zdy.

Given the geometric properties of the hole, the net area, bending moment of inertia, and polar moments of inertia used in equations 6.4 through 6.6 were calculated as

$$A_{net} = A_{no\ hole} - A_i \qquad\qquad [ 6.13 ]$$

$$I_{net} = I_{no\ hole} - I_i \qquad\qquad [ 6.14 ]$$

$$J = Izz + Iyy \qquad\qquad [6.15]$$

$$J_{net} = J_{no\ hole} - J_i \qquad\qquad [6.16]$$

The resulting net stress concentration factors are shown in Table 6.3.

Table 6.3 - Net Stress Concentration Factors

| Hole Size | None | 28% | 28% Slot | 47% | 47% Slot | 56% | 56% Slot |
|-----------|------|------|----------|------|----------|------|----------|
| Bending | 1.00 | 1.88 | 1.58 | 1.55 | 1.45 | 1.41 | 2.54 |
| Tension | 1.00 | 2.46 | 3.82 | 2.28 | 4.34 | 2.32 | 7.49 |
| Torsion | 1.00 | 2.19 | 2.85 | 2.08 | 3.70 | 2.05 | 9.19 |

It is worth noting that the finite element models predicted higher stress concentration factors for slots compared to circular holes with tension and torsional loading. Experimentally (Section 4.5), slots weakened trabecular bone more than circular holes for all types of loading, although only by about 25%, which is significantly less than that predicted by Table 6.1.

---

[1]   A. Thum and W. Kirmser, "Uberlagerte Wechselbeanspruchungen, ihre Erzeugung und ihr Einfluss auf die Dauerbarkeit und Spannungsausbildung guergebohrten Wellen," *VDI-Forschungsheft 419*, Vol 14(b) p. 1, (1943).

[2]   H.T. Jessop, C. Snell, and I.M. Allison, "The stress concentration factors in cylindrical tubes with transverse holes," *Aeronautical Q.*, 10: 326ff, 1959.

[3]   H. Fessler and E.A. Roberts, "Bending stresses in a shaft with a tranverse hole," *Selected Papers on Stress Analysis*, Stress Analysis Conference, Delft, 1959, Reinhold Publ. Co., New York, pg. 45, 1961.

[4]   M.M. Levin, "Quantitative three-dimensional photoelasticity," *Proc. SESA*, 12:157-ff, 1943.

[5]   R.F. Kuo, E.Y.S. Chao, K. Rim, and J.B. Park, "The effect of defect size on the stress concentration and fracture characteristics for a tubular torsional model with a transverse hole," *Journal of Biomechanics*, 24:147-155, 1991.

[6]   Roark, Raymond J., *Formulas for Stress and Strain*, 2d ed., McGraw-Hill, New York, p. 739, 1943.

# Appendix A
# Validation of Testing and
# Measurement Apparati

## A.1  VALIDATION OF FOUR-POINT BENDING TEST JIG

### A.1.1  SUMMARY

A cylinder of type 3003 aluminum potted with PMMA in steel endcaps and a cylinder of acrylic secured in aluminum endcaps were tested using the four-point bending apparatus. Modulus values for these materials were taken from the literature. The specimens were instrumented with strain gages, and were loaded using an Instron 8511 load frame. Load was measured using a 500 lb. Instron load cell, and load vs. strain was recorded for different orientations of the specimens.

The results show that this four-point bending jig is able to apply consistent loads with more than 98% repeatability in the measurement of rigidity. It is also able to measure the modulus of an aluminum specimen with less than 3% error and an acrylic specimen within less than 1% error, including error in the placement of the strain gages and measurement of the specimens' moments of inertia.

### A.1.2  SPECIMEN POTTING AND INSTRUMENTATION

A cylinder of acrylic 16.12 mm in diameter was cut to 129 mm in length and turned down to exactly 15.88 mm in diameter on the ends, leaving a 45.8 mm gage length. The endcaps were marked off in 45° increments. A strain gage was secured at the specimen's midspan at the 0° mark and aligned along the length of the specimen. For testing, the cylinder was secured in aluminum endcaps (15.88 mm od) with set screws as shown in Figure A.1.
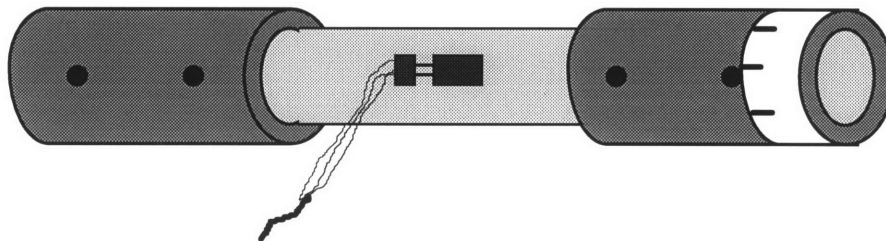
Figure A.1 - Acrylic specimen secured in aluminum endcaps with set screws

Two steel endcaps approximately 75 mm long were filled with polymethyl-methacrylate (PMMA), and the PMMA was allowed to harden. Each endcap was then placed in the chuck of a emco lathe, and a hole was drilled with a 15/16″ bit and was turned out to a diameter equal to the outer diameter of the aluminum specimen (25.4 mm). The hole was drilled approximately 40 mm into the PMMA.
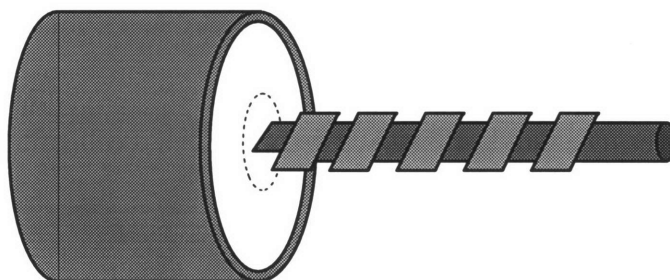


Figure A.2: Drilling Hole in Endcap

A piece of cylindrical aluminum 3003 stock was then cut to a length of approximately 150 mm. The endcap's hole was then filled with a small amount of PMMA, and one end of the aluminum cylinder was placed into the hole. Excess liquid PMMA which rose above the surface of the endcap was wiped clean. After the PMMA hardened, the second end of the aluminum tube was potted in the same manner, giving a 64.5 mm gage length. Tolerances between the outer diameter of the aluminum and the hole diameter were very tight; therefore, no additional alignment mechanism was necessary to insure that the endcaps were collinear.
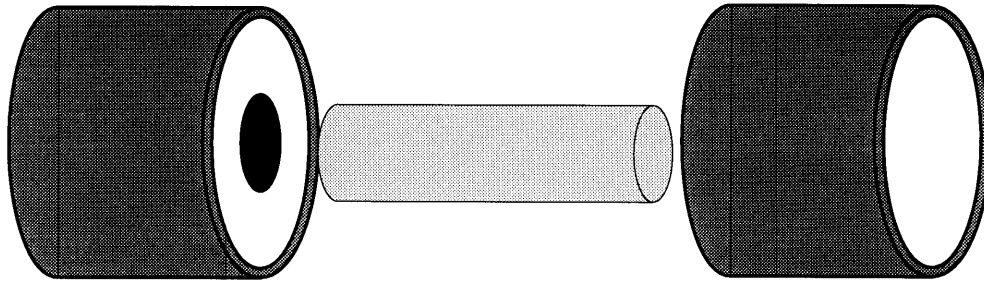
Figure A.3: Inserting the cylinder into the endcaps

The steel endcaps were marked off in 45° increments. A strain gage was secured at the specimen's midspan at the 0° mark and aligned along the length of the specimen. The same type of strain gage was mounted to the aluminum specimen as the acrylic. The specifications of the strain gage are as follows:

- Measurements Group Strain Gage
- CEA-13-125UW-350
- SN: R-A48AF131
- Resolution: 350 Ohms $\pm$ 0.3%
- Gage Factor: 2.150 $\pm$ 0.5%
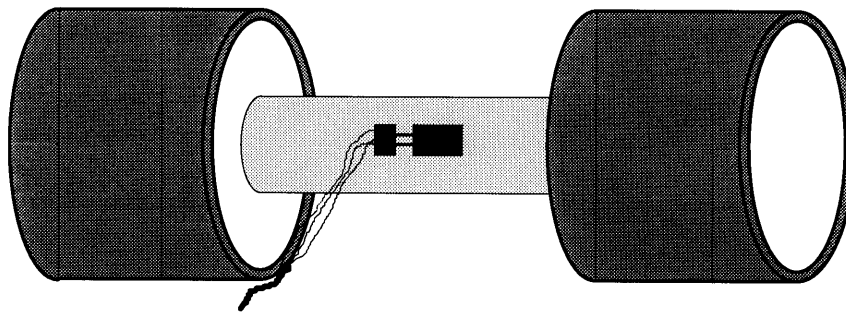


Figure A.4: Instrumenting the Strain Gage

## A.1.3 TEST SETUP

The specimen was placed in the four-point bending test jig, as shown in Figure A.5. The top half of the test jig was rigidly fixed to the load cell of an Instron 8511 load frame and was free to rotate about an axis perpendicular to the page, insuring an even load distribution. The bottom half of the jig was rigidly attached to the bottom mount of the load frame. One fixed load point and three rolling load points allowed for deformation due to bending without the introduction of undesired axial loads.
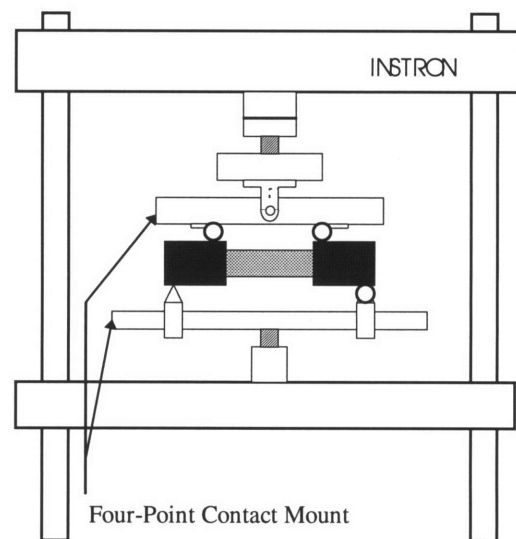
Figure A.5:  Test Setup

Figure A.6 is a close-up view of the specimen in the test jig.  The diameter of the bearing on the test jig was 41.22 mm.  The aluminum specimen had the following critical dimensions:

- $X_p$       = 39.69 mm
- Radius = 6.35 mm
- b       = 64.5 mm

The acrylic specimen had the following critical dimensions:

- $X_p$       = 23.7 mm
- Radius = 8.128 mm
- b       = 45.8 mm
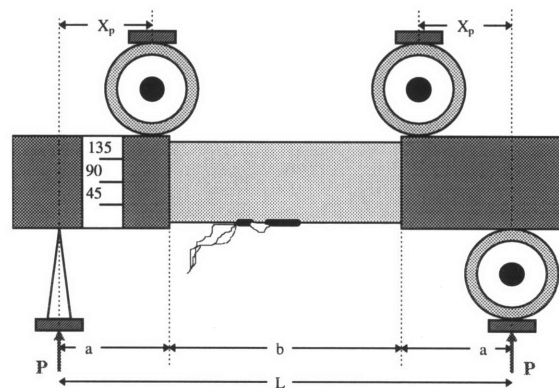


Figure A.6:  Dimensions of test setup

## A.1.4 TESTS, RESULTS, AND CONCLUSIONS

The specimen was loaded incrementally, and strain was measured with a Measurements Group P-3500 Strain Indicator and load with an 500 lb. Instron load cell. The load was allowed to settle before strain measurements were recorded since there was a slight viscoelastic response in both specimens. The specimens were loaded in four orientations: with the strain gage as shown in Figure A.6, with the strain gage oriented at 180° to that shown in Figure A.6, and in the two previous orientations with the specimen flipped horizontally. Measurements at each orientation were made six times, each time after repositioning. The same tests were performed on both the aluminum and acrylic specimens.

*ALIMINUM.* The true modulus of the aluminum 3003 specimen is 71 Gpa[1]. When the strain gage was oriented at 0°, the measured modulus of the aluminum was 72.6 GPa (2.3% error), with COV = 1.7% for six measurements. When oriented at 180°, the modulus was measured to be 70.4 GPa (-0.8% error) with COV = 1.4% for six measurements.

*ACRYLIC.* The true modulus of the acrylic specimen is 3.4 GPa. When the strain gage was oriented at 0°, the measured modulus of the acrylic was 3.42 GPa (0.5% error), with COV = 1.9% for six measurements. When oriented at 180°, the modulus was measured to be 3.37 GPa (-0.9% error) with COV = 1.1% for six measurements.

These two specimens nearly bracket the modulus expected for trabecular and cortical bone specimens (2.5 GPa and 15 GPa, respectively). Therefore, the accuracy in the modulus measurements indicates that this test setup applies predictable and measurable loads within the range expected for bone experiments. The low COV despite multiple orientations and repositioning by eye (without the aid of measurement instruments) indicates that the test setup allows for an easily-attained high degree of precision in measurements.

## A.1.5 RAW DATA

The following two pages show the raw data collected during the tests and the calculations made from that data.

**CONFIGURATION 1**

| Load (Newtons) | Adj. Load (Newtons) | Moment (Nm) | Strain | Stress (MPa) |
|---|---|---|---|---|
| 39 | 19.34 | 0.383802 | 2.70E-05 | 0.001909 |
| 83 | 63.34 | 1.256982 | 8.90E-05 | 0.006251 |
| 147 | 127.34 | 2.527062 | 1.78E-04 | 0.012566 |
| 195 | 175.34 | 3.479622 | 2.43E-04 | 0.017303 |
| Slope | | 71.23 | -5.57E-05 | |
| Corr. Coeff. (r^2) | | 1.00 | | |

| Load (Newtons) | Adj. Load (Newtons) | Moment (Nm) | Strain | Stress (MPa) |
|---|---|---|---|---|
| 44 | 24.34 | 0.483027 | 3.40E-05 | 0.002402 |
| 64 | 44.34 | 0.879927 | 6.30E-05 | 0.004376 |
| 85 | 65.34 | 1.296672 | 9.20E-05 | 0.006448 |
| 123 | 103.34 | 2.050782 | 1.43E-04 | 0.010198 |
| 175 | 155.34 | 3.082722 | 2.13E-04 | 0.015329 |
| 201 | 181.34 | 3.598692 | 2.46E-04 | 0.017895 |
| Slope | | 73.17 | -2.05E-04 | |
| Corr. Coeff. (r^2) | | 1.00 | | |

| Load (Newtons) | Adj. Load (Newtons) | Moment (Nm) | Strain | Stress (MPa) |
|---|---|---|---|---|
| 53 | 33.34 | 0.661632 | 4.50E-05 | 0.00329 |
| 78 | 58.34 | 1.157757 | 8.20E-05 | 0.005757 |
| 123 | 103.34 | 2.050782 | 1.42E-04 | 0.010198 |
| 144 | 124.34 | 2.467527 | 1.70E-04 | 0.01227 |
| 173 | 153.34 | 3.043032 | 2.10E-04 | 0.015132 |
| 200 | 180.34 | 3.578847 | 2.48E-04 | 0.017796 |
| Slope | | 72.01 | -2.52E-05 | |
| Corr. Coeff. (r^2) | | 1.00 | | |

**CONFIGURATION 1A**

| Load (Newtons) | Adj. Load (Newtons) | Moment (Nm) | Strain | Stress (MPa) |
|---|---|---|---|---|
| 52 | 32.34 | 0.641787 | 5.10E-05 | 0.003191 |
| 78 | 58.34 | 1.157757 | 8.80E-05 | 0.005757 |
| 104 | 84.34 | 1.673727 | 1.21E-04 | 0.008323 |
| 130 | 110.34 | 2.189697 | 1.55E-04 | 0.010889 |
| 182 | 162.34 | 3.221637 | 2.23E-04 | 0.01602 |
| 210 | 190.34 | 3.777297 | 2.61E-04 | 0.018783 |
| Slope | | 74.78 | -7.11E-04 | |
| Corr. Coeff. (r^2) | | 1.00 | | |

| Load (Newtons) | Adj. Load (Newtons) | Moment (Nm) | Strain | Stress (MPa) |
|---|---|---|---|---|
| 44 | 24.34 | 0.483027 | 3.40E-05 | 0.002402 |
| 66 | 46.34 | 0.919617 | 6.50E-05 | 0.004573 |
| 95 | 75.34 | 1.495122 | 1.06E-04 | 0.007435 |
| 137 | 117.34 | 2.328612 | 1.61E-04 | 0.011579 |
| 170 | 150.34 | 2.983497 | 2.07E-04 | 0.014836 |
| 212 | 192.34 | 3.816987 | 2.63E-04 | 0.018981 |
| Slope | | 72.53 | -1.38E-04 | |
| Corr. Coeff. (r^2) | | 1.00 | | |

| Load (Newtons) | Adj. Load (Newtons) | Moment (Nm) | Strain | Stress (MPa) |
|---|---|---|---|---|
| 38 | 18.34 | 0.363957 | 2.50E-05 | 0.00181 |
| 69 | 49.34 | 0.979152 | 6.70E-05 | 0.004869 |
| 104 | 84.34 | 1.673727 | 1.16E-04 | 0.008323 |
| 133 | 113.34 | 2.249232 | 1.54E-04 | 0.011185 |
| 150 | 130.34 | 2.586597 | 1.79E-04 | 0.012862 |
| 211 | 191.34 | 3.797142 | 2.62E-04 | 0.018882 |
| Slope | | 71.99 | 2.09E-05 | |
| Corr. Coeff. (r^2) | | 1.00 | | |

**CONFIGURATION 2**

| Load (Newtons) | Adj. Load (Newtons) | Moment (Nm) | Strain | Stress (MPa) |
|---|---|---|---|---|
| 45 | 25.34 | 0.502872 | 3.50E-05 | 0.002501 |
| 73 | 53.34 | 1.058532 | 7.50E-05 | 0.005264 |
| 124 | 104.34 | 2.070627 | 1.44E-04 | 0.010297 |
| 198 | 178.34 | 3.539157 | 2.45E-04 | 0.017599 |
| Slope | | 72.09 | -7.79E-05 | |
| Corr. Coeff. (r^2) | | 1.00 | | |

| Load (Newtons) | Adj. Load (Newtons) | Moment (Nm) | Strain | Stress (MPa) |
|---|---|---|---|---|
| 53 | 33.34 | 0.661632 | 5.70E-05 | 0.00329 |
| 80 | 60.34 | 1.197447 | 9.60E-05 | 0.005955 |
| 122 | 102.34 | 2.030937 | 1.59E-04 | 0.010099 |
| 145 | 125.34 | 2.487372 | 1.70E-04 | 0.012369 |
| 189 | 169.34 | 3.360552 | 2.52E-04 | 0.016711 |
| 206 | 186.34 | 3.697917 | 2.76E-04 | 0.018388 |
| Slope | | 69.05 | -4.89E-04 | |
| Corr. Coeff. (r^2) | | 0.99 | | |

| Load (Newtons) | Adj. Load (Newtons) | Moment (Nm) | Strain | Stress (MPa) |
|---|---|---|---|---|
| 36 | 16.34 | 0.324267 | 3.20E-05 | 0.001612 |
| 64 | 44.34 | 0.879927 | 8.10E-05 | 0.004376 |
| 102 | 82.34 | 1.634037 | 1.27E-04 | 0.008126 |
| 127 | 107.34 | 2.130162 | 1.61E-04 | 0.010593 |
| 161 | 141.34 | 2.804892 | 2.10E-04 | 0.013948 |
| 197 | 177.34 | 3.519312 | 2.60E-04 | 0.0175 |
| Slope | | 70.81 | -9.20E-04 | |
| Corr. Coeff. (r^2) | | 1.00 | | |

**CONFIGURATION 2B**

| Load (Newtons) | Adj. Load (Newtons) | Moment (Nm) | Strain | Stress (MPa) |
|---|---|---|---|---|
| 40 | 20.34 | 0.403647 | 3.90E-05 | 0.002007 |
| 81 | 61.34 | 1.217292 | 9.70E-05 | 0.006053 |
| 103 | 83.34 | 1.653882 | 1.28E-04 | 0.008224 |
| 123 | 103.34 | 2.050782 | 1.56E-04 | 0.010198 |
| 164 | 144.34 | 2.864427 | 2.14E-04 | 0.014244 |
| 199 | 179.34 | 3.559002 | 2.62E-04 | 0.017698 |
| Slope | | 70.29 | -7.59E-04 | |
| Corr. Coeff. (r^2) | | 1.00 | | |

| Load (Newtons) | Adj. Load (Newtons) | Moment (Nm) | Strain | Stress (MPa) |
|---|---|---|---|---|
| 36 | 16.34 | 0.324267 | 3.20E-05 | 0.001612 |
| 60 | 40.34 | 0.800547 | 6.60E-05 | 0.003981 |
| 85 | 65.34 | 1.296672 | 1.00E-04 | 0.006448 |
| 103 | 83.34 | 1.653882 | 1.26E-04 | 0.008224 |
| 152 | 132.34 | 2.626287 | 1.95E-04 | 0.01306 |
| 210 | 190.34 | 3.777297 | 2.76E-04 | 0.018783 |
| Slope | | 70.34 | -6.35E-04 | |
| Corr. Coeff. (r^2) | | 1.00 | | |

| Load (Newtons) | Adj. Load (Newtons) | Moment (Nm) | Strain | Stress (MPa) |
|---|---|---|---|---|
| 46 | 26.34 | 0.522717 | 4.70E-05 | 0.002599 |
| 67 | 47.34 | 0.939462 | 7.70E-05 | 0.004672 |
| 104 | 84.34 | 1.673727 | 1.29E-04 | 0.008323 |
| 136 | 116.34 | 2.308767 | 1.74E-04 | 0.011481 |
| 160 | 140.34 | 2.785047 | 2.08E-04 | 0.013849 |
| 210 | 190.34 | 3.777297 | 2.78E-04 | 0.018783 |
| Slope | | 70.08 | -7.13E-04 | |
| Corr. Coeff. (r^2) | | 1.00 | | |

| | | | | | |
|---|---|---|---|---|---|
| | 71.23 | SPECIMEN: 0.5" Almn Cyl. | | | 72.09 |
| | 73.17 | Moment Arm (m) | 0.03969 | | 69.05 |
| | 72.01 | Specimen Radius (m) | 0.00635 | | 70.81 |
| | 74.78 | Initial Load (N) | 19.66 | | 70.29 |
| | 72.53 | | | | 70.34 |
| | 71.99 | | | | 70.08 |
| Average | 72.62 | | | Average | 70.44 |
| Off fr/ 71 | 2.3% | | | Off fr/ 71 | -0.8% |
| Coeff. Var. | 1.7% | | | Coeff. Var. | 1.4% |

**CONFIGURATION 1**

| Load (Newtons) | Adj. Load (Newtons) | Moment (Nm) | Strain | Stress (MPa) |
|---|---|---|---|---|
| 26.3 | 9.68 | 0.114708 | 8.30E-05 | 0.00028 |
| 41.9 | 25.28 | 0.299568 | 2.02E-04 | 0.000731 |
| 66.1 | 49.48 | 0.586338 | 4.09E-04 | 0.001431 |
| 89.2 | 72.58 | 0.860073 | 5.98E-04 | 0.002099 |
| Slope | | 3.508 | 2.21E-06 | |
| Corr. Coeff. (r^2) | | 1.00 | | |

| Load (Newtons) | Adj. Load (Newtons) | Moment (Nm) | Strain | Stress (MPa) |
|---|---|---|---|---|
| 28.4 | 11.78 | 0.139593 | 1.11E-04 | 0.000341 |
| 43.7 | 27.08 | 0.320898 | 2.30E-04 | 0.000783 |
| 66 | 49.38 | 0.585153 | 4.11E-04 | 0.001428 |
| 83.4 | 66.78 | 0.791343 | 5.52E-04 | 0.001931 |
| Slope | | 3.600 | -5.27E-05 | |
| Corr. Coeff. (r^2) | | 1.00 | | |

| Load (Newtons) | Adj. Load (Newtons) | Moment (Nm) | Strain | Stress (MPa) |
|---|---|---|---|---|
| 27.1 | 10.48 | 0.124188 | 9.20E-05 | 0.000303 |
| 42.2 | 25.58 | 0.303123 | 2.11E-04 | 0.00074 |
| 65.5 | 48.88 | 0.579228 | 3.97E-04 | 0.001414 |
| 85 | 68.38 | 0.810303 | 5.59E-04 | 0.001978 |
| Slope | | 3.589 | -2.09E-05 | |
| Corr. Coeff. (r^2) | | 1.00 | | |

**CONFIGURATION 1A**

| Load (Newtons) | Adj. Load (Newtons) | Moment (Nm) | Strain | Stress (MPa) |
|---|---|---|---|---|
| 27 | 10.38 | 0.123003 | 1.06E-04 | 0.0003 |
| 44.3 | 27.68 | 0.328008 | 2.46E-04 | 0.000801 |
| 61.9 | 45.28 | 0.536568 | 3.93E-04 | 0.00131 |
| 84 | 67.38 | 0.798453 | 5.74E-04 | 0.001949 |
| Slope | | 3.517 | -6.99E-05 | |
| Corr. Coeff. (r^2) | | 1.00 | | |

| Load (Newtons) | Adj. Load (Newtons) | Moment (Nm) | Strain | Stress (MPa) |
|---|---|---|---|---|
| 25 | 8.38 | 0.099303 | 9.20E-05 | 0.000242 |
| 40.8 | 24.18 | 0.286533 | 2.17E-04 | 0.000699 |
| 67.7 | 51.08 | 0.605298 | 4.43E-04 | 0.001477 |
| 83.7 | 67.08 | 0.794898 | 5.82E-04 | 0.00194 |
| Slope | | 3.460 | -6.41E-05 | |
| Corr. Coeff. (r^2) | | 1.00 | | |

| Load (Newtons) | Adj. Load (Newtons) | Moment (Nm) | Strain | Stress (MPa) |
|---|---|---|---|---|
| 24.1 | 7.48 | 0.088638 | 8.40E-05 | 0.000216 |
| 42.1 | 25.48 | 0.301938 | 2.31E-04 | 0.000737 |
| 63.9 | 47.28 | 0.560268 | 4.19E-04 | 0.001367 |
| 85.5 | 68.88 | 0.816228 | 5.99E-04 | 0.001992 |
| Slope | | 3.437 | -6.70E-05 | |
| Corr. Coeff. (r^2) | | 1.00 | | |

**CONFIGURATION 2**

| Load (Newtons) | Adj. Load (Newtons) | Moment (Nm) | Strain | Stress (MPa) |
|---|---|---|---|---|
| 25.6 | 8.98 | 0.106413 | 9.10E-05 | 0.00026 |
| 39.6 | 22.98 | 0.272313 | 1.99E-04 | 0.000665 |
| 63.4 | 46.78 | 0.554343 | 4.05E-04 | 0.001353 |
| 84.5 | 67.88 | 0.804378 | 5.82E-04 | 0.001963 |
| Slope | | 3.446 | -4.01E-05 | |
| Corr. Coeff. (r^2) | | 1.00 | | |

| Load (Newtons) | Adj. Load (Newtons) | Moment (Nm) | Strain | Stress (MPa) |
|---|---|---|---|---|
| 25 | 8.38 | 0.099303 | 8.50E-05 | 0.000242 |
| 38 | 21.38 | 0.253353 | 1.90E-04 | 0.000618 |
| 69.2 | 52.58 | 0.623073 | 4.55E-04 | 0.001521 |
| 89 | 72.38 | 0.857703 | 6.29E-04 | 0.002093 |
| Slope | | 3.400 | -3.63E-05 | |
| Corr. Coeff. (r^2) | | 1.00 | | |

| Load (Newtons) | Adj. Load (Newtons) | Moment (Nm) | Strain | Stress (MPa) |
|---|---|---|---|---|
| 24.1 | 7.48 | 0.088638 | 8.20E-05 | 0.000216 |
| 41.3 | 24.68 | 0.292458 | 2.20E-04 | 0.000714 |
| 66.7 | 50.08 | 0.593448 | 4.34E-04 | 0.001448 |
| 85 | 68.38 | 0.810303 | 5.83E-04 | 0.001978 |
| Slope | | 3.503 | -6.60E-05 | |
| Corr. Coeff. (r^2) | | 1.00 | | |

**CONFIGURATION 2B**

| Load (Newtons) | Adj. Load (Newtons) | Moment (Nm) | Strain | Stress (MPa) |
|---|---|---|---|---|
| 24.7 | 8.08 | 0.095748 | 8.50E-05 | 0.000234 |
| 42 | 25.38 | 0.300753 | 2.24E-04 | 0.000734 |
| 66.9 | 50.28 | 0.595818 | 4.32E-04 | 0.001454 |
| 85 | 68.38 | 0.810303 | 5.82E-04 | 0.001978 |
| Slope | | 3.502 | -5.83E-05 | |
| Corr. Coeff. (r^2) | | 1.00 | | |

| Load (Newtons) | Adj. Load (Newtons) | Moment (Nm) | Strain | Stress (MPa) |
|---|---|---|---|---|
| 25.1 | 8.48 | 0.100488 | 9.20E-05 | 0.000245 |
| 42.9 | 26.28 | 0.311418 | 2.36E-04 | 0.00076 |
| 65 | 48.38 | 0.573303 | 4.22E-04 | 0.001399 |
| 83.6 | 66.98 | 0.793713 | 5.79E-04 | 0.001937 |
| Slope | | 3.469 | -6.71E-05 | |
| Corr. Coeff. (r^2) | | 1.00 | | |

| Load (Newtons) | Adj. Load (Newtons) | Moment (Nm) | Strain | Stress (MPa) |
|---|---|---|---|---|
| 27.3 | 10.68 | 0.126558 | 1.13E-04 | 0.000309 |
| 41.1 | 24.48 | 0.290088 | 2.21E-04 | 0.000708 |
| 66.3 | 49.68 | 0.588708 | 4.29E-04 | 0.001437 |
| 82.7 | 66.08 | 0.783048 | 5.73E-04 | 0.001911 |
| Slope | | 3.483 | -7.22E-05 | |
| Corr. Coeff. (r^2) | | 1.00 | | |

| | | | |
|---|---|---|---|
| | 3.508 | SPECIMEN: 0.625" Acrylic Cyl. | 3.446 |
| | 3.600 | Moment Arm (m)            0.0237 | 3.400 |
| | 3.589 | Specimen Radius (m)       0.0081 | 3.503 |
| | 3.517 | Initial Load (N)               16.62 | 3.502 |
| | 3.460 | | 3.469 |
| | 3.437 | | 3.483 |
| Average | 3.518 | | Average    3.467 |
| Off fr/ 34 | 3.5% | | Off fr/ 34  2.0% |
| Coeff. Var. | 1.9% | | Coeff. Var.  1.1% |

## A.2 VALIDATION OF UNIAXIAL TENSION TEST JIG

A cylinder of acrylic secured in aluminum endcaps was tested using the tension testing apparatus.

The specimen was instrumented with a strain gage and was loaded using an Interlaken Series 3300 hydraulic test frame. Load was measured using multiaxial Interlaken load cells, and load versus strain was recorded for different orientations of the specimen.

The results show that this uniaxial tension jig is able to maintain off-axis forces due to grip misalignment well below 5% of the applied load. It is also able to maintain strains due to uncontrolled bending in the specimen to below 25% of the applied tensile strain.

### A.2.1 TEST SETUP

A cylinder of acrylic 16.12 mm in diameter was cut to 129 mm in length and turned down to exactly 15.88 mm in diameter on the ends, leaving a 45.8 mm gage length. The endcaps were marked off in 45° increments. A strain gage was secured at the specimen's midspan at the 0° mark and aligned along the length of the specimen. For testing, the cylinder was secured in aluminum endcaps (15.88 mm od) with set screws as shown in Figure A.7.
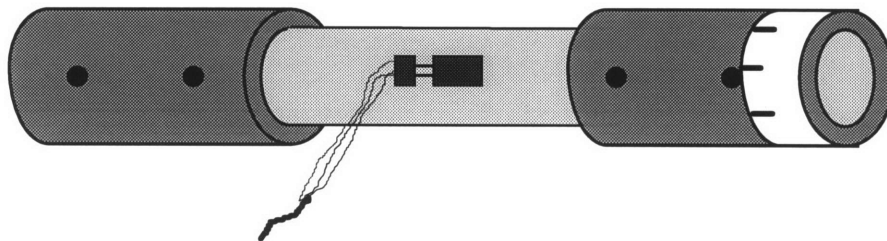


Figure A.7 - Acrylic specimen secured in aluminum endcaps with set screws

The specifications of the strain gage are as follows:

- Measurements Group Strain Gage
- CEA-13-125UW-350
- SN: R-A48AF131
- Resolution: 350 Ohms ± 0.3%
- Gage Factor: 2.150 ± 0.5%

The specimen was secured in the uniaxial tension test jig, shown in Figure A.8. Multiple links, steel cable, and a sphere/cone interface all reduced uncontrolled off-axis loads and allow for rotational and bending deformation due to inhomogeneity of the specimen.
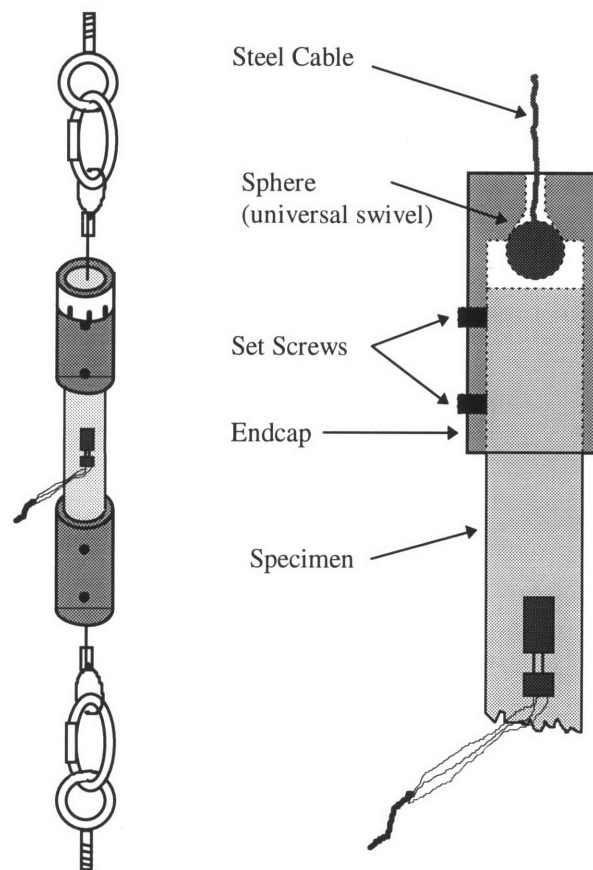


Figure A.8: Test Setup

## A.2.2 TESTS AND RESULTS

A low-density polyethylene cylinder was secured in the endcaps and loaded to between 50 N and 150 N. A 2,500 lb, six-axis, Instron load cell, was used to measure the applied axial load and loads in two directions orthogonal to the applied load. The loads were sampled at 60 Hz and recorded over a period of 10 seconds. The parasitic significance of the off-axis loads was calculated using

$$PS(Fx) = \frac{Fx}{Fz} 100\%$$

[ A.1 ]

$$PS(Fy) = \frac{Fy}{Fz} \, 100\%$$

[ A.2 ]

The parasitic significance of the off axis loads are plotted in Figure A.9 for five different loads. The plot shows that off-axis shear loads on the specimen are negligible compared to the applied tensile load.
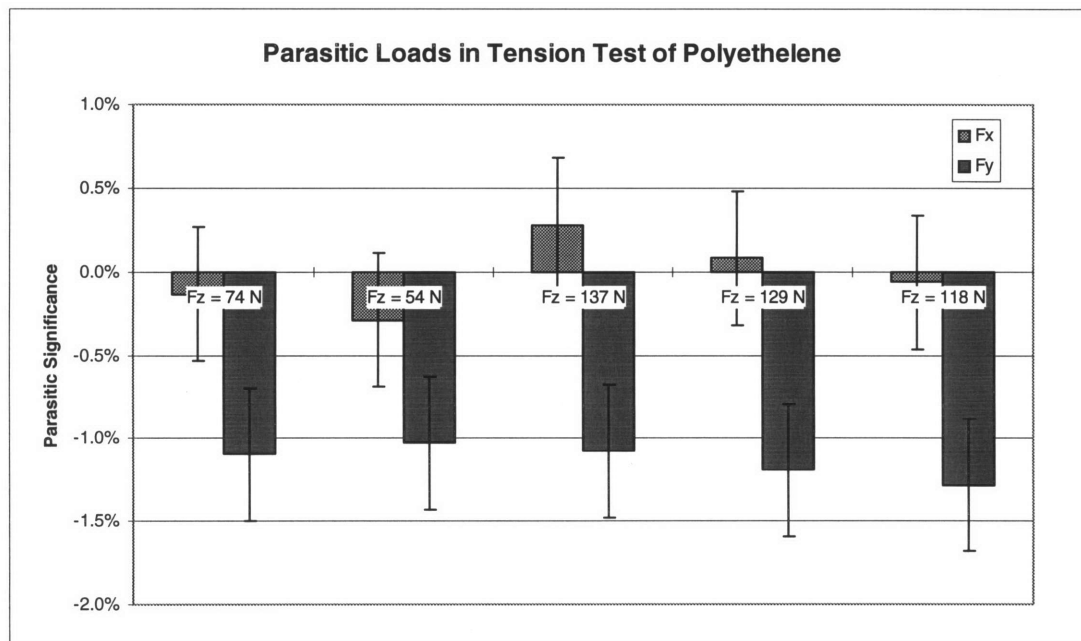


Figure A.9 - Off axis loads in a polyethylene specimen loaded in uniaxial tension are insignificant compared to the applied tensile load.

Given the dimensions of this specimen and test jig, misalignment of the specimen with respect to the load vector of less than a degree can induce bending loads that cause strain on one surface of the specimen to be double the strain on the opposite surface. In order to assess the magnitude of uncontrolled bending, the acrylic specimen was secured in the test jig as shown in Figure A.8, was loaded in tension, and the maximum and minimum strains were compared.

The specimen was loaded in four different configurations, shown in Figure A.10. In each configuration, load was applied incrementally, using an Interlaken DDC 4000 Controller. Strain was measured with a Measurements Group P-3500 Strain Indicator and load with a 5000 lb Torque-Thrust type 6467-124 Interlaken load cell. The modulus of the specimen was calculated as the slope of the stress vs. strain curve, where stress was calculated based on the applied load and the specimen's geometry. The modulus was measured with the specimen oriented at 0°, 90°, and 180°. The modulus measure-

ments were repeated five times at each angle, and the average moduli at each of these three angles were fit to an ellipse in order to determine a maximum and minimum.
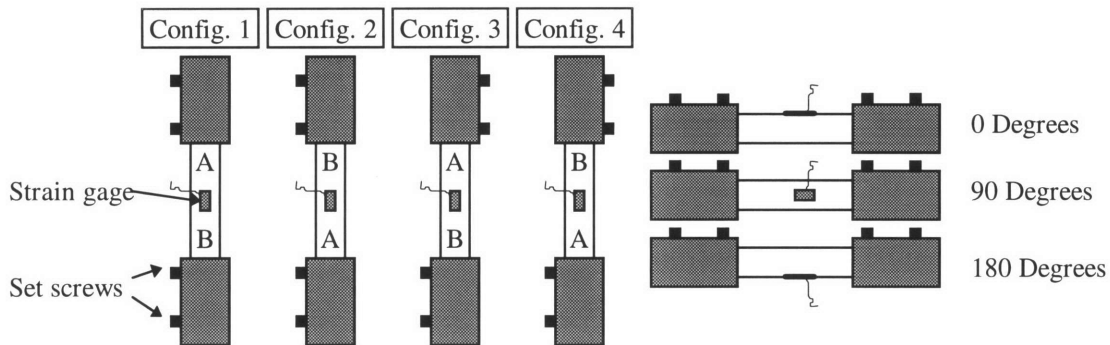


Figure A.10 - Specimens were tested at three orientations in each of four different configurations.

Table A.1 shows the results of the modulus measurements in each of the four different configurations. The table shows a relatively consistent modulus from one configuration to the next, indicating that the axes of the endcaps were well aligned and that the specimen was secured precisely in the center of the endcaps. The modulus measurements were also both accurate and fairly precise, indicating that the loads were being transmitted as pure axial tension. Finally, the difference between the minimum and maximum modulus (and hence strain) as determined by ellipse-fits of the data was less than 50% in all configurations. This means that uncontrolled bending strains (1/2 of the difference between the min and max strains) at the specimen surface are less than 25% of the applied tensile strains, and they decrease toward the radial center of the specimen.

Table A.1 - Modulus measurements of an acrylic specimen loaded in uniaxial tension

|  | Configuration 1 | Configuration 2 | Configuration 3 | Configuration 4 |
|---|---|---|---|---|
| Average (0° and 180°) | 3.41 ± 0.61 GPa | 3.24 ± 0.37 GPa | 3.48 ± .67 GPa | 3.01 ± 0.21 GPa |
| Error from 3.4 GPa | 0.3% | 4.6% | 2.3% | -11.3% |
| Min - Max | 26% | 43% | 8% | 19% |

## A.2.3 CONCLUSIONS

The tension test jig applies precise tensile loads, while still allowing for bending and rotational deformation of a specimen. The load is applied precisely along the long axis of the specimen; uncontrolled shear strains are less than 1% of the applied tensile strain; and uncontrolled bending strains at the surface are less than 25% of the applied tensile strain. The insignificance of uncontrolled loads indicates that this jig can be used to accurately and precisely measured the tensile modulus of a specimen. However, since

strain will be measured at the outer surface of the specimen, the magnitude of the bending strains at the surface suggests that modulus can only be accurately measured by averaging strain measured on opposite sides of the specimen.

Data and calculations of modulus for these tests are shown on the following four pages.

## 0 Degrees
### CONFIGURATION 2

| Load (Newtons) | Strain (micro) | Stress (MPa) |
|---|---|---|
| 80 | 161 | 0.39296 |
| 108 | 221 | 0.530496 |
| 112 | 233 | 0.550144 |
| 122 | 256 | 0.599264 |
| 154 | 319 | 0.756448 |
| Slope / Int. | 2.29 | 2.14E-02 |
| Corr. Coeff. (r^2) | | 1.00 |

| Load (Newtons) | Strain (micro) | Stress (MPa) |
|---|---|---|
| 68 | 106 | 0.334016 |
| 97 | 158 | 0.476464 |
| 127 | 209 | 0.623824 |
| 160 | 269 | 0.78592 |
| Slope / Int. | 2.78 | 3.89E-02 |
| Corr. Coeff. (r^2) | | 1.00 |

| Load (Newtons) | Strain (micro) | Stress (MPa) |
|---|---|---|
| 68 | 123 | 0.334016 |
| 96 | 178 | 0.471552 |
| 127 | 237 | 0.623824 |
| 162 | 300 | 0.795744 |
| Slope / Int. | 2.61 | 1.00E-02 |
| Corr. Coeff. (r^2) | | 1.00 |

| Load (Newtons) | Strain (micro) | Stress (MPa) |
|---|---|---|
| 59 | 108 | 0.289808 |
| 80 | 150 | 0.39296 |
| 105 | 201 | 0.51576 |
| 119 | 233 | 0.584528 |
| 153 | 299 | 0.751536 |
| Slope / Int. | 2.40 | 3.08E-02 |
| Corr. Coeff. (r^2) | | 1.00 |

| Load (Newtons) | Strain (micro) | Stress (MPa) |
|---|---|---|
| 69 | 126 | 0.338928 |
| 96 | 175 | 0.471552 |
| 112 | 200 | 0.550144 |
| 127 | 230 | 0.623824 |
| 162 | 290 | 0.795744 |
| Slope / Int. | 2.78 | -1.23E-02 |
| Corr. Coeff. (r^2) | | 1.00 |

| Modulus (GPa) | |
|---|---|
| | 2.29 |
| | 2.78 |
| | 2.61 |
| | 2.40 |
| | 2.78 |
| Average | 2.57 |
| Off fr/ 3.4 | -24.3% |
| Std. Dev. | 0.224 |
| Coeff. Var. | 8.7% |

## 90 Degrees
### CONFIGURATION 2

| Load (Newtons) | Strain (micro) | Stress (MPa) |
|---|---|---|
| 70 | 98 | 0.34384 |
| 95 | 138 | 0.46664 |
| 104 | 140 | 0.510848 |
| 120 | 170 | 0.58944 |
| 154 | 220 | 0.756448 |
| Slope / Int. | 3.37 | 1.73E-02 |
| Corr. Coeff. (r^2) | | 0.99 |

| Load (Newtons) | Strain (micro) | Stress (MPa) |
|---|---|---|
| 67 | 76 | 0.329104 |
| 99 | 117 | 0.486288 |
| 138 | 170 | 0.677856 |
| 157 | 195 | 0.771184 |
| Slope / Int. | 3.70 | 4.99E-02 |
| Corr. Coeff. (r^2) | | 1.00 |

| Load (Newtons) | Strain (micro) | Stress (MPa) |
|---|---|---|
| 76 | 120 | 0.373312 |
| 104 | 165 | 0.510848 |
| 135 | 216 | 0.66312 |
| 153 | 245 | 0.751536 |
| Slope / Int. | 3.02 | 1.14E-02 |
| Corr. Coeff. (r^2) | | 1.00 |

| Load (Newtons) | Strain (micro) | Stress (MPa) |
|---|---|---|
| 78 | 133 | 0.383136 |
| 108 | 188 | 0.530496 |
| 123 | 217 | 0.604176 |
| 140 | 247 | 0.68768 |
| 175 | 306 | 0.8596 |
| Slope / Int. | 2.75 | 1.38E-02 |
| Corr. Coeff. (r^2) | | 1.00 |

| Load (Newtons) | Strain (micro) | Stress (MPa) |
|---|---|---|
| 79 | 127 | 0.388048 |
| 110 | 177 | 0.54032 |
| 127 | 203 | 0.623824 |
| 146 | 234 | 0.717152 |
| 162 | 261 | 0.795744 |
| Slope / Int. | 3.05 | 9.14E-04 |
| Corr. Coeff. (r^2) | | 1.00 |

| Modulus (GPa) | |
|---|---|
| | 3.37 |
| | 3.70 |
| | 3.02 |
| | 2.75 |
| | 3.05 |
| Average | 3.18 |
| Off fr/ 3.4 | -6.5% |
| Std. Dev. | 0.366 |
| Coeff. Var. | 11.5% |

## 180 Degrees
### CONFIGURATION 2

| Load (Newtons) | Strain (micro) | Stress (MPa) |
|---|---|---|
| 73 | 94 | 0.358576 |
| 104 | 134 | 0.510848 |
| 122 | 157 | 0.599264 |
| 140 | 182 | 0.68768 |
| 160 | 208 | 0.78592 |
| Slope / Int. | 3.74 | 8.64E-03 |
| Corr. Coeff. (r^2) | | 1.00 |

| Load (Newtons) | Strain (micro) | Stress (MPa) |
|---|---|---|
| 63 | 62 | 0.309456 |
| 92 | 92 | 0.451904 |
| 124 | 126 | 0.609088 |
| 156 | 162 | 0.766272 |
| Slope / Int. | 4.57 | 2.91E-02 |
| Corr. Coeff. (r^2) | | 1.00 |

| Load (Newtons) | Strain (micro) | Stress (MPa) |
|---|---|---|
| 65 | 89 | 0.31928 |
| 105 | 146 | 0.51576 |
| 136 | 191 | 0.668032 |
| 169 | 242 | 0.830128 |
| Slope / Int. | 3.34 | 2.48E-02 |
| Corr. Coeff. (r^2) | | 1.00 |

| Load (Newtons) | Strain (micro) | Stress (MPa) |
|---|---|---|
| 73 | 93 | 0.358576 |
| 103 | 129 | 0.505936 |
| 135 | 172 | 0.66312 |
| 154 | 193 | 0.756448 |
| 171 | 218 | 0.839952 |
| Slope / Int. | 3.86 | 2.66E-03 |
| Corr. Coeff. (r^2) | | 1.00 |

| Load (Newtons) | Strain (micro) | Stress (MPa) |
|---|---|---|
| 67 | 82 | 0.329104 |
| 98 | 118 | 0.481376 |
| 115 | 137 | 0.56488 |
| 150 | 181 | 0.7368 |
| 170 | 207 | 0.83504 |
| Slope / Int. | 4.04 | 3.00E-03 |
| Corr. Coeff. (r^2) | | 1.00 |

| Modulus (GPa) | |
|---|---|
| | 3.74 |
| | 4.57 |
| | 3.34 |
| | 3.86 |
| | 4.04 |
| Average | 3.91 |
| Off fr/ 3.4 | 15.1% |
| Std. Dev. | 0.449 |
| Coeff. Var. | 11.5% |

| MODULUS (GPa) | |
|---|---|
| Average: | 3.24 |
| Uncertainty: | 15% |
| Off fr/ bending: | -7% |
| Off fr/ 3.4 | -4.6% |
| Max (ellipse): | 3.94 |
| Min (ellipse): | 2.56 |
| Min - Max: | 43% |

| | |
|---|---|
| Radius (m) | 0.00805 |
| Area (m^2) | 0.0002 |
| Initial Load (N) | |

## 0 Degrees
### CONFIGURATION 1

| Load (Newtons) | Strain (micro) | Stress (MPa) |
|---|---|---|
| 76 | 126 | 0.373312 |
| 102 | 170 | 0.501024 |
| 133 | 218 | 0.653296 |
| 147 | 243 | 0.722064 |
| Slope / Int. | 3.01 | -7.11E-03 |
| Corr. Coeff. (r^2) | | 1.00 |

| Load (Newtons) | Strain (micro) | Stress (MPa) |
|---|---|---|
| 73 | 90 | 0.358576 |
| 100 | 123 | 0.4912 |
| 131 | 161 | 0.643472 |
| 166 | 202 | 0.815392 |
| Slope / Int. | 4.07 | -9.39E-03 |
| Corr. Coeff. (r^2) | | 1.00 |

| Load (Newtons) | Strain (micro) | Stress (MPa) |
|---|---|---|
| 70 | 97 | 0.34384 |
| 100 | 138 | 0.4912 |
| 130 | 179 | 0.63856 |
| 165 | 225 | 0.81048 |
| Slope / Int. | 3.64 | -1.07E-02 |
| Corr. Coeff. (r^2) | | 1.00 |

| Load (Newtons) | Strain (micro) | Stress (MPa) |
|---|---|---|
| 72 | 120 | 0.353664 |
| 97 | 161 | 0.476464 |
| 128 | 212 | 0.628736 |
| 145 | 240 | 0.71224 |
| Slope / Int. | 2.99 | -4.76E-03 |
| Corr. Coeff. (r^2) | | 1.00 |

| Load (Newtons) | Strain (micro) | Stress (MPa) |
|---|---|---|
| 80 | 138 | 0.39296 |
| 109 | 181 | 0.535408 |
| 125 | 204 | 0.614 |
| 157 | 256 | 0.771184 |
| Slope / Int. | 3.21 | -4.65E-02 |
| Corr. Coeff. (r^2) | | 1.00 |

| Modulus (GPa) | |
|---|---|
| | 3.01 |
| | 4.07 |
| | 3.64 |
| | 2.99 |
| | 3.21 |
| Average | 3.38 |
| Off fr/ 3.4 | -0.5% |
| Std. Dev. | 0.466 |
| Coeff. Var. | 13.8% |

## 90 Degrees
### CONFIGURATION 1

| Load (Newtons) | Strain (micro) | Stress (MPa) |
|---|---|---|
| 76 | 114 | 0.373312 |
| 102 | 158 | 0.501024 |
| 117 | 178 | 0.574704 |
| 152 | 231 | 0.746624 |
| Slope / Int. | 3.21 | 2.48E-03 |
| Corr. Coeff. (r^2) | | 1.00 |

| Load (Newtons) | Strain (micro) | Stress (MPa) |
|---|---|---|
| 78 | 88 | 0.383136 |
| 108 | 121 | 0.530496 |
| 139 | 159 | 0.682768 |
| 160 | 181 | 0.78592 |
| Slope / Int. | 4.28 | 7.73E-03 |
| Corr. Coeff. (r^2) | | 1.00 |

| Load (Newtons) | Strain (micro) | Stress (MPa) |
|---|---|---|
| 70 | 93 | 0.34384 |
| 94 | 129 | 0.461728 |
| 120 | 170 | 0.58944 |
| 151 | 216 | 0.741712 |
| Slope / Int. | 3.22 | 4.42E-02 |
| Corr. Coeff. (r^2) | | 1.00 |

| Load (Newtons) | Strain (micro) | Stress (MPa) |
|---|---|---|
| 75 | 129 | 0.3684 |
| 101 | 172 | 0.496112 |
| 131 | 222 | 0.643472 |
| 146 | 251 | 0.717152 |
| Slope / Int. | 2.88 | -3.96E-04 |
| Corr. Coeff. (r^2) | | 1.00 |

| Load (Newtons) | Strain (micro) | Stress (MPa) |
|---|---|---|
| 75 | 115 | 0.3684 |
| 102 | 156 | 0.501024 |
| 118 | 180 | 0.579616 |
| 151 | 227 | 0.741712 |
| Slope / Int. | 3.33 | -1.72E-02 |
| Corr. Coeff. (r^2) | | 1.00 |

| Modulus (GPa) | |
|---|---|
| | 3.21 |
| | 4.28 |
| | 3.22 |
| | 2.88 |
| | 3.33 |
| Average | 3.39 |
| Off fr/ 3.4 | -0.4% |
| Std. Dev. | 0.530 |
| Coeff. Var. | 15.7% |

## 180 Degrees
### CONFIGURATION 1

| Load (Newtons) | Strain (micro) | Stress (MPa) |
|---|---|---|
| 78 | 91 | 0.383136 |
| 105 | 125 | 0.51576 |
| 120 | 143 | 0.58944 |
| 152 | 186 | 0.746624 |
| Slope / Int. | 3.83 | 3.68E-02 |
| Corr. Coeff. (r^2) | | 1.00 |

| Load (Newtons) | Strain (micro) | Stress (MPa) |
|---|---|---|
| 68 | 87 | 0.334016 |
| 92 | 124 | 0.451904 |
| 124 | 167 | 0.609088 |
| 159 | 215 | 0.781008 |
| Slope / Int. | 3.51 | 2.32E-02 |
| Corr. Coeff. (r^2) | | 1.00 |

| Load (Newtons) | Strain (micro) | Stress (MPa) |
|---|---|---|
| 80 | 97 | 0.39296 |
| 110 | 138 | 0.54032 |
| 128 | 160 | 0.628736 |
| 164 | 207 | 0.805568 |
| Slope / Int. | 3.76 | 2.56E-02 |
| Corr. Coeff. (r^2) | | 1.00 |

| Load (Newtons) | Strain (micro) | Stress (MPa) |
|---|---|---|
| 76 | 118 | 0.373312 |
| 102 | 163 | 0.501024 |
| 133 | 214 | 0.653296 |
| 156 | 243 | 0.766272 |
| Slope / Int. | 3.11 | 4.57E-04 |
| Corr. Coeff. (r^2) | | 1.00 |

| Load (Newtons) | Strain (micro) | Stress (MPa) |
|---|---|---|
| 73 | 118 | 0.358576 |
| 99 | 162 | 0.486288 |
| 129 | 210 | 0.633648 |
| 162 | 265 | 0.795744 |
| Slope / Int. | 2.98 | 5.42E-03 |
| Corr. Coeff. (r^2) | | 1.00 |

| Modulus (GPa) | |
|---|---|
| | 3.83 |
| | 3.51 |
| | 3.76 |
| | 3.11 |
| | 2.98 |
| Average | 3.44 |
| Off fr/ 3.4 | 1.2% |
| Std. Dev. | 0.382 |
| Coeff. Var. | 11.1% |

| MODULUS (GPa) | |
|---|---|
| Average: | 3.41 |
| Uncertainty: | 18% |
| Off fr/ bending: | -2% |
| Off fr/ 3.4 | 0.3% |
| Max (ellipse): | 3.87 |
| Min (ellipse): | 2.99 |
| Min - Max: | 26% |

| | |
|---|---|
| Radius (m) | 0.00805 |
| Area (m^2) | 0.0002 |
| Initial Load (N) | |

## 0 Degrees
**CONFIGURATION 3**

| Load (Newtons) | Strain (micro) | Stress (MPa) |
|---|---|---|
| 64 | 100 | 0.314368 |
| 100 | 155 | 0.4912 |
| 131 | 204 | 0.643472 |
| 149 | 230 | 0.731888 |
| Slope / Int. | 3.20 | -5.20E-03 |
| Corr. Coeff. (r^2) | | 1.00 |

| Load (Newtons) | Strain (micro) | Stress (MPa) |
|---|---|---|
| 67 | 95 | 0.329104 |
| 92 | 129 | 0.451904 |
| 124 | 175 | 0.609088 |
| 158 | 226 | 0.776096 |
| Slope / Int. | 3.41 | 9.26E-03 |
| Corr. Coeff. (r^2) | | 1.00 |

| Load (Newtons) | Strain (micro) | Stress (MPa) |
|---|---|---|
| 68 | 82 | 0.334016 |
| 97 | 116 | 0.476464 |
| 107 | 134 | 0.525584 |
| 140 | 175 | 0.68768 |
| Slope / Int. | 3.76 | 2.92E-02 |
| Corr. Coeff. (r^2) | | 1.00 |

| Modulus | 3.20 |
|---|---|
| (GPa) | 3.41 |
| | 3.76 |
| Average | 3.45 |
| Off fr/ 3.4 | 1.6% |
| Std. Dev. | 0.286 |
| Coeff. Var. | 8.3% |

## 90 Degrees
**CONFIGURATION 3**     **CONFIGURATION 3**

| Load (Newtons) | Strain (micro) | Stress (MPa) |
|---|---|---|
| 71 | 101 | 0.348752 |
| 96 | 138 | 0.471552 |
| 130 | 185 | 0.63856 |
| 165 | 237 | 0.81048 |
| Slope / Int. | 3.41 | 3.63E-03 |
| Corr. Coeff. (r^2) | | 1.00 |

| Load (Newtons) | Strain (micro) | Stress (MPa) |
|---|---|---|
| 68 | 103 | 0.334016 |
| 93 | 142 | 0.456816 |
| 120 | 184 | 0.58944 |
| 154 | 236 | 0.756448 |
| Slope / Int. | 3.18 | 6.26E-03 |
| Corr. Coeff. (r^2) | | 1.00 |

| Load (Newtons) | Strain (micro) | Stress (MPa) |
|---|---|---|
| 73 | 97 | 0.358576 |
| 102 | 138 | 0.501024 |
| 136 | 187 | 0.668032 |
| 172 | 238 | 0.844864 |
| Slope / Int. | 3.44 | 2.48E-02 |
| Corr. Coeff. (r^2) | | 1.00 |

| Modulus | 3.41 |
|---|---|
| (GPa) | 3.18 |
| | 3.44 |
| Average | 3.34 |
| Off fr/ 3.4 | -1.7% |
| Std. Dev. | 0.147 |
| Coeff. Var. | 4.4% |

## 180 Degrees
**CONFIGURATION 3**

| Load (Newtons) | Strain (micro) | Stress (MPa) |
|---|---|---|
| 66 | 87 | 0.324192 |
| 92 | 119 | 0.451904 |
| 122 | 157 | 0.599264 |
| 155 | 201 | 0.76136 |
| Slope / Int. | 3.83 | -6.45E-03 |
| Corr. Coeff. (r^2) | | 1.00 |

| Load (Newtons) | Strain (micro) | Stress (MPa) |
|---|---|---|
| 73 | 84 | 0.358576 |
| 102 | 121 | 0.501024 |
| 135 | 161 | 0.66312 |
| 169 | 205 | 0.830128 |
| Slope / Int. | 3.91 | 2.98E-02 |
| Corr. Coeff. (r^2) | | 1.00 |

| Load (Newtons) | Strain (micro) | Stress (MPa) |
|---|---|---|
| 75 | 117 | 0.3684 |
| 103 | 167 | 0.505936 |
| 136 | 225 | 0.668032 |
| 153 | 256 | 0.751536 |
| Slope / Int. | 2.76 | 4.51E-02 |
| Corr. Coeff. (r^2) | | 1.00 |

| Modulus | 3.83 |
|---|---|
| (GPa) | 3.91 |
| | 2.76 |
| Average | 3.50 |
| Off fr/ 3.4 | 3.0% |
| Std. Dev. | 0.642 |
| Coeff. Var. | 18.3% |

| MODULUS (GPa) | |
|---|---|
| Average: | 3.48 |
| Uncertainty: | 20% |
| Off fr/ bending: | -0.3% |
| Off fr/ 3.4 | 2.3% |
| Max (ellipse): | 3.63 |
| Min (ellipse): | 3.34 |
| Min - Max: | 8% |

| Radius (m) | 0.00805 |
|---|---|
| Area (m^2) | 0.000204 |
| Initial Load (N) | |

## 0 Degrees
### CONFIGURATION 4

| Load (Newtons) | Strain (micro) | Stress (MPa) |
|---|---|---|
| 68 | 109 | 0.334016 |
| 95 | 158 | 0.46664 |
| 126 | 215 | 0.618912 |
| 161 | 279 | 0.790832 |
| Slope / Int. | 2.69 | 4.17E-02 |
| Corr. Coeff. (r^2) | | 1.00 |

| Load (Newtons) | Strain (micro) | Stress (MPa) |
|---|---|---|
| 70 | 110 | 0.34384 |
| 98 | 162 | 0.481376 |
| 130 | 219 | 0.63856 |
| 165 | 281 | 0.81048 |
| Slope / Int. | 2.73 | 4.11E-02 |
| Corr. Coeff. (r^2) | | 1.00 |

| Load (Newtons) | Strain (micro) | Stress (MPa) |
|---|---|---|
| 71 | 117 | 0.348752 |
| 101 | 167 | 0.496112 |
| 134 | 226 | 0.658208 |
| 168 | 289 | 0.825216 |
| Slope / Int. | 2.76 | 2.99E-02 |
| Corr. Coeff. (r^2) | | 1.00 |

| Modulus (GPa) | |
|---|---|
| | 2.69 |
| | 2.73 |
| | 2.76 |
| Average | 2.73 |
| Off fr/ 3.4 | -19.8% |
| Std. Dev. | 0.040 |
| Coeff. Var. | 1.5% |

## 90 Degrees
### CONFIGURATION 4

| Load (Newtons) | Strain (micro) | Stress (MPa) |
|---|---|---|
| 73 | 115 | 0.358576 |
| 101 | 161 | 0.496112 |
| 123 | 211 | 0.604176 |
| 164 | 274 | 0.805568 |
| Slope / Int. | 2.76 | 4.14E-02 |
| Corr. Coeff. (r^2) | | 0.99 |

| Load (Newtons) | Strain (micro) | Stress (MPa) |
|---|---|---|
| 64 | 98 | 0.314368 |
| 95 | 143 | 0.46664 |
| 127 | 192 | 0.623824 |
| 162 | 248 | 0.795744 |
| Slope / Int. | 3.21 | 4.39E-03 |
| Corr. Coeff. (r^2) | | 1.00 |

| Load (Newtons) | Strain (micro) | Stress (MPa) |
|---|---|---|
| 71 | 108 | 0.348752 |
| 101 | 155 | 0.496112 |
| 133 | 203 | 0.653296 |
| 166 | 258 | 0.815392 |
| Slope / Int. | 3.12 | 1.29E-02 |
| Corr. Coeff. (r^2) | | 1.00 |

| Modulus (GPa) | |
|---|---|
| | 2.76 |
| | 3.21 |
| | 3.12 |
| Average | 3.03 |
| Off fr/ 3.4 | -10.9% |
| Std. Dev. | 0.238 |
| Coeff. Var. | 7.9% |

## 180 Degrees
### CONFIGURATION 4

| Load (Newtons) | Strain (micro) | Stress (MPa) |
|---|---|---|
| 70 | 97 | 0.34384 |
| 100 | 139 | 0.4912 |
| 131 | 183 | 0.643472 |
| 164 | 233 | 0.805568 |
| Slope / Int. | 3.40 | 1.70E-02 |
| Corr. Coeff. (r^2) | | 1.00 |

| Load (Newtons) | Strain (micro) | Stress (MPa) |
|---|---|---|
| 74 | 111 | 0.363488 |
| 104 | 154 | 0.510848 |
| 137 | 203 | 0.672944 |
| 174 | 258 | 0.854688 |
| Slope / Int. | 3.34 | -5.13E-03 |
| Corr. Coeff. (r^2) | | 1.00 |

| Load (Newtons) | Strain (micro) | Stress (MPa) |
|---|---|---|
| 76 | 111 | 0.373312 |
| 105 | 156 | 0.51576 |
| 141 | 210 | 0.692592 |
| 175 | 265 | 0.8596 |
| Slope / Int. | 3.17 | 2.24E-02 |
| Corr. Coeff. (r^2) | | 1.00 |

| Modulus (GPa) | |
|---|---|
| | 3.40 |
| | 3.34 |
| | 3.17 |
| Average | 3.30 |
| Off fr/ 3.4 | -2.9% |
| Std. Dev. | 0.119 |
| Coeff. Var. | 3.6% |

| MODULUS (GPa) | |
|---|---|
| Average: | 3.01 |
| Uncertainty: | 4% |
| Off fr/ bending: | -14% |
| Off fr/ 3.4 | -11.3% |
| Max (ellipse): | 3.31 |
| Min (ellipse): | 2.73 |
| Min - Max: | 19% |

| | |
|---|---|
| Radius (m) | 0.00805 |
| Area (m^2) | 0.000204 |
| Initial Load (N) | |

# A.3 VALIDATION OF MACREFLEX OPTICAL MEASUREMENT SYSTEM

## A.3.1 SUMMARY

A series of tests were conducted to validate the precision of the MacReflex Position Sensor for a variety of configurations. The MacReflex Position Sensor is a CCD camera system capable of tracking infrared-reflecting markers, using a strobe centered at 885 nm, through movements in three dimensions. It employs a 604H x 294V-pixel CCD; however, proprietary hardware and software resolve the image into a 27,000H x 19,400V pixel grid. It is guaranteed to track up to 1000 markers varying from 0.5% to 18% of FOV and samples at 60 Hz. The CCD resolves the image into pixels no greater than 1/30,000 of the FOV (field of view of the camera across the diagonal) with a standard deviation of 0.003% of FOV from spatio-temporal noise. The technical specifications claim absolute accuracy (precision of a measurement) of between 1/10,000 (or 0.01%) and 1/50,000 (or 0.002%) FOV and image linearity for 50 mm or higher lenses to within less than 0.1% FOV.

The system employs an electronic shutter that samples an object's position in the first 1/4000 second of a measurement at a rate of 60 Hz in order to prevent "smearing" of the centroid of moving objects. The system calculates a marker position as the centroid of the entire marker (not just edges) without using an averaging function to describe the threshold.

Tests were conducted to evaluate the technical claims of the system's precision for the following types of measurements, using both a 50 mm lens and an 18-180 mm zoom lens:

1) 2D Precision - tracking the stationary location of a single marker
2) 2D Relative Accuracy - measuring distance between two marker locations
3) 2D Dynamic Accuracy - tracking the movement of a single marker
4) 3D Precision - tracking marker locations using a 3D reference frame based on the CAB 80 calibration frame

The system was evaluated using a number of different marker types, camera placements, and backgrounds. Therefore, there were a number of qualitative conclusions drawn which did not warrant quantitative data.

The experiments indicated that flat, diamond-shaped markers of Scotchlite (3M) reflective materials approximately 0.2% - 5% of the FOV contrasted by a flat black background are most precisely tracked by the system. The markers may be either two- or

three-dimensional, but should be free of surface features that could change their appearance from different vantage points. The number of markers and their sizes must be determined and input to the software setup before testing to avoid poor or erratic measurements. Finally, in a three-dimensional measurement the cameras should be positioned at ±45° from the normal of the marker for maximum precision.

In general, the system is able to resolve the static location of a "good" marker to within 2 pixels (0.006% FOV) in X and 3 pixels (0.009% FOV) in Y . With 50 mm lenses (200 mm FOV), the system uncertainty is approximately 11 μm in X and 16 μm in Y for a two-dimensional measurement. With a 180 mm lens (18 mm FOV), the system uncertainty is approximately 2 μm in X and 4 μm in Y for a two-dimensional measurement. The measurement of movement in the "depth" of a camera system is about three times less precise than the measurement of movement in a plane normal to the camera system, necessitating a wide angle in the sweep between the cameras. The CAB 80 calibration frame is able to provide a precise reference frame to within 10 μm in the X-,Y-, and Z-directions when the cameras are placed 90° apart.

## A.3.2 CONCLUSIONS FROM INFORMAL EXPERIMENTS

From informal experimentation it was concluded that lightly-colored or reflective materials in the FOV can be misinterpreted (with a high degree of randomness) by the system to be markers and can blur the boundaries of actual markers, increasing the uncertainty in a measurement. Metal and water, in particular, can easily fool the system. Therefore, the material surrounding the camera should be colored flat black if possible.

The most effective markers are coated with Scotchlite (3M) tape, which is embedded with ground glass beads. Metal markers are also highly contrasting. Materials such as white or metallic silver paint on a black background do not provide sufficient contrast to act as markers. All markers, especially metal ones must be free of surface features or scratches than can be resolved by the cameras. As the marker moves, the surface features can come in and out of view, shifting the marker centroid and, therefore, adversely affecting system resolution. Should markers have unavoidable surface features that can be resolved by the monitor, adjusting the camera slightly out of focus can remove the features without significantly altering the system resolution.

The ideal marker size is about 0.5% to 10.0% of the FOV for the 50 mm lens and about half that for the zoom lens. This provides maximum resolution, compromising between a marker which is too large for a precise centroid and too small to be seen with reliability. Calibration frames should have markers of the same size (or smaller) as those used in the actual test.

When making two-dimensional measurements, a calibration scale must first be determined. This is best done by scaling to two points which bracket the range of motion expected for the actual tests. When setting up the software for a test, the marker size should be determined by setting the minimum and maximum marker sizes to their limits, monitoring the markers to determine their actual sizes, and then resetting the marker minimum to 3 pixels smaller and the marker maximum to 3 pixels larger than their actual size.

### A.3.3  2D PRECISION

The ability of the system to track the two-dimensional position of a stationary marker is a good indicator of measurement uncertainty. This precision was assessed using a variety of fields of view and different marker types. Tests were conducted using markers made of reflective, Scotchlite (3M) materials that were fixed to a piece of trabecular bone, painted black with Fabercastle waterproof black ink. The position of the marker was recorded 150 times over a period of five seconds and plotted versus time. Two standard deviations in the MacReflex position measurement was recorded as the uncertainty.

In order to scale pixels to millimeters, the marker position was recorded, and then the marker was moved a known distance (measured by an LVDT) and its second position recorded. The known distance between the two points was used to scale pixels to millimeters, using the formula

$$\text{Scale (Camera to cross-head)} = \frac{\Delta Y \text{ (cross-head)}}{\sqrt{\Delta X^2 + \Delta Y^2} \text{ (camera)}} \left(\frac{mm}{pixel}\right) \qquad [\text{A.3}]$$

During the actual test, the marker was held stationary midway between the two scaling points.

Two-dimensional measurement uncertainty was assessed in five tests of stationary markers viewed by 50 mm lens. A 9 mm displacement was used for scaling. The cameras were approximately 1.1 m from the markers. The uncertainties for the tests in the X and Y directions, expressed as two standard deviations, are shown in Table A.2. Figure A.11 shows a sample of the position vs. time plots for the high power zoom lens.

Table A.2 - Uncertainty for 2D measurements with 50 mm lenses

| Test | FOV mm | Uncertainty (X) | | | Uncertainty (Y) | | |
|---|---|---|---|---|---|---|---|
| | | pixels | % FOV | mm | pixels | % FOV | mm |
| Test 1 Camera 1 | 190 | 2.6 | 0.008 | 0.015 | 3.7 | 0.011 | 0.021 |
| Test 1 Camera 2 | 209 | 2.6 | 0.008 | 0.017 | 3.2 | 0.010 | 0.020 |
| Test 2 Camera 1 | 159 | 1.1 | 0.003 | 0.005 | 0.0 | 0.000 | 0.000 |
| Test 3 Camera 1 | 190 | 1.6 | 0.005 | 0.009 | 2.7 | 0.008 | 0.015 |
| Test 3 Camera 2 | 190 | 2.6 | 0.008 | 0.016 | 3.8 | 0.011 | 0.025 |
| Test 4 (with ink) | 156 | 1.6 | 0.005 | 0.008 | 3.0 | 0.009 | 0.014 |
| Test 5 (no ink) | 156 | 1.3 | 0.004 | 0.006 | 2.9 | 0.009 | 0.014 |
| **AVERAGE** | | **1.9** | **0.006** | **0.011** | **2.8** | **0.008** | **0.016** |

In the first through third tests, hemispherical, 3 mm markers (approximately 1.6% FOV) were used. In the first test, the marker was in the upper 10% of the camera's field of view, and in the second and third tests the marker was in the middle of the camera's field of view. In the fourth test a flat diamond maker (1.4% FOV) was placed against a bone cylinder painted black. In the fifth test, a flat diamond marker (1.4% FOV) was placed against a bone cylinder that had not been painted. The fact that the uncertainty does not change much from test to test, suggests:

1) The distortion (nonlinearity) of the lens is very small even near the edges of the field of view,
2) For the 50 mm lens, both flat diamond and hemispherical markers produce about the same resolution,
3) and the 50 mm lens is able to track markers on a natural bone background as easily as on a black bacground.
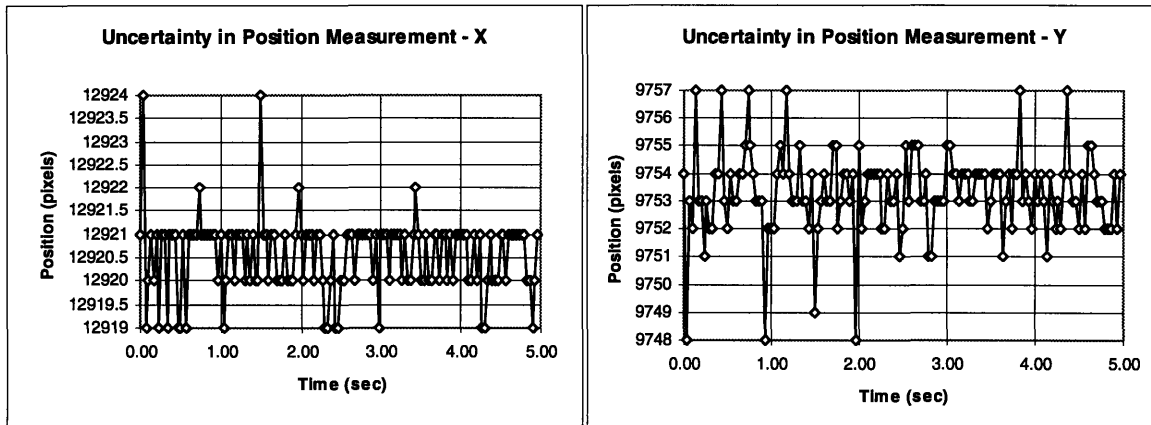
Figure A.11 - Uncertainty in the X- and Y-position of a 1.5% FOV marker using a 50 mm lens with a 156 mm FOV. Two standard deviations in the position was ± 1.6 pixels / 0.006 mm in X and ± 3.0 pixels/0.014 mm in Y.

Measurements of the diamond markers were made using a 50 mm lens at a distance from the marker of 365 mm, even though the lens is unable to focus closer than about 1000 mm. This test was performed in order to determine if a smaller field of view could be attained by tracking unfocused markers. Resolution dropped tenfold in this test to around 0.036% FOV (0.020 mm), which is actually worse resolution than with the larger field of view with a focused marker.

Two-dimensional measurement uncertainty was also assessed for stationary markers using a 180 mm zoom lens. Approximately 9 mm displacement was used for scaling. Table A.3 shows the position uncertainties, expressed as two standard deviations.

Table A.3 - Uncertainty for 2D measurements with zoom lenses

| Test | FOV mm | Uncertainty (X) | | | Uncertainty (Y) | | |
|------|--------|--------|-------|------|--------|-------|------|
|  |  | pixels | % FOV | mm | pixels | % FOV | mm |
| Test 1 (black bckgnd) | 18 | 2.7 | 0.008 | 0.0015 | 5.7 | 0.017 | 0.0032 |
| Test 2 (black bckgnd) | 35 | 1.0 | 0.003 | 0.0010 | 3.0 | 0.009 | 0.0031 |
| Test 3 (black bckgnd) | 78 | 2.1 | 0.006 | 0.0050 | 6.4 | 0.019 | 0.0152 |
| Test 5 (natural bone) | 27 | 4.0 | 0.012 | 0.0030 | 7.1 | 0.021 | 0.0057 |

It should be noted that the zoom lens did not have an infrared filter. However, informal tests showed that the uncertainty was the approximately same with or without the infrared filter for both the 50 mm lens and the zoom lens. The fact that the uncertainty did not improve linearly with the decrease in FOV may be explained by the fact that the marker in the smaller FOV appeared larger, therefore the "fuzziness" of its edges was commensurately magnified. The higher magnifications were also able to resolve the surface features of the markers into dark pixels in the otherwise white marker, perhaps making the calculation of a stable centroid more difficult. The lower resolution

of Test 5 also suggests that a black background improves the resolution over a natural bone background.

## A.3.4 2D RELATIVE ACCURACY

The previous measurements assessed the precision of a single measurement. In order to assess the accuracy of distance measurements, the distance between two marker positions as measured by the MacReflex system was compared to the distance measured by the LVDT of an Instron testing frame. This test was designed to identify problems due to nonlinearity of the image field.

Tests were conducted using markers made of reflective, Scotchlite (3M) tape fixed to a piece of trabecular bone, painted black with Fabercastle waterproof black ink. In order to scale pixels to millimeters, the marker position was recorded. Then the marker was moved a known distance (measured by an LVDT) and its second position recorded. The known distance between the two points bracketed the range of motion in the actual tests and was used to scale pixels to millimeters with equation A.3.

During the actual test, the marker was translated from one stationary point to the next in 0.1 mm increments. The expected change in X and Y (in pixels) based on the crosshead movement was compared to the change in X and Y recorded by the MacReflex system. The difference between the two (in mm) was reported as the error.

For the 50 mm lens (180 mm FOV), the distance between scaling points was approximately 20 mm. The error in nine 0.1 mm increments, two 0.5 mm increments, and four 1.0 mm increments was averaged. For the zoom lens (18 mm FOV), the scaling distance was 2 mm, and the error in thirteen 0.1 mm increments and three 1.2 mm increments was averaged. The results for the relative accuracy of the system are shown in Table A.4.

Table A.4 - Relative accuracy of position measurements

| Lens | Uncertainty (X) (mm / % FOV) | Uncertainty (Y) (mm / % FOV) |
|---|---|---|
| 50 mm (180 mm FOV) | ± 0.0100 (0.006%) | ± 0.0220 (0.012%) |
| Zoom (18.0 mm FOV) | ± 0.0010 (0.006%) | ± 0.0030 (0.017%) |

The data from these tests are shown on the following page.

| | CROSSHEAD Y mm | Delta mm | MACREFLEX X pixels | Y pixels | Delta X pixels | Delta Y pixels | Exp Delta X pixels | Exp Delta Y pixels | Error X mm | Error Y mm |
|---|---|---|---|---|---|---|---|---|---|---|
| Scaling | 10.0 | | 14374.0 | 5965.0 | | | | | | |
| Reference | 5.0 | -5.0 | 13827.0 | 15011.0 | -547.0 | 9046.0 | -547.00 | 9046.0 | 0.000 | 0.000 |
| | 8.0 | 3.0 | 14162.0 | 9617.0 | 335.0 | -5394.0 | 328.20 | -5427.6 | 0.004 | 0.019 |
| | 7.0 | -1.0 | 14051.0 | 11428.0 | -111.0 | 1811.0 | -109.40 | 1809.2 | 0.001 | 0.001 |
| | 6.9 | -0.1 | 14045.0 | 11622.0 | -6.0 | 194.0 | -10.94 | 180.9 | 0.003 | 0.007 |
| | 6.8 | -0.1 | 14031.0 | 11799.0 | -14.0 | 177.0 | -10.94 | 180.9 | 0.002 | 0.002 |
| | 6.7 | -0.1 | 14021.0 | 11986.0 | -10.0 | 187.0 | -10.94 | 180.9 | 0.001 | 0.003 |
| | 6.6 | -0.1 | 14013.0 | 12166.0 | -8.0 | 180.0 | -10.94 | 180.9 | 0.002 | 0.001 |
| | 6.5 | -0.1 | 14002.0 | 12345.0 | -11.0 | 179.0 | -10.94 | 180.9 | 0.000 | 0.001 |
| | | | | | | | | AVERAGE | 0.002 | 0.005 |
| | | | | | | | | MAX | 0.004 | 0.019 |

1.5 mm piece of tape
Zoom lense (full zoom)
Scale xhead to camera X (pixel/mm) 109.40
Scale xhead to camera Y (pixel/mm) -1809.20
Scale camera to xhead (mm/pixel) -0.00055

| | CROSSHEAD Y mm | Delta mm | MACREFLEX X pixels | Y pixels | Delta X pixels | Delta Y pixels | Exp Delta X pixels | Exp Delta Y pixels | Error X mm | Error Y mm |
|---|---|---|---|---|---|---|---|---|---|---|
| Scaling | 8.5 | | 14239.0 | 8650.0 | | | | | | |
| Reference | 6.5 | -2.0 | 14017.0 | 12265.0 | -222.0 | 3615.0 | -222.00 | 3615.0 | 0.000 | 0.000 |
| | 7.7 | 1.2 | 14148.0 | 10102.0 | 131.0 | -2163.0 | 133.20 | -2169.0 | 0.001 | 0.003 |
| | 7.6 | -0.1 | 14138.0 | 10289.0 | -10.0 | 187.0 | -11.10 | 180.8 | 0.001 | 0.003 |
| | 7.5 | -0.1 | 14125.0 | 10475.0 | -13.0 | 186.0 | -11.10 | 180.7 | 0.001 | 0.003 |
| | 7.4 | -0.1 | 14114.0 | 10656.0 | -11.0 | 181.0 | -11.10 | 180.7 | 0.000 | 0.000 |
| | 7.3 | -0.1 | 14106.0 | 10847.0 | -8.0 | 191.0 | -11.10 | 180.8 | 0.002 | 0.006 |
| | | | | | | | | AVERAGE | 0.001 | 0.003 |
| | | | | | | | | MAX | 0.002 | 0.006 |

1.5 mm piece of tape
Zoom lense (full zoom)
Scale xhead to camera X (pixel/mm) 111.00
Scale xhead to camera Y (pixel/mm) -1807.50
Scale camera to xhead (mm/pixel) -0.00055

| | CROSSHEAD Y mm | Delta mm | MACREFLEX X pixels | Y pixels | Delta X pixels | Delta Y pixels | Exp Delta X pixels | Exp Delta Y pixels | Error X mm | Error Y mm |
|---|---|---|---|---|---|---|---|---|---|---|
| Scaling | 8.0 | | 13546.0 | 6180.0 | | | | | | |
| Reference | 6.0 | -2.0 | 13330.0 | 9804.0 | -216.0 | 3624.0 | -216.00 | 3624.0 | 0.000 | 0.000 |
| | 7.2 | 1.2 | 13459.0 | 7634.0 | 129.0 | -2170.0 | 129.60 | -2174.4 | 0.000 | 0.002 |
| | 7.1 | -0.1 | 13450.0 | 7817.0 | -9.0 | 183.0 | -10.80 | 181.2 | 0.001 | 0.001 |
| | 7.0 | -0.1 | 13439.0 | 7997.0 | -11.0 | 180.0 | -10.80 | 181.2 | 0.000 | 0.001 |
| | 6.9 | -0.1 | 13430.0 | 8178.0 | -9.0 | 181.0 | -10.80 | 181.2 | 0.001 | 0.000 |
| | 6.8 | -0.1 | 13420.0 | 8358.0 | -10.0 | 180.0 | -10.80 | 181.2 | 0.000 | 0.001 |
| | | | | | | | | AVERAGE | 0.001 | 0.001 |
| | | | | | | | | MAX | 0.001 | 0.002 |

0.3 mm piece of tape
Zoom lense
Scale xhead to camera X (pixel/mm) 108.00
Scale xhead to camera Y (pixel/mm) -1812.00
Scale camera to xhead (mm/pixel) -0.00055

| | CROSSHEAD Y mm | Delta mm | MACREFLEX X pixels | Y pixels | Delta X pixels | Delta Y pixels | Exp Delta X pixels | Exp Delta Y pixels | Error X mm | Error Y mm |
|---|---|---|---|---|---|---|---|---|---|---|
| Scaling | 30.0 | | 14115.0 | 10110.0 | | | | | | |
| Reference | 10.0 | -20.0 | 14250.0 | 6719.0 | 135.0 | -3391.0 | 135.00 | -3391.0 | 0.000 | 0.000 |
| | 21.0 | 11.0 | 14172.0 | 8599.0 | -78.0 | 1880.0 | -74.25 | 1865.1 | 0.022 | 0.088 |
| | 20.5 | -0.5 | 14174.0 | 8514.0 | 2.0 | -85.0 | 3.38 | -84.8 | 0.008 | 0.001 |
| | 20.0 | -0.5 | 14182.0 | 8430.5 | 8.0 | -83.5 | 3.38 | -84.8 | 0.027 | 0.008 |
| | 19.9 | -0.1 | 14183.0 | 8417.0 | 1.0 | -13.5 | 0.68 | -17.0 | 0.002 | 0.020 |
| | 19.8 | -0.1 | 14183.0 | 8401.5 | 0.0 | -15.5 | 0.67 | -17.0 | 0.004 | 0.009 |
| | 19.7 | -0.1 | 14183.0 | 8383.5 | 0.0 | -18.0 | 0.68 | -17.0 | 0.004 | 0.006 |
| | 19.6 | -0.1 | 14183.0 | 8363.0 | 0.0 | -20.5 | 0.67 | -17.0 | 0.004 | 0.021 |
| | 19.5 | -0.1 | 14184.0 | 8348.0 | 1.0 | -15.0 | 0.68 | -17.0 | 0.002 | 0.012 |
| | | | | | | | | AVERAGE | 0.009 | 0.021 |
| | | | | | | | | MAX | 0.027 | 0.088 |

3 mm Macreflex marker
50 mm lense
Scale xhead to camera X (pixel/mm) -6.75
Scale xhead to camera Y (pixel/mm) 169.55
Scale camera to xhead (mm/pixel) -0.00589

| | CROSSHEAD Y mm | Delta mm | MACREFLEX X pixels | Y pixels | Delta X pixels | Delta Y pixels | Exp Delta X pixels | Exp Delta Y pixels | Error X mm | Error Y mm |
|---|---|---|---|---|---|---|---|---|---|---|
| Scaling | 30.0 | | 16697.0 | 12215.0 | | | | | | |
| Reference | 15.0 | -15.0 | 16605.0 | 9328.0 | -92.0 | -2887.0 | -92.00 | -2887.0 | 0.000 | 0.000 |
| | 14.0 | -1.0 | 16598.0 | 9134.5 | -7.0 | -193.5 | -6.13 | -192.5 | 0.005 | 0.005 |
| | 13.0 | -1.0 | 16593.0 | 8943.0 | -5.0 | -191.5 | -6.13 | -192.5 | 0.006 | 0.005 |
| | 12.0 | -1.0 | 16586.0 | 8740.0 | -7.0 | -203.0 | -6.13 | -192.5 | 0.005 | 0.055 |
| | 10.0 | -2.0 | 16573.0 | 8346.5 | -13.0 | -393.5 | -12.27 | -384.9 | 0.004 | 0.044 |
| | 9.9 | -0.1 | 16579.0 | 8331.0 | 6.0 | -15.5 | -0.61 | -19.2 | 0.034 | 0.019 |
| | 9.8 | -0.1 | 16577.5 | 8313.0 | -1.5 | -18.0 | -0.61 | -19.2 | 0.005 | 0.006 |
| | 9.7 | -0.1 | 16575.5 | 8286.5 | -2.0 | -26.5 | -0.61 | -19.2 | 0.007 | 0.038 |
| | 9.6 | -0.1 | 16571.5 | 8268.5 | -4.0 | -18.0 | -0.61 | -19.2 | 0.018 | 0.006 |
| | | | | | | | | AVERAGE | 0.010 | 0.022 |
| | | | | | | | | MAX | 0.034 | 0.055 |

1.5 mm piece of tape
50 mm lense
Scale xhead to camera X (pixel/mm) 6.13
Scale xhead to camera Y (pixel/mm) 192.47
Scale camera to xhead (mm/pixel) -0.00519

## A.3.5  2D Dynamic Accuracy

In order to test if there is any "smearing" of the marker centroid when tracking a moving marker, a marker was affixed to a black specimen of trabecular bone and suspended from the actuator of an Instron 8511 test frame. The actuator then described a sinusoidal wave in the vertical direction at 0.5 Hz. The marker position based on a 50 mm lens and zoom lens were compared to the location as determined by the Instron LVDT. This test was performed for 2.5 mm, 1 mm, 0.5 mm, 0.1 mm, and 0.05 mm amplitude waves. Unfortunately, the noise in the feedback loop of the Instron prevented accurate waves below about 0.5 mm in amplitude.

The 0.5 mm amplitude wave is shown in Figure A.12 to demonstrate qualitatively that there is no smearing in the marker position. The marker was too small to be resolved adequately by the 50 mm lens, explaining the inability of that camera to accurately track the marker's movement.
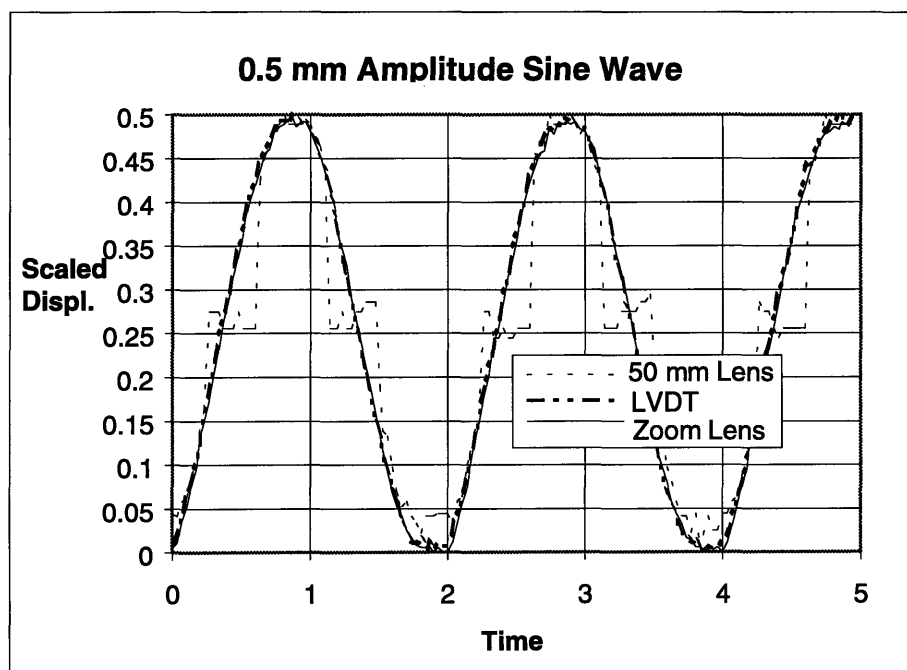


Figure A.12 - MacReflex system tracking the movement of a marker displaced in a sine wave by an Instron 8511 actuator.

## A.3.6 3D PRECISION AND ACCURACY WITH THE CAB 80 CALIBRATION FRAME

In order to assess the precision when measuring in three dimensions, the cameras were calibrated using the CAB 80 Calibration frame supplied by MacReflex. The positions of seven diamond-shaped markers on the calibration frame were recorded 150 times over a period of two seconds. The uncertainties of the seven markers, considered to be two standard deviations of the position measurement, were averaged. These uncertainties along with uncertainties in the three-dimensional measurements of a small, stationary marker placed on a black cylinder of trabecular bone are recorded in Table A.5. A plot of noise in the X- and Y-axis for one of the tests is shown in Figure A.13.

The cameras were 1.15 m from the markers, and the angle between the cameras swept 60° in the first calibration test and 90° in the second. They swept 30° the first two bone tests, 60° in the third and fourth test, and 90° (optimal) in the fifth through seventh tests.

Table A.5 - Precision of 3D measurements with the CAB 80 and 50 mm lenses

| Test | Field of View (mm) | Uncertainty (X) (mm / % FOV) | Uncertainty (Y) (mm / % FOV) | Uncertainty (Z) (mm / % FOV) |
|---|---|---|---|---|
| Cal Frame Test 1 (60°) | 190 mm | 0.006 (0.003%) | 0.022 (0.012%) | 0.009 (0.005%) |
| Cal Frame Test 2 (90°) | 190 mm | 0.008 (0.004%) | 0.008 (0.004%) | 0.009 (0.005%) |
| Bone Test 1 (30°) | 190 mm | 0.011 (0.010%) | 0.046 (0.042%) | 0.014 (0.013%) |
| Bone Test 2 (30°) | 190 mm | 0.017 (0.016%) | 0.052 (0.047%) | 0.016 (0.015%) |
| Bone Test 3 (60°) | 190 mm | 0.011 (0.010%) | 0.027 (0.025%) | 0.013 (0.012%) |
| Bone Test 4 (60°) | 190 mm | 0.009 (0.008%) | 0.025 (0.023%) | 0.013 (0.012%) |
| Bone Test 5 (90°) | 190 mm | 0.010 (0.009%) | 0.010 (0.009%) | 0.009 (0.008%) |
| Bone Test 6 (90°) | 190 mm | 0.008 (0.004%) | 0.006 (0.003%) | 0.010 (0.009%) |
| Bone Test 7 (90°) | 190 mm | 0.012 (0.011%) | 0.013 (0.012%) | 0.012 (0.011%) |
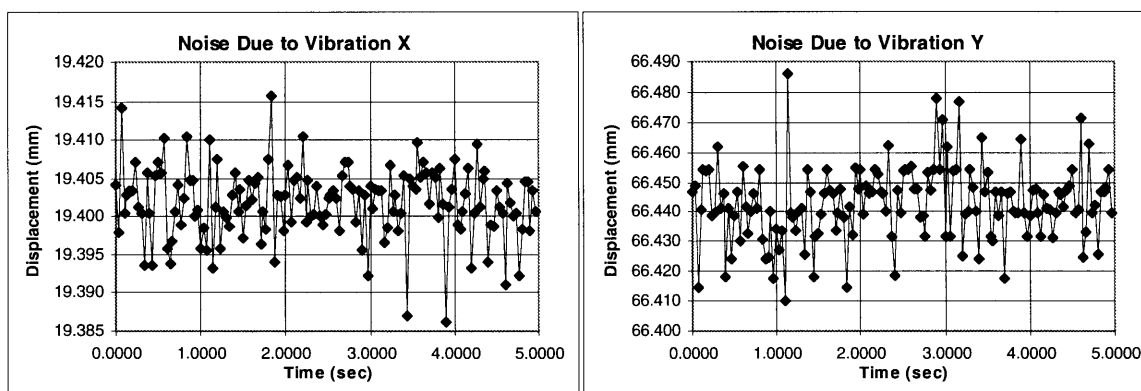


Figure A.13 - Noise due to system uncertainties in the X and Y direction of a small, square marker on a black cylinder of trabecular bone. The cameras were separated by 60° in this test.

The Y-direction represents the depth into the cameras for the calibration frame and the first three bone test. The uncertainty shows that the resolution of movement into the depth of a camera is less than half that in directions perpendicular to the camera when the cameras. However, the resolution is also seen to improve as the cameras are moved from a 30° separation to a 90° separation. At 90°, the uncertainty is the same in all three directions.

Tests 4, 5, and 6 used bone that was not colored, colored black only around the markers, and painted entirely black, respectively. Just as in the two-dimensional tests, the uncertainty was not affected by the color of the background.

The accuracy of three-dimensional measurements was also assessed by comparing the actual marker locations on the CAB 80 calibration frame (listed on the specification sheet) to the locations recorded by the MacReflex system. The errors for the seven markers were averaged, and results for tests at 60° and at 90° are shown in Table A.6.

Table A.6 - Accuracy of 3D measurements with the CAB 80 and 50 mm lenses

| Test | Field of View (mm) | Error (X) (mm / % FOV) | Error (Y) (mm / % FOV) | Error (Z) (mm / % FOV) |
|------|--------------------|------------------------|------------------------|------------------------|
| Cal Frame Test 1 (60°) | 190 mm | 0.003 (0.002%) | 0.002 (0.001%) | 0.005 (0.003%) |
| Cal Frame Test 2 (90°) | 190 mm | 0.005 (0.003%) | 0.005 (0.003%) | 0.003 (0.002%) |

Table A.6 shows that when the position is averaged over time, the accuracy is about twice as reliable as the uncertainty in a single measurement. Therefore, if the motion of a marker is slow enough compared to MacReflex sampling rate, and the data is filtered with a low pass filter, then the measurement precision may be significantly improved.

---

[1] M.F. Ashby and D.R.H. Jones, Engineering Materials I, Pergamon Press, Oxford, 1989.

# Appendix B
# Raw Data

This appendix contains the raw data from the results of the QCT scans, computer modeling, and mechanical tests. Specimens are grouped according to the type of mechanical test. The first four pages are example data sheets for the three types of mechanical tests: bending, tension, and torsion. The following six pages are the results of the QCT scans, both of the intact specimens and the specimens after the defects were introduced. The next three pages are the results of the stress concentration calculations. The following three pages are the results of the mechanical tests, and the final pages are the sketches of fracture patterns in the specimens.

The column labeled "E" in the tables is the eccentricity of the defect: 1 for a circle and 2 for a slot. The naming convention for the specimens has three parts which identifies the animal, vertebral location, and core number for each specimen, according to the following example. The data which could be contained in each part of a specimen name is also described below.

$$BCa2\_25$$

Animal B ——————————⌐ ⌐‾⌐ |

Second Caudal Vertebrae————⌐

Twenty-fifth Core Sample —————⌐
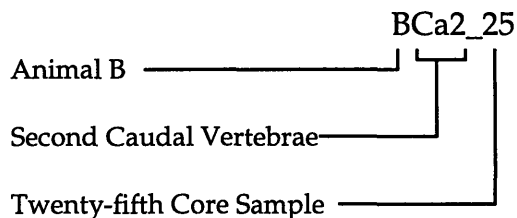
- Part 1: Animal
  - A: Infant male sperm whale
  - B: Mature female bowhead whale
  - C: Geriatric female bowhead whale
  - D: Mature male pigmy sperm whale
  - E: Immature female bowhead whale
  - F: Immature male bowhead whale: morphological variant "ingutuk"
- Part 2: Vertebral location
  - Ca: Caudal
  - C: Cervical
  - L: Lumbar
  - T: Thoracic
- Part 3: Core sample number: any number, as high as 30, to distinguish multiple cylindrical cores extracted from the same vertebrae of the same animal.

# 4-POINT BENDING: LOAD VS. ACTUATOR
## Specimen:          Aca9_3

| | | |
|---|---|---|
| Data Filter: | Hz | |
| Moment arm: | 0.0381 meters | |
| Spec length: | 0.03545 meters | |
| Yield criterion: | 30% difference of measured slope | |
| | from "linear elastic" slope | |

| | | | |
|---|---|---|---|
| Yield Load: | 4.30E-01 Nm | ENTER VALUE | |
| Ultimate Load: | 6.49E-01 Nm | | |
| Global Stiffness: | 0.305 Nm^2 | CHECK RANGE! | |
| Y-Intercept: | 0.0176 Nm | CHECK RANGE! | |

**Load vs. Actuator Deflection**



Load (Nm)

Actuator Deflection: 2δ/a/L (1/meters)
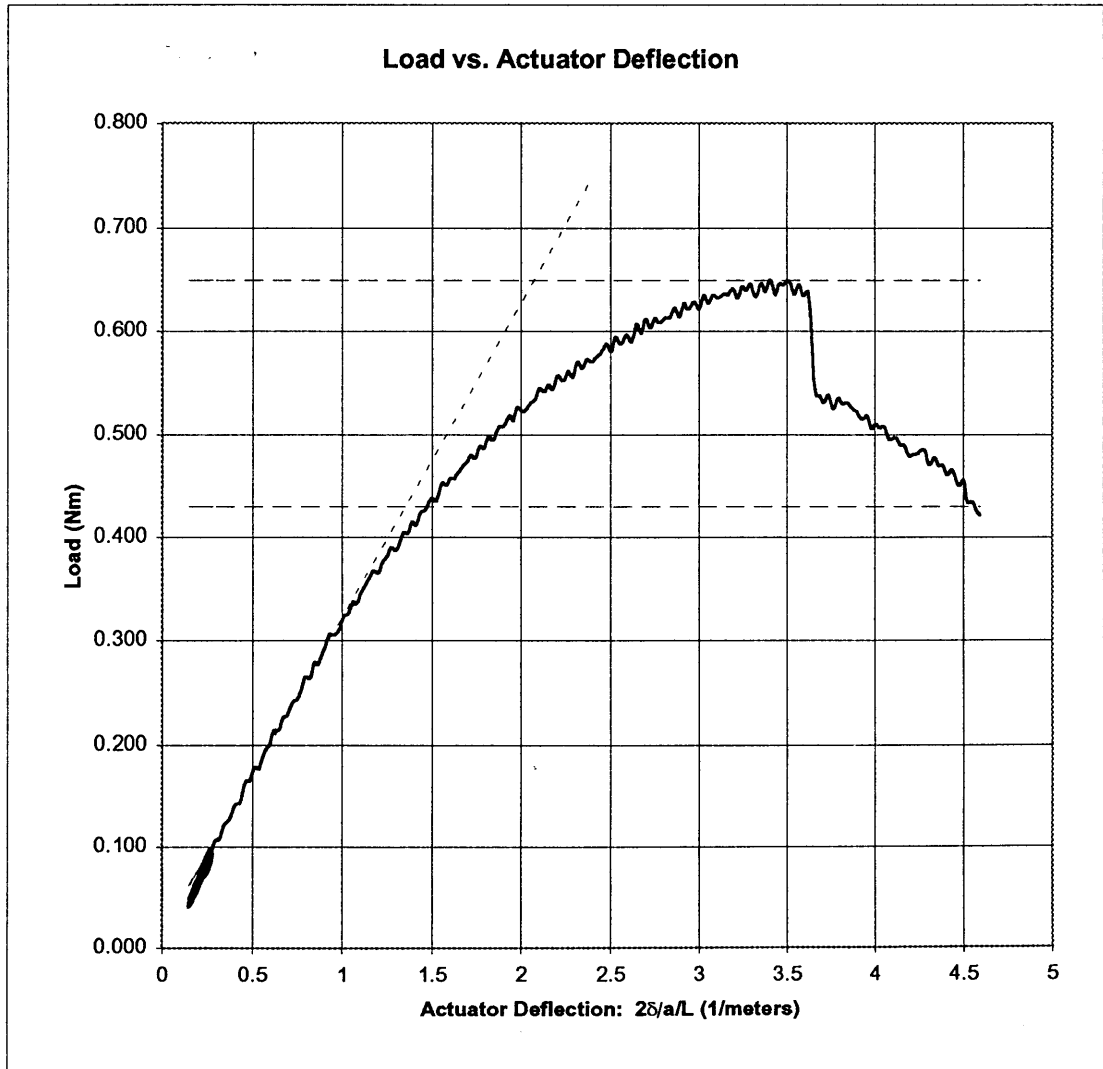
# 4-POINT BENDING: STRAIN DATA

## Specimen: AI6-6

| Yield | |
|---|---|
| Data Point: | 490 |

| | |
|---|---|
| -12642 | 195 |
| -7003 | 291 |
| 0 | 383 |
| 7316 | 301 |
| 12364 | 190 |

| a | -1.14E-06 |
|---|---|
| p | 438596 |
| x of interest | 0 |
| rad of curve | 438596 |
| curvature | 2.28E-06 |
| strain | 1.45% |

**Curvature at Yield**

$$y = -1.14E\text{-}06x^2 - 1.39E\text{-}04x + 3.67E\text{+}02$$
$$R^2 = 9.70E\text{-}01$$

X Position (microns)
Y Position (microns)
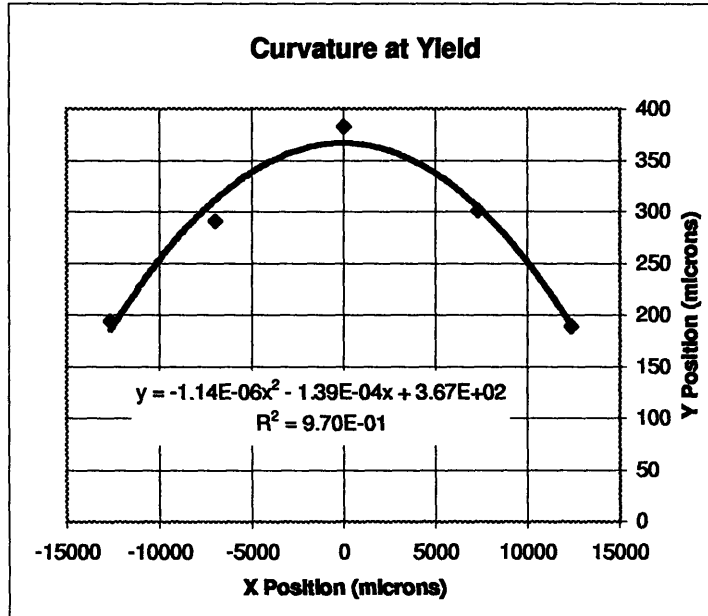
| Ultimate | |
|---|---|
| Data Point: | 827 |

| | |
|---|---|
| -12622 | 447 |
| -6992 | 670 |
| 0 | 871 |
| 7334 | 663 |
| 12384 | 452 |

| a | -2.48E-06 |
|---|---|
| p | 201613 |
| x of interest | 0 |
| rad of curve | 201613 |
| curvature | 4.96E-06 |
| strain | 3.15% |

**Curvature at ~~Yield~~ Ultimate**

$$y = -2.48E\text{-}06x^2 - 2.23E\text{-}04x + 8.26E\text{+}02$$
$$R^2 = 9.65E\text{-}01$$

X Position (microns)
Y Position (microns)
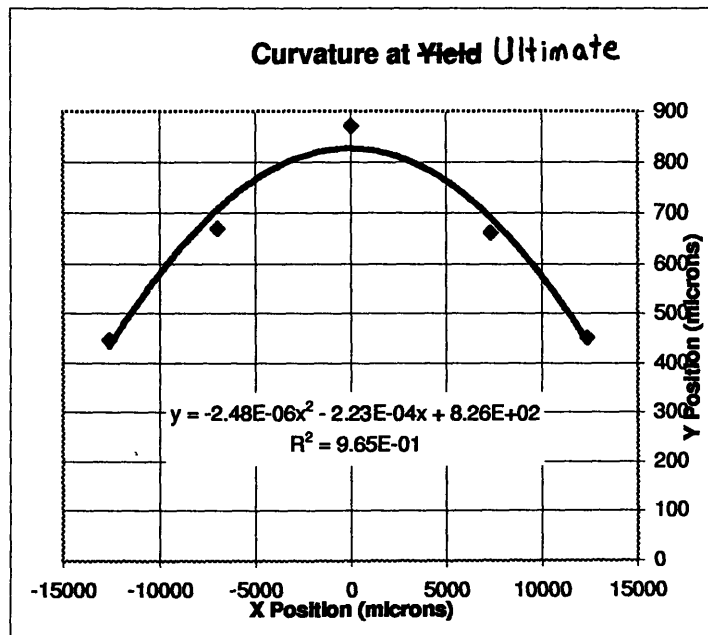
# TENSION:  LOAD VS. STRAIN
## Specimen:        AI8-4

| Data Filter: | . | 1.5 Hz | | |
|---|---|---|---|---|
| Yield criterion: | | 30% difference of measured slope<br>from "linear elastic" slope | | |
| **Stiffness:** | 49489 N | **Y-Intercept:** | 8.6 N | |
| **Yield Load:** | 156 N | **Strain:** | 0.34 % | |
| **Ultmt Load:** | 292 N | **Strain:** | 1.28 % | |
| **Avg. Strain Diff:** | 73% | | | |



## Load vs. Strain
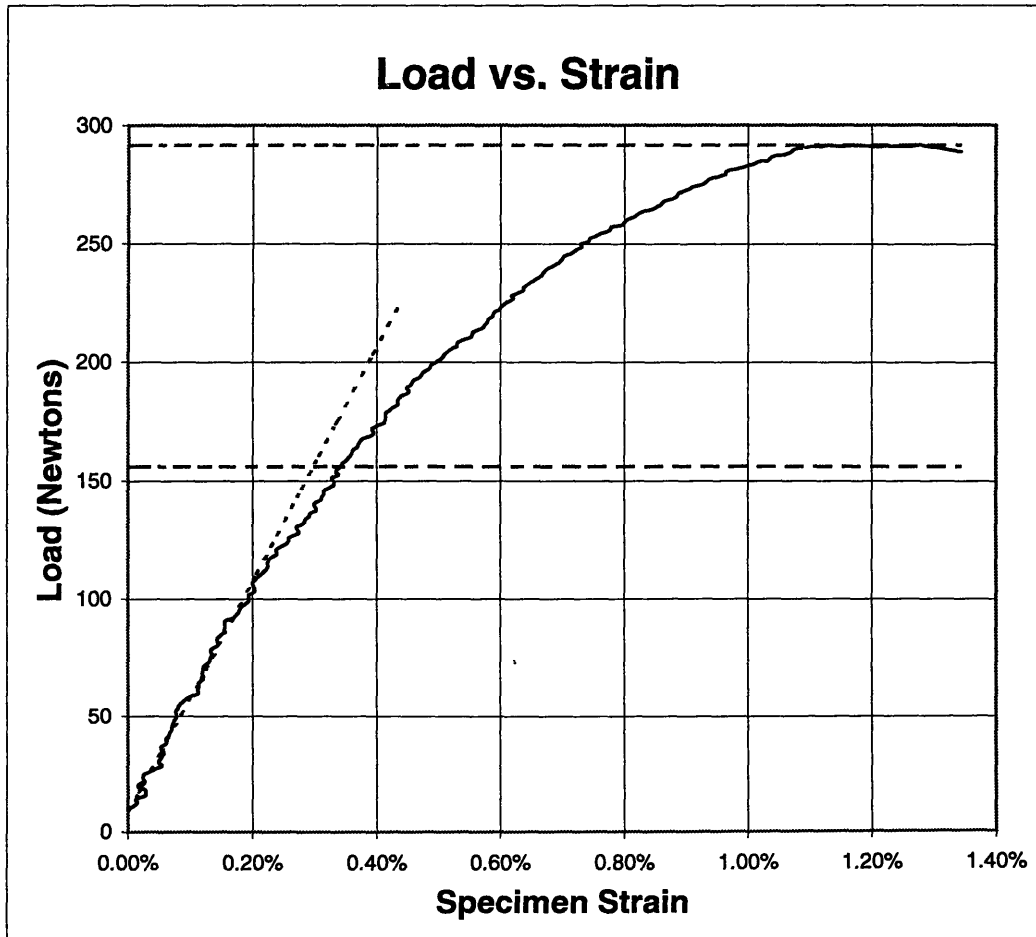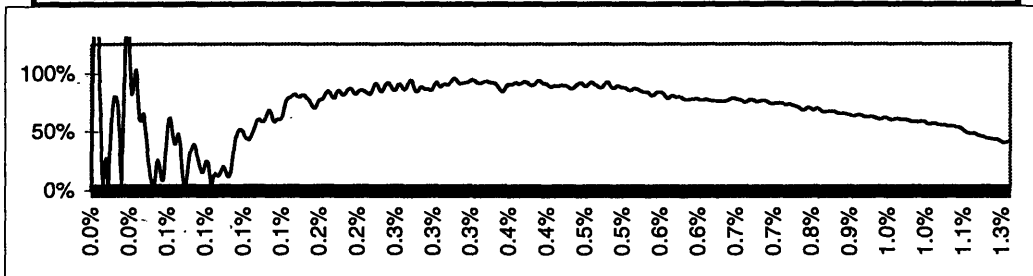
# TORSION: LOAD VS. TWIST

**Specimen:** **AI7-4**

| Data Filter: | None | Hz | |
|---|---|---|---|
| Gage Length: | 0.0244 | meters | |
| Yield criterion: | 30% | difference of measured slope from "linear elastic" slope | |

| Pre-Load: | 0.131 | Nm | |
|---|---|---|---|
| Yield Load/Twist: | 0.203 | Nm | 2.24 rad/m |
| Ultmt Load/Twist: | 0.369 | Nm | 10.21 rad/m |
| Global Stiffness: | 0.079 | Nm^2 | |
| Y-Intercept: | 0.034 | Nm | |

## Torque vs. Twist
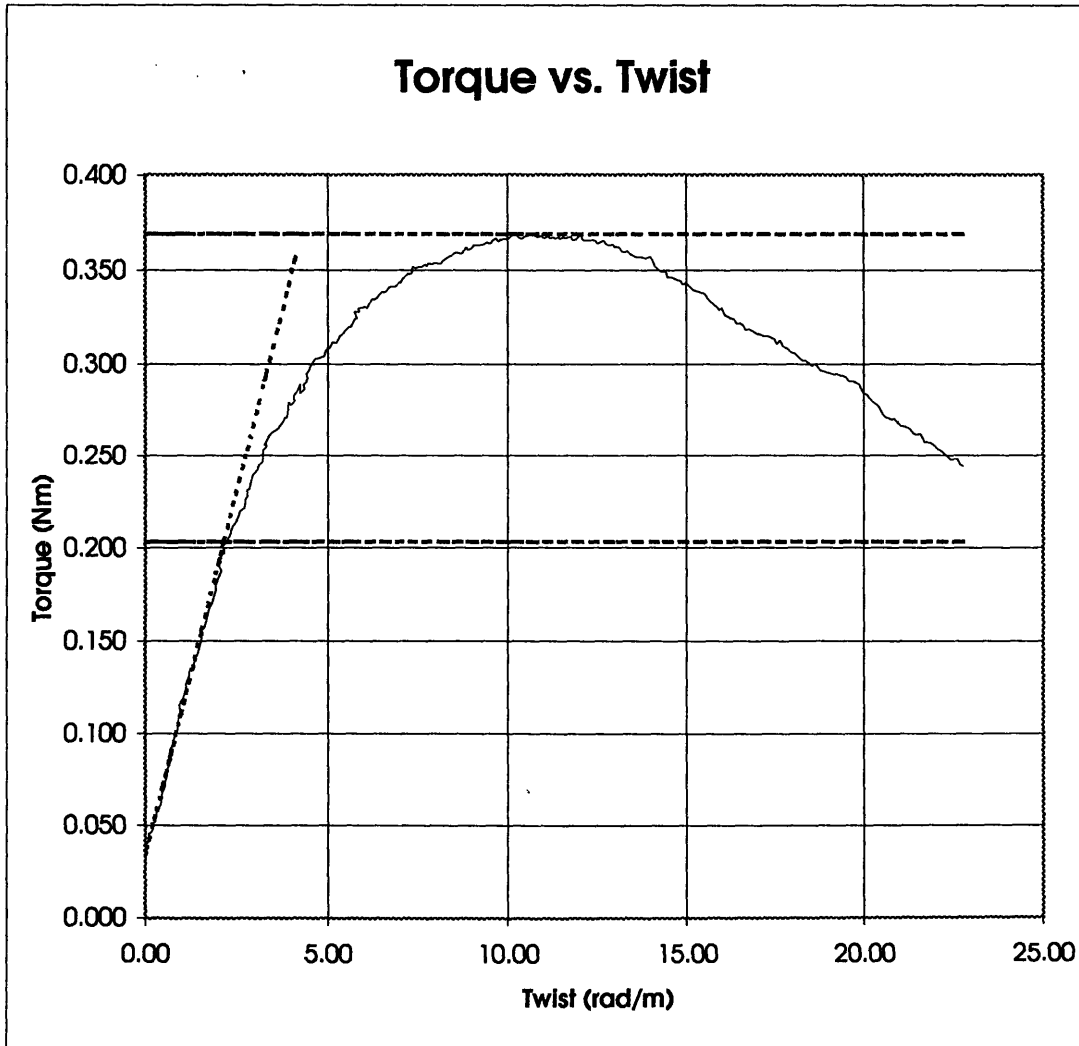
| BENDING | | | | INTACT QCT DATA | | | | | | | |
|---|---|---|---|---|---|---|---|---|---|---|---|
| **SPECIMEN DATA** | | | | **INTACT QCT DATA** | | | | | | | |
| SPECIMEN | Hole Size | E | Length mm | Area (mm^2) Area | Density (g/cc) Avg den | Modulus (GPa) Avg Mod | Axial Rig. (MN) axrig | Ix bar (cm^4) gixbar | EIx bar (Nm^2) ixbar | Polar Mom. (cm^4) Polar mom. | Tor. Rig. (Nm^2) Tors Rig |
| AL6_2 | 0.28 | 1 | 35.22 | 137 | 0.229 | 0.623 | 0.085 | 0.150 | 0.903 | 0.299 | 1.79 |
| BCa1_14 | 0.28 | 1 | 38.17 | 140 | 0.463 | 2.200 | 0.307 | 0.158 | 3.222 | 0.311 | 6.49 |
| CCa1_2 | 0.28 | 1 | 37.17 | 137 | 0.389 | 1.673 | 0.230 | 0.157 | 2.581 | 0.311 | 5.17 |
| CCa1_9 | 0.28 | 1 | 37.54 | 136 | 0.430 | 2.034 | 0.277 | 0.156 | 3.041 | 0.308 | 5.82 |
| DCa4_1 | 0.28 | 1 | 37.60 | 138 | 0.289 | 0.927 | 0.128 | 0.152 | 1.346 | 0.302 | 2.66 |
| ACa9_3 | 0.28 | 2 | 35.45 | 136 | 0.209 | 0.541 | 0.073 | 0.147 | 0.787 | 0.293 | 1.60 |
| BCa1_10 | 0.28 | 2 | 38.44 | 144 | 0.497 | 2.580 | 0.371 | 0.168 | 3.984 | 0.331 | 8.05 |
| BCa1_17 | 0.28 | 2 | 37.96 | 142 | 0.517 | 2.735 | 0.387 | 0.161 | 4.063 | 0.319 | 8.07 |
| BCa1_18 | 0.28 | 2 | 36.76 | 143 | 0.641 | 4.074 | 0.581 | 0.164 | 6.359 | 0.326 | 12.58 |
| ET1_1 | 0.28 | 2 | 36.52 | 139 | 0.476 | 2.356 | 0.328 | 0.154 | 3.041 | 0.309 | 6.58 |
| AL8_7 | 0.47 | 1 | 36.56 | 126 | 0.163 | 0.358 | 0.045 | 0.129 | 0.466 | 0.256 | 0.92 |
| BCa1_24 | 0.47 | 1 | 45.25 | 144 | 0.599 | 3.542 | 0.511 | 0.170 | 5.793 | 0.332 | 11.61 |
| DCa2_2 | 0.47 | 1 | 38.15 | 137 | 0.283 | 0.891 | 0.122 | 0.149 | 1.241 | 0.298 | 2.50 |
| DL3_1 | 0.47 | 1 | 37.15 | 136 | 0.300 | 0.985 | 0.134 | 0.147 | 1.345 | 0.293 | 2.69 |
| DL4_3 | 0.47 | 1 | 38.83 | 136 | 0.293 | 0.949 | 0.129 | 0.150 | 1.384 | 0.296 | 2.68 |
| ACa7_6 | 0.47 | 2 | 37.78 | 133 | 0.188 | 0.455 | 0.060 | 0.140 | 0.625 | 0.280 | 1.27 |
| AL4_2 | 0.47 | 2 | 35.08 | 132 | 0.201 | 0.504 | 0.066 | 0.137 | 0.661 | 0.276 | 1.34 |
| AL6_6 | 0.47 | 2 | 34.54 | 134 | 0.201 | 0.502 | 0.067 | 0.141 | 0.704 | 0.284 | 1.43 |
| DCa2_3 | 0.47 | 2 | 36.76 | 138 | 0.279 | 0.874 | 0.121 | 0.153 | 1.315 | 0.304 | 2.60 |
| FT1_7 | 0.47 | 2 | 37.50 | 144 | 0.850 | 6.694 | 0.962 | 0.167 | 10.170 | 0.329 | 20.13 |
| ACa7_1 | 0.6 | 1 | 37.84 | 135 | 0.222 | 0.602 | 0.081 | 0.147 | 0.855 | 0.294 | 1.73 |
| BCa1_25 | 0.6 | 1 | 38.81 | 142 | 0.535 | 2.943 | 0.419 | 0.162 | 4.349 | 0.323 | 8.91 |
| CCa1_6 | 0.6 | 1 | 38.00 | 138 | 0.447 | 2.158 | 0.297 | 0.156 | 3.360 | 0.313 | 6.40 |
| ET1_4 | 0.6 | 1 | 37.03 | 139 | 0.495 | 2.512 | 0.350 | 0.155 | 3.299 | 0.309 | 6.98 |
| ET1_5 | 0.6 | 1 | 37.89 | 138 | 0.527 | 2.831 | 0.390 | 0.151 | 3.720 | 0.304 | 7.77 |
| ACa9_1 | 0.6 | 2 | 39.21 | 135 | 0.206 | 0.525 | 0.071 | 0.143 | 0.703 | 0.288 | 1.51 |
| AL3_1 | 0.6 | 2 | 34.56 | 129 | 0.202 | 0.507 | 0.065 | 0.136 | 0.687 | 0.266 | 1.34 |
| AL7_3 | 0.6 | 2 | 37.60 | 133 | 0.206 | 0.531 | 0.071 | 0.143 | 0.728 | 0.284 | 1.49 |
| BCa1_28 | 0.6 | 2 | 43.94 | 145 | 0.578 | 3.414 | 0.497 | 0.170 | 5.421 | 0.337 | 11.08 |
| ET1_7 | 0.6 | 2 | 38.20 | 139 | 0.471 | 2.295 | 0.319 | 0.156 | 3.124 | 0.309 | 6.58 |
| ACa9_2 | 0 | 0 | 36.39 | 136 | 0.218 | 0.578 | 0.079 | 0.148 | 0.816 | 0.295 | 1.69 |
| AL8_3 | 0 | 0 | 37.96 | 128 | 0.172 | 0.393 | 0.050 | 0.132 | 0.517 | 0.263 | 1.03 |
| BCa1_26 | 0 | 0 | 44.34 | 143 | 0.505 | 2.594 | 0.371 | 0.165 | 4.273 | 0.326 | 8.49 |
| CCa1_5 | 0 | 0 | 39.45 | 137 | 0.418 | 1.915 | 0.262 | 0.151 | 2.811 | 0.305 | 5.90 |
| DCa4_4 | 0 | 0 | 36.45 | 141 | 0.338 | 1.243 | 0.175 | 0.158 | 1.861 | 0.317 | 3.90 |
| BCa2_5 | 0 | 0 | 36.55 | 141 | 0.477 | 2.391 | 0.336 | 0.159 | 3.465 | 0.317 | 6.98 |
| BCa2_9 | 0 | 0 | 36.89 | 139 | 0.456 | 2.206 | 0.306 | 0.159 | 3.403 | 0.315 | 6.73 |

| BENDING | | | POST-DEFECT QCT DATA | | | | | | | | | |
|---|---|---|---|---|---|---|---|---|---|---|---|---|
| **SPECIMEN DATA** | | | **POST-DEFECT QCT DATA** | | | | | | | | | |
| SPECIMEN | Hole Size | E | Area (mm^2) Area | Density (g/cc) Avg den | Modulus (GPa) Avg Mod | Axial Rig. (MN) axrig | I min (cm^4) gixbar | EI min (Nm^2) ixbar | I max (cm^4) giybar | EI max (Nm^2) iybar | Polar Mom. (cm^4) Polar mom. | Tor. Rig. (Nm^2) Tors Rig |
| AL6_2 | 0.28 | 1 | 102 | 0.216 | 0.575 | 0.059 | 0.099 | 0.545 | 0.142 | 0.780 | 0.241 | 1.325 |
| BCa1_14 | 0.28 | 1 | 107 | 0.438 | 2.088 | 0.223 | 0.105 | 1.942 | 0.150 | 3.245 | 0.255 | 5.186 |
| CCa1_2 | 0.28 | 1 | 110 | 0.379 | 1.620 | 0.177 | 0.114 | 1.695 | 0.145 | 2.600 | 0.258 | 4.294 |
| CCa1_9 | 0.28 | 1 | 110 | 0.363 | 1.524 | 0.167 | 0.121 | 1.650 | 0.140 | 2.265 | 0.261 | 3.915 |
| DCa4_1 | 0.28 | 1 | 93 | 0.266 | 0.819 | 0.077 | 0.086 | 0.666 | 0.137 | 1.106 | 0.223 | 1.772 |
| ACa9_3 | 0.28 | 2 | 92 | 0.234 | 0.657 | 0.060 | 0.079 | 0.508 | 0.145 | 0.929 | 0.223 | 1.436 |
| BCa1_10 | 0.28 | 2 | 96 | 0.483 | 2.478 | 0.239 | 0.091 | 2.088 | 0.151 | 3.656 | 0.242 | 5.744 |
| BCa1_17 | 0.28 | 2 | 93 | 0.462 | 2.303 | 0.214 | 0.081 | 1.618 | 0.149 | 3.378 | 0.230 | 4.996 |
| BCa1_18 | 0.28 | 2 | 104 | 0.588 | 3.579 | 0.372 | 0.100 | 3.176 | 0.159 | 5.591 | 0.259 | 8.767 |
| ET1_1 | 0.28 | 2 | 92 | 0.450 | 2.164 | 0.199 | 0.082 | 1.481 | 0.146 | 3.115 | 0.228 | 4.596 |
| AL8_7 | 0.47 | 1 | 62 | 0.172 | 0.395 | 0.024 | 0.047 | 0.180 | 0.115 | 0.450 | 0.162 | 0.630 |
| BCa1_24 | 0.47 | 1 | 77 | 0.529 | 2.988 | 0.231 | 0.067 | 1.743 | 0.150 | 4.810 | 0.217 | 6.554 |
| DCa2_2 | 0.47 | 1 | 63 | 0.236 | 0.665 | 0.042 | 0.046 | 0.299 | 0.123 | 0.800 | 0.169 | 1.098 |
| DL3_1 | 0.47 | 1 | 66 | 0.257 | 0.772 | 0.051 | 0.050 | 0.349 | 0.127 | 0.994 | 0.177 | 1.343 |
| DL4_3 | 0.47 | 1 | 59 | 0.226 | 0.622 | 0.037 | 0.043 | 0.256 | 0.115 | 0.683 | 0.158 | 0.939 |
| ACa7_6 | 0.47 | 2 | 57 | 0.187 | 0.455 | 0.026 | 0.041 | 0.180 | 0.112 | 0.486 | 0.153 | 0.667 |
| AL4_2 | 0.47 | 2 | 57 | 0.196 | 0.492 | 0.028 | 0.041 | 0.195 | 0.110 | 0.514 | 0.151 | 0.708 |
| AL6_6 | 0.47 | 2 | 56 | 0.183 | 0.434 | 0.024 | 0.039 | 0.166 | 0.113 | 0.498 | 0.152 | 0.664 |
| DCa2_3 | 0.47 | 2 | 64 | 0.273 | 0.863 | 0.055 | 0.050 | 0.410 | 0.128 | 1.081 | 0.178 | 1.491 |
| FT1_7 | 0.47 | 2 | 70 | 0.748 | 5.569 | 0.391 | 0.056 | 2.676 | 0.137 | 7.707 | 0.193 | 10.380 |
| ACa7_1 | 0.6 | 1 | 54 | 0.213 | 0.567 | 0.031 | 0.040 | 0.208 | 0.115 | 0.634 | 0.155 | 0.842 |
| BCa1_25 | 0.6 | 1 | 59 | 0.467 | 2.415 | 0.143 | 0.043 | 0.919 | 0.131 | 3.263 | 0.174 | 4.182 |
| CCa1_6 | 0.6 | 1 | 59 | 0.407 | 1.870 | 0.111 | 0.046 | 0.773 | 0.133 | 2.509 | 0.179 | 3.282 |
| ET1_4 | 0.6 | 1 | 56 | 0.436 | 2.095 | 0.118 | 0.039 | 0.634 | 0.124 | 2.614 | 0.162 | 3.248 |
| ET1_5 | 0.6 | 1 | 57 | 0.451 | 2.294 | 0.130 | 0.038 | 0.711 | 0.120 | 2.739 | 0.158 | 3.449 |
| ACa9_1 | 0.6 | 2 | 43 | 0.202 | 0.524 | 0.022 | 0.026 | 0.131 | 0.099 | 0.486 | 0.125 | 0.616 |
| AL3_1 | 0.6 | 2 | 44 | 0.197 | 0.492 | 0.022 | 0.027 | 0.130 | 0.098 | 0.464 | 0.125 | 0.594 |
| AL7_3 | 0.6 | 2 | 43 | 0.193 | 0.486 | 0.021 | 0.027 | 0.125 | 0.096 | 0.426 | 0.122 | 0.551 |
| BCa1_28 | 0.6 | 2 | 55 | 0.539 | 3.095 | 0.170 | 0.040 | 1.039 | 0.126 | 4.040 | 0.166 | 5.079 |
| ET1_7 | 0.6 | 2 | 52 | 0.416 | 1.934 | 0.100 | 0.035 | 0.564 | 0.117 | 2.298 | 0.152 | 2.862 |
| ACa9_2 | 0 | 0 | 136 | 0.218 | 0.578 | 0.079 | 0.148 | 0.816 | 0.148 | 0.816 | 0.295 | 1.69 |
| AL8_3 | 0 | 0 | 128 | 0.172 | 0.393 | 0.050 | 0.132 | 0.517 | 0.132 | 0.517 | 0.263 | 1.03 |
| BCa1_26 | 0 | 0 | 143 | 0.505 | 2.594 | 0.371 | 0.165 | 4.273 | 0.165 | 4.273 | 0.326 | 8.49 |
| CCa1_5 | 0 | 0 | 137 | 0.418 | 1.915 | 0.262 | 0.151 | 2.811 | 0.151 | 2.811 | 0.305 | 5.90 |
| DCa4_4 | 0 | 0 | 141 | 0.338 | 1.243 | 0.175 | 0.158 | 1.861 | 0.158 | 1.861 | 0.317 | 3.90 |
| BCa2_5 | 0 | 0 | 141 | 0.477 | 2.391 | 0.336 | 0.159 | 3.465 | 0.158 | 3.511 | 0.317 | 6.98 |
| BCa2_9 | 0 | 0 | 139 | 0.456 | 2.206 | 0.306 | 0.159 | 3.403 | 0.156 | 3.329 | 0.315 | 6.73 |

| TENSION | | | INTACT QCT DATA | | | | | | |
|---|---|---|---|---|---|---|---|---|---|
| **SPECIMEN DATA** | | | *INTACT QCT DATA* | | | | | | |
| SPECIMEN | Hole Size | E | Length mm | Area (mm^2) Area | Density (g/cc) Avg den | Modulus (GPa) Avg Mod | Axial Rig. (MN) axrig | Ix bar (cm^4) gixbar | EIx bar (Nm^2) ixbar | Polar Mom. (cm^4) Polar mom. | Tor. Rig. (Nm^2) Tors Rig |

| SPECIMEN | Hole Size | E | Length mm | Area (mm^2) | Density (g/cc) | Modulus (GPa) | Axial Rig. (MN) | Ix bar (cm^4) | EIx bar (Nm^2) | Polar Mom. (cm^4) | Tor. Rig. (Nm^2) |
|---|---|---|---|---|---|---|---|---|---|---|---|
| AL3_6 | 0 | 0 | 32.64 | 136 | 0.220 | 0.586 | 0.080 | 0.148 | 0.851 | 0.295 | 1.68 |
| BCa1_15 | 0 | 0 | 36.89 | 140 | 0.469 | 2.268 | 0.318 | 0.157 | 3.372 | 0.312 | 6.98 |
| BCa2-3 | 0 | 0 | 36.78 | 137 | 0.476 | 2.413 | 0.330 | 0.150 | 3.116 | 0.301 | 6.76 |
| DCa2_5 | 0 | 0 | 38.30 | 139 | 0.295 | 0.965 | 0.135 | 0.155 | 1.505 | 0.310 | 2.94 |
| DCa2_6 | 0 | 0 | 38.06 | 140 | 0.302 | 1.009 | 0.142 | 0.157 | 1.561 | 0.313 | 3.06 |
| FT1_5 | 0 | 0 | 37.03 | 141 | 0.855 | 6.735 | 0.949 | 0.161 | 9.548 | 0.317 | 19.12 |
| AL3_2 | 0.28 | 1 | 33.84 | 128 | 0.211 | 0.548 | 0.070 | 0.128 | 0.686 | 0.269 | 1.48 |
| AL8_4 | 0.28 | 1 | 35.41 | 132 | 0.194 | 0.476 | 0.063 | 0.139 | 0.659 | 0.279 | 1.35 |
| BCa1_19 | 0.28 | 1 | 36.74 | 143 | 0.544 | 2.998 | 0.428 | 0.164 | 4.485 | 0.324 | 9.23 |
| BCa1_29 | 0.28 | 1 | 41.91 | 145 | 0.520 | 2.740 | 0.398 | 0.173 | 4.381 | 0.338 | 8.89 |
| DCa4_3 | 0.28 | 1 | 38.05 | 137 | 0.280 | 0.879 | 0.120 | 0.151 | 1.286 | 0.299 | 2.56 |
| AL6_4 | 0.47 | 1 | 35.54 | 136 | 0.211 | 0.546 | 0.074 | 0.148 | 0.780 | 0.294 | 1.53 |
| BCa1_20 | 0.47 | 1 | 37.32 | 142 | 0.506 | 2.617 | 0.372 | 0.163 | 3.769 | 0.323 | 7.88 |
| BCa1_6 | 0.47 | 1 | 35.83 | 143 | 0.550 | 3.131 | 0.447 | 0.165 | 4.827 | 0.326 | 9.47 |
| DL5_1 | 0.47 | 1 | 37.33 | 135 | 0.261 | 0.778 | 0.105 | 0.145 | 1.072 | 0.290 | 2.12 |
| ACa7_4 | 0.6 | 1 | 35.54 | 136 | 0.209 | 0.538 | 0.073 | 0.148 | 0.825 | 0.295 | 1.57 |
| AL5_3 | 0.6 | 1 | 35.16 | 135 | 0.209 | 0.537 | 0.072 | 0.146 | 0.753 | 0.289 | 1.52 |
| AL8_11 | 0.6 | 1 | 35.50 | 129 | 0.183 | 0.432 | 0.056 | 0.134 | 0.581 | 0.266 | 1.14 |
| BCa1_11 | 0.6 | 1 | 36.99 | 139 | 0.490 | 2.529 | 0.351 | 0.156 | 3.577 | 0.311 | 7.33 |
| ET1_3 | 0.6 | 1 | 37.24 | 141 | 0.664 | 4.266 | 0.600 | 0.159 | 6.187 | 0.315 | 12.27 |
| AL8_10 | 0.28 | 2 | 37.36 | 134 | 0.196 | 0.482 | 0.064 | 0.143 | 0.660 | 0.285 | 1.35 |
| BCa1_7 | 0.28 | 2 | 37.22 | 140 | 0.525 | 2.821 | 0.395 | 0.157 | 4.200 | 0.313 | 8.24 |
| CCa1_12 | 0.28 | 2 | 38.72 | 132 | 0.521 | 2.957 | 0.389 | 0.148 | 4.136 | 0.293 | 8.29 |
| DCa2_4 | 0.28 | 2 | 38.41 | 136 | 0.260 | 0.773 | 0.105 | 0.149 | 1.063 | 0.296 | 2.30 |
| ET1_2 | 0.28 | 2 | 36.92 | 138 | 0.467 | 2.283 | 0.315 | 0.150 | 3.035 | 0.303 | 6.29 |
| ACa8_2 | 0.47 | 2 | 34.76 | 130 | 0.194 | 0.475 | 0.062 | 0.136 | 0.629 | 0.271 | 1.25 |
| AL4_4 | 0.47 | 2 | 33.78 | 133 | 0.191 | 0.463 | 0.061 | 0.141 | 0.642 | 0.279 | 1.28 |
| AL5_2 | 0.47 | 2 | 34.98 | 132 | 0.184 | 0.433 | 0.057 | 0.139 | 0.592 | 0.277 | 1.19 |
| AL8_2 | 0.47 | 2 | 33.48 | 129 | 0.186 | 0.443 | 0.057 | 0.136 | 0.592 | 0.267 | 1.19 |
| CCa1_4 | 0.47 | 2 | 38.66 | 133 | 0.401 | 1.780 | 0.237 | 0.147 | 2.464 | 0.298 | 5.04 |
| AL3_4 | 0.6 | 2 | 32.73 | 133 | 0.208 | 0.535 | 0.071 | 0.142 | 0.741 | 0.283 | 1.47 |
| AL6_3 | 0.6 | 2 | 33.44 | 134 | 0.202 | 0.504 | 0.067 | 0.141 | 0.693 | 0.284 | 1.40 |
| AL7_5 | 0.6 | 2 | 35.84 | 134 | 0.207 | 0.530 | 0.071 | 0.143 | 0.764 | 0.287 | 1.54 |
| BCa1_12 | 0.6 | 2 | 37.64 | 142 | 0.467 | 2.266 | 0.322 | 0.162 | 3.309 | 0.321 | 6.73 |
| FT1_6 | 0.6 | 2 | 37.71 | 141 | 0.787 | 5.738 | 0.810 | 0.160 | 8.449 | 0.318 | 16.72 |

| TENSION | | | POST-DEFECT QCT DATA | | | | | | | | | |
|---|---|---|---|---|---|---|---|---|---|---|---|---|
| **SPECIMEN DATA** | | | **POST-DEFECT QCT DATA** | | | | | | | | | |
| SPECIMEN | Hole Size | E | Area (mm^2) Area | Density (g/cc) Avg den | Modulus (GPa) Avg Mod | Axial Rig. (MN) axrig | I min (cm^4) gixbar | EI min (Nm^2) ixbar | I max (cm^4) giybar | EI max (Nm^2) iybar | Polar Mom. (cm^4) Polar mom. | Tor. Rig. (Nm^2) Tors Rig |
| AL3_6 | 0 | 0 | 136 | 0.220 | 0.586 | 0.080 | 0.148 | 0.851 | 0.148 | 0.851 | 0.295 | 1.68 |
| BCal_15 | 0 | 0 | 140 | 0.469 | 2.268 | 0.318 | 0.157 | 3.372 | 0.157 | 3.372 | 0.312 | 6.98 |
| BCa2-3 | 0 | 0 | 137 | 0.476 | 2.413 | 0.330 | 0.150 | 3.116 | 0.150 | 3.116 | 0.301 | 6.762 |
| DCa2_5 | 0 | 0 | 139 | 0.295 | 0.965 | 0.135 | 0.155 | 1.505 | 0.155 | 1.505 | 0.310 | 2.94 |
| DCa2_6 | 0 | 0 | 140 | 0.302 | 1.009 | 0.142 | 0.157 | 1.561 | 0.157 | 1.561 | 0.313 | 3.06 |
| FT1_5 | 0 | 0 | 141 | 0.855 | 6.735 | 0.949 | 0.161 | 9.548 | 0.161 | 9.548 | 0.317 | 19.12 |
| AL3_2 | 0.28 | 1 | 96 | 0.210 | 0.551 | 0.053 | 0.087 | 0.466 | 0.137 | 0.755 | 0.225 | 1.221 |
| AL8_4 | 0.28 | 1 | 96 | 0.198 | 0.495 | 0.048 | 0.088 | 0.417 | 0.137 | 0.673 | 0.225 | 1.090 |
| BCal_19 | 0.28 | 1 | 111 | 0.486 | 2.516 | 0.279 | 0.113 | 2.566 | 0.154 | 4.244 | 0.268 | 6.809 |
| BCal_29 | 0.28 | 1 | 116 | 0.473 | 2.390 | 0.276 | 0.116 | 2.604 | 0.158 | 4.108 | 0.274 | 6.712 |
| DCa4_3 | 0.28 | 1 | 109 | 0.263 | 0.807 | 0.088 | 0.111 | 0.845 | 0.147 | 1.256 | 0.258 | 2.102 |
| AL6_4 | 0.47 | 1 | 62 | 0.188 | 0.458 | 0.028 | 0.044 | 0.199 | 0.119 | 0.527 | 0.163 | 0.726 |
| BCal_20 | 0.47 | 1 | 78 | 0.466 | 2.370 | 0.185 | 0.065 | 1.228 | 0.148 | 3.616 | 0.213 | 4.844 |
| BCal_6 | 0.47 | 1 | 79 | 0.449 | 2.340 | 0.185 | 0.071 | 1.315 | 0.141 | 3.578 | 0.212 | 4.893 |
| DL5_1 | 0.47 | 1 | 59 | 0.213 | 0.560 | 0.033 | 0.042 | 0.227 | 0.116 | 0.644 | 0.159 | 0.871 |
| ACa7_4 | 0.6 | 1 | 48 | 0.182 | 0.434 | 0.021 | 0.031 | 0.130 | 0.105 | 0.453 | 0.136 | 0.582 |
| AL5_3 | 0.6 | 1 | 52 | 0.190 | 0.468 | 0.024 | 0.034 | 0.143 | 0.111 | 0.543 | 0.145 | 0.686 |
| AL8_11 | 0.6 | 1 | 44 | 0.168 | 0.378 | 0.017 | 0.028 | 0.104 | 0.095 | 0.353 | 0.123 | 0.457 |
| BCal_11 | 0.6 | 1 | 65 | 0.458 | 2.352 | 0.152 | 0.048 | 0.940 | 0.134 | 3.319 | 0.182 | 4.259 |
| ET1_3 | 0.6 | 1 | 57 | 0.569 | 3.415 | 0.193 | 0.039 | 1.095 | 0.125 | 4.376 | 0.163 | 5.471 |
| AL8_10 | 0.28 | 2 | 77 | 0.167 | 0.379 | 0.029 | 0.063 | 0.237 | 0.122 | 0.461 | 0.185 | 0.698 |
| BCal_7 | 0.28 | 2 | 95 | 0.494 | 2.633 | 0.250 | 0.084 | 1.787 | 0.149 | 3.674 | 0.233 | 5.461 |
| CCal_12 | 0.28 | 2 | 93 | 0.483 | 2.660 | 0.247 | 0.086 | 1.911 | 0.143 | 4.045 | 0.228 | 5.956 |
| DCa2_4 | 0.28 | 2 | 89 | 0.265 | 0.816 | 0.073 | 0.079 | 0.637 | 0.141 | 1.140 | 0.220 | 1.776 |
| ET1_2 | 0.28 | 2 | 91 | 0.446 | 2.145 | 0.195 | 0.079 | 1.472 | 0.142 | 2.875 | 0.221 | 4.347 |
| ACa8_2 | 0.47 | 2 | 54 | 0.183 | 0.436 | 0.024 | 0.037 | 0.153 | 0.106 | 0.446 | 0.144 | 0.599 |
| AL4_4 | 0.47 | 2 | 59 | 0.194 | 0.482 | 0.028 | 0.042 | 0.192 | 0.118 | 0.544 | 0.160 | 0.736 |
| AL5_2 | 0.47 | 2 | 54 | 0.166 | 0.371 | 0.020 | 0.037 | 0.142 | 0.107 | 0.395 | 0.144 | 0.537 |
| AL8_2 | 0.47 | 2 | 53 | 0.179 | 0.420 | 0.022 | 0.037 | 0.147 | 0.104 | 0.432 | 0.141 | 0.578 |
| CCal_4 | 0.47 | 2 | 66 | 0.372 | 1.586 | 0.104 | 0.051 | 0.695 | 0.133 | 2.096 | 0.185 | 2.791 |
| AL3_4 | 0.6 | 2 | 45 | 0.204 | 0.529 | 0.024 | 0.028 | 0.142 | 0.101 | 0.520 | 0.129 | 0.661 |
| AL6_3 | 0.6 | 2 | 41 | 0.175 | 0.407 | 0.017 | 0.025 | 0.098 | 0.092 | 0.369 | 0.117 | 0.467 |
| AL7_5 | 0.6 | 2 | 44 | 0.206 | 0.531 | 0.023 | 0.027 | 0.140 | 0.100 | 0.506 | 0.128 | 0.646 |
| BCal_12 | 0.6 | 2 | 53 | 0.436 | 2.078 | 0.109 | 0.036 | 0.639 | 0.120 | 2.395 | 0.156 | 3.035 |
| FT1_6 | 0.6 | 2 | 55 | 0.686 | 4.817 | 0.266 | 0.037 | 1.414 | 0.124 | 6.004 | 0.161 | 7.417 |

| TORSION | | | POST-DEFECT QCT DATA | | | | | | | | | |
|---|---|---|---|---|---|---|---|---|---|---|---|---|
| SPECIMEN DATA | | | POST-DEFECT QCT DATA | | | | | | | | | |
| SPECIMEN | Hole Size | E | Area (mm^2) Area | Density (g/cc) Avg den | Modulus (GPa) Avg Mod | Axial Rig. (MN) axrig | I min (cm^4) gixbar | EI min (Nm^2) ixbar | I max (cm^4) giybar | EI max (Nm^2) iybar | Polar Mom. (cm^4) Polar mom. | Tor. Rig. (Nm^2) Tors Rig |
| ACa7_5 | 0.28 | 1 | 93 | 0.188 | 0.461 | 0.043 | 0.084 | 0.381 | 0.132 | 0.570 | 0.216 | 0.951 |
| BCa1_21 | 0.28 | 1 | 108 | 0.436 | 2.055 | 0.222 | 0.107 | 1.950 | 0.154 | 3.330 | 0.262 | 5.280 |
| DL2_2 | 0.28 | 1 | 95 | 0.222 | 0.597 | 0.057 | 0.085 | 0.477 | 0.134 | 0.779 | 0.219 | 1.256 |
| DL4_1 | 0.28 | 1 | 102 | 0.248 | 0.731 | 0.075 | 0.098 | 0.677 | 0.139 | 1.013 | 0.237 | 1.690 |
| ET1_8 | 0.28 | 1 | 108 | 0.499 | 2.651 | 0.287 | 0.108 | 2.471 | 0.149 | 4.164 | 0.257 | 6.635 |
| AL7_4 | 0.28 | 2 | 81 | 0.181 | 0.431 | 0.035 | 0.066 | 0.276 | 0.123 | 0.496 | 0.189 | 0.772 |
| BCa1_22 | 0.28 | 2 | 95 | 0.475 | 2.370 | 0.225 | 0.089 | 1.972 | 0.148 | 3.434 | 0.238 | 5.406 |
| DL3_2 | 0.28 | 2 | 87 | 0.244 | 0.709 | 0.061 | 0.073 | 0.519 | 0.134 | 0.911 | 0.207 | 1.430 |
| DL4_2 | 0.28 | 2 | 83 | 0.244 | 0.706 | 0.058 | 0.067 | 0.458 | 0.127 | 0.826 | 0.195 | 1.284 |
| FT1_8 | 0.28 | 2 | 105 | 0.733 | 5.354 | 0.561 | 0.102 | 4.728 | 0.154 | 8.176 | 0.256 | 12.900 |
| AL3_7 | 0.47 | 1 | 59 | 0.188 | 0.463 | 0.027 | 0.042 | 0.195 | 0.114 | 0.526 | 0.156 | 0.721 |
| AL7_1 | 0.47 | 1 | 61 | 0.178 | 0.417 | 0.025 | 0.045 | 0.184 | 0.117 | 0.487 | 0.162 | 0.671 |
| AL8_5 | 0.47 | 1 | 61 | 0.188 | 0.455 | 0.028 | 0.045 | 0.197 | 0.119 | 0.535 | 0.164 | 0.733 |
| BCa1_13 | 0.47 | 1 | 74 | 0.458 | 2.264 | 0.167 | 0.062 | 1.205 | 0.141 | 3.263 | 0.204 | 4.467 |
| CCa1_13 | 0.47 | 1 | 70 | 0.369 | 1.563 | 0.109 | 0.054 | 0.759 | 0.138 | 2.253 | 0.192 | 3.011 |
| DL2_1 | 0.47 | 1 | 64 | 0.264 | 0.816 | 0.052 | 0.048 | 0.349 | 0.125 | 1.046 | 0.174 | 1.394 |
| ACa7_3 | 0.47 | 2 | 56 | 0.189 | 0.466 | 0.026 | 0.041 | 0.196 | 0.114 | 0.519 | 0.155 | 0.715 |
| AL5_1 | 0.47 | 2 | 60 | 0.189 | 0.458 | 0.027 | 0.044 | 0.202 | 0.118 | 0.526 | 0.162 | 0.727 |
| AL5_5 | 0.47 | 2 | 55 | 0.187 | 0.452 | 0.025 | 0.038 | 0.164 | 0.108 | 0.454 | 0.146 | 0.619 |
| BCa1_3 | 0.47 | 2 | 70 | 0.461 | 2.362 | 0.166 | 0.057 | 1.140 | 0.137 | 3.179 | 0.195 | 4.319 |
| DL2_3 | 0.47 | 2 | 57 | 0.224 | 0.613 | 0.035 | 0.042 | 0.239 | 0.112 | 0.672 | 0.154 | 0.911 |
| ACa8_1 | 0.6 | 1 | 49 | 0.178 | 0.415 | 0.020 | 0.031 | 0.127 | 0.107 | 0.438 | 0.138 | 0.564 |
| BCa1_8 | 0.6 | 1 | 55 | 0.428 | 2.056 | 0.112 | 0.036 | 0.692 | 0.122 | 2.496 | 0.158 | 3.187 |
| CCa1_1 | 0.6 | 1 | 55 | 0.398 | 1.792 | 0.098 | 0.039 | 0.571 | 0.122 | 2.237 | 0.161 | 2.808 |
| CCa1_14 | 0.6 | 1 | 54 | 0.368 | 1.552 | 0.083 | 0.039 | 0.558 | 0.120 | 1.861 | 0.159 | 2.419 |
| DL5_2 | 0.6 | 1 | 47 | 0.226 | 0.623 | 0.029 | 0.029 | 0.176 | 0.105 | 0.640 | 0.134 | 0.816 |
| AL7_2 | 0.6 | 2 | 43 | 0.198 | 0.503 | 0.021 | 0.026 | 0.122 | 0.096 | 0.445 | 0.122 | 0.567 |
| BCa1_1 | 0.6 | 2 | 52 | 0.450 | 2.245 | 0.117 | 0.036 | 0.633 | 0.116 | 2.558 | 0.152 | 3.190 |
| BCa1_16 | 0.6 | 2 | 53 | 0.526 | 2.985 | 0.160 | 0.037 | 0.924 | 0.121 | 3.616 | 0.158 | 4.540 |
| BCa1_5 | 0.6 | 2 | 54 | 0.457 | 2.313 | 0.124 | 0.039 | 0.685 | 0.121 | 2.833 | 0.160 | 3.518 |
| FT1_1 | 0.6 | 2 | 56 | 0.696 | 4.912 | 0.275 | 0.040 | 1.616 | 0.126 | 6.238 | 0.165 | 7.854 |
| AL3_5 | 0 | 0 | 134 | 0.208 | 0.533 | 0.071 | 0.141 | 0.726 | 0.141 | 0.726 | 0.285 | 1.52 |
| AL8_9 | 0 | 0 | 129 | 0.179 | 0.418 | 0.054 | 0.135 | 0.563 | 0.135 | 0.563 | 0.269 | 1.13 |
| BCa1_9 | 0 | 0 | 137 | 0.543 | 3.035 | 0.417 | 0.150 | 4.278 | 0.150 | 4.278 | 0.304 | 8.77 |
| DCa3_2 | 0 | 0 | 137 | 0.261 | 0.784 | 0.107 | 0.149 | 1.134 | 0.149 | 1.134 | 0.300 | 2.38 |
| DCa3_6 | 0 | 0 | 138 | 0.270 | 0.824 | 0.113 | 0.151 | 1.208 | 0.151 | 1.208 | 0.301 | 2.41 |
| BCa2_10 | 0 | 0 | 138 | 0.454 | 2.199 | 0.303 | 0.158 | 3.133 | 0.158 | 3.133 | 0.309 | 6.37 |
| BCa2_6 | 0 | 0 | 137 | 0.454 | 2.168 | 0.298 | 0.152 | 3.119 | 0.152 | 3.119 | 0.303 | 6.19 |
| CCa1_7 | 0 | 0 | 138 | 0.640 | 3.979 | 0.550 | 0.147 | 5.669 | 0.147 | 5.669 | 0.306 | 11.74 |
| CCa1_11 | 0 | 0 | 141 | 0.437 | 2.074 | 0.292 | 0.161 | 3.161 | 0.161 | 3.161 | 0.326 | 6.85 |
| ET1_21 | 0 | 0 | 143 | 0.641 | 3.963 | 0.567 | 0.160 | 6.063 | 0.160 | 6.063 | 0.326 | 12.47 |
| FT1_2 | 0 | 0 | 143 | 0.953 | 7.461 | 1.065 | 0.162 | 11.210 | 0.162 | 11.210 | 0.325 | 22.93 |
| FT1_4 | 0 | 0 | 143 | 1.031 | 8.519 | 1.216 | 0.162 | 12.640 | 0.162 | 12.640 | 0.325 | 25.50 |

# BENDING Stress Concentration Calculations

| SPECIMEN DATA | | | B-E Reductions | | | | UNIT FEM | | |
|---|---|---|---|---|---|---|---|---|---|
| SPECIMEN | Hole Size | E | d/D | Ix / Ix | Ix bar (cm^4) gixbar | EIx bar (Nm^2) ixbar | Model | Stress | K stress |
| AL6_2 | 0.28 | 1 | 0.72 | 0.54 | 0.0811 | 0.488 | ben30e1 | 2.59E-02 | 1.88 |
| BCa1_14 | 0.28 | 1 | 0.72 | 0.54 | 0.0851 | 1.740 | ben30e1 | 2.59E-02 | 1.88 |
| CCa1_2 | 0.28 | 1 | 0.72 | 0.54 | 0.0847 | 1.394 | ben30e1 | 2.59E-02 | 1.88 |
| CCa1_9 | 0.28 | 1 | 0.72 | 0.54 | 0.0840 | 1.642 | ben30e1 | 2.59E-02 | 1.88 |
| DCa4_1 | 0.28 | 1 | 0.72 | 0.54 | 0.0822 | 0.727 | ben30e1 | 2.59E-02 | 1.88 |
| ACa9_3 | 0.28 | 2 | 0.72 | 0.54 | 0.0794 | 0.425 | ben30e2 | 2.18E-02 | 1.58 |
| BCa1_10 | 0.28 | 2 | 0.72 | 0.54 | 0.0906 | 2.151 | ben30e2 | 2.18E-02 | 1.58 |
| BCa1_17 | 0.28 | 2 | 0.72 | 0.54 | 0.0871 | 2.194 | ben30e2 | 2.18E-02 | 1.58 |
| BCa1_18 | 0.28 | 2 | 0.72 | 0.54 | 0.0888 | 3.434 | ben30e2 | 2.18E-02 | 1.58 |
| ET1_1 | 0.28 | 2 | 0.72 | 0.54 | 0.0833 | 1.642 | ben30e2 | 2.18E-02 | 1.58 |
| AL8_7 | 0.47 | 1 | 0.53 | 0.29 | 0.0374 | 0.135 | ben45e1 | 3.99E-02 | 1.55 |
| BCa1_24 | 0.47 | 1 | 0.53 | 0.29 | 0.0492 | 1.680 | ben45e1 | 3.99E-02 | 1.55 |
| DCa2_2 | 0.47 | 1 | 0.53 | 0.29 | 0.0432 | 0.360 | ben45e1 | 3.99E-02 | 1.55 |
| DL3_1 | 0.47 | 1 | 0.53 | 0.29 | 0.0425 | 0.390 | ben45e1 | 3.99E-02 | 1.55 |
| DL4_3 | 0.47 | 1 | 0.53 | 0.29 | 0.0436 | 0.401 | ben45e1 | 3.99E-02 | 1.55 |
| ACa7_6 | 0.47 | 2 | 0.53 | 0.29 | 0.0405 | 0.181 | ben45e2 | 3.73E-02 | 1.45 |
| AL4_2 | 0.47 | 2 | 0.53 | 0.29 | 0.0398 | 0.192 | ben45e2 | 3.73E-02 | 1.45 |
| AL6_6 | 0.47 | 2 | 0.53 | 0.29 | 0.0409 | 0.204 | ben45e2 | 3.73E-02 | 1.45 |
| DCa2_3 | 0.47 | 2 | 0.53 | 0.29 | 0.0445 | 0.381 | ben45e2 | 3.73E-02 | 1.45 |
| FT1_7 | 0.47 | 2 | 0.53 | 0.29 | 0.0484 | 2.949 | ben45e2 | 3.73E-02 | 1.45 |
| ACa7_1 | 0.6 | 1 | 0.4 | 0.19 | 0.0279 | 0.163 | ben56e1 | 5.53E-02 | 1.41 |
| BCa1_25 | 0.6 | 1 | 0.4 | 0.19 | 0.0307 | 0.826 | ben56e1 | 5.53E-02 | 1.41 |
| CCa1_6 | 0.6 | 1 | 0.4 | 0.19 | 0.0297 | 0.638 | ben56e1 | 5.53E-02 | 1.41 |
| ET1_4 | 0.6 | 1 | 0.4 | 0.19 | 0.0295 | 0.627 | ben56e1 | 5.53E-02 | 1.41 |
| ET1_5 | 0.6 | 1 | 0.4 | 0.19 | 0.0287 | 0.707 | ben56e1 | 5.53E-02 | 1.41 |
| ACa9_1 | 0.6 | 2 | 0.4 | 0.19 | 0.0271 | 0.133 | ben56e2 | 9.97E-02 | 2.54 |
| AL3_1 | 0.6 | 2 | 0.4 | 0.19 | 0.0259 | 0.131 | ben56e2 | 9.97E-02 | 2.54 |
| AL7_3 | 0.6 | 2 | 0.4 | 0.19 | 0.0271 | 0.138 | ben56e2 | 9.97E-02 | 2.54 |
| BCa1_28 | 0.6 | 2 | 0.4 | 0.19 | 0.0324 | 1.030 | ben56e2 | 9.97E-02 | 2.54 |
| ET1_7 | 0.6 | 2 | 0.4 | 0.19 | 0.0295 | 0.594 | ben56e2 | 9.97E-02 | 2.54 |
| ACa9_2 | 0 | 0 | 1 | 1 | 0.1480 | 0.816 | ben0 | 7.46E-03 | 1.00 |
| AL8_3 | 0 | 0 | 1 | 1 | 0.1324 | 0.517 | ben0 | 7.46E-03 | 1.00 |
| BCa1_26 | 0 | 0 | 1 | 1 | 0.1645 | 4.273 | ben0 | 7.46E-03 | 1.00 |
| CCa1_5 | 0 | 0 | 1 | 1 | 0.1513 | 2.811 | ben0 | 7.46E-03 | 1.00 |
| DCa4_4 | 0 | 0 | 1 | 1 | 0.1581 | 1.861 | ben0 | 7.46E-03 | 1.00 |
| BCa2_5 | 0 | 0 | 1 | 1 | 0.1593 | 3.465 | ben0 | 7.46E-03 | 1.00 |
| BCa2_9 | 0 | 0 | 1 | 1 | 0.1590 | 3.403 | ben0 | 7.46E-03 | 1.00 |

# TENSION | Stress Concentration Calculations

| SPECIMEN DATA | | | B-E Reductions | | | | UNIT FEM | | |
|---|---|---|---|---|---|---|---|---|---|
| SPECIMEN | Hole Size | E | d/D | A/A | Area (mm^2) Area | Axial Rig. (MN) axrig | Model | Stress | K Stress |
| | | | | | | | | | |
| AL3_6 | 0 | 0 | 1 | 1 | 136 | 0.0797 | ten0 | 1.97E-06 | 1.00 |
| BCal_15 | 0 | 0 | 1 | 1 | 140 | 0.3175 | ten0 | 1.97E-06 | 1.00 |
| BCa2-3 | 0 | 0 | 1 | 1 | 137 | 0.3296 | ten0 | 1.97E-06 | 1.00 |
| DCa2_5 | 0 | 0 | 1 | 1 | 139 | 0.1345 | ten0 | 1.97E-06 | 1.00 |
| DCa2_6 | 0 | 0 | 1 | 1 | 140 | 0.1416 | ten0 | 1.97E-06 | 1.00 |
| FT1_5 | 0 | 0 | 1 | 1 | 141 | 0.9490 | ten0 | 1.97E-06 | 1.00 |
| AL3_2 | 0.28 | 1 | 0.72 | 0.65 | 83 | 0.0457 | ten30e1 | 7.48E-06 | 2.46 |
| AL8_4 | 0.28 | 1 | 0.72 | 0.65 | 86 | 0.0409 | ten30e1 | 7.48E-06 | 2.46 |
| BCal_19 | 0.28 | 1 | 0.72 | 0.65 | 93 | 0.2779 | ten30e1 | 7.48E-06 | 2.46 |
| BCal_29 | 0.28 | 1 | 0.72 | 0.65 | 95 | 0.2590 | ten30e1 | 7.48E-06 | 2.46 |
| DCa4_3 | 0.28 | 1 | 0.72 | 0.65 | 89 | 0.0783 | ten30e1 | 7.48E-06 | 2.46 |
| AL6_4 | 0.47 | 1 | 0.53 | 0.42 | 57 | 0.0311 | ten45e1 | 1.07E-05 | 2.28 |
| BCal_20 | 0.47 | 1 | 0.53 | 0.42 | 60 | 0.1563 | ten45e1 | 1.07E-05 | 2.28 |
| BCal_6 | 0.47 | 1 | 0.53 | 0.42 | 60 | 0.1876 | ten45e1 | 1.07E-05 | 2.28 |
| DL5_1 | 0.47 | 1 | 0.53 | 0.42 | 57 | 0.0441 | ten45e1 | 1.07E-05 | 2.28 |
| ACa7_4 | 0.6 | 1 | 0.4 | 0.33 | 45 | 0.0242 | ten56e1 | 1.39E-05 | 2.32 |
| AL5_3 | 0.6 | 1 | 0.4 | 0.33 | 44 | 0.0239 | ten56e1 | 1.39E-05 | 2.32 |
| AL8_11 | 0.6 | 1 | 0.4 | 0.33 | 43 | 0.0184 | ten56e1 | 1.39E-05 | 2.32 |
| BCal_11 | 0.6 | 1 | 0.4 | 0.33 | 46 | 0.1159 | ten56e1 | 1.39E-05 | 2.32 |
| ET1_3 | 0.6 | 1 | 0.4 | 0.33 | 46 | 0.1978 | ten56e1 | 1.39E-05 | 2.32 |
| AL8_10 | 0.28 | 2 | 0.72 | 0.65 | 87 | 0.0419 | ten30e2 | 1.16E-05 | 3.82 |
| BCal_7 | 0.28 | 2 | 0.72 | 0.65 | 91 | 0.2569 | ten30e2 | 1.16E-05 | 3.82 |
| CCal_12 | 0.28 | 2 | 0.72 | 0.65 | 85 | 0.2528 | ten30e2 | 1.16E-05 | 3.82 |
| DCa2_4 | 0.28 | 2 | 0.72 | 0.65 | 89 | 0.0685 | ten30e2 | 1.16E-05 | 3.82 |
| ET1_2 | 0.28 | 2 | 0.72 | 0.65 | 90 | 0.2044 | ten30e2 | 1.16E-05 | 3.82 |
| ACa8_2 | 0.47 | 2 | 0.53 | 0.42 | 55 | 0.0260 | ten45e2 | 2.04E-05 | 4.34 |
| AL4_4 | 0.47 | 2 | 0.53 | 0.42 | 56 | 0.0257 | ten45e2 | 2.04E-05 | 4.34 |
| AL5_2 | 0.47 | 2 | 0.53 | 0.42 | 55 | 0.0240 | ten45e2 | 2.04E-05 | 4.34 |
| AL8_2 | 0.47 | 2 | 0.53 | 0.42 | 54 | 0.0240 | ten45e2 | 2.04E-05 | 4.34 |
| CCal_4 | 0.47 | 2 | 0.53 | 0.42 | 56 | 0.0995 | ten45e2 | 2.04E-05 | 4.34 |
| AL3_4 | 0.6 | 2 | 0.4 | 0.33 | 44 | 0.0235 | ten56e2 | 4.48E-05 | 7.49 |
| AL6_3 | 0.6 | 2 | 0.4 | 0.33 | 44 | 0.0222 | ten56e2 | 4.48E-05 | 7.49 |
| AL7_5 | 0.6 | 2 | 0.4 | 0.33 | 44 | 0.0235 | ten56e2 | 4.48E-05 | 7.49 |
| BCal_12 | 0.6 | 2 | 0.4 | 0.33 | 47 | 0.1061 | ten56e2 | 4.48E-05 | 7.49 |
| FT1_6 | 0.6 | 2 | 0.4 | 0.33 | 47 | 0.2674 | ten56e2 | 4.48E-05 | 7.49 |

# TORSION STRESS CONCENTRATIONS

| SPECIMEN DATA | | | B-E Reductions | | | | UNIT FEM | | |
|---|---|---|---|---|---|---|---|---|---|
| SPECIMEN | Hole Size | E | d/D | J /J | Polar Mom. (cm^4) Polar mom. | Tor. Rig. (Nm^2) Tors Rig | Model | Stress | K stress |
| | | | | | | | | | |
| ACa7_5 | 0.28 | 1 | 0.72 | 0.75 | 0.203 | 0.935 | tor30e1 | 4.72E-03 | 2.19 |
| BCa1_21 | 0.28 | 1 | 0.72 | 0.75 | 0.243 | 5.635 | tor30e1 | 4.72E-03 | 2.19 |
| DL2_2 | 0.28 | 1 | 0.72 | 0.75 | 0.221 | 1.637 | tor30e1 | 4.72E-03 | 2.19 |
| DL4_1 | 0.28 | 1 | 0.72 | 0.75 | 0.218 | 1.655 | tor30e1 | 4.72E-03 | 2.19 |
| ET1_8 | 0.28 | 1 | 0.72 | 0.75 | 0.236 | 7.358 | tor30e1 | 4.72E-03 | 2.19 |
| AL7_4 | 0.28 | 2 | 0.72 | 0.75 | 0.195 | 0.764 | tor30e2 | 6.16E-03 | 2.85 |
| BCa1_22 | 0.28 | 2 | 0.72 | 0.75 | 0.237 | 5.087 | tor30e2 | 6.16E-03 | 2.85 |
| DL3_2 | 0.28 | 2 | 0.72 | 0.75 | 0.214 | 1.567 | tor30e2 | 6.16E-03 | 2.85 |
| DL4_2 | 0.28 | 2 | 0.72 | 0.75 | 0.201 | 1.247 | tor30e2 | 6.16E-03 | 2.85 |
| FT1_8 | 0.28 | 2 | 0.72 | 0.75 | 0.237 | 13.433 | tor30e2 | 6.16E-03 | 2.85 |
| AL3_7 | 0.47 | 1 | 0.53 | 0.56 | 0.157 | 0.803 | tor45e1 | 6.02E-03 | 2.08 |
| AL7_1 | 0.47 | 1 | 0.53 | 0.56 | 0.147 | 0.613 | tor45e1 | 6.02E-03 | 2.08 |
| AL8_5 | 0.47 | 1 | 0.53 | 0.56 | 0.151 | 0.633 | tor45e1 | 6.02E-03 | 2.08 |
| BCa1_13 | 0.47 | 1 | 0.53 | 0.56 | 0.175 | 3.875 | tor45e1 | 6.02E-03 | 2.08 |
| CCa1_13 | 0.47 | 1 | 0.53 | 0.56 | 0.159 | 2.471 | tor45e1 | 6.02E-03 | 2.08 |
| DL2_1 | 0.47 | 1 | 0.53 | 0.56 | 0.159 | 1.457 | tor45e1 | 6.02E-03 | 2.08 |
| ACa7_3 | 0.47 | 2 | 0.53 | 0.56 | 0.165 | 1.001 | tor45e2 | 1.07E-02 | 3.70 |
| AL5_1 | 0.47 | 2 | 0.53 | 0.56 | 0.154 | 0.683 | tor45e2 | 1.07E-02 | 3.70 |
| AL5_5 | 0.47 | 2 | 0.53 | 0.56 | 0.152 | 0.629 | tor45e2 | 1.07E-02 | 3.70 |
| BCa1_3 | 0.47 | 2 | 0.53 | 0.56 | 0.172 | 3.798 | tor45e2 | 1.07E-02 | 3.70 |
| DL2_3 | 0.47 | 2 | 0.53 | 0.56 | 0.164 | 1.196 | tor45e2 | 1.07E-02 | 3.70 |
| ACa8_1 | 0.6 | 1 | 0.4 | 0.46 | 0.132 | 0.616 | tor56e1 | 7.23E-03 | 2.05 |
| BCa1_8 | 0.6 | 1 | 0.4 | 0.46 | 0.138 | 3.133 | tor56e1 | 7.23E-03 | 2.05 |
| CCa1_1 | 0.6 | 1 | 0.4 | 0.46 | 0.145 | 2.861 | tor56e1 | 7.23E-03 | 2.05 |
| CCa1_14 | 0.6 | 1 | 0.4 | 0.46 | 0.137 | 2.047 | tor56e1 | 7.23E-03 | 2.05 |
| DL5_2 | 0.6 | 1 | 0.4 | 0.46 | 0.135 | 0.971 | tor56e1 | 7.23E-03 | 2.05 |
| AL7_2 | 0.6 | 2 | 0.4 | 0.46 | 0.136 | 0.742 | tor56e2 | 3.23E-02 | 9.19 |
| BCa1_1 | 0.6 | 2 | 0.4 | 0.46 | 0.144 | 2.962 | tor56e2 | 3.23E-02 | 9.19 |
| BCa1_16 | 0.6 | 2 | 0.4 | 0.46 | 0.141 | 3.844 | tor56e2 | 3.23E-02 | 9.19 |
| BCa1_5 | 0.6 | 2 | 0.4 | 0.46 | 0.150 | 3.770 | tor56e2 | 3.23E-02 | 9.19 |
| FT1_1 | 0.6 | 2 | 0.4 | 0.46 | 0.150 | 8.091 | tor56e2 | 3.23E-02 | 9.19 |
| AL3_5 | 0 | 0 | 1 | 1 | 0.285 | 1.523 | tor0 | 1.62E-03 | 1.00 |
| AL8_9 | 0 | 0 | 1 | 1 | 0.269 | 1.134 | tor0 | 1.62E-03 | 1.00 |
| BCa1_9 | 0 | 0 | 1 | 1 | 0.304 | 8.772 | tor0 | 1.62E-03 | 1.00 |
| DCa3_2 | 0 | 0 | 1 | 1 | 0.300 | 2.380 | tor0 | 1.62E-03 | 1.00 |
| DCa3_6 | 0 | 0 | 1 | 1 | 0.301 | 2.408 | tor0 | 1.62E-03 | 1.00 |
| BCa2_10 | 0 | 0 | 1 | 1 | 0.309 | 6.369 | tor0 | 1.62E-03 | 1.00 |
| BCa2_6 | 0 | 0 | 1 | 1 | 0.303 | 6.190 | tor0 | 1.62E-03 | 1.00 |
| CCa1_7 | 0 | 0 | 1 | 1 | 0.306 | 11.740 | tor0 | 1.62E-03 | 1.00 |
| CCa1_11 | 0 | 0 | 1 | 1 | 0.326 | 6.853 | tor0 | 1.62E-03 | 1.00 |
| ET1_21 | 0 | 0 | 1 | 1 | 0.326 | 12.470 | tor0 | 1.62E-03 | 1.00 |
| FT1_2 | 0 | 0 | 1 | 1 | 0.325 | 22.930 | tor0 | 1.62E-03 | 1.00 |
| FT1_4 | 0 | 0 | 1 | 1 | 0.325 | 25.500 | tor0 | 1.62E-03 | 1.00 |

# BENDING | | | Mechanical Test Data

| SPECIMEN DATA | | | MECHANICAL TESTS | | Acutal Strains | | | | | |
|---|---|---|---|---|---|---|---|---|---|---|
| | | | Calculations | | | | | | | |
| SPECIMEN | Hole Size | E | Yield Stn Calc % Strain | Ult Stn Calc % Strain | Yield Strain % Strain | Ult. Strain % Strain | Pre-Load Nm | Rigidity Nm^2 | Yield Load Nm | Ult. Load Nm |
| AL6_2 | 0.28 | 1 | 1.05 | 1.97 | 1.3 | 2.4 | 0.12 | 0.344 | 0.523 | 0.653 |
| BCa1_14 | 0.28 | 1 | 0.93 | 1.15 | 1.0 | 1.3 | 0.25 | 1.681 | 2.7 | 3.04 |
| CCa1_2 | 0.28 | 1 | 0.78 | 1.56 | 1.0 | 1.9 | 0.45 | 1.307 | 1.83 | 2.24 |
| CCa1_9 | 0.28 | 1 | 0.8 | 1.42 | 1.0 | 1.8 | 0.60 | 1.789 | 2.51 | 2.88 |
| DCa4_1 | 0.28 | 1 | 0.54 | 0.87 | 0.8 | 1.3 | 0.30 | 0.636 | 0.661 | 0.727 |
| ACa9_3 | 0.28 | 2 | 1.17 | 3.52 | 1.4 | 4.1 | 0.08 | 0.305 | 0.43 | 0.649 |
| BCa1_10 | 0.28 | 2 | 0.87 | 1.2 | 1.1 | 1.5 | 0.50 | 1.394 | 2.2 | 2.48 |
| BCa1_17 | 0.28 | 2 | 0.62 | ■ | 0.8 | ■ | 0.45 | 1.224 | 1.88 | 2.24 |
| BCa1_18 | 0.28 | 2 | 1.02 | 1.64 | 1.2 | 2.0 | 0.75 | 1.774 | 3.82 | 4.43 |
| ET1_1 | 0.28 | 2 | 0.56 | 0.95 | 0.7 | 1.2 | 0.60 | 1.924 | 1.95 | 2.24 |
| AL8_7 | 0.47 | 1 | 1.04 | 2.43 | 1.3 | 3.0 | 0.05 | 0.184 | 0.202 | 0.263 |
| BCa1_24 | 0.47 | 1 | 0.94 | 1.41 | 1.1 | 1.7 | 0.40 | 1.87 | 2.1 | 2.5 |
| DCa2_2 | 0.47 | 1 | 0.54 | 0.92 | 0.8 | 1.3 | 0.15 | 0.471 | 0.34 | 0.385 |
| DL3_1 | 0.47 | 1 | 0.5 | 0.67 | 0.7 | 0.9 | 0.15 | 0.628 | 0.428 | 0.481 |
| DL4_3 | 0.47 | 1 | 0.28 | 0.78 | 0.5 | 1.3 | 0.23 | 0.639 | 0.347 | 0.433 |
| ACa7_6 | 0.47 | 2 | 1.61 | 3.19 | 2.0 | 3.9 | 0.06 | 0.148 | 0.255 | 0.314 |
| AL4_2 | 0.47 | 2 | 1.21 | 3.06 | 1.5 | 3.8 | 0.08 | 0.202 | 0.292 | 0.407 |
| AL6_6 | 0.47 | 2 | 1.45 | 3.15 | 1.8 | 4.0 | 0.07 | 0.166 | 0.258 | 0.334 |
| DCa2_3 | 0.47 | 2 | 0.56 | 1.02 | 0.8 | 1.5 | 0.20 | 0.511 | 0.391 | 0.5 |
| FT1_7 | 0.47 | 2 | 0.82 | 1.33 | 1.0 | 1.7 | 0.60 | 1.725 | 2.37 | 2.74 |
| ACa7_1 | 0.6 | 1 | 1.61 | 2.46 | 1.7 | 2.6 | 0.02 | 0.198 | 0.322 | 0.371 |
| BCa1_25 | 0.6 | 1 | 0.7 | 1.78 | 0.8 | 2.1 | 0.15 | 1.024 | 0.871 | 1.27 |
| CCa1_6 | 0.6 | 1 | 0.9 | ■ | 1.0 | ■ | 0.06 | 0.903 | 0.853 | 1.14 |
| ET1_4 | 0.6 | 1 | 0.77 | 1.04 | 0.8 | 1.1 | 0.05 | 1.221 | 0.894 | 1.07 |
| ET1_5 | 0.6 | 1 | 0.65 | 1.26 | 0.9 | 1.7 | 0.30 | 1.099 | 0.9 | 1.14 |
| ACa9_1 | 0.6 | 2 | 1.97 | 3.49 | 2.1 | 3.7 | 0.01 | 0.11 | 0.175 | 0.211 |
| AL3_1 | 0.6 | 2 | 1.36 | 2.87 | 1.5 | 3.2 | 0.02 | 0.127 | 0.177 | 0.25 |
| AL7_3 | 0.6 | 2 | 1.47 | 2.83 | 1.8 | 3.5 | 0.05 | 0.137 | 0.21 | 0.26 |
| BCa1_28 | 0.6 | 2 | 0.92 | 1.95 | 1.0 | 2.1 | 0.05 | 0.942 | 0.782 | 1.07 |
| ET1_7 | 0.6 | 2 | 0.95 | 1.38 | 1.0 | 1.5 | 0.08 | 0.813 | 0.757 | 0.898 |
| ACa9_2 | 0 | 0 | 0.95 | 2.76 | 1.1 | 3.1 | 0.10 | 0.495 | 0.878 | 1.4 |
| AL8_3 | 0 | 0 | 1.2 | 2 | 1.3 | 2.2 | 0.08 | 0.417 | 0.817 | 1.05 |
| BCa1_26 | 0 | 0 | 0.81 | 1.77 | 0.8 | 1.8 | 0.03 | 1.927 | 3.77 | 5.5 |
| CCa1_5 | 0 | 0 | 0.66 | 1.6 | 0.8 | 1.9 | 0.45 | 1.617 | 2.49 | 3.93 |
| DCa4_4 | 0 | 0 | 0.55 | 1.1 | 0.6 | 1.2 | 0.15 | 0.904 | 1.15 | 1.59 |
| BCa2_5 | 0 | 0 | | | | | | | | |
| BCa2_9 | 0 | 0 | 0.63 | 1.28 | 0.8 | 1.5 | 0.70 | 2.052 | 3.55 | 4.9 |

# TENSION | Mechanical Test Data

| SPECIMEN DATA | | | MECHANICAL TESTS | | | | | | | |
| SPECIMEN | Hole Size | E | Calculations | | Acutal Strains | | | | | |
| | | | Yield Stn Calc % Strain | Ult Stn Calc % Strain | Yield Strain % Strain | Ult. Strain % Strain | Pre-Load N | Rigidity NM | Yield Load N | Ult. Load N |
|---|---|---|---|---|---|---|---|---|---|---|
| AL3_6 | 0 | 0 | | | 0.52% | 2.09% | | 51094 | 285 | 455 |
| BCa1_15 | 0 | 0 | | | 0.65% | 1.09% | | 199470 | 1317 | 1734 |
| BCa2-3 | 0 | 0 | | | 0.41% | 1.10% | | 247979 | 1034 | 1570 |
| DCa2_5 | 0 | 0 | | | 0.62% | 1.29% | | 78133 | 575 | 746 |
| DCa2_6 | 0 | 0 | | | 0.70% | 1.15% | | 61913 | 399 | 530 |
| FT1_5 | 0 | 0 | | | | | | | | |
| AL3_2 | 0.28 | 1 | | | 0.39% | 1.52% | | 50127 | 205 | 271 |
| AL8_4 | 0.28 | 1 | | | 0.34% | 1.28% | | 49489 | 156 | 292 |
| BCa1_19 | 0.28 | 1 | | | 0.44% | 0.79% | | 275438 | 1115 | 1507 |
| BCa1_29 | 0.28 | 1 | | | 0.59% | 0.90% | | 173464 | 1001 | 1168 |
| DCa4_3 | 0.28 | 1 | | | 0.28% | 0.57% | | 77098 | 198 | 290 |
| AL6_4 | 0.47 | 1 | | | 0.50% | 1.14% | | 20907 | 126 | 167 |
| BCa1_20 | 0.47 | 1 | | | 0.44% | 0.79% | | | | 779 |
| BCa1_6 | 0.47 | 1 | | | 0.62% | 0.83% | | 114464 | 701 | 802 |
| DL5_1 | 0.47 | 1 | | | 0.45% | 0.73% | | 26503 | 87 | 160 |
| ACa7_4 | 0.6 | 1 | | | 0.40% | 1.25% | | 19569 | 82 | 144 |
| AL5_3 | 0.6 | 1 | | | 0.49% | 0.99% | | 15270 | 74 | 103 |
| AL8_11 | 0.6 | 1 | | | 0.49% | 0.83% | | 15500 | 76 | 94 |
| BCa1_11 | 0.6 | 1 | | | | | | | | |
| ET1_3 | 0.6 | 1 | | | 0.38% | 0.64% | | 158378 | 658 | 863 |
| AL8_10 | 0.28 | 2 | | | 0.48% | 1.30% | | 26420 | 124 | 194 |
| BCa1_7 | 0.28 | 2 | | | 0.56% | 0.83% | | 162941 | 898 | 1072 |
| CCa1_12 | 0.28 | 2 | | | 0.39% | 1.10% | | 173726 | 756 | 1232 |
| DCa2_4 | 0.28 | 2 | | | 0.54% | 0.89% | | 42353 | 203 | 272 |
| ET1_2 | 0.28 | 2 | | | 0.38% | 0.61% | | 210086 | 727 | 890 |
| ACa8_2 | 0.47 | 2 | | | 0.61% | 1.52% | | 17431 | 99 | 153 |
| AL4_4 | 0.47 | 2 | | | 0.62% | 1.80% | | 14562 | 97 | 147 |
| AL5_2 | 0.47 | 2 | | | 0.75% | 1.84% | | 9805 | 79 | 114 |
| AL8_2 | 0.47 | 2 | | | 0.56% | 1.50% | | 16284 | 104 | 153 |
| CCa1_4 | 0.47 | 2 | | | 0.53% | 1.14% | | 98595 | 481 | 682 |
| AL3_4 | 0.6 | 2 | | | 0.87% | 2.56% | | 8481 | 89 | 117 |
| AL6_3 | 0.6 | 2 | | | 0.59% | 1.48% | | 9868 | 64 | 89 |
| AL7_5 | 0.6 | 2 | | | 0.36% | 1.56% | | 17466 | 76 | 144 |
| BCa1_12 | 0.6 | 2 | | | 0.34% | 1.28% | | 33100 | 156 | 464 |
| FT1_6 | 0.6 | 2 | | | 0.67% | 1.06% | | 107750 | 792 | 950 |

# TORSION     Mechanical Test Data

| SPECIMEN DATA | | | MECHANICAL TESTS | | | | | | | |
| SPECIMEN | Hole Size | E | Calculations | | Acutal Strains | | | | | |
| | | | Yield Stn Calc % Strain | Ult Stn Calc % Strain | Yield Strain % Strain | Ult. Strain % Strain | Pre-Load Nm | Rigidity Nm^2 | Yield Load Nm | Ult. Load Nm |
|---|---|---|---|---|---|---|---|---|---|---|
| ACa7_5 | 0.28 | 1 | 3.29 | 11.68 | 1.55 | 5.49 | | 0.1034 | 0.385 | 0.5911 |
| BCal_21 | 0.28 | 1 | 2.12 | 5.98 | 1.00 | 2.81 | | 0.855 | 1.757 | 2.846 |
| DL2_2 | 0.28 | 1 | 0.26 | 2.5 | 0.12 | 1.18 | | 0.649 | 0.498 | 0.746 |
| DL4_1 | 0.28 | 1 | 2.2 | 5.56 | 1.03 | 2.62 | | 0.263 | 0.572 | 0.846 |
| ET1_8 | 0.28 | 1 | 2.89 | 6.8 | 1.36 | 3.20 | | 0.888 | 2.4 | 3.778 |
| AL7_4 | 0.28 | 2 | 2.24 | 10.21 | 1.05 | 4.80 | | 0.079 | 0.203 | 0.369 |
| BCal_22 | 0.28 | 2 | 2.7 | 6.22 | 1.27 | 2.93 | | 0.609 | 1.549 | 2.394 |
| DL3_2 | 0.28 | 2 | 1.96 | 4.73 | 0.92 | 2.22 | | 0.184 | 0.417 | 0.624 |
| DL4_2 | 0.28 | 2 | 1.99 | 4.94 | 0.94 | 2.32 | | 0.12 | 0.275 | 0.397 |
| FT1_8 | 0.28 | 2 | 2.63 | 8.81 | 1.24 | 4.14 | | 1.431 | 3.65 | 6.229 |
| AL3_7 | 0.47 | 1 | 2.29 | 9.83 | 1.08 | 4.62 | | 0.079 | 0.219 | 0.429 |
| AL7_1 | 0.47 | 1 | | | | | | | | |
| AL8_5 | 0.47 | 1 | 2.96 | 8.85 | 1.39 | 4.16 | | 0.077 | 0.251 | 0.376 |
| BCal_13 | 0.47 | 1 | | | | | | | 2.3 | 2.512 |
| CCal_13 | 0.47 | 1 | 2.62 | 7.38 | 1.23 | 3.47 | | 0.392 | 1.012 | 1.772 |
| DL2_1 | 0.47 | 1 | | | | | | | | |
| ACa7_3 | 0.47 | 2 | | | | | | | | |
| AL5_1 | 0.47 | 2 | 4.27 | | 2.01 | | | 0.043 | 0.187 | 0.277 |
| AL5_5 | 0.47 | 2 | | | | | | | | |
| BCal_3 | 0.47 | 2 | 2.09 | 5.1 | 0.98 | 2.40 | | 0.516 | 0.948 | 1.497 |
| DL2_3 | 0.47 | 2 | 0.84 | 4.19 | 0.40 | 1.97 | | 0.174 | 0.169 | 0.36 |
| ACa8_1 | 0.6 | 1 | 1.45 | 7.99 | 0.68 | 3.76 | | 0.1951 | 0.333 | 0.5908 |
| BCal_8 | 0.6 | 1 | 2.91 | 5.16 | 1.37 | 2.43 | | 0.411 | 1.136 | 1.489 |
| CCal_1 | 0.6 | 1 | 1.4 | 4.24 | 0.66 | 1.99 | | 0.559 | 0.776 | 1.279 |
| CCal_14 | 0.6 | 1 | 2.12 | 5.57 | 1.00 | 2.62 | | 0.357 | 0.784 | 1.278 |
| DL5_2 | 0.6 | 1 | 1.38 | 3.34 | 0.65 | 1.57 | | 0.188 | 0.281 | 0.416 |
| AL7_2 | 0.6 | 2 | 1.95 | | 0.92 | | | 0.031 | 0.102 | 0.17 |
| BCal_1 | 0.6 | 2 | 2.65 | 5.68 | 1.25 | 2.67 | | 0.276 | 0.729 | 1.013 |
| BCal_16 | 0.6 | 2 | 2.79 | 4.96 | 1.31 | 2.33 | | 0.339 | 0.876 | 1.205 |
| BCal_5 | 0.6 | 2 | 2.28 | 5.12 | 1.07 | 2.41 | | 0.308 | 0.694 | 1.098 |
| FT1_1 | 0.6 | 2 | 3.19 | 4.69 | 1.50 | 2.21 | | 0.727 | 2.21 | 2.709 |
| AL3_5 | 0 | 0 | 3.42 | 17.45 | 1.61 | 8.21 | | 0.15 | 0.531 | 0.928 |
| AL8_9 | 0 | 0 | 3.85 | 13.33 | 1.81 | 6.27 | | 0.115 | 0.519 | 0.774 |
| BCal_9 | 0 | 0 | 3.81 | | 1.79 | | | 0.956 | 3.136 | 4.777 |
| DCa3_2 | 0 | 0 | 2.06 | 6.13 | 0.97 | 2.88 | | 0.334 | 0.771 | 1.272 |
| DCa3_6 | 0 | 0 | 1.98 | 6.68 | 0.93 | 3.14 | | 0.495 | 0.697 | 1.248 |
| BCa2_10 | 0 | 0 | 3.08 | 8.3 | 1.45 | 3.90 | | 0.872 | 2.63 | 4.068 |
| BCa2_6 | 0 | 0 | 3.03 | 8.66 | 1.43 | 4.07 | | 0.901 | 2.73 | 4.335 |
| CCal_7 | 0 | 0 | | | | | | | | |
| CCal_11 | 0 | 0 | | | | | | | 2.191 | 3.138 |
| ET1_21 | 0 | 0 | 2.76 | 5.35 | 1.30 | 2.52 | | 0.92 | 2.43 | 3.368 |
| FT1_2 | 0 | 0 | 1.58 | | 0.74 | | | 2.615 | 4.26 | |
| FT1_4 | 0 | 0 | 2.86 | | 1.35 | | | 2.643 | 7.4 | |

# TORSION | INTACT QCT DATA

| SPECIMEN DATA | | | | INTACT QCT DATA | | | | | | | |
|---|---|---|---|---|---|---|---|---|---|---|---|
| SPECIMEN | Hole Size | E | Length mm | Area (mm^2) Area | Density (g/cc) Avg den | Modulus (GPa) Avg Mod | Axial Rig. (MN) axrig | Ix bar (cm^4) gixbar | EIx bar (Nm^2) ixbar | Polar Mom. (cm^4) Polar mom. | Tor. Rig. (Nm^2) Tors Rig |
| ACa7_5 | 0.28 | 1 | 40.75 | 130 | 0.191 | 0.467 | 0.061 | 0.135 | 0.634 | 0.270 | 1.25 |
| BCa1_21 | 0.28 | 1 | 37.78 | 143 | 0.491 | 2.476 | 0.354 | 0.163 | 3.718 | 0.325 | 7.51 |
| DL2_2 | 0.28 | 1 | 36.91 | 136 | 0.262 | 0.781 | 0.106 | 0.148 | 1.100 | 0.294 | 2.18 |
| DL4_1 | 0.28 | 1 | 37.25 | 135 | 0.264 | 0.793 | 0.107 | 0.148 | 1.123 | 0.291 | 2.21 |
| ET1_8 | 0.28 | 1 | 37.51 | 141 | 0.583 | 3.356 | 0.472 | 0.160 | 4.840 | 0.315 | 9.81 |
| AL7_4 | 0.28 | 2 | 35.76 | 128 | 0.174 | 0.400 | 0.051 | 0.132 | 0.512 | 0.261 | 1.02 |
| BCa1_22 | 0.28 | 2 | 38.01 | 141 | 0.472 | 2.271 | 0.320 | 0.159 | 3.368 | 0.316 | 6.78 |
| DL3_2 | 0.28 | 2 | 37.83 | 134 | 0.260 | 0.773 | 0.104 | 0.141 | 1.035 | 0.286 | 2.09 |
| DL4_2 | 0.28 | 2 | 37.32 | 130 | 0.233 | 0.646 | 0.084 | 0.134 | 0.853 | 0.269 | 1.66 |
| FT1_8 | 0.28 | 2 | 37.75 | 141 | 0.817 | 6.153 | 0.867 | 0.159 | 9.125 | 0.316 | 17.91 |
| AL3_7 | 0.47 | 1 | 32.34 | 132 | 0.203 | 0.516 | 0.068 | 0.140 | 0.724 | 0.280 | 1.43 |
| AL7_1 | 0.47 | 1 | 36.33 | 128 | 0.179 | 0.418 | 0.054 | 0.133 | 0.549 | 0.262 | 1.09 |
| AL8_5 | 0.47 | 1 | 36.84 | 130 | 0.180 | 0.419 | 0.054 | 0.134 | 0.565 | 0.270 | 1.13 |
| BCa1_13 | 0.47 | 1 | 38.06 | 140 | 0.481 | 2.380 | 0.334 | 0.156 | 3.393 | 0.313 | 6.92 |
| CCa1_13 | 0.47 | 1 | 37.59 | 129 | 0.371 | 1.568 | 0.202 | 0.139 | 2.066 | 0.283 | 4.41 |
| DL2_1 | 0.47 | 1 | 38.64 | 134 | 0.291 | 0.938 | 0.125 | 0.145 | 1.241 | 0.285 | 2.60 |
| ACa7_3 | 0.47 | 2 | 35.37 | 136 | 0.222 | 0.598 | 0.081 | 0.148 | 0.895 | 0.294 | 1.79 |
| AL5_1 | 0.47 | 2 | 37.60 | 131 | 0.186 | 0.444 | 0.058 | 0.138 | 0.624 | 0.276 | 1.22 |
| AL5_5 | 0.47 | 2 | 34.37 | 131 | 0.178 | 0.413 | 0.054 | 0.135 | 0.564 | 0.271 | 1.12 |
| BCa1_3 | 0.47 | 2 | 37.73 | 138 | 0.483 | 2.454 | 0.340 | 0.151 | 3.340 | 0.307 | 6.78 |
| DL2_3 | 0.47 | 2 | 38.74 | 136 | 0.258 | 0.766 | 0.104 | 0.148 | 1.089 | 0.292 | 2.14 |
| ACa8_1 | 0.6 | 1 | 37.23 | 134 | 0.194 | 0.477 | 0.064 | 0.143 | 0.675 | 0.286 | 1.34 |
| BCa1_8 | 0.6 | 1 | 36.70 | 137 | 0.479 | 2.381 | 0.327 | 0.149 | 3.444 | 0.301 | 6.81 |
| CCa1_1 | 0.6 | 1 | 38.50 | 139 | 0.436 | 2.062 | 0.287 | 0.160 | 3.099 | 0.316 | 6.22 |
| CCa1_14 | 0.6 | 1 | 38.59 | 132 | 0.371 | 1.584 | 0.209 | 0.150 | 2.273 | 0.297 | 4.45 |
| DL5_2 | 0.6 | 1 | 37.76 | 136 | 0.259 | 0.769 | 0.104 | 0.147 | 1.061 | 0.293 | 2.11 |
| AL7_2 | 0.6 | 2 | 34.70 | 136 | 0.216 | 0.566 | 0.077 | 0.148 | 0.813 | 0.295 | 1.61 |
| BCa1_1 | 0.6 | 2 | 38.01 | 140 | 0.468 | 2.267 | 0.317 | 0.158 | 3.223 | 0.312 | 6.44 |
| BCa1_16 | 0.6 | 2 | 37.04 | 138 | 0.522 | 2.830 | 0.391 | 0.153 | 3.593 | 0.306 | 8.36 |
| BCa1_5 | 0.6 | 2 | 38.13 | 143 | 0.513 | 2.717 | 0.389 | 0.164 | 4.048 | 0.327 | 8.20 |
| FT1_1 | 0.6 | 2 | 37.50 | 143 | 0.787 | 5.715 | 0.819 | 0.164 | 8.861 | 0.327 | 17.59 |
| AL3_5 | 0 | 0 | 33.66 | 134 | 0.208 | 0.533 | 0.071 | 0.141 | 0.726 | 0.285 | 1.52 |
| AL8_9 | 0 | 0 | 36.25 | 129 | 0.179 | 0.418 | 0.054 | 0.135 | 0.563 | 0.269 | 1.13 |
| BCa1_9 | 0 | 0 | 37.62 | 137 | 0.543 | 3.035 | 0.417 | 0.150 | 4.278 | 0.304 | 8.77 |
| DCa3_2 | 0 | 0 | 38.05 | 137 | 0.261 | 0.784 | 0.107 | 0.149 | 1.134 | 0.300 | 2.38 |
| DCa3_6 | 0 | 0 | 37.15 | 138 | 0.270 | 0.824 | 0.113 | 0.151 | 1.208 | 0.301 | 2.41 |
| BCa2_10 | 0 | 0 | | 138 | 0.454 | 2.199 | 0.303 | 0.158 | 3.133 | 0.309 | 6.37 |
| BCa2_6 | 0 | 0 | | 137 | 0.454 | 2.168 | 0.298 | 0.152 | 3.119 | 0.303 | 6.19 |
| CCa1_7 | 0 | 0 | | 138 | 0.640 | 3.979 | 0.550 | 0.147 | 5.669 | 0.306 | 11.74 |
| CCa1_11 | 0 | 0 | | 141 | 0.437 | 2.074 | 0.292 | 0.161 | 3.161 | 0.326 | 6.85 |
| ET1_21 | 0 | 0 | | 143 | 0.641 | 3.963 | 0.567 | 0.160 | 6.063 | 0.326 | 12.47 |
| FT1_2 | 0 | 0 | | 143 | 0.953 | 7.461 | 1.065 | 0.162 | 11.210 | 0.325 | 22.93 |
| FT1_4 | 0 | 0 | | 143 | 1.031 | 8.519 | 1.216 | 0.162 | 12.640 | 0.325 | 25.50 |

# BENDING

TEST WAVE FORM:     gdcben.utp   (controller setup)
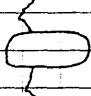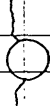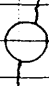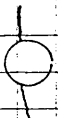
1) 5 cycles between 0.0mm and -0.1mm @ 0.05mm/sec
2) 1 ramp to ~~2~~ -4.0mm @ 0.025mm/sec

SPECIMEN TEMP:     specimens were tested @ room temp and
were thawed for approximately 20-30 minutes before
testing. They were kept moist using a damp piece of ~~guaz~~ gauze.
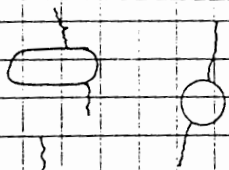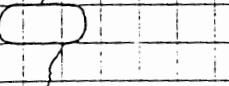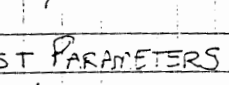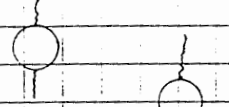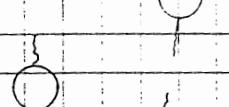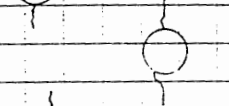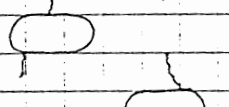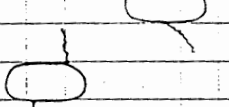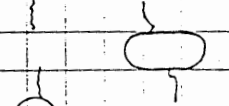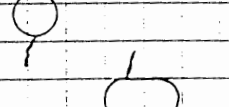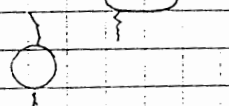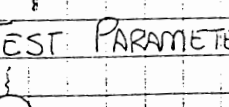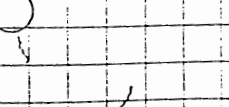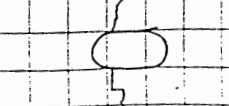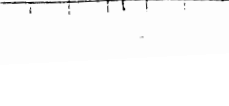
ROOM TEMP:   21°C / 70°F

HUMIDITY:    63%
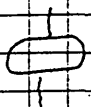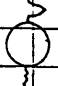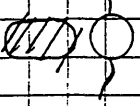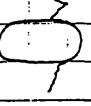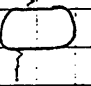
RESULTS:     The following specimens were tested using the protocol
above ~~with~~ the except() where noted:

| SPECIMEN | HOLE SIZE | FRACTURE PATTERN/LOCATION (view from bottom) | NOTES |
|---|---|---|---|
| BCal-26 | None | 25.8mm / 19.3mm from Left/Right Edges | BCal-26 was tested once to a displacem of about 1.8mm and then to failure. In t first test, it had not yielded. |
| DCa4-4 | None | 29.5mm / 4.5mm | |
| CCal-5 | None | 28.8mm / 9.4mm | |
| ACa9-2 | None | At left endcap | |
| AL8-3x | None | At left endcap | Needs investigation in Abaqus |
| BCal-18 | 28% slot | | |
| DCa4-1 | 28% | | |
| BCal-10 | 28% slot | | |
| BCal-17 | 28% slot | | |
| CCal-9 | 28% | | |
| CCal-2 | 28% | | |
| BCal-14 | 28% | | |

# BENDING

| Specimen | Hole Size | Fracture Pattern | Notes |
|---|---|---|---|
| ET1.1 | 28% Slot | | |
| Al 6.2 | 28% | | |
| ACa 9.3 | 28% Slot | | |

**✻ NEW SET OF TEST PARAMETERS (SEE "SETUP B") FOR 47% HOLE ✻**

| Specimen | Hole Size | Fracture Pattern | Notes |
|---|---|---|---|
| DL4.3 | 47% | | Collected @ 6 Hz, same as "SETUP A" except load full scale set to 88 Newtons |
| DL3.1 | 47% | | Data collected @ 12 Hz |
| BCa1.24 | 47% | | Sampling rate = 6 Hz ; Full scale load "1V" = 220N |
| DCa2.2 | 47% | | 6 Hz ; 10V = 88N |
| Al 4.2 | 47% Slot | | 10V = 88N |
| ACa7.6 | 47% Slot | | 10V = 88N    ✻ All 47% specimens - the load goes |
| ET1.7 | 47% Slot | | 10V = 220N     to zero by the time the visible |
| DCa2.3 | 47% Slot | | 10V = 44N     crack has propagated ½ way |
| AL2.7 | 47% | | 10V = 44N     through the specimen |
| AL6.6 | 47% Slot | | 10V = 44N |
| ET1.5 | 56% | | 10V = 88N |

**✻ NEW SET OF TEST PARAMETERS (SEE "SETUP C") FOR 56% HOLE ✻**

| Specimen | Hole Size | Fracture Pattern | Notes |
|---|---|---|---|
| ACa7.1 | 56% | | Note: ACa 7.1 was tested @ 0.006 mm/sec and may not have yielded. It was tested again @ 0.01 mm/sec and did reach ultimate load (10V = 44N) |
| BCa1.28 | 56% Slot | | 10V = 88N |

# BENDING

| Specimen | Hole Size | Fracture Pattern/Location | | Notes |
|----------|-----------|---------------------------|--|-------|
| ET 1.7 | 56% Slot | | 10V=88N | Note: In all 56% hole specimens the |
| CCa1.6 | 56% | | 10V=88N | was noticeable crack propagation th |
| ET.4 | 56% Slot | | 10V=88N | arrest, followed by more propagation |
| | | | | Sharp drops (discontinuities) in |
| BCa1.25 | 56% | | 10V=88N | load were ALWAYS accompanied by |
| | | | | audible cracking sounds. |
| ACa9.1 | 56% Slot | | 10V=44N | |
| AL 3.1 | 56% Slot | | 10V=44N | |
| AL 7.3 | 56% Slot | | 10V=44N | |

* TESTED USING SETUP ON PG. 50-52. These last two specimens were
added to the intact group from the good extras. They were QCT scanned with
all of the other specimens.

| BCa2.5 | None | 6.85mm/30.30mm from lft/rt. | 10V=440N | Load may be bad (drill in tare of loc |
| BCa2.9 | None | 33.8mm/2.8mm from lft/rt. | 10V=440N | |

## TEST SETUP B:

TEST WAVEFORM: 5 cycles between 0.0mm and -0.05mm @ 0.025 mm/sec
1 ramp to -4.0mm @ 0.015 mm/sec

SAMPLING FREQ. FOR DATA COLLECTION: 12 Hz

## TEST SETUP C:

TEST WAVEFORM: 5 cycles between 0.0mm and -0.03mm @ 0.02 mm/sec
1 ramp to -4.0mm @ 0.015 mm/sec

SAMPLING FREQ. FOR DATA COLLECTION: 12 Hz

# TENSION

| Specimen | Hole Size | Disp. Rate (in/ms) | Load Gauge | Fracture Pattern / Location | Notes |
|---|---|---|---|---|---|
| CCa1-4 c | 47% Slot | 0.035 | (2200N) | | |
| AL3-2 | 28% | 0.02 | (440N) | Broke at endcap (growth plate) | |
| DCa2-4 c | 28% Slot | 0.02 | " | | May have been a little dry and tested a little too fast for plastic |
| AL8-4 | 28% | 0.012 | " | | |
| AL8-10 | 28% Slot | 0.015 | " | | |
| DCa4-3 | 28% | 0.015 | " | | |
| BCa1-19 | 28% | 0.06 | (2200N) | | Tested once nondestructively to 5% the grips slipped |
| BCa1-29 | 28% | 0.06 | 2200N | | |
| BCa1-7 | 28% Slot | 0.05 | 2200N | | |
| ET1-2 | 28% Slot | 0.05 | 2200N | | |
| CCa1-12 | 28% Slot | 0.04 | 2200N | | Test once nondestructively to ~1% the grips slipped |
| AL3-6 | Intact | 0.05 | (1100N) | fracture @ endcap | |
| DCa2-5 | Intact | 0.04 | " | | |
| DCa2-6 | Intact | 0.04 | " | | May have been too dry |
| BCa1-15 | Intact | 0.06 | " | Broke straight ( I ) inside endcap endcap remained intact | Broke where set screws were s... into the specimen |
| BCa2-3 | Intact | 0.06 | " | | |
| ET1-5 | Intact | 0.08 | 8000N | Endcap broke - specimen did not break | |

# TENSION

RESULTS: The following specimens were tested to failure using the protocol described above:

| SPECIMEN | | HOLE SIZE | DISP RATE (in/s) | LOAD CELL | FRACTURE PATTERN/LOCATION | NOTES |
|---|---|---|---|---|---|---|
| AL8-11 | MY | 56% | 0.02 | 2000 lb (4000 N) | | May have been a little |
| AL5-3 | MY | 56% | 0.01 | 500 lb (440 N) | | |
| AL7-5 | CY | 56% Slot | 0.01 | " | | |
| AL6-3 | CY | 56% Slot | 0.01 | " | | |
| ACa7-4 | MY | 56% | 0.01 | " | | |
| AL3-4 | CN | 56% Slot | 0.01 | " | | LVDT data probab |
| BCa1-11 | CN | 56% | LOST | | | |
| BCa1-12 | CN | 56% Slot | 0.01 | (1100 N) | | Ultimate load & stra |
| ET1-3 | MY | 56% | 0.015 | (2200 N) | | |
| ET-6 | CN | 56% Slot | 0.03 | (2200 N) | | |
| AL4-4 | CN | 47% Slot | 0.025 | (440 N) | | |
| AL6-4 | MY | 47% | 0.025 | (440 N) | | |
| ACa8-2 | CN | 47% Slot | 0.015 | " | | |
| AL8-2 | CY | 47% Slot | 0.015 | " | | |
| AL5-2 | CY | 47% Slot | 0.015 | " | | |
| DL5-1 | MY | 47% | 0.015 | " | | |
| BCa1-6 | MY | 47% | 0.035 0.045 | 2200 " | | May not have valu |

# TORSION

| SPECIMEN | Hole Size | NSP RATE (mm/s) | Preload (Nm) | Load Gain | FRACTURE PATTERN/LOCATION | NOTES |
|---|---|---|---|---|---|---|
| BCa1-3 | 47% Slot | 0.20 | 0.1305 | 4000 | | |
| BCa1-13 | 47% | " | " | " | | Markers lost b4 yield |
| BCa1-16 | 56% Slot | " | " | " | | |
| BCa1-1 | 56% Slot | " | " | " | | |
| BCa1-5 | 56% Slot | " | " | " | | |
| BCa1-8 | 56% | " | " | " | | |
| CCa1-1 | 56% | " | " | " | | |
| CCa1-14 | 56% | " | " | " | | |
| FT1-1 | 56% Slot | " | " | " | | |
| UL5-2 | 56% | " | " | " | | |
| ACa8-1 | 56% Slot | 0.15 | " | " | | |
| AL7-2 | 56% Slot | 0.15 | 0.117 | " | | No ultimate strain - ma. |
| AL3-5 | Intact | 0.25 | " | " | (not spiral) | Broke near middle |
| DCa3-6 | Intact | " | " | " | | Broke near middle |
| AL8-9 | Intact | " | " | " | (not spiral) | Broke near middle |
| DCa3-2 | Intact | " | " | " | | Broke near middle |
| BCa1-9 | Intact | 0.30 | " | 2000 | | Broke @ bottom endcap |
| BCa2-10 | Intact | " | " | " | (short spiral) | Broke near bottom endc. |
| BCa2-6 | Intact | " | " | " | | Broke @ bottom endcap |
| ET1-21 | Intact | " | " | " | spiral | Broke @ bottom endcap |

# TORSION

RESULTS: The following specimens were tested using the protocol described above:

| SPECIMEN | HOLE SIZE | DISP. RATE (mm/sec) | FRACTURE PATTERN / LOCATION | | NOTES | | |
|---|---|---|---|---|---|---|---|
| | | | | | Gain (Load) | Pre load | |
| BCa1.22 | 30% Slot | 0.25 | | | 4000 | 0.1308 | |
| BCa1.21 | 30% | 0.25 | | | " | " | |
| ET1-8 | 30% | 0.25 | | | " | " | |
| FT1-8 | 30% Slot | 0.25 | | | " | " | |
| AL7-4 | 30% Slot | 0.25 | | | " | " | NOT SPIRA |
| ACa7-5 | 30% | 0.25 | | | " | " | ~~NOT SPIRAL~~ |
| L3-2 | 30% Slot | 0.85 | | | " | " | |
| 4-1 | 30% | 0.25 | | | " | " | |
| DL2-2 | 30% | 0.25 | | | " | " | |
| DL4-2 | 30% Slot | 0.25 | | | " | " | |
| DL2-3 | 47% Slot | 0.25 | | | " | " | |
| AL7-1 | 47% | 0.25 | | | " | " | SPECIMEN LOS |
| ~~AL5-5~~ AL8-5 | 47% | 0.20 | | | " | " | |
| AL5-1 | 47% Slot | 0.20 | | | " | " | |
| AL5-5 | 47% Slot | 0.20 | SPECIMEN LOST | | " | " | |
| DL2-1 | 47% | 0.20 | | | " | 0.1305 | SPECIMEN L |
| ACa7-3 | 47% Slot | | SPECIMEN LOST | | | | Broken while M |
| CCa1-13 | 47% | 0.20 | | | " | 0.1305 | |

# Appendix C
# Finite Elemnt Analysis

This appendix contains sample plots of the strain concentrations in each of the three types of testing, one plot for a circular hole and one for a slot. Strain was plotted rather than stress, so that high stresses at the load point, particularly in bending, would not distort the gray-scale. Following the plots is a Patran session file used to create the a model with a slotted defect. All the models were identical, except for the parameters discussed in Chapter 6. Depending on the loading type, one of three sets of boundary conditions at the end of the model were un-commented and made active.

Ben 56el

| EP1 | VALUE |
|---|---|
| | -3.67E-02 |
| | -3.38E-02 |
| | -3.10E-02 |
| | -2.82E-02 |
| | -2.54E-02 |
| | -2.26E-02 |
| | -1.97E-02 |
| | -1.69E-02 |
| | -1.41E-02 |
| | -1.13E-02 |
| | -8.47E-03 |
| | -5.65E-03 |
| | -2.82E-03 |
| | -1.04E-10 |

TIME COMPLETED IN THIS STEP    2.220E-16 TOTAL ACCUMULATED TIME          0
ABAQUS VERSION: 5.4-1     DATE: 18-AUG-96   TIME: 20:06:48
STEP 1 INCREMENT 1
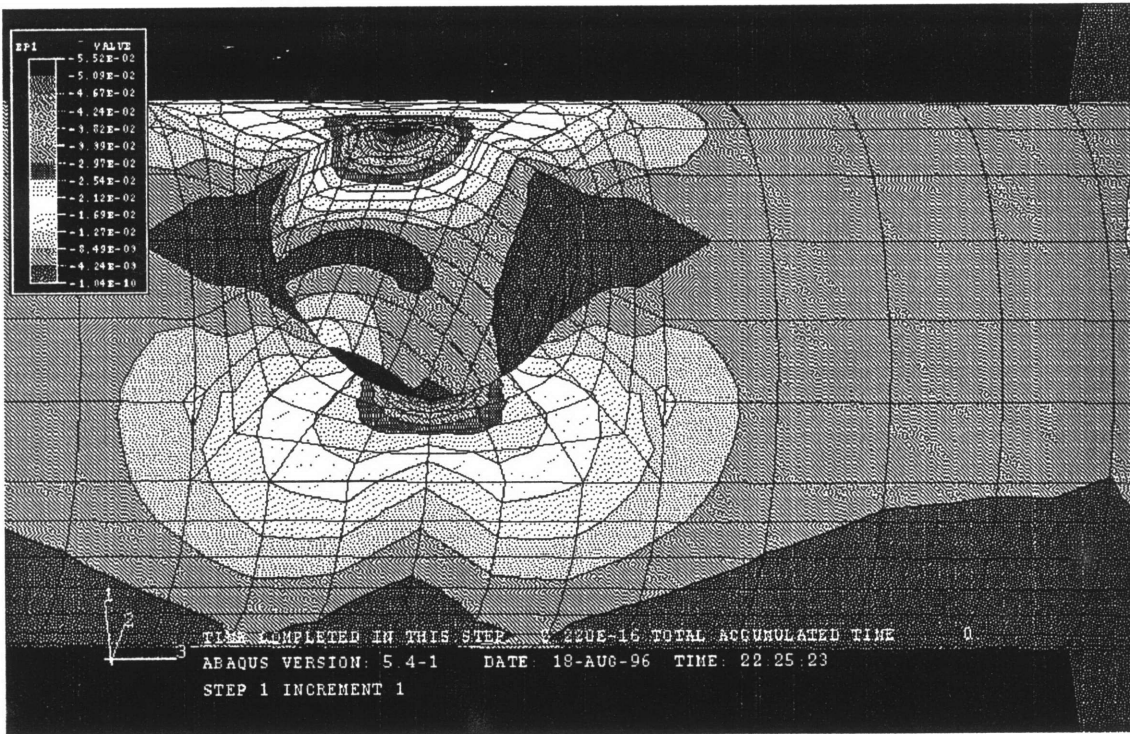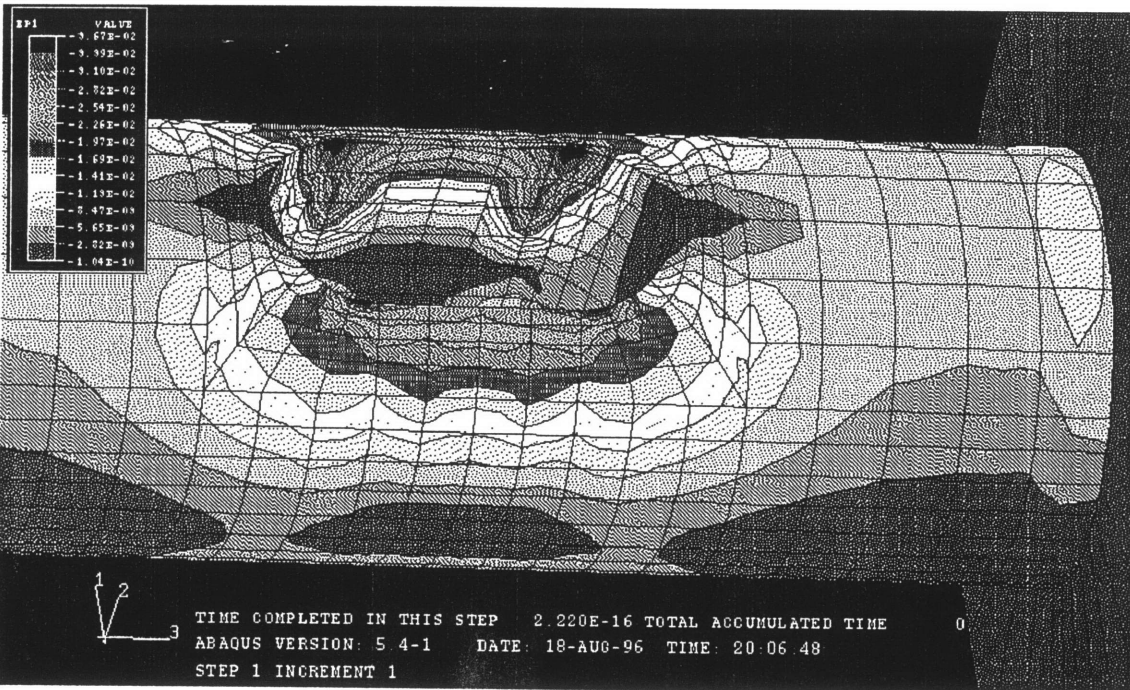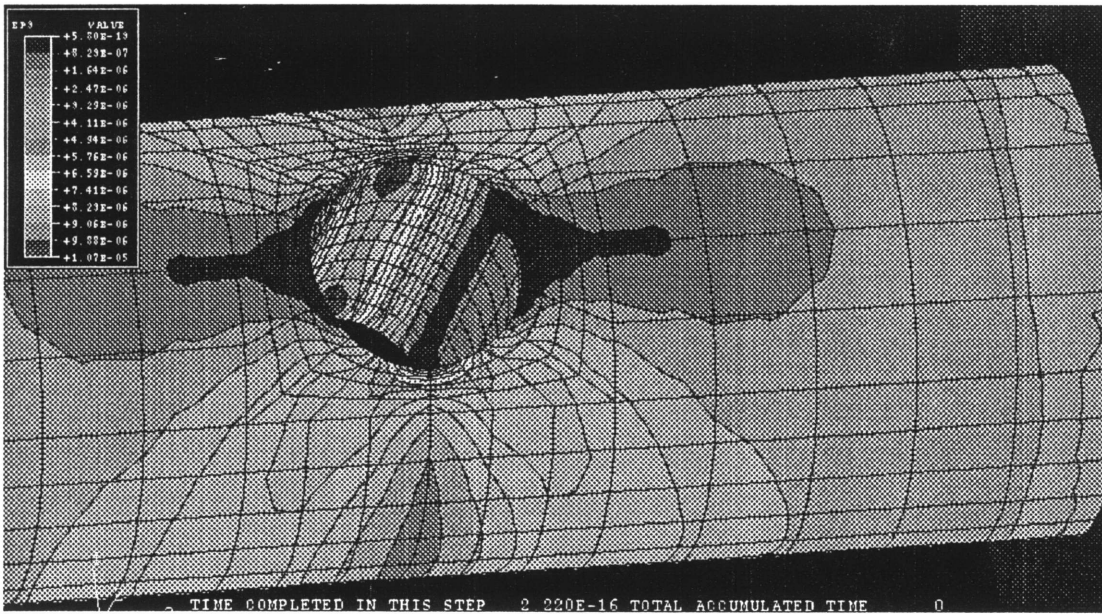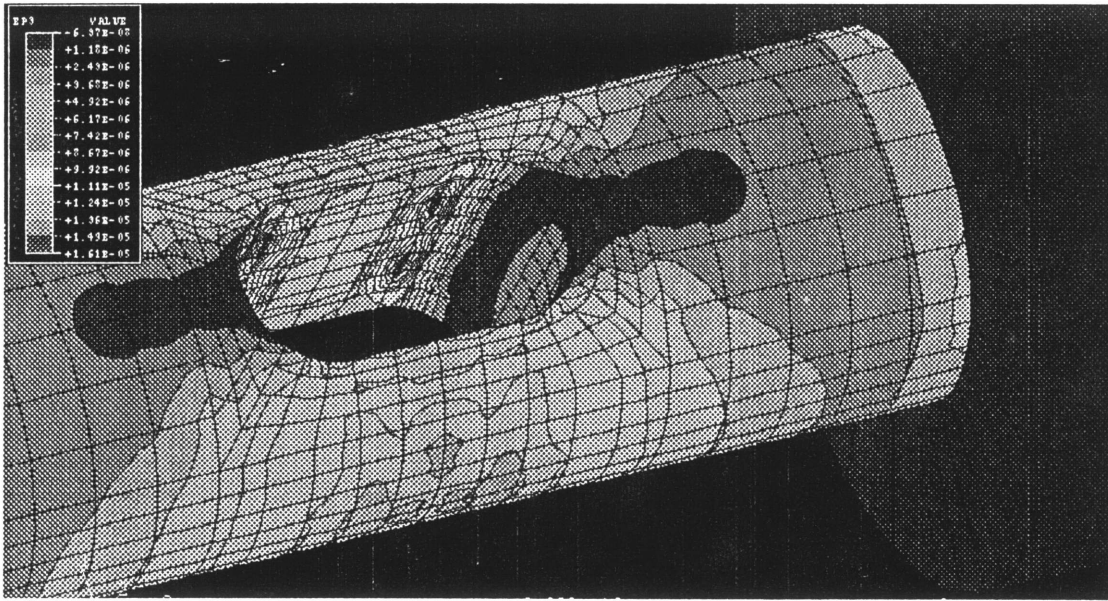
Ben 45e2

Ten45el

Ten 45e2
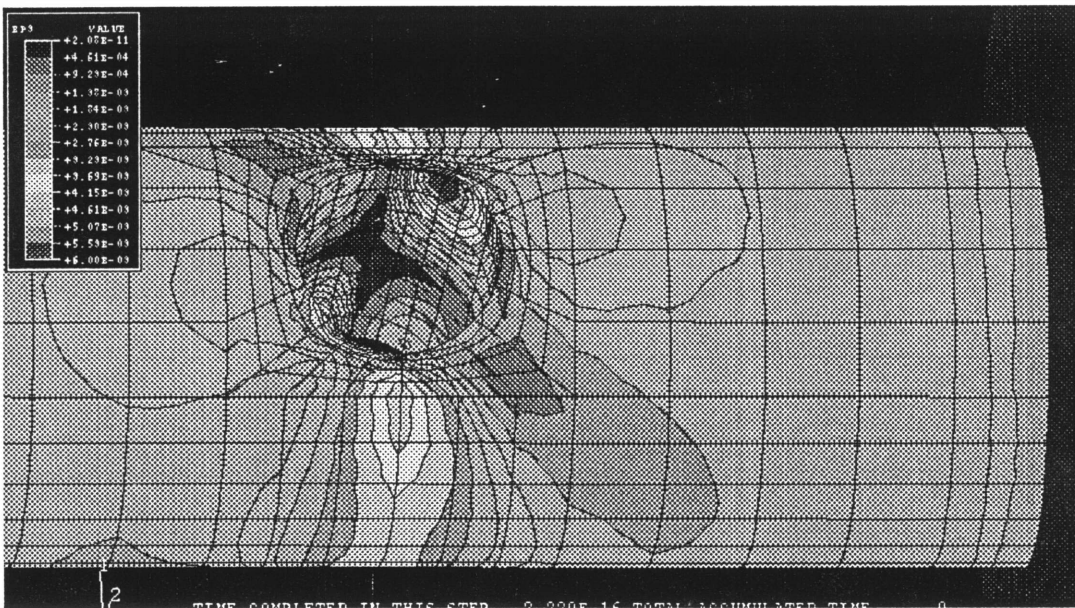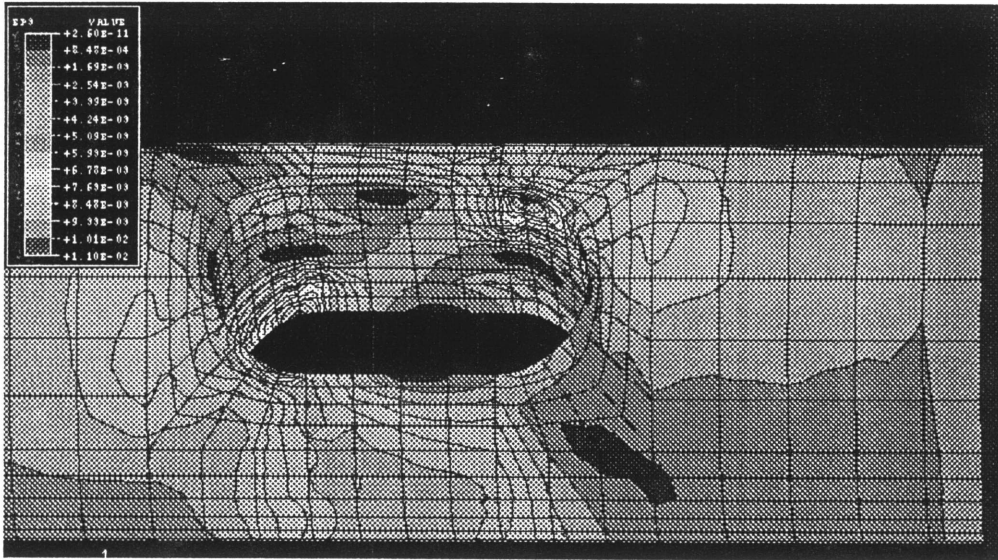
Tor45e#1

Tor 45e2

```
GO
1
SET,ALPHA,8
SET,LI,0
VI
1
45/50


$$$$$$$$$$$$$$$$$$$$$$$$$$$$ MODEL $$$$$$$$$$$$$$$$$$$$$$$$$$$$$$$$$$$
$                                                                   $
$  MODEL:      28% Hole / 200% Eccentricity                         $
$  MESH:       ID- / Max aspect = 5.3 / Max edge angle = 59 deg.    $
$     Nodes:    11420                                               $
$     Elements: 2312                                                $
$  COMMENTS:    This is the setup with a fixture on the end         $
$       for applying tension and torsion, and it has all three      $
$       modes of loading listed.  It has the new method of mesh     $
$       generation.  The high edge angles can't be avoided.  The    $
$       maxium aspect ratio not in the bone is 10.8 and is in the   $
$       bone underneath the endcaps.  The max edge angles are at    $
$       the corners of the hole.                                    $
$                                                                   $
$$$$$$$$$$$$$$$$$$$$$$$$$$$$$$$$$$$$$$$$$$$$$$$$$$$$$$$$$$$$$$$$$$$$$$$


$$$$$$$$$$$$$$$$$$$$$$$$$$$$$ LEGEND $$$$$$$$$$$$$$$$$$$$$$$$$$$$$$$$$$$
$                                                                   $
$       IIII = A value initialized by the user                      $
$       DDDD = A value dependent on some previous value             $
$       FFFF = A value which must remain fixed (e.g always zero)    $
$       Units System: kg/cm/s                                       $
$                                                                   $
$ SPECIMEN                                                          $
$       Radius:         0.635 cm                                    $
$       Gage length:    3.76  cm                                    $
$       Potted length:  3.81  cm                                    $
$ ENDCAPS                                                           $
$       Thickness:      0.635 cm                                    $
$       Length:         3.81  cm                                    $
$ DEFECT                                                            $
$       Hole Radius:    0.179 cm        28% d/D                     $
$       Slot Length:    0.625 cm        200% eccentricity           $
$ REGION WITH REFINED MESH (local to the defect)                    $
$       Length:         1.27 cm                                     $
$       Width:          0.7  cm                                     $
$ MESH                                                              $
$  This is the basic mesh, but is refined in the radial direction.  $
$  It is tight in the radial direction near the hole (HP1,2,5,7)    $
$  but is normal in the radial direction away from the hole (HP3,4) $
$                                                                   $
$$$$$$$$$$$$$$$$$$$$$$$$$$$$$$$$$$$$$$$$$$$$$$$$$$$$$$$$$$$$$$$$$$$$$$$

$$$ MAKING THE CYLINDER WITH THE HOLE $$$$$$$$$$$$$$$$$$$$$$$$$$$$$$$$
$                                                                   $
$ First, one octant of a cylinder is created, with the user         $
$ defining the radius of the cylinder and the extruded length of    $
$ the initial segment.  This length will contain a tighter mesh     $
$ than the rest of the bone.  A hole is then created, with the user $
$ defining the radius of the hole.  The initial octant is then      $
$ trimmed to the hole and segmented into three separate segments.   $
$ The hyperpatches are built from lines and patches generated by    $
$ the hole and the original segments.  The length of the bone is    $
$ then extruded as a set of new HPATs.  Then the length of the      $
$ slot is extruded as a set of new HPATs.  Finally the octant is    $
$ mirrored about each of the three axes to produce the complete     $
```

```
$ bone.                                                             $
$                                                                   $
$$$$$$$$$$$$$$$$$$$$$$$$$$$$$$$$$$$$$$$$$$$$$$$$$$$$$$$$$$$$$$$$$$$$$$$

$$$ CREATING INITIAL OCTANT OF THE CYLINDER $$$$$$$$$$$$$$$$$$$$$$$$$$
$ Make two grid points, connect them with a line,
$ and rotate it so you have the radius of the cyl.

$%%%%%%%%%%%%%% Length of the hole segment %%%%%%%%%%%%%%%%%%%%%$
$IIII  Z = defines 1/2 extruded length of the local region  $
$          (1/2 region around hole + 1/2 length of slot)     $
$FFFF  X,Y should always be zero                             $
$%%%%%%%%%%%%%%%%%%%%%%%%%%%%%%%%%%%%%%%%%%%%%%%%%%%%%%%%%%%%%%%$

GR,1#,,0/0/-.679

$%%%%%%%%%%%%%% Radius of the Cylinder %%%%%%%%%%%%%%%%%%%%%%%%%$
$IIII   Y = Radius of the cylinder                           $
$FFFF   X = 0.0 / should always be zero                      $
$DDDD   Z = extruded length (Z-value) of segment from above  $
$%%%%%%%%%%%%%%%%%%%%%%%%%%%%%%%%%%%%%%%%%%%%%%%%%%%%%%%%%%%%%%%$

GR,1#,,0/.635/-.679
LI,1#,2G,,1,2
PA,1#,ARC,0/0/0/0/0/1/90,1

$ Extrude arc as hpat to make the octant of the cyl.
$ Make patches from the hpat then delete the original
$%%%%%%%%%%%%%%%%%%%%%%%%%%%%%%%%%%%%%%%%%%%%%%%%%%%%%%%%%%%%%%%$
$FFFF   X,Y = 0, should always be zero                       $
$DDDD   Z = 1/2 (length of local region - slot length)       $
$%%%%%%%%%%%%%%%%%%%%%%%%%%%%%%%%%%%%%%%%%%%%%%%%%%%%%%%%%%%%%%%$

HP,1#,EXTRUDE,0/0/.5/0/0/0,1
PA,4#,HPAT,3/2/4/6,1
HPAT,1,DEL

$$$ CREATING THE HOLE $$$$$$$$$$$$$$$$$$$$$$$$$$$$$$$$$$$$$$$$$$$$$$$$
$ Make a grid point, and sweep an arc that extends
$ to the boundaries of the hpat. Extrude that arc
$ so that you have a "hole". Then make a break where
$ the hole and hpat intersect.  Delete the unnecc.
$ patches which are created.

$ Make the grid point
$%%%%%%%%%%%%%% Radius of the Hole %%%%%%%%%%%%%%%%%%%%%%%%%%%%%$
$IIII   X = defines Radius of hole, must be negative         $
$DDDD   Y = 0.1 higher than Radius of cyl. (defines Height)  $
$FFFF   Z = 1/2 length of slot, must be negative             $
$%%%%%%%%%%%%%%%%%%%%%%%%%%%%%%%%%%%%%%%%%%%%%%%%%%%%%%%%%%%%%%%$

GR,1#,,-.179/.7/-.179

$ Sweep the arc 90 degrees

LI,1#,ARC,G4/G6/-90,7

$ Extrude the curved patch
$%%%%%%%%%%%%%%%%%%%%%%%%%%%%%%%%%%%%%%%%%%%%%%%%%%%%%%%%%%%%%%%$
$FFFF   X,Z = 0 / should always be zero                      $
$DDDD   Y = 0.2 higher than Radius of cyl., must be neg.     $
$           / hole must always be taller than the cylinder   $
$%%%%%%%%%%%%%%%%%%%%%%%%%%%%%%%%%%%%%%%%%%%%%%%%%%%%%%%%%%%%%%%$
```

```
PA,1#,EXTRUDE,0/-.8/0,2

        $ Trim the faces of the octant to the hole

PA,8#,BREAK,P6,2/3/4/5
PA,8/9,DEL
PA,10T12,DEL
PA,14,DEL
PA,5/2,DEL

        $ Make lines at the intersection of the hole with
        $ the base and the top face of the quadrant and
        $ break the lines into two segments each.

LI,,INT,,6,4
LI,3/4,BREAK,0.5,3
Y
LI,,INT,,6,3
LI,5/6,BREAK,0.5,5
Y


$$$ SEGMENTING THE OCTANT $$$$$$$$$$$$$$$$$$$$$$$$$$$$$$$$$$$$$$$$$$$$$$
        $ Make grid points, lines, and extruded patches
        $ that divide original octant into 3 segments plus the hole

        $%%%%%%%%%%%%%%%%%%%%%%%%%%%%%%%%%%%%%%%%%%%%%%%%%%%%%%%%%$
        $IIII   X = 1/2 width of tight-mesh region local to hole  $
        $        X should be neg.                                 $
        $FFFF   Y = 0.0 / should always be zero                   $
        $DDDD   Z = 1/2 length of slot  (should be neg.)          $
        $%%%%%%%%%%%%%%%%%%%%%%%%%%%%%%%%%%%%%%%%%%%%%%%%%%%%%%%%%$

GR,1#,,-.35/0/-.179

        $%%%%%%%%%%%%%%%%%%%%%%%%%%%%%%%%%%%%%%%%%%%%%%%%%%%%%%%%%$
        $DDDD   X = 1/2 width of tight-mesh region local to hole  $
        $        X,Z should be negative                           $
        $FFFF   Y = 0 / should always be zero                     $
        $DDDD   Z = 1/2 length of tight-mesh region local to hole $
        $%%%%%%%%%%%%%%%%%%%%%%%%%%%%%%%%%%%%%%%%%%%%%%%%%%%%%%%%%$

GR,1#,,-.35/0/-.679
LI,1#,2G,,17,18
LI,1#,2G,,15,18

        $%%%%%%%%%%%%%%%%%%%%%%%%%%%%%%%%%%%%%%%%%%%%%%%%%%%%%%%%%$
        $FFFF   X,Z = 0 / should always be zero                   $
        $DDDD   Y = 0.1 higher than Radius of the cylinder        $
        $%%%%%%%%%%%%%%%%%%%%%%%%%%%%%%%%%%%%%%%%%%%%%%%%%%%%%%%%%$

PA,1#,EXTRUDE,0/.8/0,7
PA,1#,EXTRUDE,0/.8/0,8

        $$$ Make lines at the intersection of the dividing patches
        $$$ with the base and the top face of the quadrant $$$

LI,1#,INT,,3,14
LI,1#,INT,,3,15

        $ Trim the dividing patches down to size

PA,1#,BREAK,9L,14
PA,17,D
PA,14,D
```

```
PA,1#,BREAK,10L,15
PA,15,D
PA,18,D

        $ Trim the hole patch down to size - you have to make
        $ lines to trim to first.

LI,1#,MERGE,,5/6
PA,1#,BREAK,11L,6
PA,6,D
PA,18,D
LI,1#,MERGE,,3/4
PA,1#,BREAK,12L,19
PA,19,D
PA,21,D
LI,2,DEL


$$$ MAKING THE PATCHES FOR THE FRONT FACE $$$$$$$$$$$$$$$$$$$$$$$$$$$$$

PA,1#,BR,P16,13
PA,13,D


$$$ MAKING THE PATCHES OF THE BASE $$$$$$$$$$$$$$$$$$$$$$$$$$$$$$$$$$$$
        $ Split the base in two.  Delete the original and
        $ delete the new patch near the hole.

PA,1#,BR,7L,4
PA,4,D
PA,23,D

        $ Make the two lines still needed for the two
        $ patches near the holes.  Then build those two
        $ patches from 4 lines.
        $%%%%%%%%%%%%%% Check the line numbers %%%%%%%%%%%%%%%%%$
        $ Be careful!!!! Depending on the size of the hole, Patran $
        $ might reverse lines 5 with 6 and 3 with 4.  If the model $
        $ doesn't initially run, this might be a problem.         $
        $%%%%%%%%%%%%%%%%%%%%%%%%%%%%%%%%%%%%%%%%%%%%%%%%%%%%%%%$

LI,1#,2G,,14,17
PA,1#,EDGE,,7/13/3/8
LI,2#,2G,,18/1,1/12
PA,1#,EDGE,,8/4/15/14


$$$ MAKING PATCHES OF BACK, LEFT FACE $$$$$$$$$$$$$$$$$$$$$$$$$$$$$$$$$
$$$ (Building patches from lines) $$$$$$$$$$$$$$$$$$$$$$$$$$$$$$$$$$$$$
        $ Break the top, curved face into two patches.

PA,1#,BREAK,9L,3
PA,3,D

        $ Make lines from the two new patches.

LI,1#,PATCH,4,27
LI,1#,PATCH,4,28

        $ Make a line parallel with y-axis.
        $ Then make a line parallel with x-axis.
        $%%%%%%%%%%%%%% Check the line numbers %%%%%%%%%%%%%%%%%$
        $ Be careful!!!! Depending on the size of the hole, Patran $
        $ might reverse points 22 and 23.  This also affects the  $
        $ reparameterizing.                                       $
        $%%%%%%%%%%%%%%%%%%%%%%%%%%%%%%%%%%%%%%%%%%%%%%%%%%%%%%%$
```

```
LI,1#,2G,,18,23
LI,1#,2G,,18,3

        $ Make a dummy line @ degenerate edge.

LI,1#,2G,,23,23

        $ Make patches from four edges.

PA,1#,EDGE,,19/18/20/17
PA,1#,EDGE,,14/1/16/18

        $ Get rid of original patch.

PA,1,D

$$$ MAKING PATCHES ON THE TOP, CURVED FACE $$$$$$$$$$$$$$$$$$$$$$$$$$$$$
        $ Make some lines to construct the patches.

LI,1#,2G,,2,6
LI,1#,PA,2,27
PA,27,DEL
LI,2#,BREAK,G11,21
LI,21/24,DEL
LI,2#,BREAK,G13,22
LI,22/24,DEL

        $ Make the two patches near the hole.
        $%%%%%%%%%%%%%% Check the line numbers %%%%%%%%%%%%%%%%%%%$
        $ Be careful!!!! Depending on the size of the hole, Patran $
        $ might reverse lines 5 with 6 and 3 with 4.  If the model $
        $ doesn't initially run, this might be a problem.          $
        $%%%%%%%%%%%%%%%%%%%%%%%%%%%%%%%%%%%%%%%%%%%%%%%%%%%%%%%%%$

PA,1#,EDGE,,9/25/5/10
PA,1#,EDGE,,10/6/23/16


$$$ MAKING THE HYPERPATCHES $$$$$$$$$$$$$$$$$$$$$$$$$$$$$$$$$$$$$$$$$$
        $ Build the hpat from the existing patches.
        $%%%%%%%%%%%%%%%%%%%%%%%%%%%%%%%%%%%%%%%%%%%%%%%%%%%%%%%%%$
        $ For HPAT 3:
        $FFFF   X,Y = 0 / should always be zero                    $
        $DDDD   Z = 1/2 (length of local region - slot length)     $
        $%%%%%%%%%%%%%%%%%%%%%%%%%%%%%%%%%%%%%%%%%%%%%%%%%%%%%%%%%$

HPAT,1,2P,,25,31
HPAT,2,2P,,26,32
HPAT,3,EXTRUDE,0/0/.5,29

$$$ THE GAGE LENGTH FROM THE HOLE TO THE ENDCAP $$$$$$$$$$$$$$$$$$$$$$$$

        $ Extrude the patches on the back, left side.
        $%%%%%%%%%% Length of the Gage Section %%%%%%%%%%%%%%%%%%%$
        $FFFF   X,Y = 0 / should always be zero                    $
        $IIII   Z = 1/2 length of gage section - 1/2 length of     $
        $          tight-mesh region local to hole                 $
        $%%%%%%%%%%%%%%%%%%%%%%%%%%%%%%%%%%%%%%%%%%%%%%%%%%%%%%%%%$

PA,2#,TRANS,0/0/-1.201,29/30
HPAT,4/5,2P,,30/29,34/33

$$$ MAKING THE PART OF THE BONE THAT GOES IN THE ENDCAPS $$$$$$$$$$$$
```

```
        $ Extrude the patches on the back, left side.  Make two
        $ HPATs from those two patches.  Then mirror those two
        $ HPATs to make the full eight HPATs.

        $%%%%%%%%% Length of the Endcap %%%%%%%%%%%%%%%%%%%%%%%%%%$
        $FFFF   X,Y = 0 / should always be zero                    $
        $IIII   Z = extruded length of the Endcap, neg. value      $
        $%%%%%%%%%%%%%%%%%%%%%%%%%%%%%%%%%%%%%%%%%%%%%%%%%%%%%%%%%$

PA,2#,TRANS,0/0/-3.81,33/34
HPAT,6/7,2P,,34/33,36/35

$$$ MAKING THE PMMA ENDCAPS $$$$$$$$$$$$$$$$$$$$$$$$$$$$$$$$$$$$$$$$$$$
$                                                                    $
$ The endcaps must overlap the bone such that the mesh of the        $
$ endcap and the mesh of the bone will match.  This means the        $
$ endcap mesh must also be properly defined.                         $
$                                                                    $
$$$$$$$$$$$$$$$$$$$$$$$$$$$$$$$$$$$$$$$$$$$$$$$$$$$$$$$$$$$$$$$$$$$$$$$$

        $ Make a point that defines the inner diameter of endcap
        $%%%%%%%%%%%%%%%%%%%%%%%%%%%%%%%%%%%%%%%%%%%%%%%%%%%%%%%%%$
        $FFFF   X = 0.0 / should always be zero                    $
        $DDDD   Y = Radius of the cylinder                         $
        $DDDD   Z = Beginning of the endcap.  Must equal 1/2       $
        $          length of the gage section.                     $
        $%%%%%%%%%%%%%%%%%%%%%%%%%%%%%%%%%%%%%%%%%%%%%%%%%%%%%%%%%$

GR,1#,,0/.635/-1.88

        $ Make second point that defines the thickness of endcap   $
        $%%%%%%%%%%%%%%%% Thickness of the Endcap %%%%%%%%%%%%%%%%$
        $FFFF   X = 0.0 / should always be zero                    $
        $IIII   Y = Radius of cylinder + thickness of endcap       $
        $DDDD   Z = Beginning of endcap (Z-value of point defined  $
        $          above)                                          $
        $%%%%%%%%%%%%%%%%%%%%%%%%%%%%%%%%%%%%%%%%%%%%%%%%%%%%%%%%%$

GR,1#,,0/1.27/-2

        $ Connect the two lines, sweep 90 degree arc, extrude the HP

LI,1#,2G,,34,35
PA,1#,ARC,0/0/0/0/0/1/90,26

        $%%%%%%%%%%%%%%%%%% Length of the Endcap %%%%%%%%%%%%%%%%%$
        $FFFF   X,Y = 0.0 / should always be zero                  $
        $DDDD   Z = length of endcap. Must equal length of endcap $
        $          as defined in the bone section above.          $
        $%%%%%%%%%%%%%%%%%%%%%%%%%%%%%%%%%%%%%%%%%%%%%%%%%%%%%%%%%$

HPAT,8,EXTRUDE,0/0/-3.81/0/0/0,37

        $ Break the HP into two segments corresponding to HP4 and
        $ HP5 so that it can have different appropriate mesh
        $ densities.  Make a line between HP4 and HP5,
        $ break HP41 at the line, and then get rid of the line

LI,1#,2G,,26,31
HP,8/9,BREAK,27L,8
Y
LI,27,DEL

$$$ THE FIXTURE $$$$$$$$$$$$$$$$$$$$$$$$$$$$$$$$$$$$$$$$$$$$$$$$$$$$$$$$
```

```
$ A fixture ring at the end of the endcap
PA,2#,HPAT,6,8/9
HP,10/11,EXTRUDE,//-.2,38/39

$ A fixture disk inside the ring
PA,2#,TRANSLATE,//-.1,35/36
HP,12/13,EXTRUDE,//-.1,41/40

$$$ THE SLOT $$$$$$$$$$$$$$$$$$$$$$$$$$$$$$$$$$$$$$$$$$$$$$$$$$$$$$$$$$

        $ Extrude the patches on the front side. Use the patch from
        $ from HP3 to create HP15 so that it will have the correct
        $ degenerate edge.

        $%%%%%%%%% Length of the Slot %%%%%%%%%%%%%%%%%%%%%%%%%%%%%%%$
        $FFFF   X,Y = 0 / should always be zero                     $
        $DDDD   Z = 1/2 (length of local region - slot length)      $
        $DDDD   Z = 1/2 extruded length of slot   (HPAT)            $
        $%%%%%%%%%%%%%%%%%%%%%%%%%%%%%%%%%%%%%%%%%%%%%%%%%%%%%%%%%%%%$

PA,#,TR,//.5,29
HPAT,14/15,EXTRUDE,//.179///,21/42

$$$ REPARAMATERIZING $$$$$$$$$$$$$$$$$$$$$$$$$$$$$$$$$$$$$$$$$$$$$$$$$$$
$ psi1 = -x (tan)                                                    $
$ psi2 = +y (rad)                                                    $
$ psi3 = -z (length)                                                 $
$$$$$$$$$$$$$$$$$$$$$$$$$$$$$$$$$$$$$$$$$$$$$$$$$$$$$$$$$$$$$$$$$$$$$$$$

HP,1 ,LAB,,14/13
HP,2 ,LAB,,12/11
HP,3 ,LAB,,17/22
HP,4 ,LAB,,1/2
HP,5 ,LAB,,18/23
HP,6 ,LAB,,27/28
HP,7 ,LAB,,25/26
HP,8 ,LAB,,28/35
HP,9 ,LAB,,26/37
HP,10,LAB,,33/38
HP,11,LAB,,31/39
HP,12,LAB,,50/51
HP,13,LAB,,48/49
HP,14,LAB,,55/54
HP,15,LAB,,56/57


$$$ MIRROR OCTANTS $$$$$$$$$$$$$$$$$$$$$$$$$$$$$$$$$$$$$$$$$$$$$$$$$$$$$
$ Mirror all 8 octants.  Then delete the unecessary endcaps.

HP,16 T30 ,MIRROR,Y,1 T15
HP,31 T45 ,MIRROR,Z,1 T15
HP,46 T60 ,MIRROR,Z,16T30
HP,61 T75 ,MIRROR,X,1 T15
HP,76 T90 ,MIRROR,X,16T30
HP,91 T105,MIRROR,X,31T45
HP,106T120,MIRROR,X,46T60


$ Delete the fixture disk inside the ring.  It won't be used.
HP,12/13/27/28/42/43/57/58/72/73/87/88/102/103/117/118,DEL


$ Delete the fixture ring on the bottom face.  Loads are only
$ applied through a ring at the top.
HP,40/41/55/56/100/101/115/116,DEL
```

```
$$$ MESHING THE FIRST OCTANT (1-5) $$$$$$$$$$$$$$$$$$$$$$$$$$$$$$$$$$$$$$$
$                                                                      $
$       H1  - right, inner segment, adjacent to hole                   $
$       H2  - left,  inner segment, adjacent to hole                   $
$       H3  - outside segment, behind H1                               $
$       H4  - inside  segment, in front of H4, along gage length       $
$       H5  - outside segment, beside H3, along gage length            $
$       H6  - inside  segment, in endcap                               $
$       H7  - outside segment, in endcap                               $
$       H8  - inside  segment of endcap                                $
$       H9  - outside segment of endcap                                $
$       H10 - inside  segment of fixture ring                          $
$       H11 - outside segment of fixture ring                          $
$       H12 - inside  segment of fixture disk                          $
$       H13 - outside segment of fixture disk                          $
$       H14 - inside  segment of slot                                  $
$       H15 - outside  segment of slot                                 $
$                                                                      $
$    OCTANTS:                                                          $
$           OCT1:   HP1   - HP15                                       $
$           OCT2:   HP16  - HP30 Reversed                              $
$           OCT3:   HP31  - HP45 Reversed                              $
$           OCT4:   HP46  - HP60                                       $
$           OCT5:   HP61  - HP75 Reversed                              $
$           OCT6:   HP76  - HP90                                       $
$           OCT7:   HP91  - HP105                                      $
$           OCT8:   HP105 - HP120 Reversed                             $
$                                                                      $
$    COORDS of OCT1:                                                   $
$           psi1 = /2/ /4/  = -X (usually tan)                         $
$           psi2 = 1/ /3/ /  = Y (usually rad)                         $
$           psi3 = / / / /9 = -Z (long axis)                           $
$                                                                      $
$    RULES:                                                            $
$                                                                      $
$    HP1 -  rad     1/3     you define                                 $
$            tan     2/4     you define                                $
$            z       9       you define                                $
$    HP2 -  rad     1/3     must match 1/3 of HP1, scale neg.          $
$            tan     2/4     you define                                $
$            z       9       must match 2/4 of HP1                     $
$    HP3 -  tan     1/3     must match 1/3 of HP1                      $
$            (-x)    2/4     you define must be even                   $
$            z       9       must match 9   of HP1                     $
$    HP4 -  rad     1/3     must match 1/3 of HP1                      $
$            tan     2/4     must match 2/4 of HP2                     $
$            z       9       you define                                $
$    HP5 -  tan     1/3     must match 1/3 of HP1                      $
$            (-x)    2/4     must match 2/4 of HP3                     $
$            z       9       must match 9   of HP4                     $
$    HP6 -  rad     1/3     must match 1/3 of HP1                      $
$            tan     2/4     must match 2/4 of HP2                     $
$            z       9       you define                                $
$    HP7 -  tan     1/3     must match 1/3 of HP1                      $
$            (-x)    2/4     must match 2/4 of HP3                     $
$            z       9       must match 9   of HP6                     $
$    HP8 -  rad     1/3     you define                                 $
$            tan     2/4     must match 2/4 of HP2                     $
$            z       9       must match 9   of HP6                     $
$    HP9 -  rad     1/3     must match 1/3 of HP8                      $
$            tan     2/4     must match 1/3 of HP1                     $
$            z       9       must match 9   of HP6                     $
$    HP10 - rad     1/3     must match 1/3 of HP8                      $
$            tan     2/4     must match 2/4 of HP2                     $
```

```
$              Z      9       you define                    $
$        HP11 - rad    1/3     must match 1/3 of HP8         $
$               tan    2/4     must match 1/3 of HP1         $
$               Z      9       must match 9   of HP10        $
$        HP12 - rad    1/3     must match 1/3 of HP1         $
$               tan    2/4     must match 2/4 of HP2         $
$               Z      9       equal half 9   of HP10/11     $
$        HP13 - tan    1/3     must match 1/3 of HP1         $
$               (-x)   2/4     must match 2/4 of HP3         $
$               Z      9       equal half 9   of HP10/11     $
$        HP14 - rad    1/3     must match 1/3 of HP1         $
$               tan    2/4     must match 2/4 of HP1         $
$               Z      9       you define                    $
$        HP15 - rad    1/3     must match 1/3 of HP1         $
$               tan    2/4     must match 2/4 of HP3         $
$               Z      9       must match 9   of HP14        $
$                                                            $
$$$$$$$$$$$$$$$$$$$$$$$$$$$$$$$$$$$$$$$$$$$$$$$$$$$$$$$$$$$$$$$$

$ Meshing Octants 1,4,6,7

ME,H1 /H46/H76/H91 ,HEX/20,N,4/4/4/4/3/ /2/ /2/
ME,H2 /H47/H77/H92 ,HEX/20,N,4/2/4/2/4/ / / / /2
ME,H3 /H48/H78/H93 ,HEX/20,N,4/2/4/2/3
ME,H4 /H49/H79/H94 ,HEX/20,N,4/2/4/2/5/ / / / /
ME,H5 /H50/H80/H95 ,HEX/20,N,4/2/4/2/5/ / / / /
ME,H6 /H51/H81/H96 ,HEX/20,N,4/2/4/2/4/ / / / /
ME,H7 /H52/H82/H97 ,HEX/20,N,4/2/4/2/4/ / / / /
ME,H8 /H53/H83/H98 ,HEX/20,N,1/2/1/2/4/ / / / /
ME,H9 /H54/H84/H99 ,HEX/20,N,1/4/1/4/4/ / / / /
ME,H10/H55/H85/H100,HEX/20,N,1/2/1/2/2/ / / / /
ME,H11/H56/H86/H101,HEX/20,N,1/4/1/4/2/ / / / /
ME,H12/H57/H87/H102,HEX/20,N,4/2/4/2/1/ / / / /
ME,H13/H58/H88/H103,HEX/20,N,4/2/4/2/1/ / / / /
ME,H14/H59/H89/H104,HEX/20,N,4/4/4/4/1/ /2/ /2/
ME,H15/H60/H90/H105,HEX/20,N,4/2/4/2/1/ / / / /

$ Meshing Octants 2,3,5,8

ME,H16T30/H31T45/H61T75/H106T120,HEX/20,ISO
1

$$$ NODE EQUIVALENCING $$$$$$$$$$$$$$$$$$$$$$$$$$$$$$$$$$$$$$$$$$$$$$$$$

EQUIV
       $ Tolerance = 0.005
N
       $ Use geometric equivalencing
2
       $ Apply to all nodes
1
       $ Have the active set reflect the changes
Y
            $$$ VERIFYING ELEMENTS $$$
5
       $ Verify elements
1
       $ Verify by shape
1
       $ Hex elements
5
       $ Verify all elements
1
       $ Exiting
```

```
8
3
7
7

$$$ ADDING MATERIAL PROPERTIES $$$$$$$$$$$$$$$$$$$$$$$$$$$$$$$$$$$$$$$$$$$$$$$$$

$ The bone's material properties
$ 1 GPa - 100000 N/cm^2

PMAT,1,ISO,100000,,.3
PFEG,H1T120,HEX/20,1

$ The endcaps' material properties
$ 50 GPa - 5000000 N/cm^2 - a composite of aluminum and PMMA

PMAT,2,ISO,5000000,,.3
PFEG,H8/9/23/24/38/39/53/54/68/69/83/84/98/99/113/114,HEX/20,2
S

$ The fixture's material properties

PMAT,3,ISO,2E11,,.3
PFEG,H10T13/25T28/40T43/55T58/70T73/85T88/100T103/115T118,HEX/20,3
S

$$$ BOUNDARY CONDITIONS - 4-POINT BEND, CONTROLLED LOAD = -39.4 N $
       $ 2.54 cm moment arm gives -1 Nm load
       $ Fix inner top left     in X
       $ fix inner top right    in X
       $ Fix outer lower left   in X and Y and Z
       $ Fix outer lower right  in X and Y

$DFEG,H8 ,DISP/N,0//,,N7041
$DFEG,H38,DISP/N,0//,,N7308
$DFEG,H23,DISP/N,0/0/0,,N7295
$DFEG,H53,DISP/N,0/0/,,N7206

$DFEG,H8 ,FORCE/N,0/-39.37/,,N7041
$DFEG,H38,FORCE/N,0/-39.37/,,N7308

$$$ BOUNDARY CONDITIONS - TORSION, CONTROLLED LOAD = 9.8 N $$$$$$$$$
$ Fix endcap on the bottom end (bone is not fixed).  Then apply a
$ distributed couple about the center of the fixture's end disk.
$ 2.54 cm moment arm gives 1 Nm load

DFEG,H38/39/53/54/98/99/113/114,DISP/N,0/0/0,,F6
DFEG,H10,FORCE/N,+9.843/  /,,N8055
DFEG,H11,FORCE/N,  /+9.843/,,N8199
DFEG,H85,FORCE/N,-9.843/  /,,N8106
DFEG,H86,FORCE/N,  /-9.843/,,N8288

$$$ BOUNDARY CONDITIONS - TENSION, CONTROLLED LOAD = 1 N $$$$$$$$$$
$ Fix endcap on the bottom end (bone is not fixed).  Then apply a
$ distributed tension load to the fixture's end disk and ring.
$ 0.0658 N/cm distributed over 15.2 cm gives a 1 N load.

$DFEG,H38/39/53/54/98/99/113/114,DISP/N,0/0/0,,F6
$DFEG,H10T11/25T26/70T71/85T86,PRES/E,//0.0658,,F6

$$$ REDRAW $$$$$$$$$$$$$$$$$$$$$$$$$$$$$$$$$$$$$$$$$$$$$$$$$$$$$$$$$$$$$$$

SET,LABE,OFF
NO,1T#,ERASE
```

```
PL
VI
1
45/235
PL
RUN,HIDE
4
DISP,1T#,PL
FORCE,1T#,PL
PRES,1T#,PL
```

$$$ CREATING OUTPUT THROUGH INTERFACE $$$$$$$$$$$$$$$$$$$$$$$$$$$$$$$$$


```
$5
$1
$1
$1
$4-POINT BEND OF BONE WITH 20% HOLE - VERSION 5
$Y
$Y
```

# Appendix D

# QCT Scanning

This appendix contains the protocol for the QCT scans and data analysis of the resulting image files. Following the protocol are two scripts for analyzing the data, the C program used to calculate the average CT numbers of the phantom hydroxyapatite rods, and the C program used to calculate the cross-sectional properties of the specimens from the QCT image files.

# Protocol for QCT Scanning and Analysis

## D.1 PREPARATION

1) Allow specimens to thaw for 45 minutes in the refrigerator.
2) Allow specimens to thaw in warm 0.9 % saline solution for 15 minutes.
3) Degass specimens with Labconco vacuum pump at 200 microns of Hg for 20 minutes or until bubbles become insignificant.
4) Move specimens to iced saline bath until scanning (approx. 3 hours).

## D.2 SCANNING

1) Use the wooden scanning gantry with acrylic specimen tubes and the following five solid hydroxyapatite phantoms, placed with respect to the front of the gantry as follows:
   - 0.05 g/cc lower left
   - 0.15 g/cc lower right
   - 0.518 g/cc center
   - 0.56 g/cc upper left
   - 1.518 g/cc upper right
2) Place specimens in acrylic tubes filled with iced saline bath, with the left end of each specimen always pointed forward.
3) Record the position of each specimen in the gantry and the scan number and name under which the scan set will be saved.
4) Scan on a GE High Speed Advantage Helical CT Scanner.
5) Place the gantry on the CT scanning table with the left front of the gantry facing towards the "left foot" of the table.
6) Configure the scanner so that "left" on the wooden gantry is "left" on the CT scan and so that the scan images are number sequentially, beginning with the "front" of the gantry.
7) Configure the scanner as follows:
   - Bone Algorithm
   - Small FOV option
   - 12 cm FOV (to encompass entire gantry)
   - 120 kV
   - 220 mA
   - 3 mm thick by 3 mm separation slices
8) Save the scans to a GE Optical WORM disk.

9) Remove the specimens from the gantry and store them in an iced saline bath until they can be wrapped in wet gauze and re-frozen.

# D.3  DATA TRANSFER

1) Using GE Optical 1.93 software on the MacIntosh, copy the scan files to OBL4-temp directory and from there to the obl3/gdc/ directory.
2) In the directory where the scans are stored, convert the scans to a series of short integer files (.sht) with the command:
   ■ medviz2raw #< filename
3) In AVS, determine which series of .sht files belong to which specimen. Separate the .sht files into separate directories for each specimen, but keep a master directory of scans.
4) Run the following batch file, to make a hard copy of the scans. Change the numbers to reflect the number of slices in the scan:

```
@ i = 1

foreach file (*.sht)
                sht2byt < $file | rawtopgm 512 512 | pgmnorm>! $i.pnm
                @ i += 1
end
@ i -= 1


                pnmcat -lr 1.pnm 2.pnm 3.pnm 4.pnm 5.pnm >! r1.pnm
                pnmcat -lr 6.pnm 7.pnm 8.pnm 9.pnm 10.pnm >! r2.pnm
                pnmcat -lr 11.pnm 12.pnm 13.pnm 14.pnm 15.pnm >! r3.pnm
                pnmcat -lr 16.pnm 17.pnm 18.pnm 19.pnm 20.pnm >! r4.pnm
                pnmcat -lr 21.pnm 22.pnm 23.pnm 24.pnm 25.pnm >! r5.pnm
                pnmcat -lr 26.pnm 27.pnm 28.pnm 29.pnm 30.pnm >! r6.pnm
                pnmcat -tb r1.pnm r2.pnm r3.pnm r4.pnm r5.pnm r6.pnm | \
                        pnminvert | pnmscale 0.5 | \
                        pnmdepth 255 | pnmtorast > ! all1.rs
                pnmcat -lr 31.pnm 32.pnm 33.pnm 34.pnm 35.pnm >! r1.pnm
                pnmcat -lr 36.pnm 37.pnm 38.pnm 39.pnm 40.pnm >! r2.pnm
                pnmcat -tb r1.pnm r2.pnm | \
                        pnminvert | pnmscale 0.5 | \
                        pnmdepth 255 | pnmtorast > ! all2.rs
lpr all1.rs all2.rs
\rm *pnm*
compress *rs*
```

# D.4  DETERMINE ANALYSIS PARAMETERS

1) Determine pixel size = FOV (120 mm) / FOV (512 pixels)
2) Load AVS network /qct/jah/avs/QCT/QCT_setup.net

3) Determine the coordinates of each chamber in the first and last slice of each scan.

4) Determine the region of interest for each specimen using QCT_rect_reg.net and stepping the cropped region of interest using the sleep button.

5) Create the centers.dat file, with the following data on each line:
   - pixel size in mm/pixel
   - threshold (always = 0)
   - diameter of phantoms (usually 10)
   - number of slices in the scan
   - number of phantom chambers
   - coords of centers of phantom chambers in first and last slices. Coords. for the lowest density chamber on the first line (x,y of first slice then x,y of last slice) followed by coords for the rest of the phantoms, one phantom per line.

## D.5 CHECK THE ANALYSIS PROGRAM

1) Load the /qct/jah/avs/SLICE/whpslice.net AVS network

2) Check to determine if the square region of interest adequately calculates bone properties compared to a "free-form" region of interest. Check the threshold. If the threshold is to be changed, then change it in gdc_hpslice.c and recompile the program before running the analysis.

3) Be sure that the density to modulus relation is also correct.

4) If the program needs to be recompiled, use the compile command list at the beginning of the C code.

NOTE: The following are analysis routines:

   - pslice:      for liquid phantoms
   - hpslice:     for solid phantoms
   - whpslice:    for solid phantoms, with loads to calc. failure data
   - dwhpslice:   for solid phantoms, with loads, for 3D field files

## D.6 PERFORM THE ANALYSIS

1) Run the following batch job:
   - \rm *.rig mask* pslice* *.sht.pslice
   - ls *.sht >! files.lst
   - whpslice_gen xmin ymin xmax ymax 0.0 0.0 1.0 0.0 0.0 0.0
   - foreach file (*.sht)
   - cat $file.whpslice >! whpslice.dat
   - /home/gdc/progs/gdc_hpslice < $file >>! whpslice_1.rig
   - cat mask.byt >>! mask.dat
   - end

2) NOTE: whpslice_gen requires the centers.dat file and creates .whpslice files which define the region of interest and the QCT numbers for each phantom. It requires the coords. of the region of interest as well as a force vector and a force application point. whpslice.dat contains

3) information necessary to run gdc_hpslice. gdc_hpslice is a routine modified from whpslice. It calculates certain structural properties given a .whpslice file for each scan slice and writes them to a .rig ASCII file. It requires a whpslice.dat file and needs a foce vector and load application vector to run.

4) The .rig file will contain a list of data (one line per slice) that includes:
   ■ area, cbone, tbone, avgden, avgmod, axrig, gixbar, ixbar, giybar, iybar, polar_moment, torrig)

5) NOTE: The following are the variables calculated in whpslice.C

| Variables | Meaning | Units |
| --- | --- | --- |
| cbone | cortical bone area | mm$^2$ |
| tbone | trabecular bone area | mm$^2$ |
| avgden | average density of all pixels above threshold | g/cc |
| avgmod | average modulus of all pixels above threshold | GPa |
| area | area of all pixels above threshold | mm$^2$ |
| axrig | axial rigidity | MN |
|  |  |  |
| gxbara | geometric centroid of specimen (pixels above threshold) | mm |
| gybara | " | mm |
| gix | moment of inertia about centroid of entire scan | mm$^4$ |
| giy | " | mm$^4$ |
| gixy | " | mm$^4$ |
| gixbar | moment of inertia about centroid of specimen | mm$^4$ |
| giybar | " | mm$^4$ |
| gixybar | " | mm$^4$ |
| polar_moment | " | mm$^4$ |
| gphi | orientation to principle axes based on geometry | radians |
| gixbph | minimum principle moment of inertia | mm$^4$ |
| giybph | maximum principle moment of inertia | mm$^4$ |
|  |  |  |
| xbara | center of mass of specimen | mm |
| ybara | " | mm |
| ix | rigidity about centroid of entire scan | Nm$^2$ |
| iy | " | Nm$^2$ |
| ixy | " | Nm$^2$ |
| torrig | " | Nm$^2$ |
| phi | orientation to principle axes based on mass distribution | radians |
| eimax | maximum principle bending rigidity | Nm$^2$ |
| eimin | minimum principle bending rigidity | Nm$^2$ |

```
cd qct_i2
foreach dir (*)
        cd $dir

        \rm whpslice* *.sht.whpslice *.*% left* *.lst

*****   ls *.sht >! files.lst
*****   /home/gdc/progs/whpslice_gen 75 190 190 305 0.0 0.0 1.0 0.0 0.0 0.0

        set temp=`pwd`_1.rig
        echo $temp
        echo "file       cbone      tbone     avgden    avgmod    axrig    gixbar    ixbar
        echo "           mm^2       mm^2      g/cc      GPa       MN       mm^4      Nm^2
        echo "512 512"               >>! left.region
        echo "75 190 190 305"        >>! left.region
        echo "0.2343000"             >>! left.region
        echo "0.00 0.00 1.00"        >>! left.region
        echo "0 0 100"               >>! left.region
        cat left.region $dir.phant >! left.whpslice
        cat left.whpslice >! whpslice.dat
        foreach file (*.sht)
                echo -n $file >>! $temp
                /home/gdc/progs/gdc_hpslice < $file >>! $temp
        end
        echo " " >>! $temp
        echo "WHPSLICE.DAT DATA" >>! $temp
        cat whpslice.dat >>! $temp
        \rm left.region
        cd ..
****    enscript -r $temp
end
```

```
cd qct_i2
foreach dir (*)
        cd $dir

        \rm whpslice* *.sht.whpslice *.*% right* *.lst

*****   ls *.sht >! files.lst
*****   /home/gdc/progs/whpslice_gen 320 190 435 305 0.0 0.0 1.0 0.0 0.0 0.0

        set temp=`pwd`_r.rig
        echo $temp
        echo "file        cbone       tbone       avgden      avgmod      axrig       gixbar      ixbar          ç
        echo "            mm^2        mm^2        g/cc        GPa         MN          mm^4        Nm^2
        echo "512 512"               >>! right.region
        echo "320 190 435 305"       >>! right.region
        echo "0.2343000"             >>! right.region
        echo "0.00 0.00 1.00"        >>! right.region
        echo "0 0 100"               >>! right.region
        cat right.region $dir.phant >! right.whpslice
        cat right.whpslice >! whpslice.dat
        foreach file (*.sht)
                echo -n $file >>! $temp
                /home/gdc/progs/gdc_hpslice < $file >>! $temp
        end
        echo " " >>! $temp
        echo "WHPSLICE.DAT DATA" >>! $temp
        cat whpslice.dat >>! $temp
        \rm right.region
        cd ..
****    enscript -r $temp
end
```

```
/**********************************************************************/
/*                                                                    */
/*      COPYRIGHT NOTICE:  This software was written and/or developed  */
/*      by John A. Hipp, Ph.D. at the Orthopaedic Biomechanics Lab     */
/*      of Beth Israel Hospital and Harvard Medical School.            */
/*                                                                    */
/**********************************************************************/
/*                                                                    */
/*      It may NOT BE USED without the EXPRESS consent of John Hipp.   */
/*                                                                    */
/**********************************************************************/
/*  This program reads all of the images in a QCT exam, and calculates
    average CT numbers for the phantom chambers - it then writes the
    data for each slice to a whpslice parameter file.

        Programs expects a file named files.lst conmtaining the
        filenames for the short integer image arrays for each slice

        It also expects a file called centers.dat containing
                the pixel size,
                the threshold (ideal CT # for water),
                the diameter of the chambers (in mm),
                the number of slices, and
                the number of chambers.
    The next lines contain the
    coordinates of the centers of the phantom chambers for the
    first and last slices in the exam.  The program uses these
    coordinates to find the centers of the chambers in all slices

        Compile the program using

                cc whpslice_gen.c -o whpslice_gen -O3 -Bdynamic -lm

        Call the program using

                whpslice_gen xmin ymin xmax ymax Fx Fy Fz rx ry rz
*/

#include <stdio.h>
#include <math.h>
char *calloc();

FILE *fp, *fps, *fpo;

double shiftx[6], shifty[6];
int xcent_first[6], ycent_first[6], xcent_last[6], ycent_last[6];
char fname[64];

main(argc,argv)
int argc;
char *argv[];
{

double pixel_size, diameter, dx, dy, dist, xcent, ycent;
double csx,csxx,mean,sd;
double Fx, Fy, Fz, zpos;
int rx, ry, rz;
int i, j, k, row, col, nslices, nchambers, threshold, cnt;
int xstr, xend, ystr, yend, pixval, xmin, ymin, xmax, ymax;
short *image;

if((image = (short *)calloc((512 * 512), sizeof(short))) == NULL) {
        fprintf(stderr,"ERROR: could not get memory for images\n");
        exit(-1);
```

```c
        }
/* check for proper command line paramaters */
if(argc != 11) {
        fprintf(stderr,"ERROR: wrong command line format\n\n");
        fprintf(stderr,"use: whpslice_gen xmin ymin xmax ymax Fx Fy Fz rx ry rz\n");
        exit(-1);
        }

xmin = atoi(argv[1]);
ymin = atoi(argv[2]);
xmax = atoi(argv[3]);
ymax = atoi(argv[4]);
Fx = atof(argv[5]);
Fy = atof(argv[6]);
Fz = atof(argv[7]);
rx = atoi(argv[8]);
ry = atoi(argv[9]);
rz = atoi(argv[10]);

if((fp = fopen("centers.dat","r")) == NULL) {
        fprintf(stderr,"ERROR: could not find data file centers.dat\n");
        exit(-1);
        }

fscanf(fp,"%lf",&pixel_size);
fscanf(fp,"%d",&threshold);
fscanf(fp,"%lf",&diameter);
fscanf(fp,"%d",&nslices);
fscanf(fp,"%d",&nchambers);

for(i=0;i<nchambers;i++) {
        fscanf(fp,"%d %d %d %d",
                &xcent_first[i],&ycent_first[i],
                &xcent_last[i],&ycent_last[i]);
        shiftx[i] = (double)(xcent_last[i] - xcent_first[i]) /
                        (double)nslices;
        shifty[i] = (double)(ycent_last[i] - ycent_first[i]) /
                        (double)nslices;
        }


fclose(fp);

if((fp = fopen("files.lst","r")) == NULL) {
        fprintf(stderr,"ERROR: could not find list of files files.lst\n");
        exit(-1);
        }
/*fprintf(stderr,"psize= %lf, thresh = %d, diam = %lf, nslices = %d, nchamb = %d\n",pixel_size
for(i=0;i<nslices;i++) {

        fscanf(fp,"%s",fname);
        if((fps = fopen(fname,"rb")) == NULL) {
                fprintf(stderr,"ERROR: could not findimage file %s\n",fname);
                exit(-1);
                }

        j = fread((char *)image,sizeof(short),(512 * 512),fps);
        if(j != (512 * 512)) {
                fprintf(stderr,"ERROR: Only found %d pixels for %s\n",
                        j,fname);
                exit(-1);
                }
        fclose(fps);
```

```c
        strcat(fname,".whpslice");
        fpo = fopen(fname,"w");
        fprintf(fpo,"512 512\n");
        fprintf(fpo,"%d %d %d %d\n",xmin,ymin,xmax,ymax);
        fprintf(fpo,"%lf\n",pixel_size);
        fprintf(fpo,"%lf %lf %lf\n",Fx,Fy,Fz);
        rz = i * 3;
        fprintf(fpo,"%d %d %d\n",rx,ry,rz);

        for(j=0;j<nchambers;j++) {
                csx = csxx = 0.000000000000;
                cnt = 0;
                xcent = xcent_first[j] + (double)i * shiftx[j];
                ycent = ycent_first[j] + (double)i * shifty[j];

                xstr = xcent - (diameter / pixel_size) / 2.0;
                xend = xcent + (diameter / pixel_size) / 2.0;
                ystr = ycent - (diameter / pixel_size) / 2.0;
                yend = ycent + (diameter / pixel_size) / 2.0;

                for(col = xstr; col < xend; col++) {
                        for(row = ystr; row < yend; row++) {

                                dx = xcent - col;
                                dy = ycent - row;
                                dist = sqrt(dx * dx + dy * dy);
                                if(dist <= (diameter / 2.0)) {
                                        pixval = *(image + 512 * row + col);
                                        if(pixval > threshold) {
                                                csx  += pixval;
                                                csxx += pixval * pixval;
                                                cnt++;
/*                                              *(image + 512 * row + col) =
                                                        4000;*/
                                        }

                                }
                        }
                }

                mean = csx / (double)cnt;
                sd = sqrt((cnt * csxx - csx * csx) /
                                ((double)cnt * (cnt - 1)));

                fprintf(fpo,"%5.0lf\n",mean);

        }
        fclose(fpo);
/*      strcat(fname,"zzz");
        fps =fopen(fname,"wb");
        fwrite((char *)image,sizeof(short),(512 * 512),fps);

        fclose(fps);*/

        }
fclose(fp);
}
```

```
/**********************************************************************/
/*                                                                    */
/*      COPYRIGHT NOTICE:  This software was written and/or developed  */
/*      by John A. Hipp, Ph.D. at the Orthopaedic Biomechanics Lab     */
/*      of Beth Israel Hospital and Harvard Medical School.            */
/*                                                                    */
/**********************************************************************/
/*                                                                    */
/*      It may NOT BE USED without the EXPRESS consent of John Hipp.   */
/*                                                                    */
/**********************************************************************/
/*      whpslice uses a nearest neighbor approach to determining if a pixel
        is trabecular or cortical bone.
        Prior to running this program, you must create an ascii file
        named pslice.dat with the following format:

                X_size Y_size
                xmin ymin xmax ymax
                pixel_size
                CT# 0 mg/cc HA
                CT# 50 mg/cc HA
                CT# 150 mg/cc HA
                CT# 500 mg/cc HA
                CT# 1000 mg/cc HA
                CT# 1500 mg/cc HA


        where X_size and Y_size are the overall array size,
        xmin, ymin, xmax and ymax define the rectangular subregion of
        interest, pix size is the actual pixel size in mm,
        The CT#'s are the CT#'s for the six phantom chambers, from
        which the program will calculate the linear regression between
        CT# and HA density

        The relationship between bone density and modulus is hard coded.

        The relationship between houndsfield units and density is hard coded.

        The array is passed to the program via stdin and the results
        are written to stdout

        compile:

                cc gdc_hpslice.c -o gdc_hpslice -lm -lMath++
*/


#include <stdio.h>
#include <math.h>
#include </usr/local/Math++/Math++.h>
double sqrt();
double pow();
double sin();
double acos();
double fabs();
double log10();


char *calloc();
FILE *fpd, *fpi, *fpo;
int ctnums[6];

/* solid HA phantom chamber densities in gm/cc */
/*double kdens[6] =
```

```c
{0.00000000, 0.0500000000, 0.150000000, 0.518000000, 1.05600000,
1.5560000}; manufacturer's best guess */

/*   adjusted manufacturers specs based on analysis of 419 slices
double kdens[6] =
{0.00487000, 0.0432000000, 0.142000000, 0.526000000, 1.07100000,
1.5440000}; */

/* ash densities physically measured from 3 specimens of each rod */
/* measurements were made by Matt Silva. This change made 07-06-95 */

/* double kdens[6] =
{0.00300000, 0.0780000000, 0.178000000, 0.538000000, 1.04800000,
1.5970000}; */

double kdens[6] =
{0.0780000000, 0.178000000, 0.538000000, 1.04800000,
1.5970000};

main()
{
double slope, yintcp, pslope, pyintcp, r;
double avgct, avgden, avgmod, modulus, modsum, axrig;
double density, area, phi, gphi;
double x,y,da,ix,iy,ixy, dx, dy, dz, zx, zy, FFZ;
double gxbara,gybara,gixbar,giybar,gixbyb,gixbph,giybph;
double gix,giy,gixy;
double xbara,ybara,ixbar,iybar,ixbyb,ixbph,iybph, eimax, eimin;
double sumx,sumy,sumyy,sumxy,sumxx,sxx,syy,sxy;
double Fx, Fy, Fz, pixel_size;
double fstress, stress, dval, cstress, bstress, astress, strain;
double max_strain, min_strain, max_cstress, min_cstress, max_stress, min_stress;
double a[3][3], b[3];
double polar_moment, torrig;

/* Threshold values go here */

float bone_thresh_gpercc = 0.13;        /* app density threshold for bone - notbone g/cc */
float cthresh = 1.5;                    /* threshold for seperating cbone & tbone */

float *image, pixval, tpix, hipix, tbone, cbone;
float *temp2;
unsigned char *flip;
int rx, ry, rz;
int i,j,got,row,col,X_size,Y_size,X_min,Y_min,X_max,Y_max, nchamb;
int pixcnt, totcnt,idens;
int ipvt[3], maxdim, order;
short *temp;

/* Read in the parameters, and exit with error msg if not found */

if((fpd = fopen("whpslice.dat","r")) == NULL) {
        fprintf(stderr,"ERROR: the parameter file - whpslice.dat was not found\n");
        fprintf(stderr,"You must first create this file\n");
        exit(-1);
        }


fscanf(fpd,"%d %d",&X_size,&Y_size);
fscanf(fpd,"%d %d %d %d",&X_min,&Y_min,&X_max,&Y_max);
fscanf(fpd,"%lf",&pixel_size);
fscanf(fpd,"%lf %lf %lf",&Fx,&Fy,&Fz);
fscanf(fpd,"%d %d %d",&rx,&ry,&rz);
```

```c
nchamb = 0;
while(!feof(fpd)) {
        fscanf(fpd,"%d",&ctnums[nchamb]);
        nchamb++;
        }

fclose(fpd);
nchamb--;

/* fprintf(stderr,"%d %d %d %d %d %d\n",X_size, Y_size, X_min, Y_min, X_max, Y_max);
fprintf(stderr,"%lf %lf %lf %d %d %d %d\n",Fx,Fy,Fz,rx,ry,rz,ctnums[2]); */

/* allocate memory for data and temp image storage */

temp = (short *)calloc(X_size,sizeof(short));
temp2 = (float *)calloc(X_size * Y_size,sizeof(float));
flip = (unsigned char *)calloc(X_size,sizeof(char));
image = (float *)calloc(X_size * Y_size,sizeof(float));
if(image == NULL || temp == NULL || temp2 == NULL || flip == NULL) {
 fprintf(stderr,"ERROR: could not allocate memory for temporary image storage\n");
 exit(-1);
 }

fpi = stdin, fpo = stdout;

/* zero out the temp2 array */
for(row = 0; row < Y_size; row++) {
        for(col = 0;col < X_size; col++) *(temp2 + row * X_size + col) = 0.0000000;
        }

/* calculate the slope and y-intercept for the linear regression relating
 CT# to K2HPO4 density */

sumx = sumy = sumxy = sumxx = sumyy = 0.000000000000;
for(i=0;i<nchamb;i++) {
        sumx += (double)ctnums[i];
        sumy += kdens[i];
        sumxy += (double)ctnums[i] * kdens[i];
        sumxx += (double)ctnums[i] * (double)ctnums[i];
        sumyy += kdens[i] * kdens[i];
        }
pslope = ((double)nchamb * sumxy - sumx * sumy) / ((double)nchamb * sumxx - sumx * sumx);
pyintcp = sumy / (double)nchamb - pslope * sumx / (double)nchamb;
sxx = sumxx - (sumx * sumx) / (double)nchamb;
syy = sumyy - (sumy * sumy) / (double)nchamb;
sxy = sumxy - (sumx * sumy) / (double)nchamb;
r = (sxy * sxy) / (sxx * syy);

fprintf(stderr,"Phantom(%d chambers): %3.2e %.3f %.3f\n",nchamb,pslope,pyintcp,r);

if(r < 0.925) {
        fprintf(stderr,"ERROR: phantom data are not good - check CT#'s\n");
        exit(-1);
        }

/* read in the entire image array, and convert CT numbers to density */

avgct = 0.0;
avgden = 0.0;
pixcnt = 0;
for(row = 0; row < Y_size; row++) {
got = fread((char *)temp,sizeof(short),X_size,fpi);
if(got < X_size) {
        fprintf(stderr,"ERROR: out of input data at y = %d (%d)\n",row,got);
```

```c
                exit(-1);
                }
if(row >= Y_min && row < Y_max) {
        for(col = X_min; col < X_max; col++) {
                pixval = (float)*(temp + col);
                avgct += pixval;
                /* convert CT# to HA density(gm/ml) */
                pixval = pslope * pixval + pyintcp;
                avgden += pixval;
                *(image + X_size * row + col) = pixval;
                if(pixval > bone_thresh_gpercc) pixcnt++;
                }
        }
}

avgden /= (double)pixcnt;
avgct = avgct / (double)pixcnt;

/* fprintf(stderr,
        "Whole box(%d pixs)- Average ct num is %lf average den is %lf\n",
                pixcnt, avgct, avgden); */


fclose(fpi);

/* loop over the rows of the entire array */
avgden = 0.0000000000;
avgmod = 0.0000000000;
area = 0.0000000000;
axrig = 0.0000000000;
gxbara = 0.0000000000;
gybara = 0.0000000000;
gix = 0.0000000000;
giy = 0.0000000000;
gixy = 0.0000000000;
gixbph = 0.0000000000;
giybph = 0.000000000;
gphi = 0.0000000000;
xbara = 0.0000000000;
ybara = 0.0000000000;
ix = 0.0000000000;
iy = 0.0000000000;
ixy = 0.0000000000;
zx = 0.0000000000;
zy = 0.0000000000;
totcnt = 0000000000;
pixcnt = 0000000000;
ixbph = 0.0000000000;
iybph = 0.000000000;
phi = 0.0000000000;
tbone = 0.0000000000;
cbone = 0.000000000;

da = pixel_size * pixel_size;
/* fprintf(stderr,"pixel_size = %f; da = %lf, thresh = %f\n",pixel_size,da, bone_thresh_gpe:

for(row = Y_min; row < Y_max; row++) {
 for(col = X_min; col < X_max ; col ++) {
        totcnt++;

        /* this is where any thresholding is installed */

        pixval = *(image + row * X_size + col);
        if(pixval > bone_thresh_gpercc) {
```

```c
                avgden += (double)pixval;

/* this is where the algorithm relating modulus and density is installed */

                /* density is in gm/cm3, modulus in N/mm2 */

                /* Keller manuscript E (GPa) = 10.5 * (ash density) ** 2.57 */
                /* Whale modulus based on compressive tests by James Hong in '95
                where E (GPa) = 7.584 (ash density)**2 + 0.9403 (ash density) */

                density = (double)pixval;
                if(density < cthresh) tbone += 1.0;
                else cbone += 1.0;

                modulus = (7584.0 * pow(density,2.0) + 940.3 * density);
                avgmod += modulus;
                x = ((double)col - 0.5) * pixel_size;
                y = ((double)row - 0.5) * pixel_size;

                /* calculate */
                axrig += da * modulus;
                area += da;
                gxbara += x * da;
                gybara += y * da;
                gixy += x * y * da;
                giy += x * x * da;
                gix += y * y * da;
                xbara += x * da * modulus;
                ybara += y * da * modulus;
                ixy += x * y * da * modulus;
                iy += x * x * da * modulus;
                ix += y * y * da * modulus;
                zx += x * da * modulus;
                zy += y * da * modulus;
                pixcnt++;
                } /* end if pixval > threshold */

        }               /* end col loop */

}                       /* end row loop */


/* calculate the cross sectional properties */

if(pixcnt > 10) {
        avgmod /= pixcnt;
        avgden /= pixcnt;
        gxbara /= area;
        gybara /= area;
        gixbar = gix - area * gybara * gybara;
        giybar = giy - area * gxbara * gxbara;
        gixbyb = gixy - area * gxbara * gybara;
        polar_moment = giybar + gixbar;
        gphi = 0.5 * atan2((2.0 * gixbyb),(gixbar-giybar));
        gixbph = gixbar *
                (cos(gphi) * cos(gphi)) + giybar *(sin(gphi) * sin(gphi));
        gixbph += gixbyb * sin(2.0 * gphi);
        giybph = giybar *
                (cos(gphi) * cos(gphi)) + gixbar *(sin(gphi) * sin(gphi));
        giybph -= gixbyb * sin(2.0 * gphi);
        giybph = fabs(giybph);
        xbara /= axrig;
        ybara /= axrig;
        ixbar = ix - axrig * ybara * ybara;
```

```
                iybar = iy - axrig * xbara * xbara;
                ixbyb = ixy - axrig * xbara * ybara;
                torrig = iybar + ixbar;

                phi = 0.5 * atan2((2.0 * ixbyb),(ixbar-iybar));
                ixbph = ixbar * (cos(phi) * cos(phi)) + iybar *(sin(phi) * sin(phi));
                ixbph += ixbyb * sin(2.0 * phi);
                iybph = iybar * (cos(phi) * cos(phi)) + ixbar *(sin(phi) * sin(phi));
                iybph -= ixbyb * sin(2.0 * phi);
                iybph = fabs(iybph);
                }
if(ixbph > iybph) {
                eimax = ixbph;
                eimin = iybph;
                phi += M_PI / 2.0;
                }
else {
                eimax = iybph;
                eimin = ixbph;
                }
ixbph = eimin;
iybph = eimax;
if(gixbph > giybph) {
                x = gixbph;
                gixbph = giybph;
                giybph = x;
                gphi += M_PI / 2.0;
                }


if(pixcnt > 10) {
                /* convert the results to more presentable units */
                avgmod /= 1000.0;        /* average modulus in GPa */
                axrig /= 1000000.0;      /* axial rigidity in N * 10**6 */
                ix /= 1000000.0;         /* bending rigidities in N-m**2 */
                iy /= 1000000.0;
                ixy /= 1000000.0;
                torrig /= 1000000.0;
                ixbar /= 1000000.0;
                iybar /= 1000000.0;
                ixbph /= 1000000.0;      /* min bend rigidity in n-m**2 */
                iybph /= 1000000.0;      /* max bend rigidity in n-m**2 */


                /* write the data out */
                tbone *= da;
                cbone *= da;
                phi *= 360.0/(2.0 * M_PI);
                }                                       /* end loop over if pixcnt > 10 */

fprintf(fpo," %4.3e %4.3e %4.3e %4.3e %4.3e %4.3e %4.3e %4.3e %4.3e %4.3e %4.3e\n",
cbone,tbone,avgden,avgmod,axrig,gixbar,ixbar,giybar,iybar,polar_moment,torrig);
/*fprintf(fpo,"%f %f %lf %lf %lf %lf %lf %lf %lf %lf %lf\n",
cbone,tbone,avgden,avgmod,axrig,gixbar,ixbar,giybar,iybar,polar_moment,torrig); */

fclose(fpo);
}
```